

### LIBRARY Michigan State University

This is to certify that the

dissertation entitled

The Velocity and Vorticity Fields of a Single Stream Shear Layer

presented by

Scott C. Morris

has been accepted towards fulfillment of the requirements for

Ph.D. degree in Engineering

Date 6 May 2002

MSU is an Affirmative Action/Equal Opportunity Institution

0-12771

## PLACE IN RETURN BOX to remove this checkout from your record. TO AVOID FINES return on or before date due. MAY BE RECALLED with earlier due date if requested.

DATE DUE	DATE DUE	DATE DUE
	· · · · · ·	

6/01 c:/CIRC/DateDue.p65-p.15

# THE VELOCITY AND VORTICITY FIELDS OF A SINGLE STREAM SHEAR LAYER

Ву

Scott C. Morris

#### A DISSERTATION

Submitted to

Michigan State University
in partial fulfillment of the requirements
for the degree of

DOCTOR OF PHILOSOPHY

Department of Mechanical Engineering

2002

#### **ABSTRACT**

### THE VELOCITY AND VORTICITY FEILDS OF A SINGLE STREAM SHEAR LAYER

By

#### Scott C. Morris

Measurements of velocity and vorticity have been acquired in a large scale single stream shear layer. These data provided information regarding the nature of turbulent fluid flow at a relatively high Reynolds number. The Reynolds number dependence of phenomena is important given that many technological applications involve Reynolds numbers that are higher than those which are typically achieved in the laboratory. The use of the vorticity vector as an alternative variable to the velocity vector provides additional insight into the nature of these phenomena. Single and multi point measurements of both the velocity and vorticity have allowed the examination and comparison of the different scales of motion. The research project was effectively divided into two parts. The first involves the very near separation region in which a turbulent boundary layer separates at zero pressure gradient at a 90 degree edge. The measurements have shown the existence of a "subshear" layer.. The vorticity that participates in the first instability is found to originate from the very near wall region. At larger y values, the separated turbulent boundary layer convects downstream adjacent to the sub-shear layer, "seemingly unaware" of the separation. The second part of the research involves measurements in the developed region of the shear layer. Several conclusions have been drawn from these data. For example, it has been shown that the dimensionless vorticity fluctuations do not scale in a self-similar way, but increase with Reynolds number. The cause of this is related to the large scale motions of the flow that lead to nonzero spatial correlations in vorticity over relatively large length scales.

DEDICATED TO THE MEMORY OF MY FATHER, JOHN E. MORRIS

#### **ACKNOWLEDGMENTS**

I would like to thank my committee members, Charles Petty, Ahmed Naguib,

Manoochehr Koochesfahani, C.Y. Wang, and John Foss for their contributions and comments on this research. Special thanks goes to my advisor, John Foss, for providing me with an environment in which creativity and ideas can be explored.

I would also like to thank a number of my colleges whom I have worked with over the last several years. This includes Dr. Alptekin Aksan, Dr. Paul Hoke, Doug Neal, Richard Prevost, Al Lawrenz, Matt Maher, and many others who helped with the assembly of the shear layer facility.

Lastly, I thank my wife Yvonne, and son John. Research would not be worth the trouble if it weren't for family.

#### TABLE OF CONTENTS

List	of Figur	res	vii
List	of Table	es	xii
Nom	enclatu	re	xiii
1.0	Intro	duction	1
2.0	Expe	erimental Apparatus and Techniques	8
	2.1	The Single Stream Shear Layer Facility	
	2.2	Hot-wire Techniques and processing	
		2.2.1 Calibration	
		2.2.2 X-wire probe calibration and processing	13
		2.2.3 Multi-sensor Probe Configurations and Processing	15
3.0	Turb	ulent Boundary Layer to Single Stream Shear Layer	28
	3.1	Introduction	28
	3.2	Upstream Boundary Layer	31
		3.2.1 Boundary Layer - Shear Layer "Communication"	
		3.2.2 Boundary Layer Statistics Near x=0	33
	3.3	Point Statistics And The "Sub-shear Layer"	37
	3.4	Shear Layer Diagnostics From Entrainment Measurements	41
		3.4.1 Convection Speed of the Coherent Motions	
		3.4.2 Spectral Properties of the Entrainment Stream	
		3.4.3 The Initial Instability	
	3.5	Spanwise Correlation Field of the Near Separation Region	
		3.5.1 Example realizations in the irrotational stream	
		3.5.2 Correlation Coefficient Data	
	3.6	Summary and Conclusions	55
4.0	The l	Developed Single Stream Shear Layer	88
	4.1	Introduction	88
		4.1.1 Motivation and literature survey	89
		4.1.2 Measurement program	92
	4.2	The Velocity Field	94
		4.2.1 Integral constraints on the mean flow	
		4.2.2 Velocity in Self-Similar Coordinates	
		4.2.3 Profiles of the velocity gradient variance	
	4.3	Statistics of the Vorticity Field	
		4.3.1 Examples of Vorticity Time Series	
		4.3.2 Histograms of Vorticity	
		4.3.3 Profiles of the Vorticity RMS	
	4.4	Analysis of the Reynolds Stress	116

4.5	Turbu	lent Kinetic Energy	120
	4.5.1	Dissipation Measurements	121
	4.5.2	Measurement of Kinetic Energy Budget	127
4.6	The So	cales of Turbulent Motion	129
	4.6.1	Correlation measurements of velocity and vorticity	129
	4.6.2	Spectral representation of velocity and vorticity	137
4.7	Circul	ation Density	143
	4.7.1	Experimental Configuration	147
	4.7.2	Circulation Density Results	148
4.8	Concl	usions	150
Appen	dix A		193
REFEI	RENCE	S	197

#### LIST OF FIGURES

Figure 1.1 Idealized schematic of the single stream shear layer geometry	7
Figure 2.1 Primary flow delivery system	21
Figure 2.2 Schematic of SSSL facility	22
Figure 2.3 Geometry of single hot-wire probe	23
Figure 2.4 Schematic of Calibration Facility	24
Figure 2.5 Sample calibration and fit, $\gamma$ =0 degrees.	24
Figure 2.6 Geometry of the X-wire probe	25
Figure 2.7 Example of the locating algorithm of the intersection point for X-wire	
processing.	25
Figure 2.8 Predicted values of angle (γ) from re-processed calibration data at	
nominal values of 18, 0, and -30 degrees.	25
Figure 2.9 Schematic of spanwise vorticity probe	26
Figure 2.10 Schematic of micro-circulation used for the spanwise vorticity calculation	126
Figure 2.11 Schematic of the streamwise vorticity probe.	27
Figure 2.12 Schematic of the multiple X-wire probe.	27
Figure 3.1 Schematic representation of near separation region.	63
Figure 3.2 Boundary Layer Mean Velocity.	63
Figure 3.3 Boundary Layer Velocity RMS	64
Figure 3.4 Mean and RMS of vorticity at separation.	64
Figure 3.5 Spectrum of vorticity fluctuations at $y/\delta=0.6$ .	65
Figure 3.6 Sample flow visualization of the near separation region.	65
Figure 3.7 Figure of flow regions; not to scale.	66
Figure 3.8 Mean velocity profiles for 0 <x td="" θo<100<=""><td>66</td></x>	66
Figure 3.9 Contour plot of mean velocity,	67
Figure 3.10 RMS of velocity for 0 <x td="" θo<100<=""><td>67</td></x>	67
Figure 3.11 Contour plot of velocity RMS	68
Figure 3.12 Streamwise evolution of velocity histogram at constant $y/\theta o=2.0$	68
Figure 3.13 Momentum thickness vs. x/θo.	69
Figure 3.14 Maximum velocity gradient vs. x/θo	69
Figure 3.15 Peak value of velocity r.m.s as a function of streamwise location	70

Figure 3.16 Convection velocity of spanwise motions.	70
Figure 3.17 Fourier transform of all 12 streamwise locations measured	71
Figure 3.18 Sample of the autocorrelation function in the entrainment stream,	
at x/θo=7.17	71
Figure 3.19 Streamwise variation in peak frequency.	72
Figure 3.20 Non-dimensional frequency vs. x/θo	72
Figure 3.21 Time series samples from $x/\theta o=0.73$ .	73
Figure 3.22 Autocorrelations of the time series at $x/\theta o=0.73$	73
Figure 3.23 Histogram of observed frequencies from short time autocorrelations	74
Figure 3.24 Comparison between tanh function shown and the velocity data at	
x/θo=0.73	74
Figure 3.25 Schematic of 8 wire rake in shear layer.	75
Figure 3.26 Velocity fluctuations at $x/\theta o=3.53$ , $y/\theta o=-3.7$	76
Figure 3.27 Velocity fluctuations at $x/\theta o=12.0$ , $y/\theta o=-5.37$	77
Figure 3.28 Velocity fluctuations at $x/\theta o=40.5$ , $y/\theta o=-10.9$	78
Figure 3.29 Velocity fluctuations at $x/\theta o=84.2$ , $y/\theta o=-19.6$	79
Figure 3.30 Spanwise correlation coefficient of the data shown in Figures 3.26	
through 3.29.	80
Figure 3.31 Spanwise correlation field at $x/\theta o=3.53$ .	81
Figure 3.32 Spanwise correlation field at $x/\theta o=12.0$	82
Figure 3.33 Spanwise correlation field at x/θo=40.6	83
Figure 3.34 Spanwise correlation field at x/θo=87.2	84
Figure 3.35 Correlation coefficient at Δz/θo=2.08.	85
Figure 3.36 Correlation coefficient at $\Delta z/\theta$ 0=4.16. See Figure 3.31 for description.	86
Figure 3.37 Correlation coefficient at $\Delta z/\theta$ 0=6.24. See Figure 3.31 for description.	86
Figure 3.38 Correlation coefficient at $\Delta z/\theta o=8.32$ . See Figure 3.31 for description.	86
Figure 3.39 Correlation coefficient at $\Delta z/\theta$ 0=14.5. See Figure 3.31 for description.	87
Figure 4.1 Schematic of control volume and coordinate system used in Section 4.1.	
Note that the growth rate is not shown to scale.	161
Figure 4.2 Illustration of the physical interpretation of $\delta^*$ in the shear layer	161
Figure 4.3 Schematic of the un-tilted coordinates (left and the tilted coordinates	
(right) for use in similarity analysis	162

Figure 4.4 Streamwise mean velocity f(η)	.162
Figure 4.5 Lateral mean velocity: $g(\eta)$ in tilted and untilted coordinates.	.163
Figure 4.6 Root mean square of the streamwise velocity fluctuations	.163
Figure 4.7 Root mean square of the lateral velocity fluctuations	.164
Figure 4.8 Root mean square of the spanwise velocity fluctuations	.164
Figure 4.9 Profile of correction factor for streamwise and transverse velocity gradients	S
(see equations 4.25 and 4.26)	
Figure 4.10 Profile of velocity gradient fluctuations: du/dx	166
Figure 4.11 Profile of velocity gradient fluctuations: dv/dx	.166
Figure 4.12 Profile of velocity gradient fluctuations: dw/dx	167
Figure 4.13 Profile of velocity gradient fluctuations: du/dy	.167
Figure 4.14 Profile of velocity gradient fluctuations: du/dz	.168
Figure 4.15 Profile of velocity gradient fluctuations: dv/dz	.168
Figure 4.16 Ratio of velocity gradient variances for $x/\theta_0$ =384.	169
Figure 4.17 Ratio of velocity gradient variances for $x/\theta_0$ =675.	169
Figure 4.18 Example of vorticity time series at $x/\theta_0=707$ , $\eta\approx0$ . Periods of irrotational	
fluid are observed.	170
Figure 4.19 Example of vorticity time series at $x/\theta_0=707$ , $\eta\approx0$	.170
Figure 4.20 Example of vorticity time series at $x/\theta_0 = 707$ , $\eta = 3.9$	170
Figure 4.21 Histogram of vorticity from conditions A,B,C, and D; see Table 4.1	171
Figure 4.22 Comparison of vorticity histogram between points of high and low	
intermittency.	171
Figure 4.23 Histogram or spanwise vorticity in the atmospheric boundary layer at Reλ=2500. Solid line represents the curve fit given by equation 4.87	172
Figure 4.24 The RMS of the spanwise and lateral vorticity fluctuations at $x/\theta_0$ =384 (Re $\theta$ =7.1x104).	173
Figure 4.25 The RMS of the spanwise and lateral vorticity fluctuations at $x/\theta_0$ =675 (Re $\theta$ =1.2x105).	173
Figure 4.26 RMS of streamwise vorticity	174
Figure 4.27 Measured and calculated Reynolds stress.	175
Figure 4.28 Gradient of the Reynolds stress.	175
Figure 4.29 Measured velocity-vorticity correlations.	176
Figure 4.30 Measured dissipation from compensated energy spectra: E11(k1)	176

Figure 4.31 Measured dissipation from compensated third order structure function177
Figure 4.32 Comparison of the profiles of several dissipation estimates at $x/\theta_0$ =675177
Figure 4.33 The measured budget of turbulent kinetic energy
Figure 4.34 Velocity autocorrelations from three η locations
Figure 4.35 The autocorrelations of Figure 4.34show in semilog format
Figure 4.36 Autocorrelations of u,v, and w at $x/\theta_0$ =675, $\eta$ =0
Figure 4.37 Cross Correlation between probe (a) located at $\eta$ =4.53, and probe (b)
located at η=1.26180
Figure 4.38 Cross Correlation between probe (a) located at $\eta$ =3.08, and probe (b)
located at η=-0.194
Figure 4.39 Cross Correlation between probe (a) located at $\eta$ =1.76, and probe (b)
located at η=-1.52
Figure 4.40 Cross Correlation between probe (a) located at $\eta$ =.434, and probe (b)
located at η=-2.84
Figure 4.41 Cross Correlation between probe (a) located at η=-0.888, and probe (b)
located at η=-4.16
Figure 4.42 Spanwise correlation of velocity at x/θo=101
Figure 4.43 Spanwise correlation of velocity at x/θo=650
Figure 4.44 Autocorrelation of spanwise and lateral components of vorticity184
Figure 4.45 Autocorreltion of spanwise vorticity in semilog format
Figure 4.46 Close view of the zero crossing region of the ωz autocorrelation185
Figure 4.47 Spanwise correlation of u and $\omega_{z,at}$ Autocorrelations of $\omega_{z}$ and u are
included for comparison
Figure 4.48 Correlation between high speed irrotational velocity fluctuations and $\omega_z$ at
η=0
Figure 4.49 Measured and modeled one dimensional energy spectra: E11(k1)187
Figure 4.50 Measured and modeled one dimensional energy spectra: E22(κ1)187
Figure 4.51 Measured and modeled one dimensional energy spectra: E33(κ1)188
Figure 4.52 Spectral coherence function H12. Note the k1η rage is changed from
previous figures
Figure 4.53 Autospectral function of vorticity. Model spectrum is from isotropic
relation to E11189
Figure 4.54 Compensated vorticity spectra to show energy contribution to enstrophy

integral.	189
Figure 4.55 Schematic examples of $\gamma$ for: (a) a thin uniform sheet of vorticity, (b) a idally perturbed shear layer, (c) a rolled up shear layer into Gaussian von The P( $\gamma$ ) curves on the right show a likely pdf that would be experiment	rtices. ally re-
covered for each condition with Gaussian noise.	190
Figure 4.56 Schematic of showing the finite area of integration for the	
calculation of γ	191
Figure 4.57 Experimental configuration for γ measurement	191
Figure 4.58 Histogram of measured $\gamma$ values. Note that the measured vales have	
been corrected by a factor of 1.19 to account for the limited field of	
view; see Section 4.7.2.	192
Figure 4.59 Peak vorticity measured by various researchers.	192

#### LIST OF TABLES

Table 4.1: Measurement conditions data shown in Figure 4.21	111
Table 4.2: Dissipation estimates	. 126
Table 4.3: Summary of zero crossing points of correlation functions acquired at $\eta=0$ .	.154

#### **NOMENCLATURE**

**A.B.**n Coeficients of hot-wire calibration, Chapter 2 only.

E Voltage output of the anemometer, Chapter 2 only.

 $E_{11}$ ,  $E_{22}$ ,  $E_{33}$  Components of the one dimensional velocity spectra, Chapter 4 only.

 $f_{\rm m}$  Preffered frequency observed in irrotatoinal flow.

H<sub>12</sub> Coherence spectra

k<sub>1</sub> Wave number in the x direction

 $K_1, K_2, K_3, K_4$  Ratios of velocity gradient variances.

q Magnitued of the velocity vector in the x-y plan

R Normalized correlation function.

Re<sub>o</sub> Reynolds number of the boundary layer at separation

 $Re_{\theta}$  Reynolds number based on local momentum thickness

*t*\* Dimensionless time deley used in autocorrelation function

U<sub>c</sub> Convection velocity of large scale motions measured in the irrotational

stream

U<sub>0</sub> Freestream velocity

U<sub>eff</sub> Effective freestream velocity for scaling of the first instability

u,v,w Components of the velocity vector

v <sub>e</sub>	Velocity of the entrainment flow
x,y,z	Carteasian coordinates originating from the sparation point
δ*	Displacement thickness
Δy	Separation of straight wire sensors in the vorticity probe.
Δs,Δn	Size of the microcirculation domain used in the vorticity calculation.
ε	Dissipatoin
γ	Angle of the velocity vector with respect to an X-wire probe, Chapter 2
	only.
γ	Circulation density, Chapter 4 only.
κ	Three dimensional wave number.
$\theta_{\rm o}$	Momentum thickenss of boundary layer at separation
θ	Local momentum thickness
$\theta_{eff}$	Effective momentum thickess for scaling the first instability
σ	Spreading parameter.
$\omega_x, \omega_y, \omega_z$	Components of the vorticity vector

#### 1.0 Introduction

The study of fluid mechanics at high Reynolds number is quite unique among the physical sciences. This uniqueness can be partially characterized by the full knowledge of the governing equations of fluid motion without a complete understanding of the phenomenon, despite over a century of intense research. One source of the difficulty in turbulence research is the number of different phenomenon that occur with different boundary conditions. As a result, theory, modeling, or experiments which characterize a single given set of flow conditions will usually fail to provide similar insight for a geometry which is different from the original.

Most studies in fluid mechanics can therefore be categorized as belonging to one of two research "modes." The first, is to choose a set of boundary conditions which is relevant to an important engineering problem. For example, most research in turbomachinery would fall into this category. The second mode, is to chose a small number of canonical flows in which the physics of the fluid motions can be studied in great detail. One goal of these fundamental studies is to incorporate the acquired knowledge into the applied studies, and ultimately into engineering design.

This dissertation follows the second approach, and utilizes the *single stream shear layer* as the canonical flow field of interest. This geometry is, in the author's opinion, a very simple one which is applicable to the wide range of potential applications. An idealized schematic of the planar flow geometry is shown in Figure 1.1. The irrotational freestream enters the domain from the left, with a smooth wall boundary layer developing on the only bounding wall. The boundary layer undergoes transition to a turbulent boundary layer, and

develops with a zero pressure gradient (constant velocity) free stream. After a specified length, the boundary layer plate ends with a 90 degree angle as shown. This defines the streamwise location of the separation point which marks the transition from a wall bounded shear flow to a free shear flow. The free shear flow is characterized by a zero pressure gradient free stream on one side, and fluid which is "entrained" into the shear layer from the other side. From this basic description of the flow field, it is considered to be apparent that many of the important flow phenomena of applied fluid mechanics can be studied in the single stream shear layer.

It can be observed from Figure 1.1 that the only length scale of the problem is given by the length of the boundary layer plate. An equivalent characterization which is often preferred is the momentum thickness of the boundary layer at separation ( $\theta_0$ ). This, along with the specification of the free stream velocity ( $U_0$ ) and the kinematic viscosity of the working fluid (v) completely characterizes the boundary value problem. The only parameter is the Reynolds number,  $Re_o = U_o\theta_o/v$ . One of the unique features of the present research project is the large scale of the experimental facility which was constructed in the Turbulent Shear Flows Laboratory at Michigan State University. This facility, which is described in detail in Chapter 2, uses air as the working fluid and has the characteristics:  $U_o = 7.1 \text{ m/s}$ ,  $\theta_o = 9.62 \text{mm}$ . This provides a Reynolds number at the separation point of  $Re_o = 4650$ .

Note that the dimensionless entrainment velocity  $(v_c/U_o)$  is not an independent parameter. This is because the boundary conditions specify that the free stream velocity (and pressure) are streamwise invariant. That is,  $\partial U_o/\partial x = \partial P_o/\partial x = 0$ . There exists a "natural"

value of v<sub>e</sub>/U<sub>o</sub> that will allow the shear layer to grow in a zero pressure gradient environment. The magnitude of the entrainment velocity is therefore not known a priori, and must be determined experimentally. This may seem odd at first, that the boundary conditions of an experiment are not known before the experiments are started. To clarify why this is the case, consider a finite entrainment domain with  $v_e=0$ . This represents the backward facing step geometry in which the separation streamline must diverge away from the high speed fluid and re-attach to a bounding wall, leading to a recirculation region in the entrainment side and an adverse pressure gradient condition in the free stream region. In contrast, if v<sub>e</sub> were to be forced to be arbitrarily large, the shear layer would deflect towards the high speed fluid, thereby accelerating the shear layer in a favorable pressure gradient condition. The "natural" value of v<sub>e</sub> is that which would be observed if the entrainment region were of infinite extent for a finite height primary flow. Since a truly infinite domain is not experimentally possible, the entrainment flow is "fed" into the shear layer at the rate which provides the zero pressure gradient conditions. The experimental determination of the entrainment velocity is described in Chapter 2.

There exists a large number of research papers in the literature which have focused on the single stream shear layer. In addition, there is a distinctively larger body of literature which examines the two-stream shear layer. The latter flow field uses a thin splitter plate to divide two parallel fluid streams with different velocities:  $U_1$  and  $U_2$ . The shear layer is created by the trailing edge of the splitter plate. It is incorrect to think of the single-stream shear layer as the limiting case of a two-stream shear layer with the slower velocity reduced to zero. The reason for this is the direction of the entrainment stream, which, in the single stream shear layer is directed perpendicular to the primary flow direction. In the

two stream shear layer the entrainment phenomenon caused by the high speed flow will "pull" fluid from the second flow region, leading to a complicated and undesired flow field. The difference between parallel and perpendicular entrainment streams has been examined by Schmidt et al. (1986). In summary, despite many useful similarities, the single stream shear layer is a distinct flow field from the two stream flow, and not simply the limiting case of  $U_2$ =0.

As already noted, there are a number of research papers in the literature which have documented the physical characteristics of the single stream shear layer. These include Liepmann and Laufer (1947), Freymuth (1966), Wygnanski and Fiedler (1970), Champagne et al. (1976), Hussain and Zedan (1978), Hussain and Zaman (1985), Mehta and Westphal (1986), Haw et al. (1989), Bruns (1990), Bruns et al. (1991), Foss (1994). Given the large amount of information already available on the subject, it is appropriate to establish the reason for the continued interest in this flow field. It is noteworthy, in this context, that Wygnanski and Fiedler in 1970 found it necessary to justify why they found it "worthwhile to reconsider this flow". Following an additional three decades of research, an updated justification is given by outlining several of the open questions which still exist in the literature whose answers are of considerable interest.

The affects of the inflow boundary conditions on the downstream flow are of interest in the study of both single and two stream shear layers. The dynamics of the flow field in the very near separation region has not been documented or properly understood. As a result, most differences that are noted between the results of different researchers using different shear layer facilities are attributed to the differences in the inflow conditions. In addition, the inflow conditions for most experimental facilities are either laminar, or low Reynolds

number tripped boundary layers. These facilities are therefore not representative of the flow separation phenomenon that exist in engineering applications which are characterized by very high Reynolds numbers.

The experimental facility used in the present work provides a unique opportunity to "fill the gap" in the available literature. This is because of the relatively large scale of the facility, which provides excellent spatial resolution for measurements ( $\delta_{99}(x=0) \approx 100 mm$ ) in a moderately high Reynolds number boundary layer (Re<sub>0</sub>=4650). A detailed experimental investigation of the near separation field is presented in Chapter 3. This research project is self-contained, and distinctive from the downstream measurements. Therefore, Chapter 3 is complete in the sense that an introduction, motivation, background, literature review, experimental results, and conclusions are provided.

The next portion of this dissertation, Chapter 4, describes measurements that were acquired in the self similar region of the flow field. This chapter is also self contained with introduction, literature review, etc. There are numerous outstanding questions in the research literature which have motivated these measurements. A first example regards the nature of shear layers in terms of how the stochastic variables of interest scale with downstream distance. It has long been known that linear growth and self-similarity are standard features of free shear flows. However, the scaling of quantities such as dissipation, vorticity fluctuations and their spectra have not previously been examined. Again, the present facility provides a unique opportunity to investigate these issues because of the relatively large scale, and hence adequate spatial resolution of the measurements. It will be shown in

terms of the vorticity spectra that true self-similarity is not achieved. Rather, the dimensionless vorticity fluctuations increase with Reynolds number.

In addition to the novel research issues which have been addressed in this dissertation, many of the previously documented features of shear layers have been repeated in this work. The reason for this repetition is (i) to validate the present facility, and (ii) to validate claims made in previous research efforts. In doing so, this volume represents a more comprehensive study of the flow field than that which has been previously reported.

The outline of this document can be summarized as follows. The experimental facility and measurement techniques which are common to all of the experiments are described in Chapter 2. The two "halves" of the research project are represented by the near separation region, and fully developed region, and are described in Chapters 3 and 4 respectively.

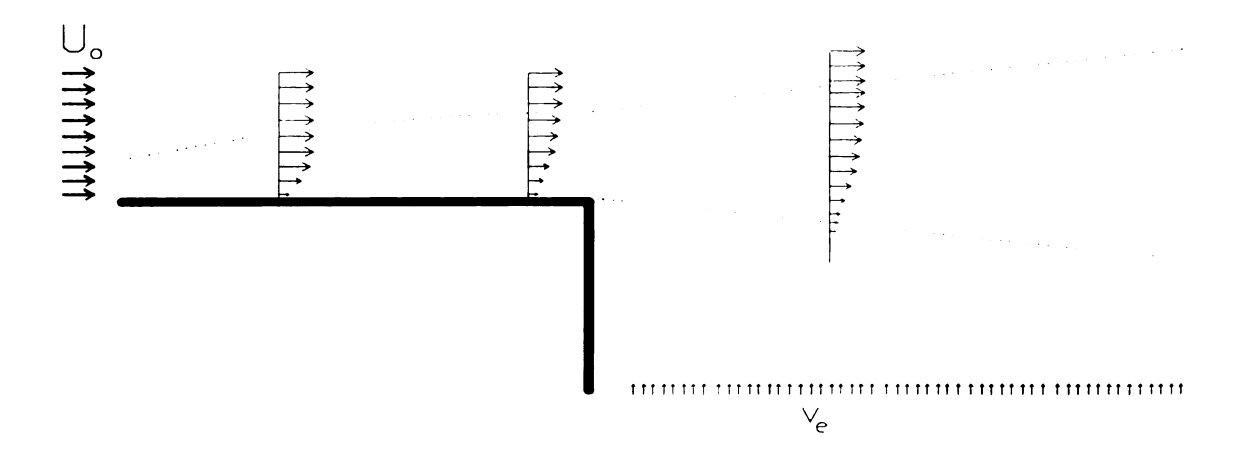


Figure 1.1 Idealized schematic of the single stream shear layer geometry. The thick line represents the only solid boundary. The dotted lines bound the region of non-zero vorticity. The velocity vectors are schematic, and not shown to scale.

#### 2.0 Experimental Apparatus and Techniques

The experimental apparatus and methods used in this dissertation are described in this chapter. First, the Single Stream Shear Layer Facility (SSSL) will be described. This facility was designed and assembled by the author, and is documented in Section 2.1. This information can serve as a reference for future research which will utilize the facility.

Hot-wire anemometry was the primary experimental method for the measurement of velocity. The basic sensor geometry and calibration technique are described in Section 2.2.1. X-wire probes were used to measure one or two components of the velocity vector. The algorithm for obtaining the fluid speed and flow angle from the two sensors of the X-wire is outlined in Section 2.2.2. Multi-sensor arrays of wires were used to obtain velocity gradient and vorticity information. These are discussed in Section 2.2.3.

#### 2.1 The Single Stream Shear Layer Facility

The Single Stream Shear Layer (SSSL) facility is located in the Turbulent Shear Flows
Laboratory at Michigan State University. The majority of the facility including the test
section was constructed at an elevated level (its floor is ~2.1m) above the laboratory floor.
The primary flow intake and delivery system were located at the floor level as shown in
Figure 2.1. An axial fan accelerates the laboratory air from rest. The fan exit is connected
to a 1m x 1m square section. Acoustic dampening material was placed 1.4m upstream
from the blower entrance to limit the propagation of blower noise into the room and test
section. The fan used a constant speed AC motor attached directly to the 48" diameter
blades. The exit of the axial fan housing was connected directly to a diffuser section that
expands to a 2m x 2m cross section. In this diffuser, flow dividers (not shown) were used

through two sets of 90 degree turning vanes which first turn the flow direction vertically upwards and then horizontally at the elevation of the test section. Standard 5µm furnace filters were attached to the first set of turning vanes to eliminate dust from the free stream flow. A second acoustic dampening wall was placed at the back wall of the turning vane section as shown.

Following the second turning vane section, a set of flow conditioners were installed to provide a uniform velocity with minimal unsteadiness to the test section. This conditioning section consisted of a 25mm long honeycomb section with 3mm tube diameters, followed by three sections of stretched steel screen material. The screens were made from 0.060" wire mesh with 40 wires per inch (0.635mm spacing between wires).

The outflow from this conditioning section is connected directly to the inlet of the main tunnel entrance. This is shown as "primary inflow" in Figure 2.2. The height (i.e., "out of the page") of the entire working section of the tunnel was 1.96m. The width of the primary flow inlet was 1.96m wide. A planar contraction was placed downstream from the inlet which accelerates the flow to a width of 1.1m. The elliptical shaped leading edge of the boundary layer plate then splits the primary flow such that the boundary layer from the curved wall of the contraction is "bled" off and returned to the laboratory as shown. This point of the tunnel and all downstream locations are at nearly zero gage pressure with respect to the laboratory pressure. The majority of the flow moves through the 0.98m wide boundary layer development section. The boundary layer plate is 5.74m long, with a free stream velocity of 7.1m/s. The boundary layer plate was laminated with 1mm thick PVC sheeting to provide a smooth boundary condition. The boundary layer plate ends at the

separation point which was created using a machined 90 degree edge. The free stream velocity was measured during all experiments by monitoring the differential pressure drop across the planar contraction. This pressure difference was acquired during all experiments and found to vary by less than 0.5% for the data reported in Chapters 3 and 4.

The shear layer test section begins at the separation edge. The entrainment flow is provided by four 48 inch (1.2m) diameter axial propeller type fans with an AC speed controller. This fan type is designed to move large volumes of air at relatively low pressure rise (~25Pa). For this reason, bypass holes were created such that the fans would operate at design conditions to prevent unsteadiness from blade stall. That is, most of the air moved by the fans is recirculated back to the laboratory. The "plenum" between the fans and the flow conditioning is maintained at a pressure which is slightly higher than the atmospheric value. The entrainment flow conditioning is identical to the primary flow conditioning. The length of the entrainment screens is 9.5m which defines the working length of the shear layer test section. The location of the final entrainment screen is y=-2.75m, using the coordinate system shown with origin at the separation edge. The exit of the tunnel is open to the laboratory. The nearest obstruction to the outflow is a building wall located 6.1m from the tunnel exit. This provided sufficient room to turn the exiting flow without disturbing the shear layer.

The entrainment velocity was set using an AC frequency control unit to drive the electric motors connected to the entrainment fans. An experiment was conducted to identify the correct motor speed in order to create a shear layer with a zero streamwise pressure gradient. Specifically, data were obtained using a single hot-wire probe in the free stream at two streamwise locations (x=0.5m and 4.0m) in the high speed irrotational flow. The controller

frequency was adjusted until the hot-wire readings at these two locations indicated the same velocity. This implies  $dU_0/dx = 0$ , i.e., a zero pressure gradient condition.

A traverse system was constructed to support and move the hot-wire sensors during data acquisition. This system used a wheel and track for movement in the streamwise direction (x) and a precision lead screw and stepper motor drive for the transverse (y) direction. The probes were mounted on a rotating shaft which was also motor driven. This permitted angular positioning of the sensors for calibration and data acquisition.

#### 2.2 Hot-wire Techniques and processing

This section will describe the details of the hot-wire calibration and processing methods used in this work. A schematic of a single sensor is shown in Figure 2.3. The active portion of the sensor was a 1mm long, 5µm diameter Tungsten wire. The end regions were electro-plated with 30µm copper and soldered to stainless steel supports. The wires were connected to DISA 55m anemometers. The frequency response of the sensors at 7m/s was typically greater than 20kHz.

#### 2.2.1 Calibration

The wires were calibrated using a newly constructed calibration facility shown schematically in Figure 2.4. The unit used a constant speed cross-flow blower and throttle to vary the exit velocity from 0.5 to 12m/s. Screens, filters and honeycomb were placed upstream of a contraction to achieve a low disturbance free stream for calibration. The contraction exit flow dimensions were 2.5 x 24 cm which provided sufficient area to calibrate up to 10 probes simultaneously. The probe holder was connected to a stepping motor which varied the angle of the X-wire probes with respect to the jet exit.

The calibration technique used a continuously variable "quasi-steady" method. That is, the sensor was subjected to a velocity which was varied continuously from shutoff to maximum flow over the duration of approximately 40 seconds. Data samples of the hotwire(s), pressure transducer, and thermistor were acquired at a sample rate of 500Hz.

These data were used to fit the equation

$$E^{2} = A(\gamma) + B(\gamma)O^{n(\gamma)}$$
2.1

where E represents the output voltage from the anemometer, and Q represents the exit velocity, and γ represents the pitch angle with respect to the probe axis. This velocity was calculated from the pressure measurement using Bernoulli's equation. Note that this method assumes that the unsteady effects of the continuously varied velocity are not sufficient to cause error in the steady Bernoulli equation. This assumption was tested by performing several standard (steady state) calibrations for comparison with the quasi-steady results. These experiments have shown no measurable differences between the two types of calibratoins. The primary reason for using the quasi-steady method is the speed of calibration. For example, single wires were calibrated in less than one minute. The x-wire probes, for example, were calibrated at 13 angles which required approximately 12 minutes of total calibration time, which include angle changes between measurements. If the sensors were calibrated with the alternative technique: establish the flow angle, record time series data for a period of 10 seconds at each flow speed, then an X-wire probe would take typically 45minutes to calibrate.

An example of a wire calibration and fit is shown in Figure 2.5. The quality of the fit was determined from the standard deviation between the measured velocity and the predicted velocity from equation 2.1. In all experiments, this was found to be less than 0.05m/s. If a

sensor/anemometer were found to have a higher value for the standard deviation, the probe was not used. The sensors were calibrated before and after each experiment. If the predicted velocity from the two calibrations changed by more than 2%, the data were discarded and the experiment was repeated. In most experiments, the velocity calculated from the "pre-calibration" and "post-calibration" agreed to better than 1%.

#### 2.2.2 X-wire probe calibration and processing

X-wire probes were used for the simultaneous measurement of two velocity components. The probe geometry is illustrated in Figure 2.6. Two sensors were oriented at nominally  $\pm 45$  degrees to the probe axis. The spacing between the sensors was 1mm. The output from the two sensors is denoted as  $E_1$  and  $E_2$ . The goal of the calibration and processing algorithm is to obtain a transfer function between these voltages and the desired variables: the speed (Q) and angle ( $\gamma$ ) of the fluid velocity with respect to the probe. The optimal transfer function, which provides the most accurate estimate of Q and  $\gamma$ , has been the subject of considerable research. Techniques which are used in the literature vary from the very simple cosine law to very complex algorithms such as mapping techniques; these are described by Bruun (1995). Since all techniques seem quite accurate for small angles, say,  $|\gamma| < 12$  degrees, it is the largest angles where the differences between algorithms has the most effect. Because the angles found in the shear layer can fluctuate considerably, a new measurement technique was developed which provides the most reliable speed and angle estimates for  $|\gamma| < 36$  degrees.

The present technique, is a modification of the "speed-wire/angle-wire" (SWAW) technique proposed by Foss (1981). The SWAW algorithm uses the sensor more parallel with

the velocity vector to determine the angle  $(\gamma)$ , and the sensor which is more perpendicular to the velocity vector is used to obtain the speed (Q). An iterative algorithm is used which converges to the correct  $(Q,\gamma)$  pair. The present technique is similar, although the iterative nature of the SWAW technique was replaced with a "curve intersection" method.

The new algorithm is described as follows. First, the X-wire probe is calibrated using the spin-down technique (described in Section 2.2.1) in the range  $-36 < \gamma < 36$  degrees, in 6 degree intervals. This calibration results in 13 sets of (A,B,n) values for each sensor. The experimental data are then acquired as time series values of the voltage pair (E<sub>1</sub>,E<sub>2</sub>). From each of the recorded (E<sub>1</sub>,E<sub>2</sub>) pairs, equation 2.1 can be solved for Q<sub>1</sub>(E<sub>1</sub>, $\gamma_i$ ), Q<sub>2</sub>(E<sub>2</sub>, $\gamma_i$ ) where i=1,2,...13. That is, Q<sub>1</sub> and Q<sub>2</sub> represent predicted velocities which are calculated for each sensor using the wire voltages (E<sub>1</sub>, E<sub>2</sub>), and the calibration coefficients for i=1,2...13 representing the 13 angles used in the calibration. Figure 2.7 shows an example of the 13 predicted velocities that were calculated from a voltage pair. The "true" value of (Q, $\gamma$ ) is now represented by the intersection of the two curves shown. This intersection point is found by fitting the neighboring points of each curve with a second order polynomial fit, and then solving for the intersection point.

One method of testing the accuracy of the calibration/processing algorithm is to calculate the speed and flow angle of an X-wire probe placed a known angle with respect to a steady flow. The calculated velocity agreed with the actual value to within 2% at angles less than 18 degrees, and within 4% at angles less than 36 degrees. Figure 2.8 shows the results of time series data of the predicted flow angle with a probe placed at +18, 0, and -30 degrees with respect to the jet of the calibration unit. The standard deviation of the error in pre-

dicted angle was typically less than 0.5 degrees, and often as good as 0.2 degrees. These errors reflect the contribution of electronic noise to the processed time series. Errors due to calibration drift were typically less than 1 degree.

#### 2.2.3 Multi-sensor Probe Configurations and Processing

The previous sections have described the calibration and processing algorithms for both single wire probes and X-array probes. In the following three sub-sections, probes which utilize combinations of single and X-arrays to compute vorticity and velocity gradients are described. The use of multi-sensor probes leads to a number of complications regarding the uncertainty of the measurements. These can be dependent on the probe configuration, probe-scale to flow-scale effects, and the presence of electronic noise in the time series. Because the measurement techniques described were not developed as a part of this dissertation, they will be described only briefly along with the estimated uncertainty. Additional information can be found from references to those communications in which the developed techniques are described. These references provide more comprehensive uncertainty evaluations.

#### 2.2.3.1 Spanwise Vorticity Probe

A schematic representation of the spanwise vorticity probe, or "Mitchell" Probe, is shown in Figure 2.9. This probe consists of an X-array with two parallel wires. These were calibrated using the procedures described above. The time series output from the probe is the magnitude of velocity in the plane of the probe as determined by the two straight wires:  $(q_1, q_2)$ , and the angle  $(\gamma)$  determined from the X-array. This section will review the method by which the time series values of  $(q_1, q_2, \gamma)$  were used to calculate the spanwise

vorticity. The probe geometry and processing algorithm were originally developed by Foss and co-workers, and can be found in the references by Foss and Haw (1990), and Wallace and Foss (1995).

The data processing algorithm can be summarized as follows. The average of the two recorded velocities  $(q_1+q_2)/2$  is used as a convection velocity to create a parallelogram shaped micro-circulation domain using a local (in time) Taylor's hypothesis; see Figure 2.10. The height  $(\Delta y)$  of the microcirculation is fixed by the physical separation distance between the two straight wire sensors. The length of the domain  $(\Delta s)$  was set to be roughly equal to  $\Delta y$ . Specifically, from the discrete time records of  $q_1(t_n)$ , etc., the sum was computed for each  $t_n$  as:

$$\Delta s_n(m) = \frac{1}{2m+1} \sum_{i=n-m}^{i=n+m} \left( \frac{q_1(t_i) + q_2(t_i)}{2} \right) \Delta t.$$
 2.2

The value of m was increased, starting from m=1, until  $\Delta s_n > \Delta y$ . This defines M, the integer number of time records needed to create the one half of the micro-domain. The value of M for each calculation time  $(t_n)$  would vary depending on the flow speed. Typical values of 2M were between 6 and 20 time steps.

The mean value of a given quantity during the interval  $t_{n-M} < t < t_{n+M}$  is denoted by the brackets  $\langle \rangle$ . For example, the angle of the microcirculation parallelogram was the mean value of  $\gamma$  during the time period of the microcirculation:

$$\langle \gamma_n \rangle = \frac{1}{2M+1} \sum_{i=n-M}^{i=n+M} \gamma(t_i)$$
 2.3

Once the microcirculation domain has been "created", the average vorticity of the domain is calculated from the velocity circulation around the domain. The magnitude of the velocity can be projected onto the "top" and "bottom" of the micro-domain as  $q_1 \cdot \cos(\gamma(t_i) - \langle \gamma \rangle)$  and  $q_2 \cdot \cos(\gamma(t_i) - \langle \gamma \rangle)$ , and then integrated along the length circulation domain. The normal velocity component is calculated from  $v = (q_1 + q_2)(\sin\gamma)/2$  at both the upstream and downstream sides of the domain. For each point of the time series (n), the vorticity is calculated from:

$$\langle \omega_n \rangle = \frac{1}{(\Delta s)(\Delta y)} \oint (\vec{V} \cdot d\vec{s}) = \frac{v(t_{n+M}) - v(t_{n-M})}{\Delta s} - \frac{\langle q_2 \rangle - \langle q_1 \rangle}{\Delta y}$$
 2.4

The approximation  $\cos((\gamma(t_i) - \langle \gamma \rangle) \approx 1)$  was made in order to decrease the computational time required to process the time series. This assumption is justified based on the realization that the differences between the instantaneous values of  $\gamma(t_i)$  and  $\langle \gamma \rangle$  were less than 5 degrees. Since the cosine can be factored out from the  $q_1$  and  $q_2$  terms, the approximation  $\cos(|\gamma| < 5) \approx 1$  is reasonable.

A detailed uncertainty analysis of the vorticity probe and processing algorithm has been given by Foss and Haw (1990). One of the primary sources of error was found to be due to the presence of electronic noise in the time series data. The contribution of electronic noise to the uncertainty is reported to be of order 20 (1/sec) in Foss and Haw (1990). This is well supported by the measurements of vorticity in the free stream of the shear layer where little or no vorticity is assumed to exist. Specifically, at  $x/\theta_0=384$ , values of  $\tilde{\omega}_z < 25(1/\text{sec})$  were measured at the transverse locations ( $\eta>3.8$ ).

#### 2.2.3.2 Streamwise Vorticity Probe

A schematic of the streamwise vorticity probe is shown in Figure 2.11. This probe uses 8 senors configured as four X-arrays in a square pattern. From this, two of the opposing X-wires will provide time series of  $(v_1, v_2)$ , separated by a distance of  $\Delta z$ =5.6mm. The other two X-wire will then measure time series of  $(w_1, w_2)$ , separated by  $\Delta y$ =5.6mm. The vorticity calculation is then straightforward:

$$\omega_{x} = \frac{w_2 - w_1}{\Delta v} - \frac{v_2 - v_1}{\Delta z}$$
2.5

The uncertainty of this probe is dictated by the ability of the X-wire processing to recover the true value of the lateral component of velocity. The errors will be due to electronic noise and calibration errors. Electronic noise was shown in Section 2.2.2 to contribute to a random error of typically 0.2 degrees. At a flow speed of, say, 7.0m/s, this would lead to a random error of roughly 24mm/s in the normal component of velocity. If these errors are Gaussian distributed and equal for the four X-wire probes, then the standard deviation of the sum  $(w_2 - w_1 - v_2 + v_1)$  is twice that of the single measurement. That is the standard deviation for  $\omega_x$  in an irrotational flow would be  $2 \cdot (0.024)/(0.005) = 9.8(1/\text{sec})$ . The measurements support this conclusion. For example, at  $x/\theta_0 = 384$ , values of  $\tilde{\omega}_z < 8$  (1/sec) were measured at the transverse locations ( $\eta > 3.8$ ).

Additional details regarding the use and uncertainty of this probe configuration can be found in Kock am Brink and Foss (1993).

#### 2.2.3.3 Multiple X-wire Configuration

A four wire sensor was configured as two adjacent X-wire probes in a single probe body; see Figure 2.12. The same probe configuration was used in the measurements made by

George and Hussein (1991), and by Lui (2001). This probe is similar to the streamwise vorticity probe discussed in the previous section, in that closely spaced X-wires are used to determine the lateral derivative of a velocity component which is normal to the streamwise direction. In this case, the probe was used to estimate the mean squared value of  $\partial v/\partial z$ . This measurement was required for the dissipation estimate which uses the assumptions of axisymmetric turbulence; see Section 4.5.

The four sensors shown were arranged such that wires 1 and 2 were processed as a single X-wire, with the output  $v_1$ . Similarly, wires 3 and 4 are processed to provide  $v_2$ . The desired velocity gradient is simply the difference between these, divided by the spatial separation, which was 3.0mm. With this probe separation, the electronic noise from the anemometers leads to an RMS of the velocity gradient of about 16 (1/sec) in the free stream of the shear layer.

The finite separation between the two X-wire probes can lead to an underestimate of the true velocity gradient. In the present flow field, the separation between the X-wires was of order  $15\eta_K$ , where  $\eta_K$  represents the Kolmogorov length scale of the flow. Wallace and Foss (1995) review several references which discuss the attenuation due to finite probe scale. Figure 2 of Wallace and Foss (1995) indicates that there is reasonable agreement between different authors on this issue, and that the present configuration likely underestimates the true RMS of  $\partial v/\partial z$  by roughly 50%. However, the present data indicate that the performance of the probe is likely better than this estimate. Specifically, the variance of  $\partial v/\partial z$  was found to be larger than the isotropic value, which is twice the variance of

 $\partial w \partial x$ ; see Section 4.1. Given these already larger than expected values for the variance of  $\partial w \partial z$ , it is unlikely that significant attenuation has occurred in the measurements.

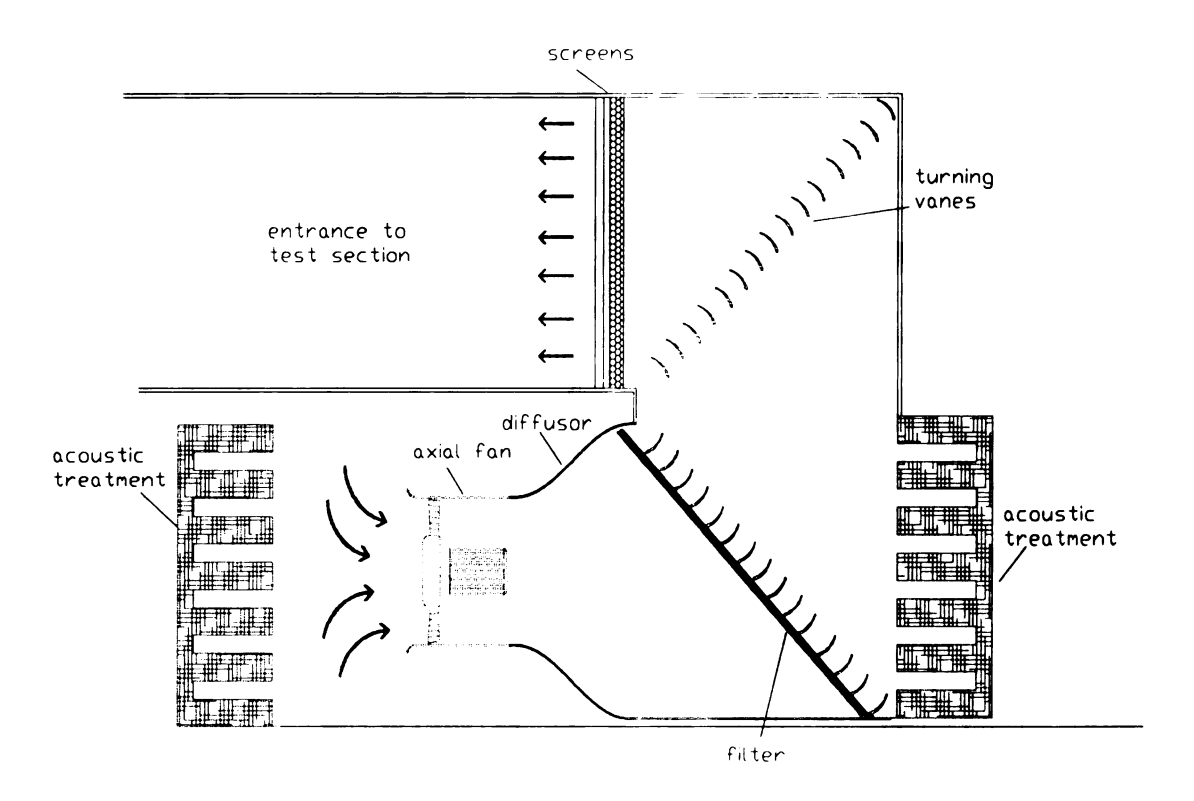


Figure 2.1 Primary flow delivery system

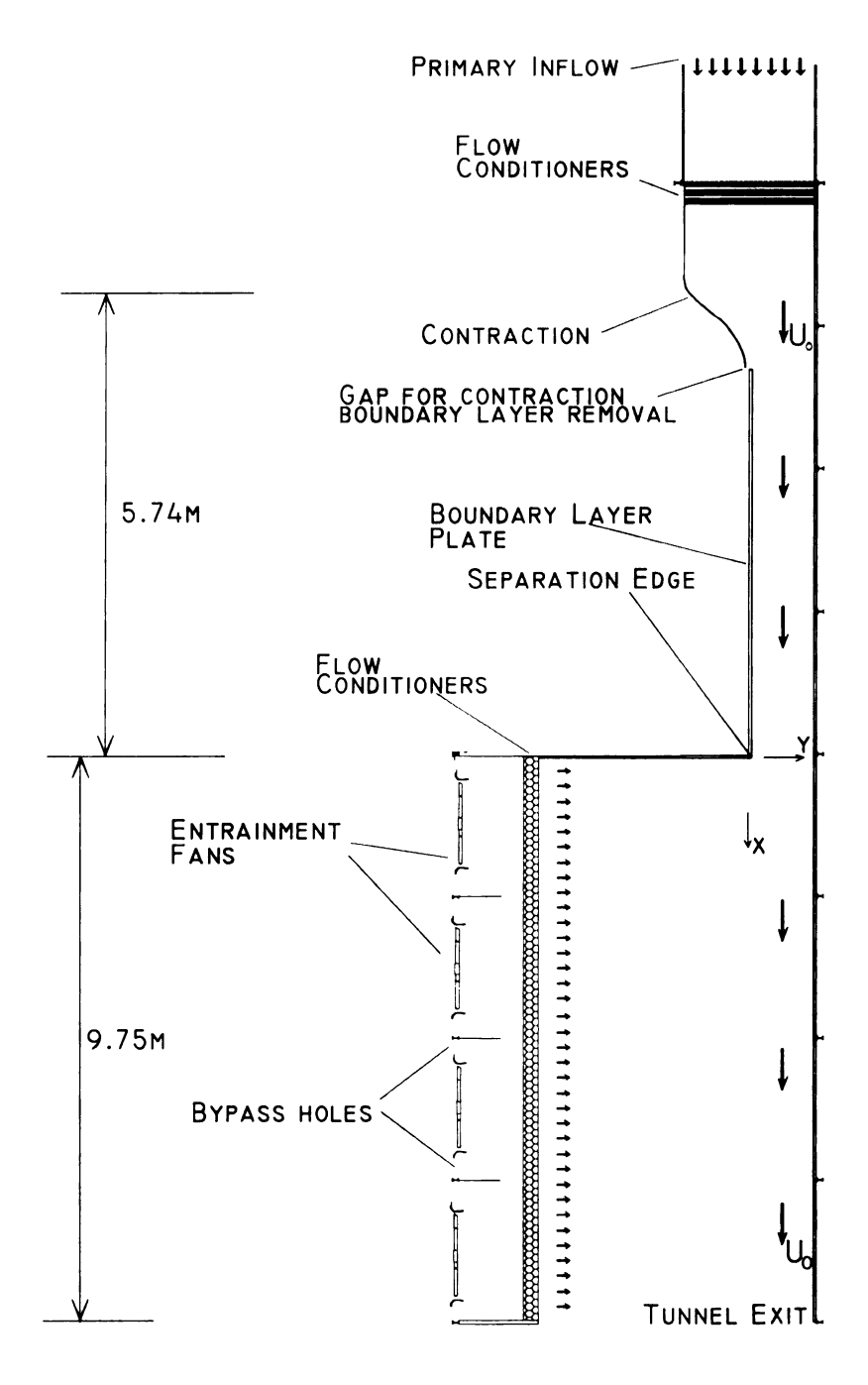


Figure 2.2 Schematic of SSSL facility

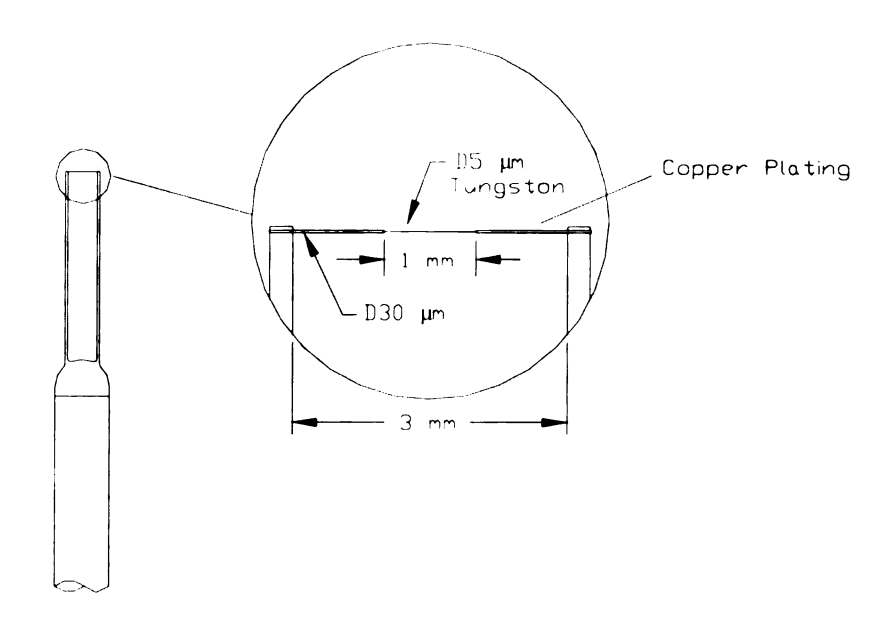


Figure 2.3 Geometry of single hot-wire probe

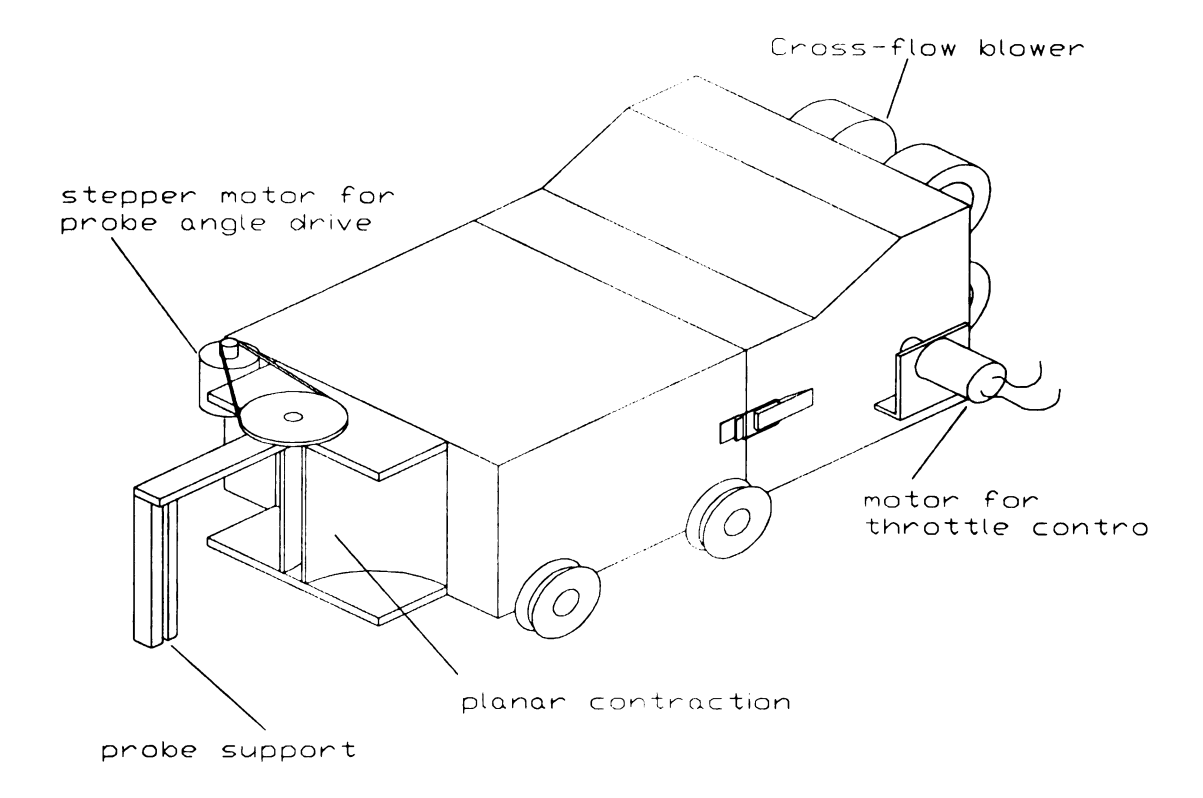


Figure 2.4 Schematic of Calibration Facility

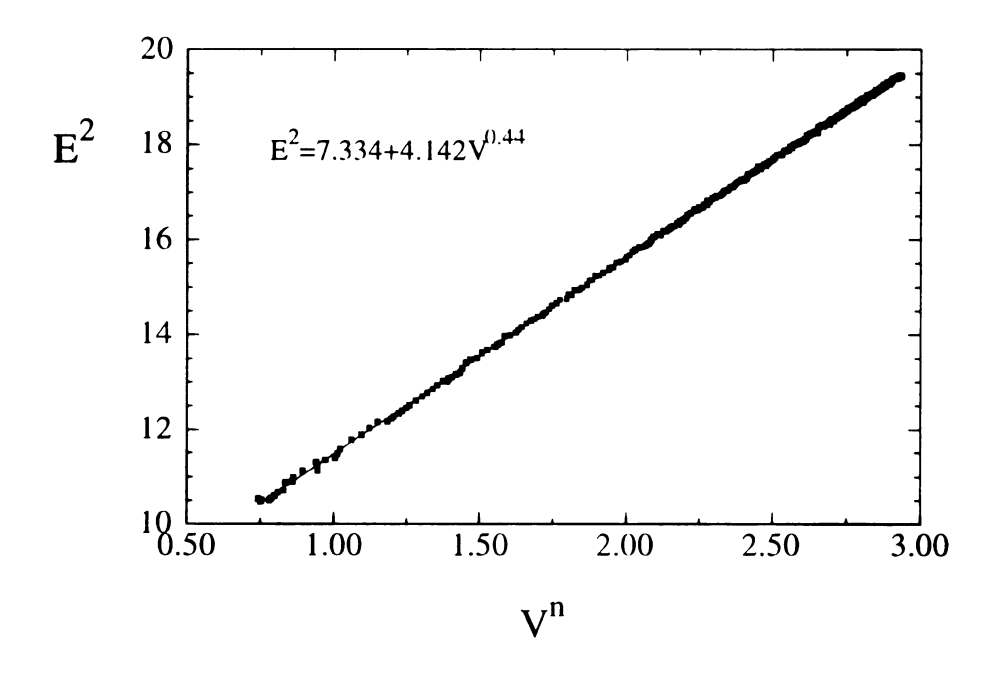


Figure 2.5 Sample calibration and fit,  $\gamma$ =0 degrees.

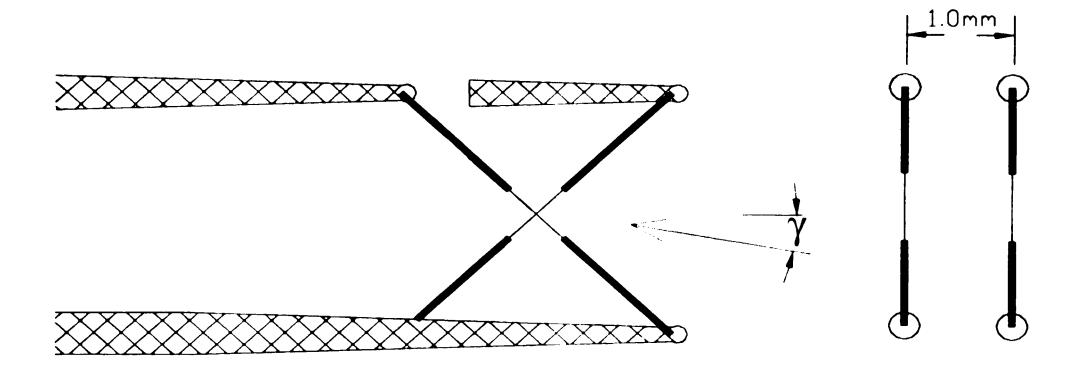


Figure 2.6 Geometry of the X-wire probe

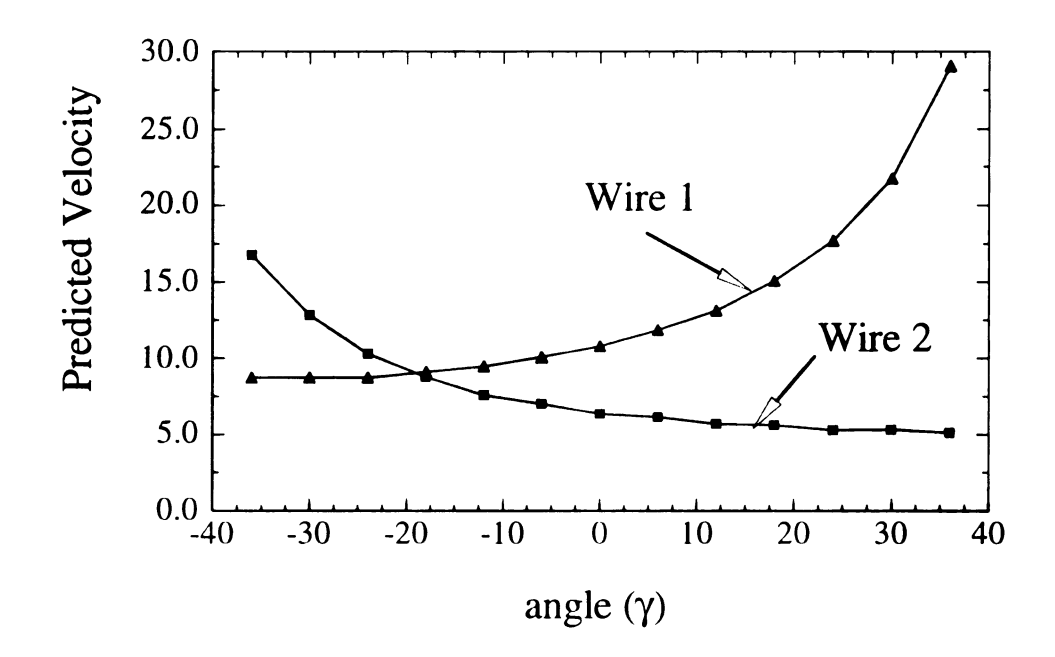


Figure 2.7 Example of the locating algorithm of the intersection point for X-wire processing.

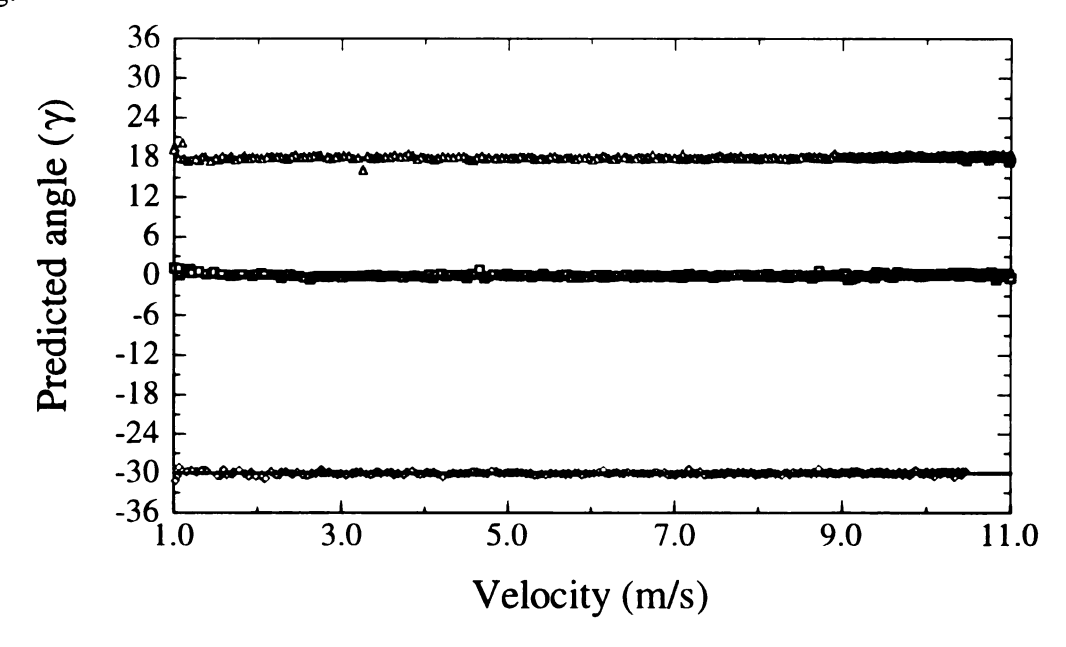


Figure 2.8 Predicted values of angle ( $\gamma$ ) from re-processed calibration data at nominal values of 18, 0, and -30 degrees. The standard deviation of these measurements was 0.18, 0.17, 0.21 degrees, respectively.

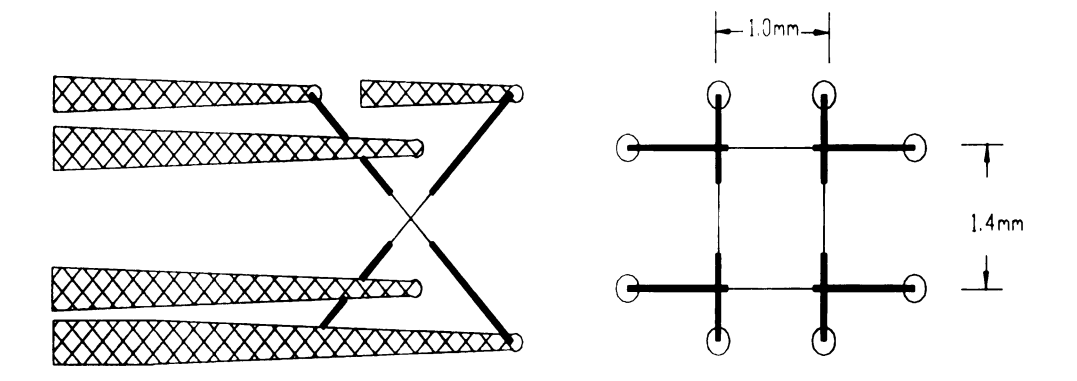


Figure 2.9 Schematic of spanwise vorticity probe

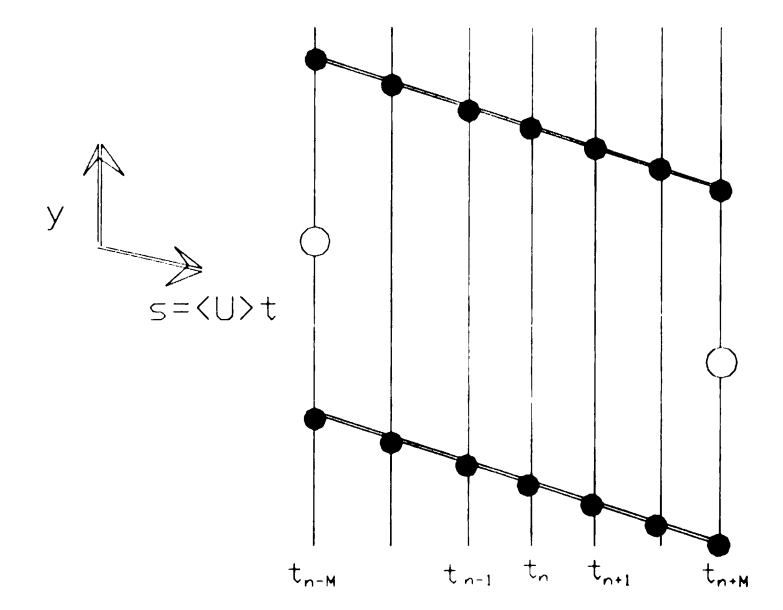


Figure 2.10 Schematic of micro-circulation used for the spanwise vorticity calculation. The velocities  $q_1$  and  $q_2$  are known at the points represented by the dark circles on the top and bottom of the domain, respectively. The normal component of velocity, v, is known at the open circles at the left and right sides of the domain.

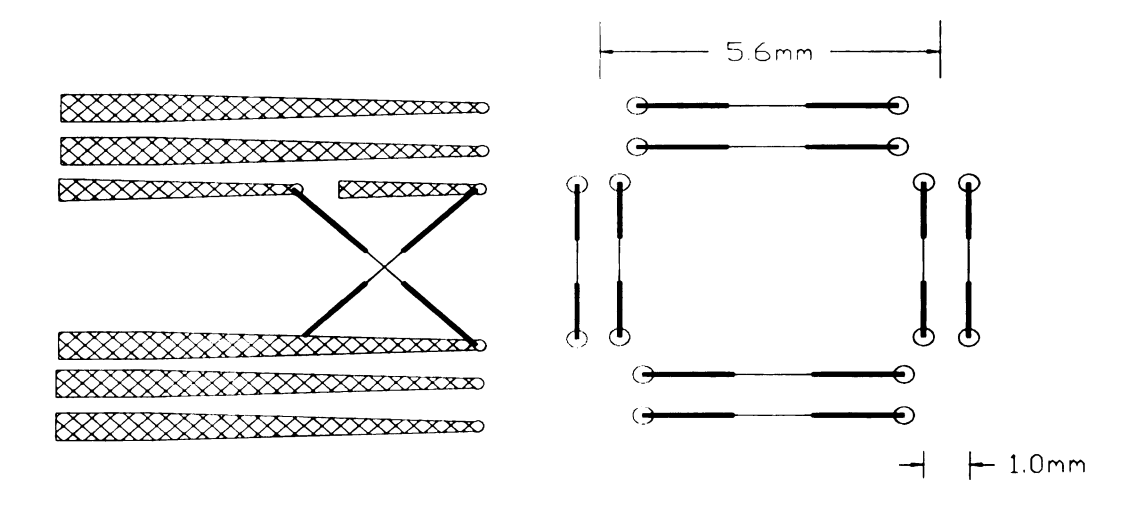


Figure 2.11 Schematic of the streamwise vorticity probe.

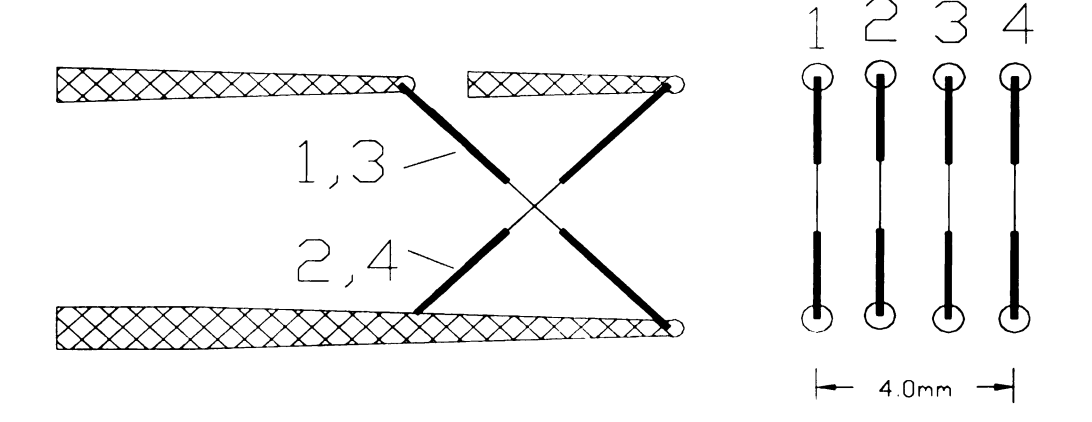


Figure 2.12 Schematic of the multiple X-wire probe.

3.0 Turbulent Boundary Layer to Single Stream Shear Layer - The initial transition region.

#### 3.1 Introduction

A detailed investigation of the near separation region of the single stream shear layer was conducted. A schematic representation of the area of interest and coordinate system is shown in Figure 3.1. Measurements were acquired in the region  $0 < x/\theta_0 < 100$ . This study is distinctive with respect to the existing literature because of the relatively high Reynolds number of the separating boundary layer ( $Re_{\theta}$ =4650), and because the large  $\theta$  value (9.6mm) permitted detailed measurements to be acquired in the very near separation region. This flow region is important both fundamentally and technologically. The region can serve as the archetype flow for a backward facing step, a jet exhausting from a plane surface, and other flows characterized by the 90 degree interaction between a turbulent separating primary flow and the induced secondary or entrained flow.

A high Reynolds number separating boundary layer can be viewed as the transition region between two well studied canonical flow fields: the flat plate turbulent boundary layer and the single stream shear layer. This leads to two possible perspectives from which to view the acquired data. The first perspective is to view the region shown in Figure 3.1 as a boundary layer with a sudden change in the wall boundary conditions. The data then serve to answer the question: how does a turbulent boundary layer react to this abrupt "removal" of the wall boundary condition? A similar question was addressed using a moving wall geometry in Hamelin and Alving (1996, hereafter referred to as HA). It will be demonstrated in the following sections (in agreement with the results of HA) that the

"outer region" of the separated boundary layer remains statistically identical to the upstream (canonical) boundary layer for several integral length scales in the streamwise direction. The insensitivity of the outer region of the boundary layer from the effects of separation is remarkable, and is expected to be of interest to researchers who study boundary layers as well as separated flows.

The second viewpoint considers this region to be the developing region of the shear layer. The data then explain: how does a self-similar single stream shear layer develop from its parent boundary layer? Implicit in the ideas of self similarity is the idea that the initial conditions are "forgotten" (Townsend, 1974). The effects of inflow conditions on the downstream region of a shear layer have been studied by, for example, Bradshaw (1966), Hussain and Zedan (1978), Slessor et al. (1998), and Browand and Latigo (1979). The references report experiments in which the upstream boundary condition is modified, and measure the "effect" on the developed downstream flow. In contrast, the present effort investigated the evolution of the initial turbulent boundary layer as it transitions into a self-similar shear layer. This region has been extensively studied for the case of laminar boundary layers at separation. For example, Ho and Huerre (1984) provides a thorough review and a substantial list of both single stream and two stream shear layer references. Many of these studies consider the near separation region using linear stability theory. The results of the present work will be compared and contrasted to this established theory. Most previous shear layer studies have been conducted with boundary layer Reynolds numbers less than 1000. The use of lower Reynolds number boundary layers is most often justified based on the idea that the details of the initial conditions are unimportant in the fully developed flow. However, this is still a topic of some debate. The present measurements will show that the Reynolds number is of substantial importance in the near separation field. For example, an important feature of the transition from boundary layer to shear layer is the change in length scales. The turbulent boundary layer is known to have both "outer" and "inner" scales, corresponding to the integral length ( $\theta$ ) and viscous wall units ( $v/u_{\tau}$ ) respectively. The ratio of these scales varies as  $\theta u_{\tau}/v \sim Re_{\theta}^{(7/8)}$ (Bejan 1995). In contrast, the fully developed shear layer is typically characterized only by its integral scale. This change in length scales from boundary layer to shear layer will be shown to be an important factor in the physical attributes of the near separation field. Many technologically important devices have Reynolds numbers ( $U_{0}\theta/v$ ) that are very large, say  $10^{6}$  or greater. Since many of the phenomena described in this chapter are distinctive to higher Reynolds numbers, the conclusions could be important in engineering design.

Section 3.2 presents statistics of the boundary layer at separation. Section 3.3 introduces the concept of the "sub-shear layer" and it presents single point statistics acquired in the region downstream of separation. In Section 3.4 measurements in the entrainment stream are used to characterize shear layer features such as the convection velocity and average passing frequency of the large scale motions of the flow. Section 3.5 presents spanwise correlation measurements in the sub-shear layer region. It should be noted that these sections present the experimental data with a limited amount of discussion. This format was chosen so that the many different types of data acquired could be presented prior to the conclusions which are provided in Section 3.6.

#### 3.2 Upstream Boundary Layer

The study of the near separation region was begun with detailed measurements that were acquired near the separation point ( $x\approx0$ ). These data and their interpretation serve to document the inflow boundary conditions to the separated flow discussed in the next sections. The boundary layer portion of this study was separated into two experiments. First measurements to identify the "communication" between the shear layer and the boundary layer were executed; see section 3.2.1. Second, point statistics in the boundary layer were measured with enough detail to ensure that a nearly canonical zero pressure gradient boundary layer existed and that it compared well with standard measurements and correlations. These data are presented in Section 3.2.2.

## 3.2.1 Boundary Layer - Shear Layer "Communication"

The communication between the downstream shear layer and the boundary layer was investigated prior to the determination of the stochastic features of the boundary layer at separation. The purpose of this experiment was to answer the question: "do the pressure fluctuations from the shear layer significantly alter the characteristics of the boundary layer at separation?", Foss (1998). In other words, do the large scale spanwise coherent motions in the shear layer cause a measurable change in the boundary layer characteristics upstream of separation? A previous study discussed in Holmes et al. (1992) has indicated that unsteady effects in the shear layer that originates from a laminar boundary layer, do cause fluctuations in the upstream flow field. That is, "yes", the shear layer does influence the separating boundary layer for laminar separation. The present data will show that this is not true for the present (high Reynolds number turbulent) boundary layer.

The velocity field in the entrainment stream near separation is greatly influenced by the large scale motions which exist in the separated turbulent flow. If these motions also affect the boundary layer flow before separation, it is intuitively reasonable that a non zero correlation between velocities in the boundary layer and in the entrainment stream would provide evidence that the shear layer was effecting the boundary layer. It is noted, however, that statistical quantities such as linear correlations to not indicate causation, and should only be used as an indicator of such effects. Simultaneous hot-wire measurements were taken in both the entrainment stream and the boundary layer flows to test this hypothesis. Four hot-wire sensors were placed in the entrainment stream near the separation point with the sensors aligned with the z-direction such that they would recover the components of velocity in the x-y plane. Note that the w component should be quite small in the essentially 2-dimensional entrainment region. The entrainment probes were then traversed through a range of locations in the region  $0 < x/\theta_0 < 20$ , y<0 area. An X-wire probe was placed in the boundary layer in the range  $0 < y/\theta_0 < 10$ ,  $-4 < x/\theta_0 < 0$ , such that the u and v components of velocity were recovered. These data were recorded for 40 seconds at 5,000Hz. The normalized cross correlation is a function of the discrete time delay variable, defined as:

$$R(\tau_n) = \frac{\overline{\mathbf{v}_1(t_n) \cdot \mathbf{v}_2(t_n + \tau_n)}}{\tilde{\mathbf{v}}_1 \cdot \tilde{\mathbf{v}}_2}$$
 3.1

where  $v_1$  is the u or v component of velocity measured from the X-wire, and  $v_2$  is one of the signals from the entrainment probes, and the overbar represents the time average. The tilde symbol (~) represents the RMS value of that signal.

The results of these calculations have shown nearly zero correlation values for all of the above measurement locations. That is, there was no measurable correlation between the two signals for any of the spatial locations measured. A second calculation was performed in which a low pass filter was used to allow only frequencies less than, for example,  $f_c$ =100Hz (where  $f_c\theta(0)/U_o=0.135$ ) to be correlated. This type of filtered cross-correlation has been shown to be effective in detecting non-zero correlations in highly turbulent flow fields which contain broad-band spectra information; see, e.g., Naguib (1992). These cross-correlations, however, were also found to be negligible in magnitude for all of the acquired data.

It is inferred from the above observations that the upstream "communication" is not measurable in a separating turbulent boundary layer. It is therefore reasonable to assume that the measurable characteristics of a high Reynolds number turbulent boundary layer upstream from a fixed separation point with zero pressure gradient are identical to that which would exist if the separation was not present. These conclusions are further supported by the results of the following section, which presents detailed velocity measurements for  $x\approx 0$ .

#### 3.2.2 Boundary Layer Statistics Near x=0.

The single point statistics of the boundary layer in the very near region of separation were measured using a single hot-wire sensor. The probe was calibrated and traversed through the boundary layer at the streamwise locations  $x/\theta_0 = -0.1$  and +0.1. Each data point was acquired at a sampling frequency of 5,000Hz for 30 seconds. The sensor was aligned in the z direction, such that the magnitude of the velocity in the x-y plane was recovered:

$$a(t) = \sqrt{u^2 + v^2}$$
 3.2

Most authors do not make the distinction between u and q in single probe hot-wire measurements. This is because the v component is small compared to u in wall bounded flows. The emphasis on q in the present work is important because the surveyed region: y<0, will be dominated by the v component of velocity. In the region ( $x\approx0$ , y>0) the approximation  $q\approx u$  is nearly exact.

The time average and standard deviation of the velocity measurements will be denoted by  $\bar{q}$  and  $\tilde{q}$  respectively. The profiles  $\bar{q}(x=\pm\,0.1\theta_o,y)$  are shown in Figure 3.2. Note that these data are normalized by the standard viscous units in log-linear coordinates. The wall shear stress was computed from the slope of a linear fit of the data points closest to the wall at  $x/\theta_o$ = -0.1. The standard log-linear region can be observed through the range  $40 < y^+ < 800$ . This region roughly approximates the standard fit  $q+=2.5*\ln(y^+)+5.5$ . The present data are best represented by  $q+=2.3*\ln(y^+)+6.7$  for 30 < y+<500.

It is of interest to compare the two velocity profiles which have been acquired. The measured  $x/\theta_0$ =±0.1 mean values agree for all locations of  $y^+>5(0.25\text{mm})$ . The insert to the figure shows the deviation of the two traverses for  $y^+<5$  in linear coordinates since negative y values were measured at the downstream location. The deviation between the two profiles indicates a strong streamwise gradient in velocity given that the x displacement of the sensor for the two traverses was 1.8mm. For example,  $\Delta \bar{q}/\Delta x \approx 400(1/\text{sec})$  at y=0. The integral statistics of interest, which were calculated from the mean profile, were the momentum thickness:  $\theta=9.62\text{mm}$ , and the displacement thickness:  $\delta^*=12.6\text{mm}$ . The Reynolds number based on momentum thickness was  $Re_{\theta}=4650$ . Additional parameters are

the friction coefficient and the shape factor, which are defined as  $C_f = 2(u_{\tau}/U_n)^2$  and  $H=\delta^*/\theta$ , respectively. These were determined to be  $C_f=0.00295$  and H=1.31.

The  $\bar{q}(x=\pm\,0.1\theta_o,y)$  profiles in viscous units are shown in Figure 3.3. The observations that can be made from the profiles of  $\bar{q}$  are similar to those already mentioned for  $\bar{q}$ . That is, differences between the two profiles can only be observed in the very near wall region. Note that the maximum value for the  $x/\theta$ =-0.1 data is  $\bar{q}/u_{\tau}=2.74$ . Other researchers (for example Klewicki and Falco (1992)) have found a peak in the fluctuation intensity to be ~2.9 for similar Reynolds numbers. This discrepancy can be explained by the relatively large sensor length used in the present study. Specifically, the hot wire length in viscous units was  $\lambda^+=20v/u_{\tau}$ , where Klewicki and Falco (1992) recommend a sensor length of less than  $10v/u_{\tau}$  in order to avoid spatial averaging of the velocity fluctuations.

The spanwise vorticity in the boundary layer is also a variable of interest. The magnitude of the time averaged vorticity in viscous units is approximated by  $|\widetilde{\omega_z^+}| = \partial u^+/\partial y^+$ . The slope of the mean velocity profile shown in Figure 3.2 was computed; see Figure 3.4. The standard deviations of the fluctuations in spanwise vorticity:  $\widetilde{\omega_z}$ , were measured using the four-wire vorticity probe described in Chapter 2; these data are also shown on Figure 3.4. The measured values of  $\widetilde{\omega_z}$  are consistent with the data presented in Klewicki et al. (1992) and references therein. These data show that both positive and negative values of vorticity were realized for y+>20. This can be compared with the near wall region wherein only one sign of vorticity that is consistent with that of the mean shear is observed. The vorticity

fluctuations normalized by the local mean value:  $\tilde{\omega}_z/|\overline{\omega}_z|$  have been plotted for the region  $10 < y^+ < 800$  as the insert to Figure 3.4. Note that the values of  $\tilde{\omega}_z/|\overline{\omega}_z|$  are uncertain for  $y^+ > 800$  because both the numerator and denominator are approaching zero. The data show that the relative fluctuation levels of vorticity increase approximately logarithmically (linear in semi-log coordinates) throughout the "log region" ( $10 < y^+ < 600$ ) of the boundary layer.

Qualitative aspects of the vorticity filament topology can be inferred from these measurements and the solenoidal condition of the vorticity vector field. At a small distance from the wall the filaments are necessarily perpendicular to the local shear stress vector, and parallel to the surface. The highly fluctuating values of single signed spanwise vorticity near the wall indicate that the near wall filament topology is relatively simple. In contrast, the measurements farther from the wall  $(y^+\sim 20)$  indicate that the vorticity filaments must be sufficiently complex or "twisted" such that vorticity values of both sign are realized at a given y location. Farther from the wall, the statistics of the velocity and vorticity fields exhibit many of the properties of isotropic turbulence; see, for example, Saddoughi and Veeravalli (1994) for examples of velocity statistics. An example of this from the present measurements is the vorticity spectrum at location y+=400 ( $\bar{u}/U_0$  = 0.77) as shown in Figure 3.5. These data are presented along with a model spectrum which was derived using the assumption of isotropic, homogeneous turbulence, (see Anonia et al (1998) and Section 4.6). The variables have been normalized using Komogorov variables defined in Chapter 4. The agreement between the measured and isotropic spectra support the idea that the vorticity filaments in the outer region of the boundary layer are not directly

effected by the wall. These features of the vorticity field will be considered in the following sections which describe dynamics of the near separation region of the boundary layer.

# 3.3 Point Statistics And The "Sub-shear Layer"

A flow visualization image of the near separation region is shown in Figure 3.6. This digital image was acquired using a Kodak 1k x 1k camera and a 1mm thick laser light sheet oriented in the x-y plane. The boundary layer flow was seeded using an oil-fog system located upstream of the boundary layer leading edge. The unmarked entrainment flow provided the contrast between the two fluid streams. Specifically, the marked primary fluid appears white, and the clean entrainment fluid appears dark in the figure. Note the scale and orientation with respect to Figure 3.1. Specifically, recall that the boundary layer thickness  $\delta$  is of order 100. This picture is not repeatable in detail because the flow is turbulent in this region. However, the general features represented and described are common to all realizations.

Several interesting observations can be made from this visualization. First, a streakline from the separation point can be easily identified. This shows a "wavy" or "flag-flapping" type of behavior. The first disturbance occurs at a streamwise location of  $x \approx \theta_0$ . The "size" of this motion appears to be of order  $0.5\theta_0$ . This observation is consistent with the "communication" results of Section 3.1.1. That is, it would seem unlikely that the pressure fluctuations from this first or downstream disturbances would influence the upstream boundary layer given their relatively small scale. Note also that the asymmetry of the shear layer is evident from the movement of the marked fluid into the entrainment region (y<0), whereas very little clean fluid is observed for y>0. The visually apparent "growth"

of the shear layer is clearly at a length scale which is significantly smaller than the boundary layer thickness.

Based on these observations, and equipped with the data to be presented in this and subsequent sections, several distinct regions of the flow field have been identified. These are shown schematically in Figure 3.7. These regions and their defining characteristics will provide a conceptual framework and vocabulary which will be useful in describing the results to follow. The "canonical turbulent boundary layer" is the region which exhibits stochastic values of the velocity field that reflect the evolution of a boundary layer that is still attached to a flat plate. The "sub-shear layer" represents the turbulent region where the flow is measurably different from that which would be present if the bounding wall were present. The region marked "significant irrotational fluctuations" represents the domain where measurements of the velocity fluctuations exhibit essentially no high frequency (small scale) motions. It is inferred that these motions are driven only by the unsteady pressure field created by the shear layer. Lastly, the transitions between subshear layer and the developing shear layer are not well defined. Hence no such boundaries are drawn in Figure 3.6.

Point statistics were acquired using a single hot-wire probe which was traversed across the shear layer at 12 streamwise locations. The data were acquired at 5 kHz for 60 seconds. If the characteristic velocity is taken as  $U_0/2$ , and if the shear layer width is taken to be 60(x), then the 60 seconds represents 500 to 2000 shear layer widths for the 12 locations. The sensor was aligned in the z direction to recover the time series of q as described in Section 3.1.2. Note that in the high speed free stream the sensor records  $q=u=U_0$ , and in the entrainment stream the sensor records  $q=v=v_0$ . The time average velocity  $(\bar{q})$  and the

standard deviation of the fluctuations  $(\tilde{q})$  were then computed from the time series values. The mean velocity is shown in Figure 3.8 as an x-y plot, and in Figure 3.9 as a contour plot. The values of  $\tilde{q}$  are shown in Figures 3.10 and 3.11 in x-y and contour formats, respectively.

A striking feature observed in these data is the streamwise invariance of the boundary layer statistics. As a specific example, the mean profiles are identical to the boundary layer profile for  $y/\theta_0>2$  in the range  $0< x/\theta_0<29$ . The profiles of  $\tilde{q}$ , are streamwise invariant for  $y/\theta_0>4$  in the range  $0< x/\theta_0<29$ . This can be observed by the horizontal (i.e., streamwise invariant) contours in Figures 3.9 and 3.11, or by close examination of the individual profiles in Figures 3.8 and 3.10. Several histograms of velocity are given in Figure 3.12 for the points:  $(x/\theta_0, y/\theta_0)=(0.73, 2)$ . (7.2, 2) and (19, 2). The similarity of these histograms provides a specific example of the nominal streamwise invariance of the velocity field.

It is noteworthy that these results are consistent with those of Hamelin and Alving (1996), referred to as HA. In this reference, a moving belt was used to remove the inner layer of an  $Re_{\theta}$ =2800 turbulent boundary layer in order to study the stochastic evolution of the outer scales. The present work is similar in that the streamwise evolution of the boundary layer is measured after an abrupt change in wall boundary conditions. In the case of the moving wall boundary condition, the mean flow field was streamwise invariant for  $y/\theta_0>2$  in the range  $0< x/\theta_0<34$  (see Figure 5 of HA). The RMS of the velocity fluctuations at a given y location was streamwise invariant for  $y/\theta_0>4$  in the range  $0< x/\theta_0<30$  (Figure 7 of HA).

These regions of streamwise invariance are nearly identical to those realized in the present experiment.

Two variables of interest were calculated from the mean velocity profiles: the momentum thickness of the shear layer  $\theta(x)$  and the maximum slope of the mean velocity. The calculation of  $\theta$  requires the integration of velocity across the shear layer. Because the magnitude of the velocity was measured as opposed to strictly the u component (see equation 3.2), an arbitrary cut-off of  $\bar{q}/U_o$ =0.05 was used to end the integration on the low speed side. This is a common technique used by Foss (1977) and Hussain and Zaman (1985). These results are shown in Figure 3.13. The growth rate in the region  $x/\theta_o$ >60 was found to be 0.035 as measured previously by Foss et al. (1977). Note that Hussain and Zaman (1985) found a linear growth rate of 0.032. The second variable derived from the point statistics that will be of interest in subsequent sections is the maximum slope of the velocity profile. These data are shown in log-log format in Figure 3.14 for streamwise locations (1.8< $x/\theta_o$ <550). This extended domain shows that the function  $(dq/dy)_{max}$ ~1/ $x^{0.79}$  matches well throughout the sub-shear layer region as well as further downstream.

A variable of interest is the maximum value of  $\tilde{q}$  obtained at a given streamwise location. This information was extracted from the data shown in Figure 3.10, and plotted in Figure 3.15. The most interesting feature of these data is the local maximum value realized at  $x/\theta_0\approx 2$ . This peak occurs at a lateral position of  $y/\theta_0=0.15$ . Previously, the existence of a local maximum has only been observed in shear layers with a laminar separating boundary layer, whereas the tripped or high Reynolds number boundary layers lead to a monotonic increase in  $\tilde{q}$ ; see Hussain and Zedan (1978). The present data support the concept that the

sub-shear layer region near the separation point is a viscously dominated flow region which shares many of the characteristics of low Reynolds number separations.

## 3.4 Shear Layer Diagnostics From Entrainment Measurements

A ubiquitous feature of the single stream shear layer is the existence of large scale coherent motions. These motions are characterized by a correlation length in the spanwise (homogeneous) direction that is many times larger than the local shear layer thickness. The existence, physical makeup, and dynamic significance of these large scales are still topics of debate and research. The origin of these motions is believed to be from the inflectional instability of the shear layer velocity profile. The flow visualization and point statistics described in the previous section indicate that this instability does not influence the entire separating boundary layer. Rather, it is likely that the influence of these motions is limited to the shear layer region.

A simple method of detecting these large scale motions is to acquire velocity time series in the irrotational flow field near the shear layer. Many studies have made use of the fact that the time signature of velocity in both the high speed and low speed streams can be used to identify features of the large scale motions within the shear layer; see for example, Browand and Weidman (1976), Koochesfahani et al. (1979), Browand and Trout (1985), or Narayanan and Hussain (1996). The efficacy of this technique is based upon the pressure fluctuations which are mechanistically linked to the motions. This leads to easily detectable fluctuations in the velocity field of the irrotational flow surrounding the shear layer. The following subsections will utilize the q(t) data that were used to create the point statis-

tics in section 3.3. Specifically, at each of the 12 streamwise positions (see Figure 3.8), a

single y location on the entrainment side of the shear layer was selected which exhibited notable fluctuation levels with minimal turbulent intermittency. These locations were determined by visually inspecting the time series data of q(t). If high frequency fluctuation were not present, the flow was assumed to be relatively irrotational. The locus of points which satisfied this criterion can be described by the line  $y/\theta_0=0.0259(x/\theta_0)-4.0$ . The fluctuation intensity at these points was approximately  $\tilde{q}/U_o\approx 0.02$ .

## 3.4.1 Convection Speed of the Coherent Motions

A variable of interest is the "convection velocity" of the spanwise motions,  $U_c$ . Many investigators of both single and two stream shear layers have found the convection velocity to be the mean velocity of the two streams with equal density. See for example, Dimotakis (1986) and references therein. The ratio would be predicted to be  $U_c/U_0=0.5$  in the single stream shear layer. The time averaged convection velocity was measured from time series data of two hot-wires placed in the entrainment stream with a streamwise displacement  $\Delta x$ . The lateral locations where  $\bar{q}(y) \approx 0.05 U_o$  were determined to have significant signal amplitude in the irrotational region. The time-delayed cross correlation of the two hot-wire signals was computed from these time series to locate the time delay to the first observed positive peak:  $\Delta t$ . The average convection velocity is defined as  $U_c = \Delta x/\Delta t$ .

Figure 3.16 shows the normalized convection velocity  $2U_c(x)/U_o$ . Of interest is the low value of 0.54 near x=0 and the increase to the expected value of 1.0 for  $x/\theta_o>120$ . This is inferred to be a result of the sub-shear layer phenomena where only the vorticity from the near wall region participates in an inflectional instability. Several statements can be made

to support this inference. The first observation is that the velocity gradients are very steep in the region x=y=0 which lead to length scales which are considerably smaller than the local integral scales. Since the length scale of the most amplified motions will scale with the velocity gradient at the point of inflection, it is reasonable that only the fluid in the y=0 region will participate in the instability.

A second argument to support this idea is related to the vorticity field of the turbulent boundary layer upstream of separation. It is known that the filaments of vorticity in the very near wall region (say y+<1) are parallel to the wall, and are perpendicular to the wall shear stress vector. In contrast the outer region of the boundary layer does not have this constraint which leads to a vorticity field with a high level of disorganization. It can be inferred from these observations that the "organized" near wall vorticity participates in the first instability, whereas the "disorganized" outer motions do not.

It is possible to calculate "how much" of the time averaged vorticity participates in the first instability based on the above observations. Given the relatively small contribution of the y component of velocity to the vorticity in the near wall region, the mean streamwise velocity can be written as:

$$\bar{u}(y) = \int_0^y \overline{\omega} dy$$
 3.3

The velocity scale of the first instability is observed to be  $0.54U_0$  from Figure 3.14 near x=0. This corresponds to  $y^+<42$  at x=0 in terms of the mean velocity as observed from Figure 3.2. Evaluating equation (3.3) at  $y^+<42$  shows that 54% of the vorticity which separates from the boundary layer participates in the first instability. The growth of the sub-

shear layer in the streamwise direction indicates that an increasing amount of vorticity from the boundary layer participates in the coherent motions as the flow evolves in the streamwise direction. This is also supported by the slow increase in  $U_c$  to the nominal predicted value of  $0.5U_0$  at large  $x/\theta_0$  locations.

## 3.4.2 Spectral Properties of the Entrainment Stream

The spectral properties of the near entrainment stream were used to investigate the coherent motions of the sub-shear layer region. The power spectral density (the Fourier transform of the autocorrelation) was computed for the 12 streamwise locations (identified in Section 3.2),. These data are shown in "log-log" format in Figure 3.17. The amplitude of each data set was shifted vertically in order to distinguish the data sets on one figure. These data show a distinct local maximum, or "hump" in the spectrum for all streamwise locations except  $x/\theta_0 = 0.73$ . For example, the hump at  $x/\theta_0 = 29.5$  occurs at 10Hz. Nearly identical results for the range  $37 < x/\theta_0 < 4800$  can be found in Hussain and Zaman (1985) hereafter, referred to as H-Z. It can also be observed that the frequency, where the local maximum occurs:  $f_{\rm m}$ , decreases with downstream distance. This frequency can also be identified using the first peak of the autocorrelation function. This leads to a similar, although not necessarily the same, identification of the preferred frequency. Figure 3.18 shows an example of the autocorrelation function for  $x/\theta_0 = 7.17$ . It should be noted that at all locations, the "hump" does not imply that the signal is periodic. These humps should be interpreted only as a preferred frequency at that streamwise location.

The frequency values:  $f_{\rm m}$  (normalized by  $\theta_{\rm o}$  and  $U_{\rm o}$ ) were calculated from both the spectra and autocorrelations for the region 1.8<x/ $\theta_{\rm o}$ <650; see Figure 3.19. The frequency data

from H-Z in the region  $37 < x/\theta_0 < 4800$  (taken from Figure 5 of that reference) are also shown in Figure 3.19. Note that the boundary layer Reynolds number at separation was  $Re_{\theta}$ =428 in H-Z. The agreement is quite good in the overlap region between these data sets, which indicates that the dimensionless frequency is not a strong function of the Reynolds number of the separating boundary layer.

The frequency data can also be made non-dimensional using the free stream velocity and the local momentum thickness. That is, a non-dimensional frequency:  $f^*$  can be defined as  $f^*=f_m\theta(x)/U_0$ . These data are shown in Figure 3.20. The  $f^*$  value measured at the location  $x/\theta_0$ =600 is also shown on the figure. The functional dependence of  $f^*$  can best be interpreted by considering the functional dependence of both the momentum thickness and the frequency from the respective curve fits of the data. Although the momentum thickness does not grow linearly in the very near separation region, the data shown in Figure 3.13 can be roughly approximated by:

$$\frac{\theta(x)}{\theta_0} = 0.0312 \left(\frac{x}{\theta_0}\right) + 1.079.$$
 3.4

in the region  $0 < x/\theta_0 < 100$ . A fit of the frequency data is represented by:

$$\frac{f_m \theta_o}{U_o} = \frac{0.133}{(x/\theta_o)^{0.714}}.$$
 3.5

The dimensionless frequency becomes:

$$f^*(x) = \frac{f_m \cdot \theta(x)}{U_o} = 0.0041(x/\theta_o)^{0.286} + 0.143(x/\theta_o)^{-0.714}$$
. 3.6

Equation 3.5 is shown as the solid curve on Figure 3.20. This presents two limiting regions of interest: the very near separation region, and the limiting behavior for large x. The larger values of  $x/\theta_0$  are clearly dominated by the first term of equation 3.5. This equation

would predict an  $f^*$  which is slowly increasing for large  $x/\theta_0$  values because the momentum thickness grows linearly, and the exponent of the frequency dependence is -0.71. This is in contrast to the expected result that the dimensionless frequency would be constant. It is also noted that the largest downstream distance measurement provided  $f^*(x/\theta_0=600)=0.026$ . This is slightly larger than the apparent value of 0.021 from the  $x/\theta_0<100$  data, although this difference is close to the uncertainty of the measurement. Note also that H-Z measured a value of 0.024, although the uncertainty in those measurements seems to be considerably greater.

The x dependence of  $f^*$  has two possible explanations: either the  $f^*$  values are dependent on x position, or the shear layer is still "relaxing" from the initial upstream boundary conditions (i.e., the turbulent boundary layer). The latter of these explanations is likely the correct one. It can be observed from the H-Z data in Figure 3.19 that a  $f_m$ ~1/x dependence approximates the data for  $x/\theta_0$ >1000, where  $f_m$ ~1/ $x^{0.71}$  as measured in the present data, seems to correlate well with the H-Z data for  $x/\theta_0$ <1000. It is possible that the present shear layer would also tend towards a 1/x dependence for larger x values given the agreement withe the H-Z data in the region where the data overlap.

The non-dimensional frequency in the limit of small x values is also of interest, particularly with regards to the sub-shear layer described in the previous sections. In terms of equation 3.6, the second term dominates the magnitude of  $f^*$  for small  $x/\theta_0$ . This is because the frequency grows exponentially for small x, and the momentum thickness approaches the value at separation. A preferred scaling might be considered by relating the frequency to the local maximum velocity gradient:  $f^*_{grad}(x) = f_m/\left(\frac{d\bar{u}}{dy}\right)_{max}$ . Note that

this definition is equivalent to using the "vorticity thickness" scaling. These data are also shown on Figure 3.20. This definition was motivated by the fact that both variables follow a power law  $\sim x^{-n}$  as shown in Figures 3.14 and 3.19. In fact, the exponent of the maximum velocity gradient: n=0.79 closely matches the values of 0.71 measured for the frequency dependence. The gradient based definition provides a dimensionless frequency with considerably less streamwise dependence than  $f^*$  for  $x/\theta_0 < 20$ .

# 3.4.3 The Initial Instability

The frequency of the initial instability has been the focus of numerous studies (see, e.g., Ho and Huere (1984)). The understanding of how the boundary layer vorticity is re-distributed downstream of separation is of considerable interest both fundamentally and technologically. Manipulation and periodic forcing of the boundary layer at separation can take particular advantage of the first instability in order to control the unsteady dynamics of the shear layer.

The near separation region of a laminar shear layer is known to be unstable to small amplitude perturbations due to Kelvin-Helmholtz instability. Linear stability theory has been used by many authors to understand and predict the frequency and growth rate of the first instability; (see, e.g., Ho and Huere (1984)). There are several important assumptions of the linear theory which often include parallel flow, laminar flow with infinitesimal disturbances, and a specific velocity profile such as a hyperbolic-tangent function. Although these assumptions are not physically realized in any shear flow, the theory predicts the frequency of the fundamental instability for various geometries with great success. The efficacy of this theory for shear layers and jets was reviewed by Ho and Huere (1984) and

 $St_o = f_m \theta_o / U_o$ . Note that some references use the average velocity in the case of two stream shear layer. This would change the definition by a factor of two; the referenced values have been divided by two where appropriate for comparison to single stream results. In contrast, the effects of laminar-turbulent boundary layer states and Reynolds number on the initial instability have not been previously been extensively investigated. Although the initial development region for laminar flow has been studied extensively, most shear layer studies which have a turbulent boundary layer do not consider the initial instability of the shear layer. Ho and Huere (1984) comment that the most amplified Strouhal number changes from 0.016 for a laminar flow to 0.022-0.024 for turbulent flow due to "presently unexplained reasons." The remainder of this section will explain their observation in terms of the sub-shear layer phenomenon presented in Section 3.2.

Thomas (1991). The Strouhal number of the most amplified frequency is defined as

The single sensor hot-wire data described in the previous sections was used to observe the frequency of the initial instability. Using the spectral information shown in Figure 3.17 it can be observed that the time-averaged spectra of velocity shows a local maximum at the streamwise locations  $x/\theta_0 \ge 1.87$ . Although these time series are not periodic, the local maximum is interpreted to represent the *preferred* frequency at that location. However, the lack of a local maximum in the spectra for  $x/\theta_0 = 0.73$  does not imply that a preferred frequency does not exist. The flow visualization shown in Figure 3.5 indicates that the first instability does occur in this region. This has motivated a more detailed examination of the time series data at this location to identify if a preferred frequency exists at this location.

Several segments of time series data are shown in Figure 3.21. These data show that pseudo-periodic motions do exist, although the frequency, phase and amplitude vary considerably during a relatively short time period. This explains why the spectra failed to show a local maximum value at a particular frequency. This result is also physically reasonable given that the vorticity, which is convected from the viscous region of the boundary layer, is highly unsteady and highly perturbed by the turbulence in the "log region". An alternative method of determining the frequency content of a signal is to look for the time delay of the first local maximum of the autocorrelation. The inverse of this time will indicate the frequency. The autocorrelation of the entire signal, along with several short time autocorrelations is shown in Figure 3.22. The time series data were divided into 0.1 and 0.2sec segments for analysis. The autocorrelation was then calculated for each of these time segments. A distinct local maximum was found in the autocorrelation function for 51% of the 0.1sec data and for 37% of the 0.2sec data. A histogram of the observed frequencies is shown in Figure 3.23. The mean frequency from the 0.1sec samples was 130Hz. The mean value from the 0.2sec samples was 146Hz. This value corresponds well with  $f_{\rm m}$ =124 which is calculated from equation 3.4. This agreement adds confidence that a preferred frequency does exist for the initial instability, and that its value can be accurately determined.

The next step in the determination of the initial Strouhal number is to choose velocity and length scales to non-dimensionalize the indicated frequency. The standard choice of  $U_0$  and  $\theta_0$  would not be appropriate since it is only the inner most wall region that is participating in this first instability. It seems illogical to use, for example, the boundary layer

momentum thickness  $(\theta_0)$  to scale a phenomenon which does not involve the entire boundary layer. The new scales of velocity and length will be  $U_{eff}$  and  $\theta_{eff}$  to imply that it is the effective velocity scale and only the effective momentum thickness that lead to the first instability and roll-up.

A logical choice for the velocity scale is  $U_{eff} = 0.54U_o$ . This is justified by the apparent convection velocity of the first instability discussed in Section 3.3.1. The *effective* momentum thickness of the sub-shear layer was determined by fitting the hyperbolic tangent profile to the mean flow measurements acquired at  $x/\theta_o = 0.73$ . The data were fit to the equation:

$$\frac{q(y)}{U_o} = \frac{U_{eff}}{2} \left[ 1 + \tanh\left(\frac{y}{2\theta_{eff}}\right) \right]$$
 3.7

in the range  $0 < \bar{q} < 0.56 U_o$ . The mean velocity data and equation 3.6 are in good agreement over this range; see Figure 3.24. This equation was chosen specifically because the linear stability theory calculation of the most amplified wave number is derived from the tanh profile. The effective momentum thickness was determined to be  $\theta_{\rm eff}$ =0.5mm ( $\theta_o/\theta_{\rm eff}$ =19.2) by a least squares fit between the data points and equation 3.6.

Finally, the values  $f_{\rm m}=130$ Hz,  $U_{\rm eff}=0.56U_{\rm o}=4.06$ m/s, and  $\theta_{\rm eff}=0.5$ mm lead to St<sub>o</sub>=0.0165. The uncertainty of this measurement is estimated to be  $\pm 10\%$ . This value is in excellent agreement with both linear theory, and all existing literature for laminar shear layers. This indicates that the highly unsteady and turbulent sub-shear layer is likely dominated by a viscous, linear stability mechanism. This result is both unique and surprising given the strict assumptions which are required by the theoretical calculation of the most amplified

Strouhal number. It is argued that the methods by which the frequency, length, and velocity scales were chosen are logical, and not arbitrary. Additionally, only high Reynolds number separated boundary layers will have such a large discrepancy between the true and the effective momentum thickness values.

#### 3.5 Spanwise Correlation Field of the Near Separation Region

The data which have been presented thus far have been statistics acquired at a single x-y plane. Because the flow is stochastically homogeneous, these data are representative of the entire flow field excluding the side wall boundary layers. In addition to these data, it is of interest to document the multi-point correlation of the velocity field in the spanwise direction. For example, the velocity measurements taken in the entrainment side of the shear layer indicated that motions exist within the shear layer with sufficient coherence to be detected well into the irrotational flow. The spanwise extent of these coherent motions is of considerable interest. For example, fluid-structure interactions will depend greatly on the coherence of the pressure field created by the large scale motions. That is, a flow with a high level of coherence will tend to cause large fluctuating forces on mechanical structures because the net force is the integral of the pressure field. The pressure fluctuations from smaller scale motions will tend to cancel in magnitude leading to smaller fluctuations in the applied forces.

The data were acquired using a rake of 8 single wire sensors in the flow aligned with the z direction. The sensors were equally spaced at  $\Delta z/\theta_0$ =2.05. A schematic of the rake and its orientation is shown in Figure 3.25. These probes were traversed through the near separation region using the same experimental grid as shown in Figure 3.8. Specifically, the rake

was traversed through the y direction at 12 streamwise coordinates. The time series data were recorded for 60 seconds at a data acquisition rate of 5000Hz at each spatial location. The presentation of these results is divided into the two following sub-sections. First, several short time segments of velocity from the low speed side will be presented in Section 3.5.1. These data will help to orient the reader to the data acquisition procedures and they will assist in the interpretation of the results. Secondly, the zero time delay cross-correlation was calculated for all the  $(x,y,\Delta z)$  positions measured. These data are described in Section 3.5.2.

#### 3.5.1 Example realizations in the irrotational stream

Four locations in the domain were selected on the low speed side of the shear layer corresponding to  $x/\theta_0=3.53$ , 12.0, 40.5, and 84.2. The respective  $y/\theta_0$  locations (-3.7, -5.37, -10.9, and -19.6) correspond to the positions that were used in the determination of the spectral content of the entrainment stream; see Section 3.4.2 and Figure 3.17. The time coordinate was non-dimensionalized using the *local* value of the peak frequency as shown in Figure 3.17. That is,  $\lambda \equiv (\text{time}) * f_m$  for Figures 3.26 through 3.29. This represents the data in terms of the integer number of averaged wave periods.

Time series data from these locations are shown in Figures 3.26 through 3.29. The beginning of each time record shown in these figures was chosen arbitrarily (i.e. when the A/D system was activated) and was not intended to isolate any specific observed features.

Longer time records yield qualitatively similar representations of the flow field. The contour plots show the fluctuating component of velocity from all 8 sensors normalized by the standard deviation of the respective signals. The legend for the gray scale shows that light

shading implies positive fluctuations in velocity, and dark shading indicates negative fluctuations. For each of the contour plots, the time traces from the wires located at  $z/\theta_0=2.05$  and 12.4 are shown for comparison.

A feature observed in these figures is the growth in the spanwise coherence of the entrainment velocity as x is increased from  $3.53\theta_0$  to  $84.2\theta_0$ . Specifically, Figure 3.26 shows clear evidence that the motions which led to these fluctuations do exhibit a coherence in the spanwise direction, although the spatial extent is limited. Figure 3.27 could be described similarly, although the spatial extent of the coherent motions has obviously "grown". It is instructive to reiterate the idea of the sub-shear layer when considering these spanwise correlations. As a specific example, recall that at the streamwise location  $x/\theta_0=12$ , the flow field for  $y/\theta_0>2$  is stochastically identical to the boundary layer.

In order to directly contrast this large spanwise coherence with the boundary layer flow, the correlation coefficient for these four locations as well as one position within the boundary layer (at x=0,  $y=0.5\theta_0$ ) are shown in Figure 3.30. It is clear from these measurements that the larger spanwise coherence is developed downstream of the separation point, and within the sub-shear layer region. The length scale of the correlation measurements is clearly many times greater in the region near the sub-shear layer compared with the boundary layer, even at small  $x/\theta_0$  values.

The continued growth in coherence is also seen in Figures 3.28 and 3.29, where the irrotational fluid motion is beginning to appear nearly two dimensional. These measurements closely parallel those of Bowand and Trout (1980, 1985, collectively referred to as BT) where 12 wires were placed in the low speed side of a two stream shear layer facility. They

also found the correlation field to increase in the streamwise direction. The short time realizations of the velocity fluctuations shown in BT look very similar to those shown in Figure 3.29.

#### 3.5.2 Correlation Coefficient Data

The correlation coefficient  $R(\Delta z)$  was calculated (as shown in Figure 3.30) for each of the (x,y) locations (see Figure 3.9 for the grid of data points used). The data set can be represented by the "volume" of points  $(x,y,\Delta z)$ . The visualization of these data was made possible by "slicing" the volume in planes perpendicular to the x and z directions. First, the streamwise locations  $x/\theta_0$ =3.53, 12.0, 40.5, and 84.2 (i.e., the positions used in Figures 3.26-3.29) were selected. Figures 3.31 through 3.34 show contours of the correlation coefficient at these locations. The mean velocity profile is included with each of the figures for reference. Figures 3.35 through 3.39 show contours of R at specific  $\Delta z$  values. The solid boundary surrounding the contour plot represents the spatial extent where the data were acquired. The dashed boundary represents the contour line where the fluctuation levels are 1% of the free stream velocity (see Figure 3.10). Correlation data are shown in the region where the fluctuations exceed 1% of  $U_0$ .

Several important features of the flow field can be observed from these measurements. First, the central region of the shear layer shows quite low spanwise correlation values. This is in contrast to the low speed irrotational flow measurements which exhibit a large correlation length with respect to the local length scales. Although it is apparent that the irrotational fluctuations are caused by the motions existing in the turbulent fluid, the corre-

lation measurements in the central region of the shear layer are "washed out" by the high levels of small scale turbulence.

A second feature observed from these data is the difference between the high and low speed sides of the shear layer. Specifically, the correlation length grows smoothly and continuously from the separation point, whereas the high speed side shows a discontinuity in the data near  $x/\theta_0$ =55. These data are consistent with the concept of the sub-shear layer, and also provide insight as to how the sub-shear layer evolves into a fully developed shear layer. Specifically, the vortical fluid which occupied the outer region of the boundary layer does not participate in the instability which leads to the large scale spanwise motions. As the flow progresses in the streamwise direction, more of this vortical fluid is drawn in to "participate" with the coherent motions. The dramatic change in the correlation field near  $x/\theta_0\approx55$  indicates that the motions have become strong enough to have a measurable effect on the high speed irrotational fluid. The time averaged convection velocity of the coherent motions at this location is approximately 82% of the final value of  $0.5U_0$ .

## 3.6 Summary and Conclusions

A number of observations can be drawn from the collection of data described in the preceding sections. These data have revealed information which does not currently exist in the fluid mechanics literature. As stated in the introduction, the unique features of the current facility that have allowed these discoveries are the high Reynolds number at separation (4650) and large length scale ( $\theta_0$ =9.6mm) of the flow. For comparison, Hussain and Zaman (1985) studied a similar geometry, albeit the boundary layer Reynolds number at separation was 428, and the momentum thickness  $\theta_0$ =0.5mm. Many of the features

described in this chapter have been at scales of the order of  $\theta_0$  or smaller which would make them unnoticeable in a facility with a small value of  $\theta_0$ . In the following, the main conclusions are given in a numbered format followed by a discussion and interpretation of the relevant data sets.

1. The stochastic properties of the boundary layer at separation (x=0) appear to be unaffected by the flow field downstream of separation.

This conclusion is supported by several of the experiments. First, the zero cross-correlation magnitudes between velocities measured in the boundary layer and in the entrainment stream is a strong indication that a causal relationship does not exist between the two regions. The lack of correlation in the low-pass filtered time series further supports this result. The reported stochastic properties of the boundary layer show that the moments of the velocity and vorticity field are in good agreement with the existing literature on boundary layers without separation. If the shear layer did have an effect on the boundary layer at separation, it was not apparent in any of the point statistics or correlation measurements.

The streamwise invariance of the statistics in the outer region of the boundary layer provides additional evidence to support this conclusion. In other words, not only do the shear layer fluctuations not effect the boundary layer at x=0, there is no measurable effect on much of the y>0 region for a considerable length downstream. This will be discussed further as conclusion number (2) below.

The fact that a high Reynolds number boundary layer which separates at a 90 degree edge is not affected by the separation is important for several reasons. If the separation region

was to be modeled using a computational method, the upstream boundary conditions could be completely specified at x=0 by the stochastic properties of the approach boundary layer. If in contrast, the separated flow field were to effect the stochastic properties upstream of separation, then the inlet conditions to the computation would have to be specified at some x<0, rather than at x=0.

It is likely that the boundary layer to shear layer communication is quite dependent on the Reynolds number. Laminar and low Reynolds number turbulent flows at separation are likely to be more sensitive to the perturbations caused by the downstream motions. A future study of this topic may attempt to measure an objective indication of the communication for a range of Reynolds numbers.

2. The outer region of the boundary layer is stochastically streamwise invariant for several integral lengths downstream of separation.

This streamwise invariance of the boundary layer properties is quite evident in all of the data identified above. For example, the contour plots showing statistics in the x-y plane (Figures 3.9, 3.11, 3.35-3.39) all show invariant properties of the flow from in the region  $0< x/\theta_0< 50$ . This adds information to a body of literature which exists on the topic of inner and outer scales in the boundary layer; see, for example Klewicki (1989), and Marusic and Perry (1990). The present observations indicate that not only are the outer scales not dependent on the local production of near wall turbulence, but that the flow is not even effected by the large scale fluctuations of the shear layer measured in the  $y\approx 0$  region.

3. The separation region can be described by the "sub-shear layer" in which only the near wall vorticity participates in the initial shear layer instability.

The region which defines the sub-shear layer can most easily be identified by the wedge shaped region defined by  $u_{rms}/U_o>0.07$  on Figure 3.11. Many of the salient features that are associated with canonical shear layers have been identified in this region. It can also be observed from the  $u_{rms}/U_o>0.07$  contour on Figure 3.11 that the "spread angle" of the subshear layer and of the fully developed shear layer are the same.

An important feature of shear layers is the presence of coherent motions which develop from the inflectional instability mechanism (see Ho and Huere (1984 for a review). These motions are known to move in the streamwise direction with a well defined convection velocity. In fully developed single stream shear layers, this velocity is known to be approximately  $2U_{conv}/U_o=1.0$ . The convection velocity in the sub-shear layer region is shown in Figure 3.16. These data indicate a dramatic rise in the convection velocity from  $\approx 0.54$  at separation to 1.0 near  $x/\theta_o=120$ . It is inferred from these data that only the near wall vorticity is "rolling up" or participating in the inflectional instability. A quantitative estimate of the fluid domain which participates in the initial roll-up has been identified as that below the  $q/U_o=0.54$  isotach. Equivalently, this bound is given by  $y^+<42$  for the present boundary layer. As the sub-shear layer grows into the outer part of the boundary layer, more of the vorticity is pulled into the coherent motions thereby increasing both the width of the sub-shear layer and the convection velocity.

The present understanding of the vorticity field within a turbulent boundary layer is consistent with the current findings. That is, the stochastic and instantaneous properties of the motions which define the inner and outer scales of the boundary layer are significantly different. The near wall motions are described by, for example Adrian et al. (2000), and Pan-

ton (1999). In these references, the near wall region is understood to be comprised of groups of coherent motions which define localized shear layers. These result in "vortex packets" which evolve into the outer scales of motion. It is intuitively reasonable that the near wall region with a high level of organization of vorticty would be subject to inflectional instability immediately downstream of separation. In contrast, the motions farther from the wall are usually considered to be more "disorganized" and not closely correlated with the motions very near to the wall. The current measurements of spanwise vorticity fluctuations at x=0 support this viewpoint. Again, it is intuitively reasonable that these motions would not participate in the roll-up phenomenon.

4. The recognition of the sub-shear layer allows a physical explanation for why shear layers with a turbulent boundary layer at separation approach self-similarity at smaller  $x/\theta_0$  values compared with shear layers with a laminar separation.

The streamwise location where the flow field becomes self-similar has been found to be quite dependant on the state and Reynolds number of the boundary layer at separation. For example, Bradshaw (1966) recommends a value of  $x/\theta_0>1000$  for self similarity given a laminar separation. Hussain and Zaman (1985), Bruns (1990), and the present study have found that  $x/\theta_0>100$  is sufficient for the mean velocity to exhibit self-preservation when the separating boundary layer is turbulent.

These differences can be explained in terms of the length scales of the turbulent vs. laminar boundary layers. The suggestion was given by Dimotakis and Brown (1976) that it is not the downstream location as defined by a number of original integral length scales (e.g.,  $\theta_0$ ) that is important for the establishment of a self-similar condition. Rather, it is the num-

ber of "interactions" between the large scale motions of the flow. The number of interactions will depend on the ratio of the streamwise location to the spacing of the initial disturbance. Specifically, the number of interactions m(x) is estimated (equation 14 of Dimotakis and Brown) to be

$$m(x) = \log_2(x/l_a)$$
3.8

where  $l_0$  is the spacing of the initial disturbance. For a laminar boundary layer at separation, the criteria  $x/\theta_0 > 1000$  equivalent to a value of  $m \approx 4$ . In the present study the streamwise location  $x/\theta_0 = 100$  corresponds to a value of m between 6 and 7, given that the spacing of the initial disturbance was  $l_0 \approx \theta_0$ . This small value of initial disturbance length compared with  $\theta_0$  is a direct result of the presence of the sub-shear layer as described in Section 3.3.

5. The dimensionless frequency of the initial instability agrees with linear stability theory when appropriate effective velocity and length scales are identified.

The measurement and prediction of the dimensionless frequency of the initial stability has received considerable attention in the literature; see, for example, Ho and Huerre (1984) and Thomas (1991). This focus is a result of the universal nature of the initial instability in a variety of shear layer and jet flow fields. Additionally, linear theory has been quite successful in the prediction of this dimensionless frequency for many experiments with laminar boundary layers at separation. However, differences in the measured frequencies have been found in shear layers with turbulent boundary layers at separation.

The present study has shown that the above noted differences are a result of the different length and velocity scales that exist in a turbulent boundary layer. Specifically, a laminar

boundary layer can be fully characterized by the free stream velocity and momentum thickness. In contrast, a turbulent boundary layer has outer scales (free stream and momentum thickness) and inner scales ( $u_{\tau}$  and  $v/u_{\tau}$ ). The data presented suggest that only the near wall vortical fluid participates in the initial instability at this Reynolds number. It is then quite reasonable that the outer scales would not be functionally related to the measured frequencies. A hypothesis that can be inferred from the above statements is that the Strouhal number will properly collapse using inner scaling. From the present data, this suggests that  $U_{eff} \approx 15u_{\tau}$ , and  $\theta_{eff} \approx 10v/u_{\tau}$ . Additional measurements are required to test this hypothesis.

6. Preferred frequency and spanwise correlation measurements have shown that the characteristic large scale motions observed in self-similar single and two-stream shear layers are present in the sub-shear layer region.

Several investigators have studied the properties and importance of the largest scales of motion in shear layers. These motions appear to have a large spanwise coherence and a significant fraction of the total turbulent kinetic energy of the flow. Experimentalists have sought to measure these features in order to better understand their role and dynamic significance; see, for example, Hussain and Zaman (1985), Browand and Weidman (1976), and Browand and Trout (1980, 1985).

The present experiments have found that a number of the features measured in both two stream and single stream shear layers in the self-similar regions have also been observed in the sub-shear layer region. For example, the preferred frequency exhibited by both the sub-shear layer and self-similar shear layer can be described by the relatively simple equa-

tion:  $f_m \sim x^{-0.71}$  (for  $x/\theta_0 > 1$ ) as shown in Figure 3.19. It can be inferred that the physical mechanisms which lead to this preferred frequency are present throughout the flow field downstream of separation. Similar results were found from streamwise dependence of the maximum slope of the mean velocity profile; see Figure 3.14. Note that the y location of the maximum slope was found in the center of the sub-shear layer.

A third feature, observed in the sub-shear layer region, was the large spanwise correlation length; see Figure 3.31. These data clearly show that large scale motions develop at small  $x/\theta_0$  values. The spanwise correlation of the velocities in the entrainment stream increases as these motions convect downstream. These observations are consistent with observations made by Browand and Trout (1980, 1985) in the self-similar region of a two stream shear layer.

The above noted observations justify the terminology "sub-shear layer." Specifically, the region exhibits characteristics which are associated with self-similar shear layers, while the prefix "sub" is meant to describe the fact that the shear layer is growing adjacent to what appears to be the outer region of a flat plate boundary layer. One distinct difference noted between the sub-shear layer and the self similar shear layer is the peak value of  $\tilde{u}$  which increases smoothly from  $0.12U_0$  in the boundary layer to a constant value of nominally  $0.16U_0$  for  $x/\theta_0>150$ .

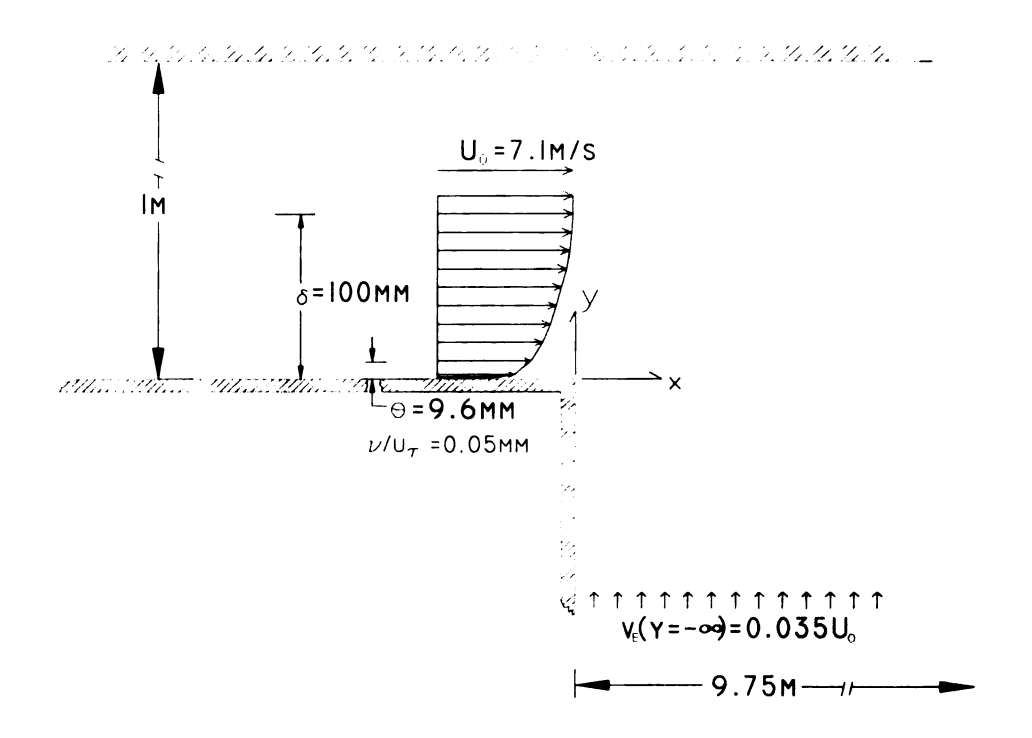


Figure 3.1 Schematic representation of near separation region.

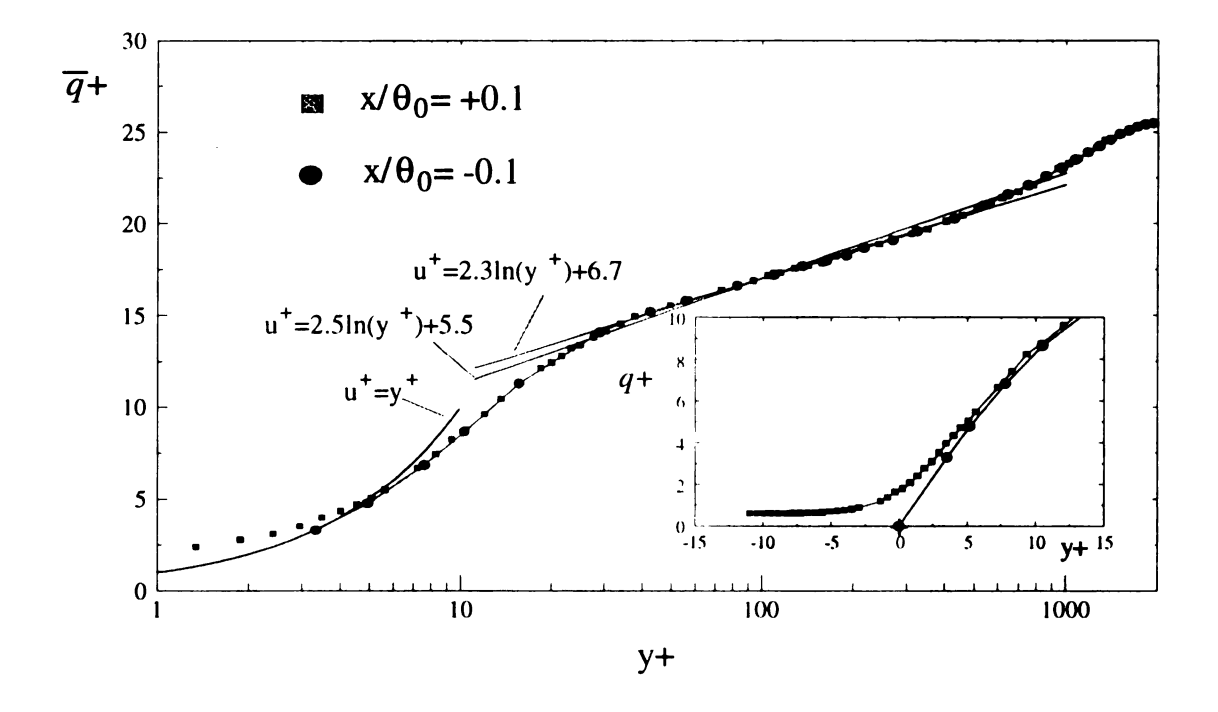


Figure 3.2 Boundary Layer Mean Velocity. The  $y^+=0$  point (x) on the inset figure was added based upon the no-slip condition for clarity. Note that  $U_0/u_\tau=25.5$ .

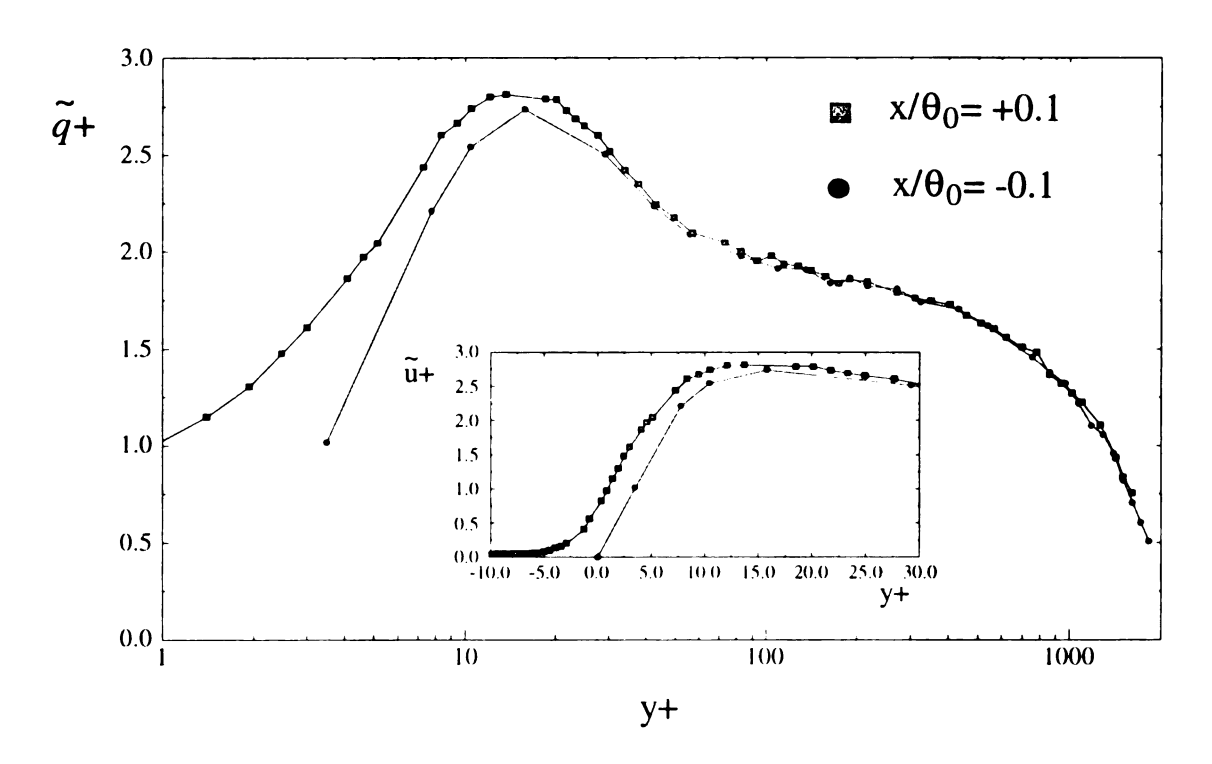


Figure 3.3 Boundary Layer Velocity RMS

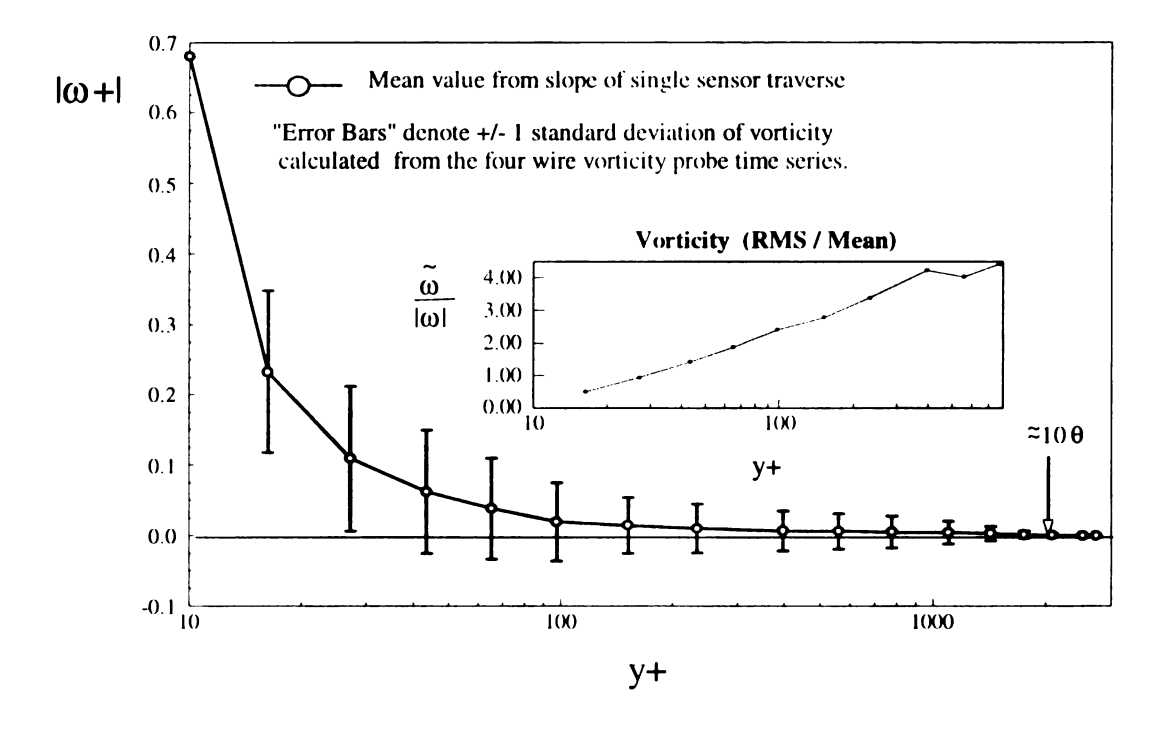


Figure 3.4 Mean and RMS of vorticity at separation.

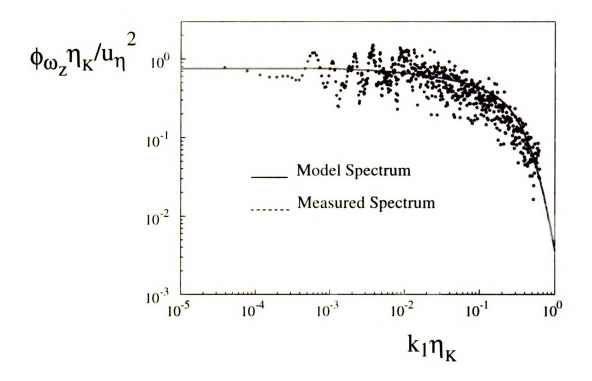


Figure 3.5 Spectrum of vorticity fluctuations at  $y/\delta=0.6$ .

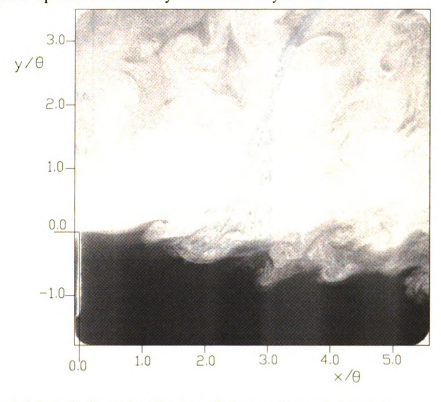


Figure 3.6 Sample flow visualization of the near separation region.

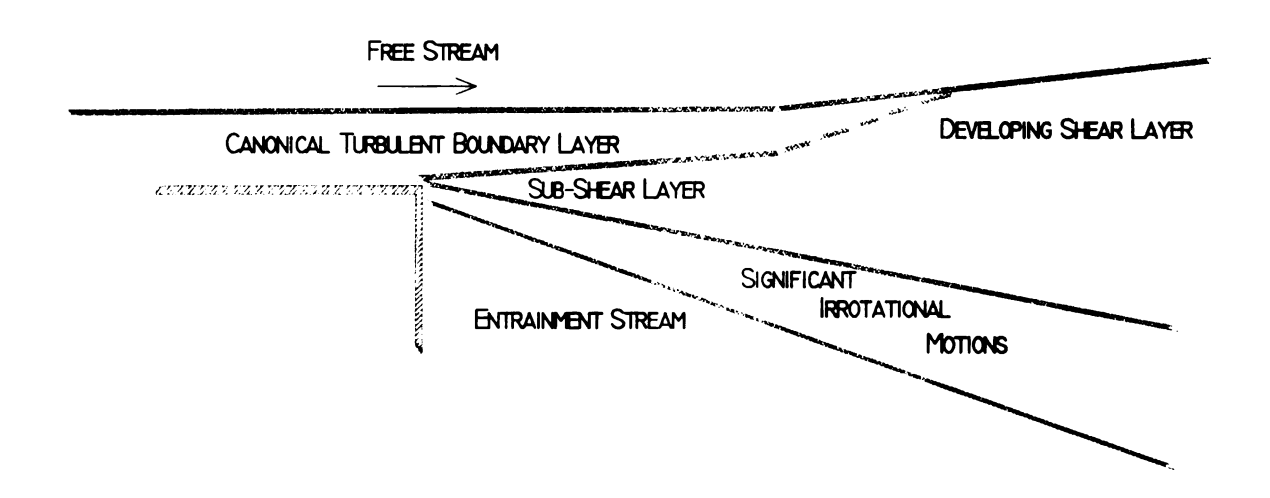


Figure 3.7 Figure of flow regions; not to scale.

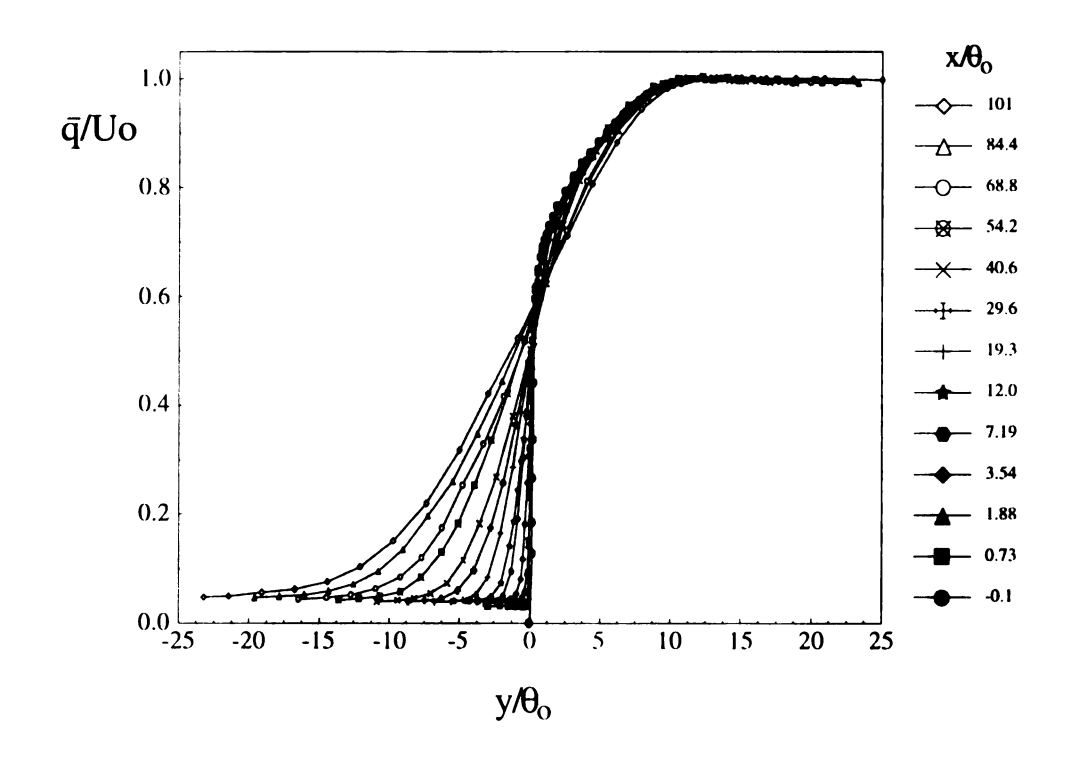


Figure 3.8 Mean velocity profiles for  $0 < x/\theta_0 < 100$ 

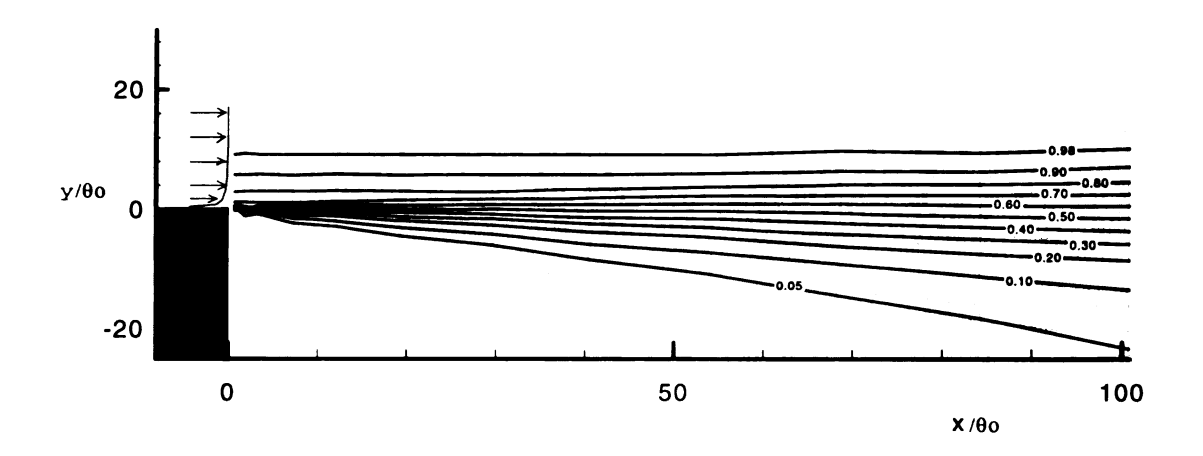


Figure 3.9 Contour plot of mean velocity,  $q/U_{\scriptscriptstyle O}$ 

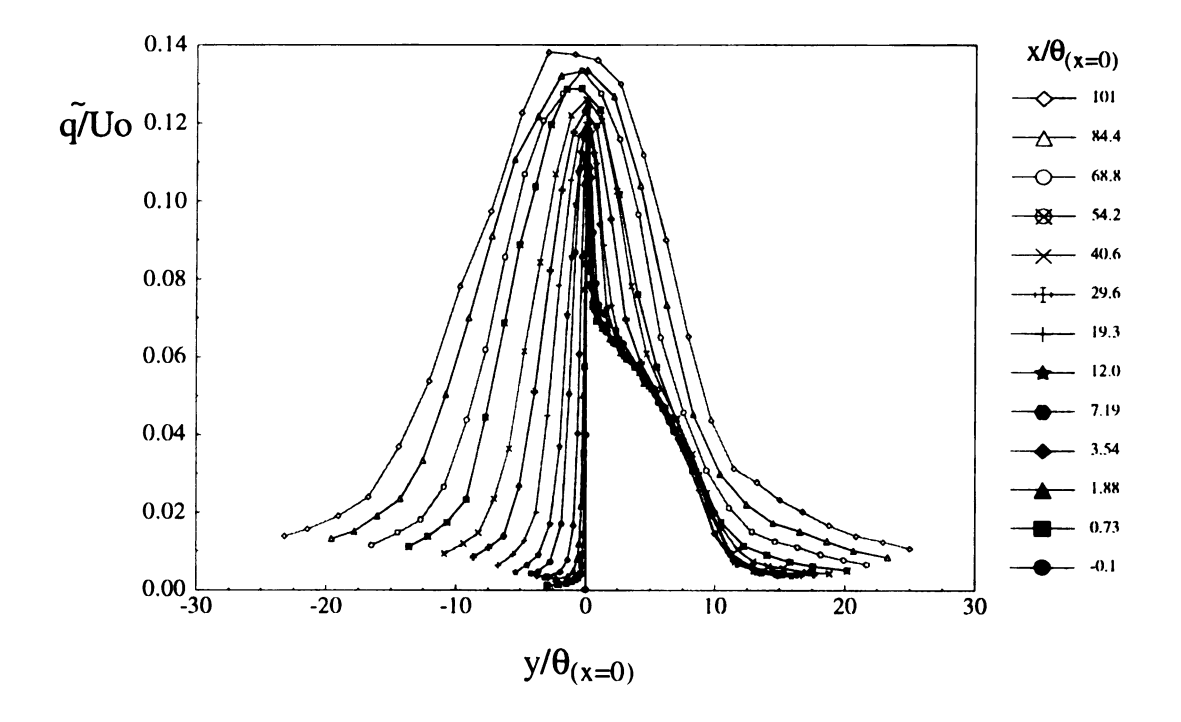


Figure 3.10 RMS of velocity for  $0 < x/\theta_0 < 100$ 

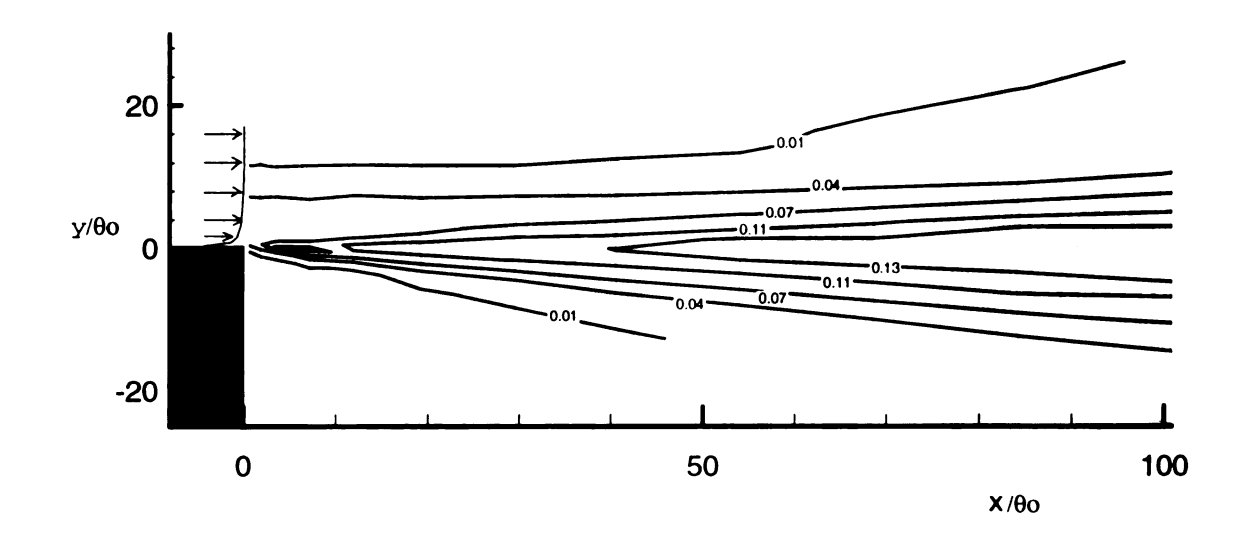


Figure 3.11 Contour plot of velocity RMS  $\bar{q}/U_o$ 

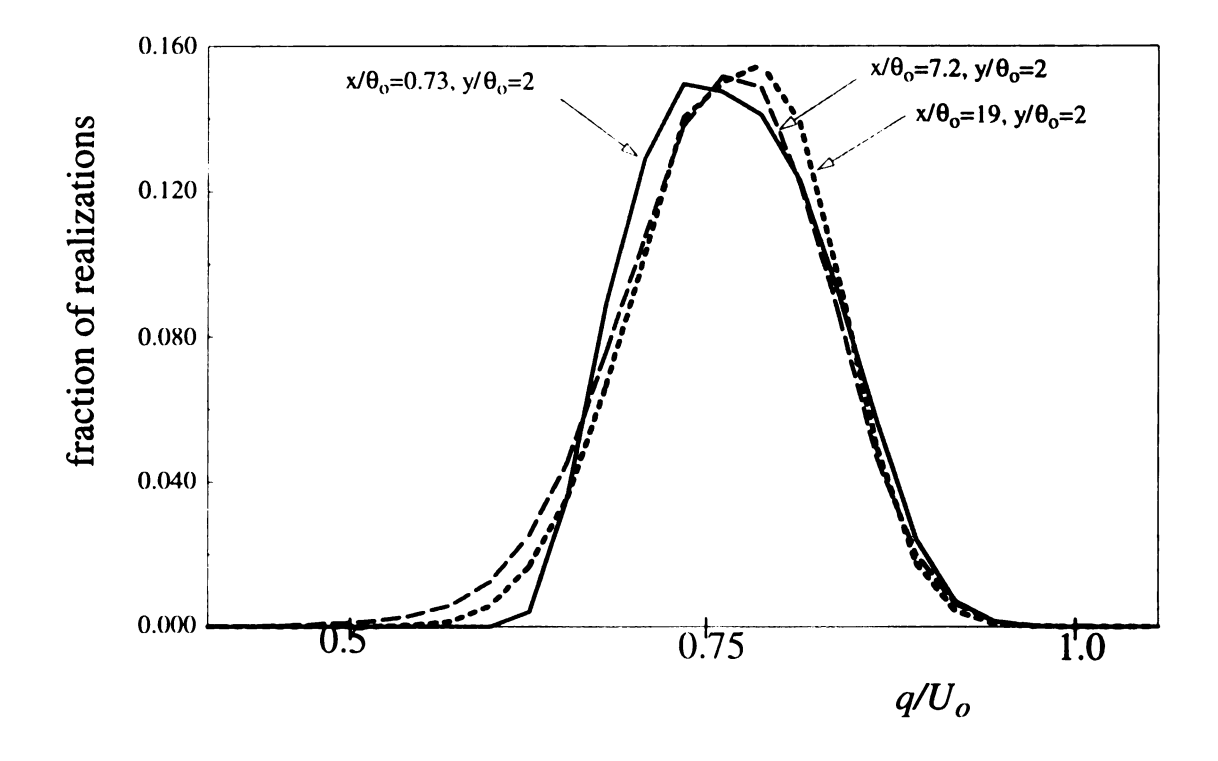


Figure 3.12 Streamwise evolution of velocity histogram at constant  $y/\theta_0=2.0$ .

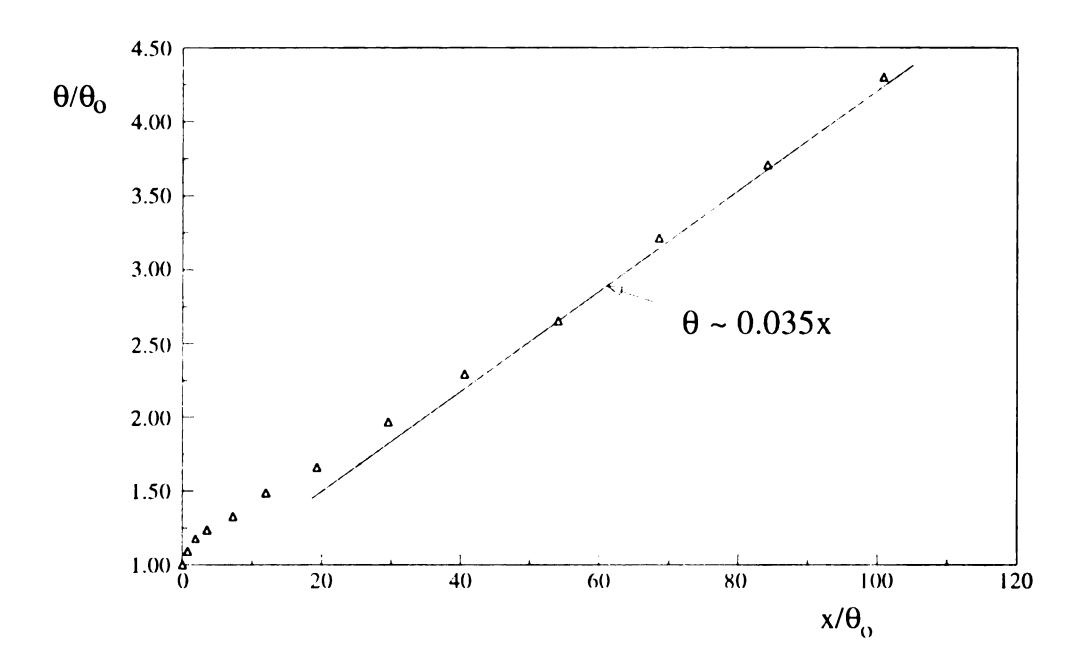


Figure 3.13 Momentum thickness vs.  $x/\theta_o$ .

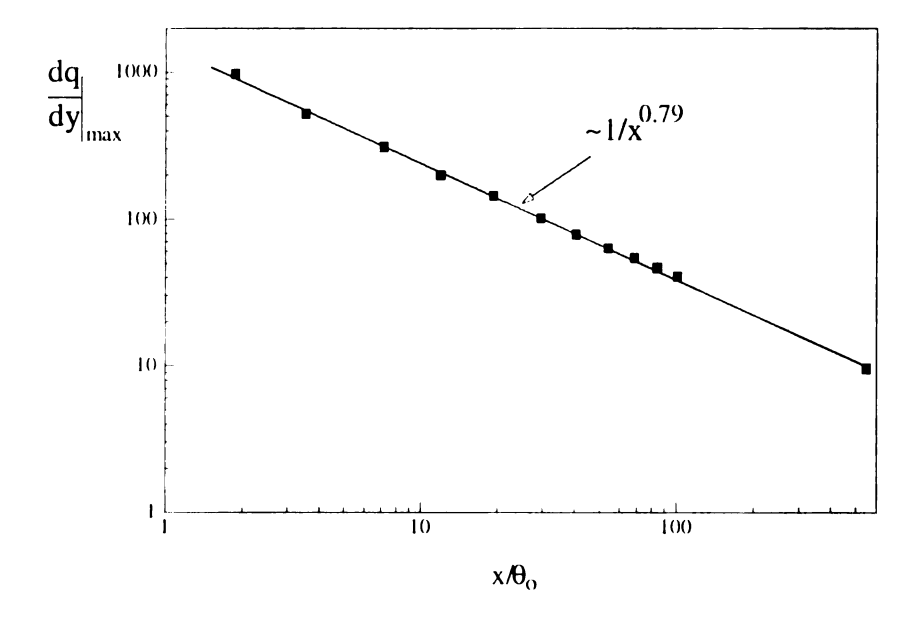


Figure 3.14 Maximum velocity gradient vs.  $x/\theta_o$ 

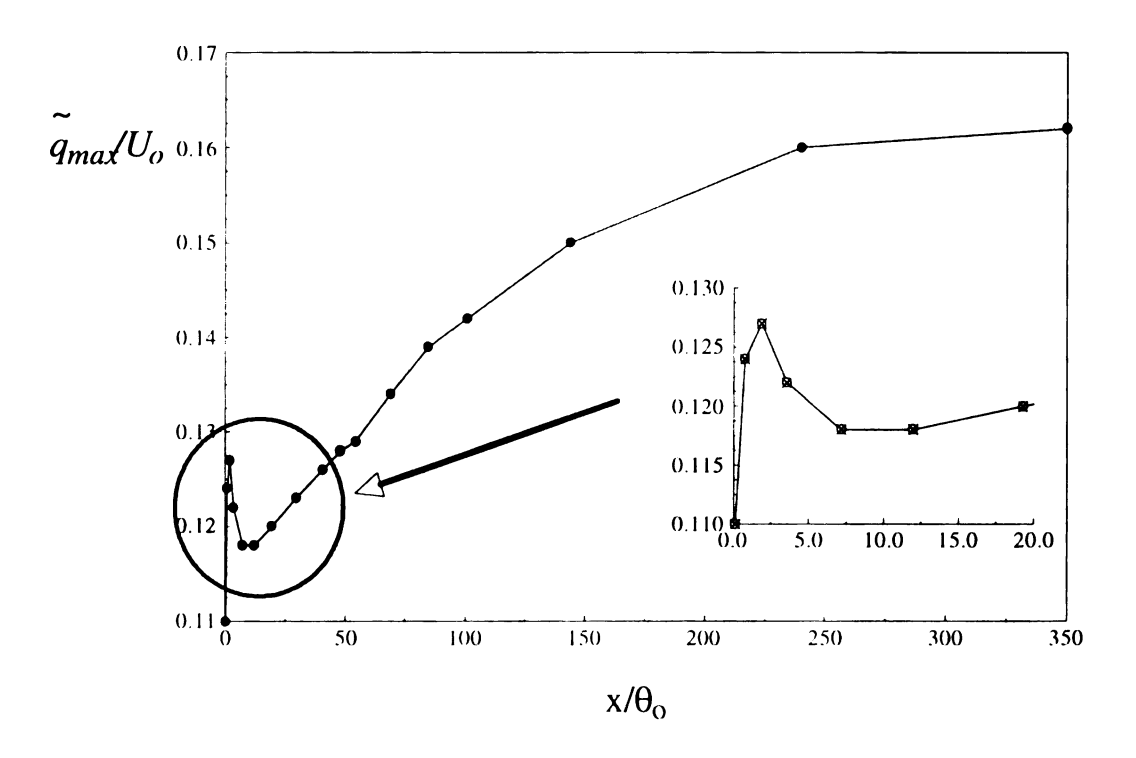


Figure 3.15 Peak value of velocity r.m.s as a function of streamwise location.

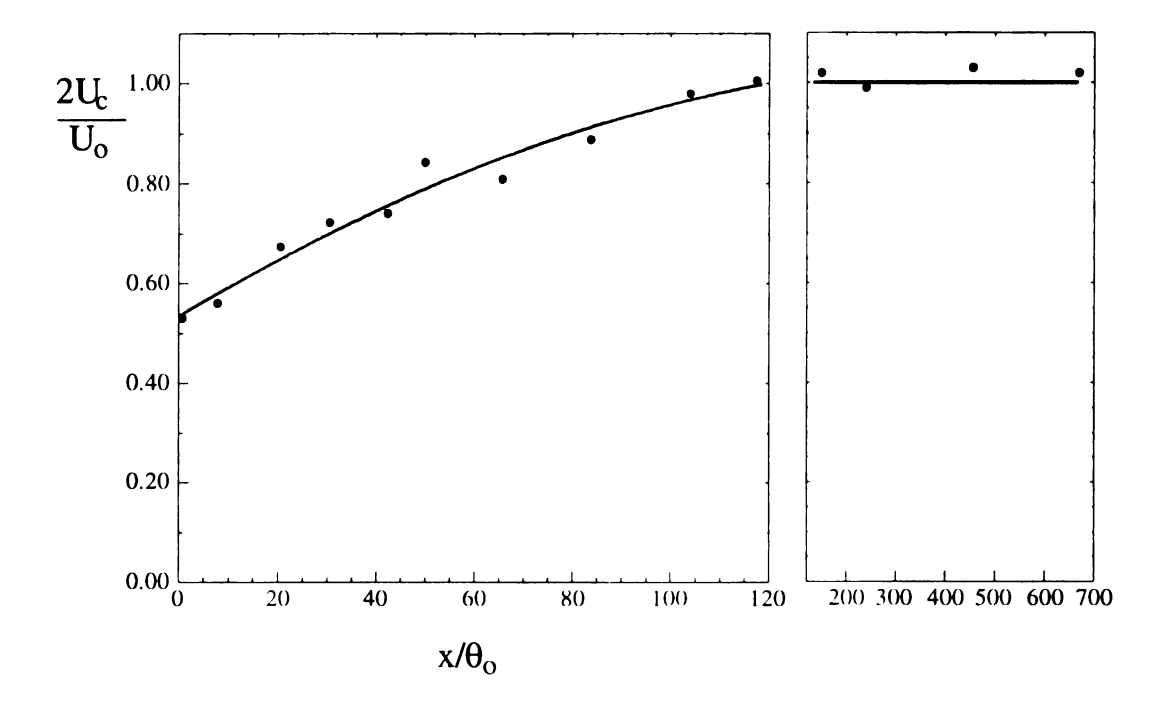


Figure 3.16 Convection velocity of spanwise motions. Note the break in the x-axis is used to show the  $x/\theta_0$ <120 region in more detail.

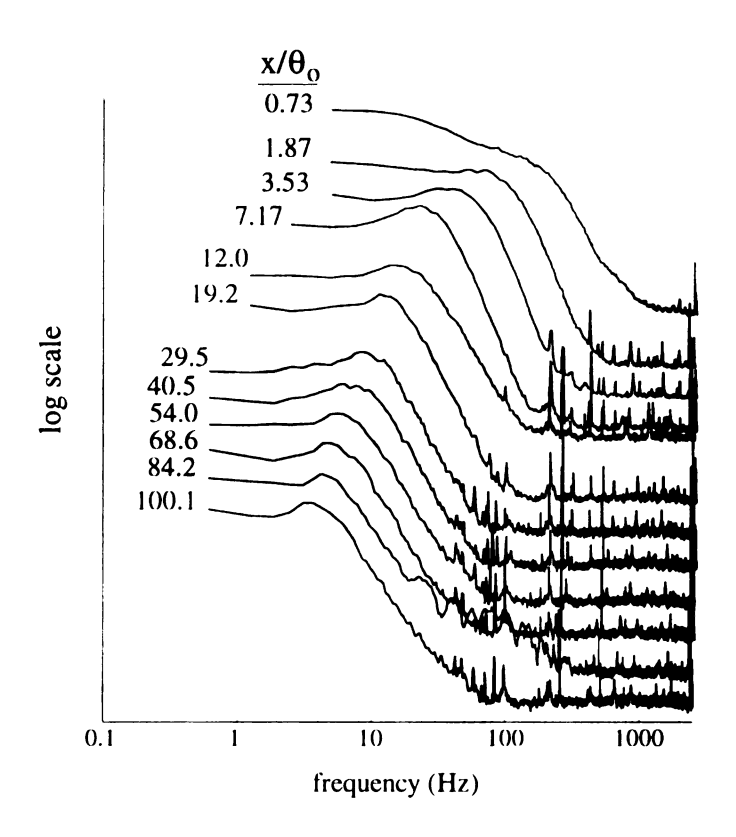


Figure 3.17 Velocity spectra of entrainement for the 12 streamwise locations measured.

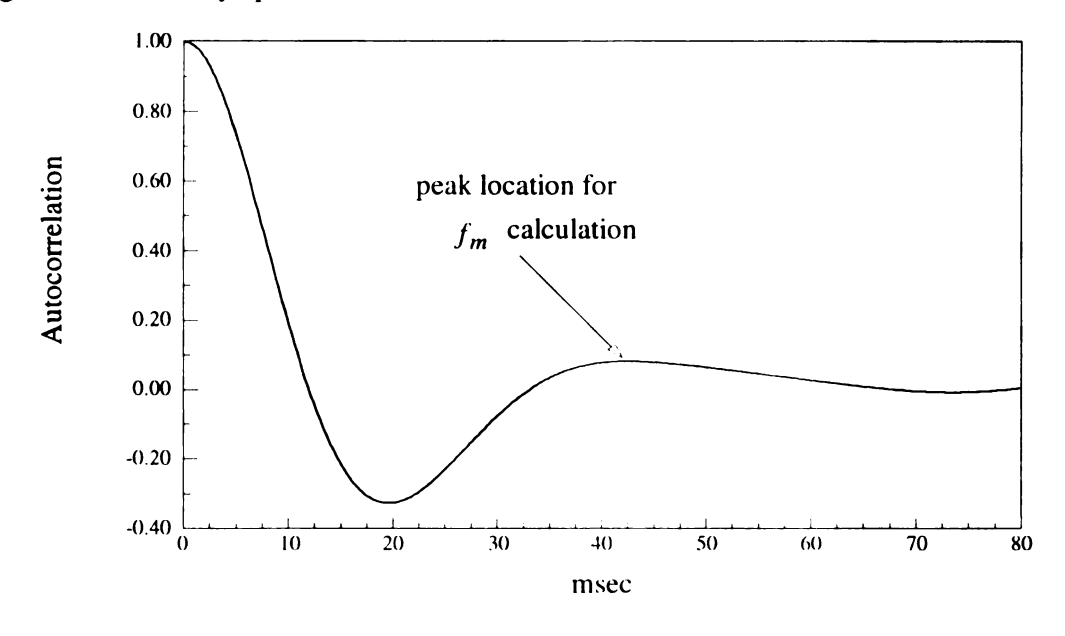


Figure 3.18 Sample of the autocorrelation function in the entrainment stream at  $x/\theta_0$ =7.17

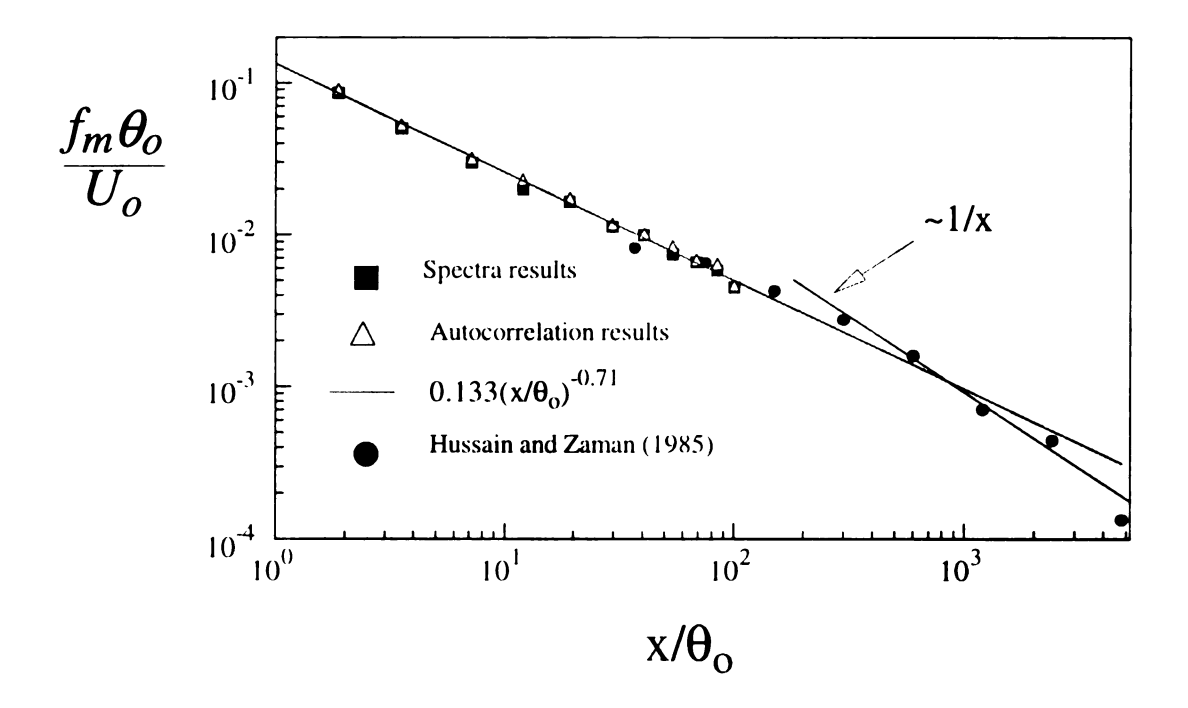


Figure 3.19 Streamwise variation in peak frequency.

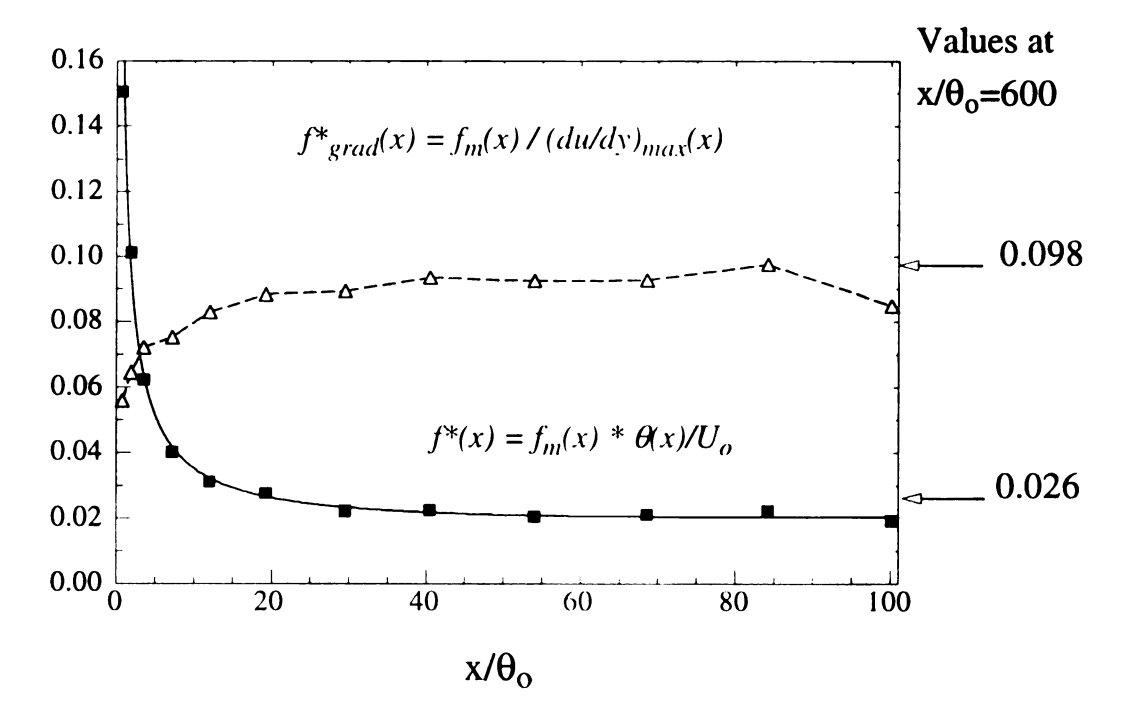


Figure 3.20 Non-dimensional frequency vs.  $x/\theta_0$ 

г

Fig

We

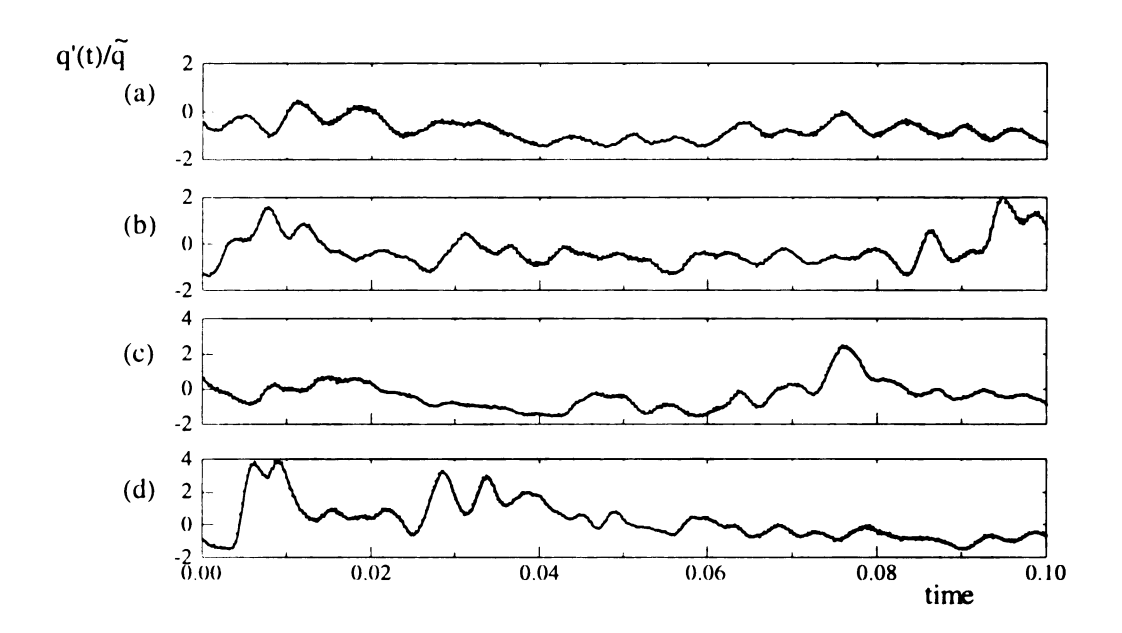


Figure 3.21 Time series samples from  $x/\theta_0$ =0.73.

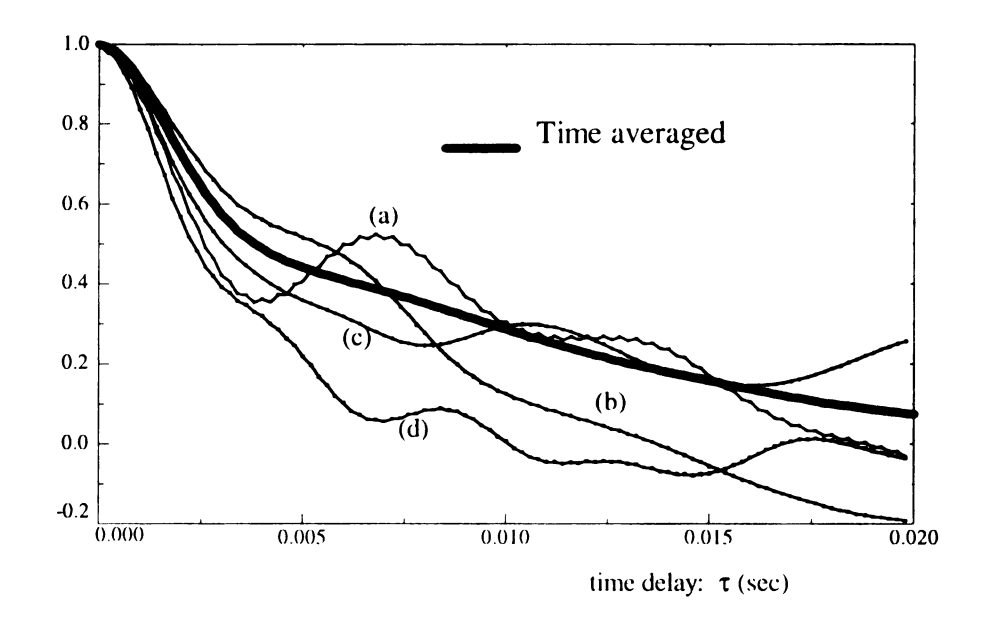


Figure 3.22 Autocorrelations of the time series at  $x/\theta_0$ =0.73. The long time averaged as well as 0.1 second averages from the time series in Figure 3.21 are shown.

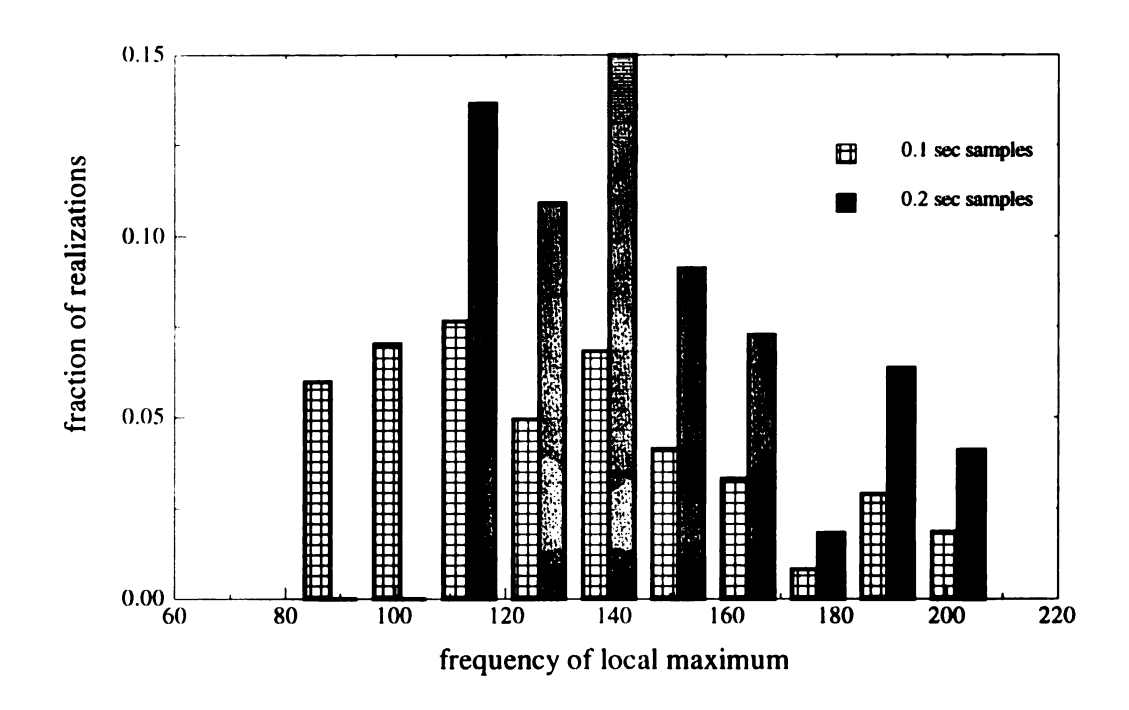


Figure 3.23 Histogram of observed frequencies from short time autocorrelations.

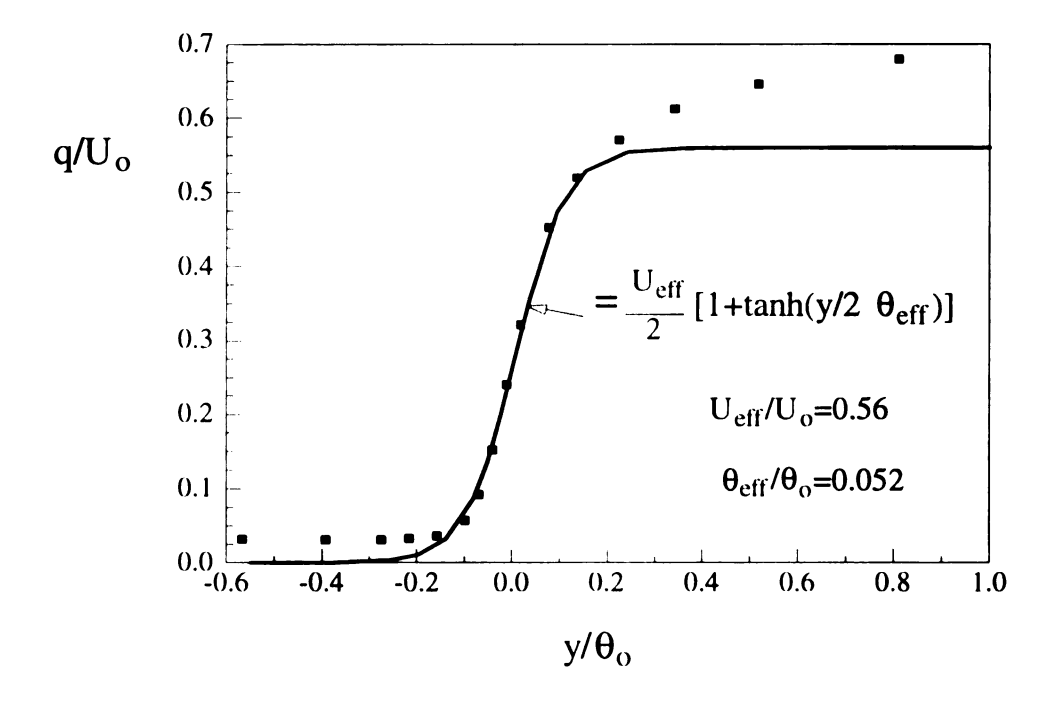


Figure 3.24 Comparison between *tanh* function shown and the velocity data at  $x/\theta_0$ =0.73.

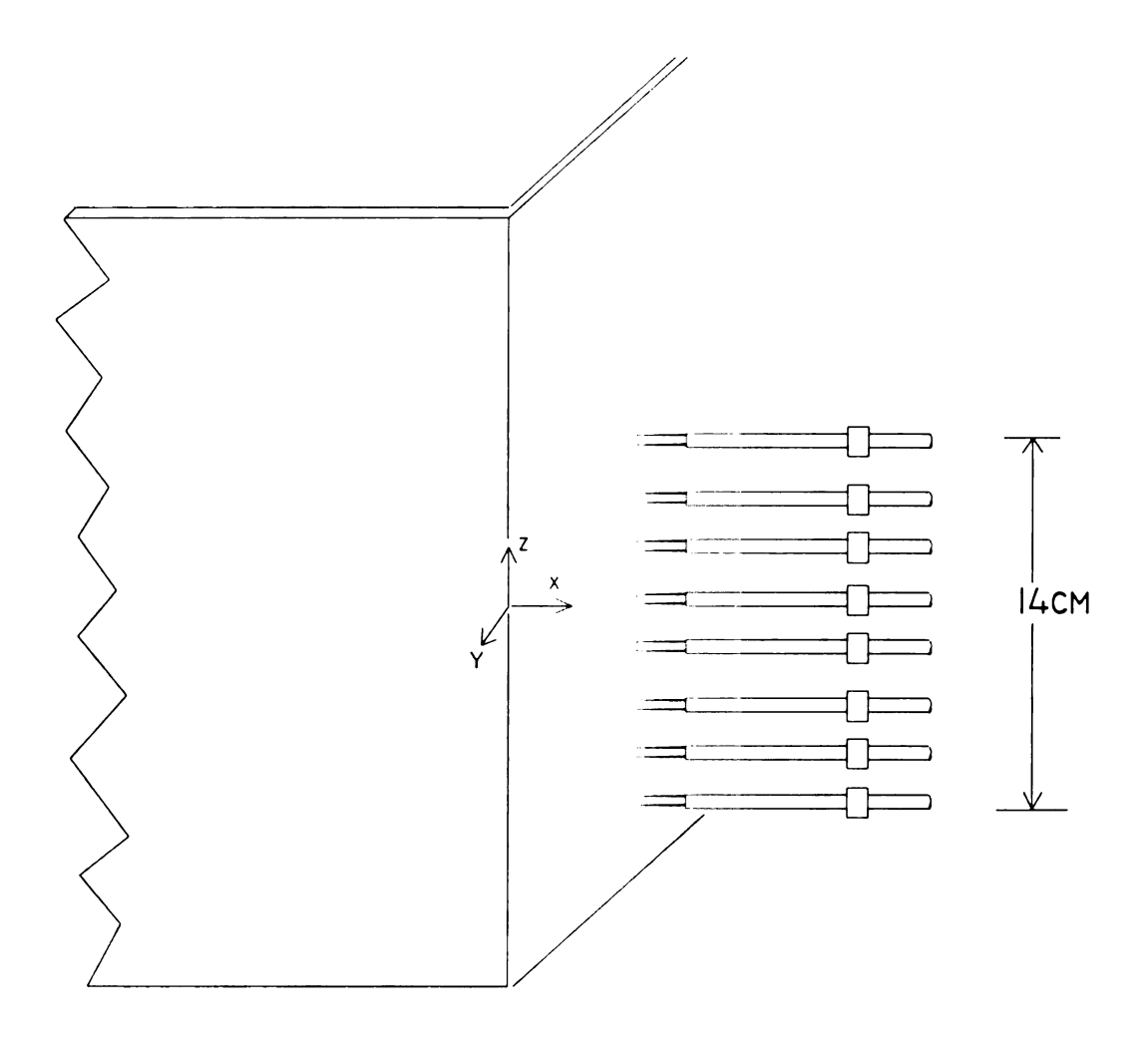


Figure 3.25 Schematic of 8 wire rake in shear layer.

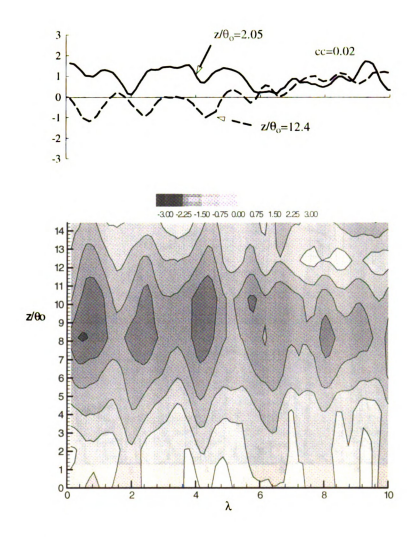


Figure 3.26 Velocity fluctuations at  $x/\theta_0$ =3.53,  $y/\theta_0$ =-3.7. Contour plot shows magnitude of velocity from 8 sensors normalized by the standard deviation. X-Y plot shows time traces taken from wires located at  $z/\theta_0$ =2.05 and 12.4 for the same time period. Note that the correlation coefficient indicated in the top figure by 'cc' represents the long time average and not that for the time segment shown.

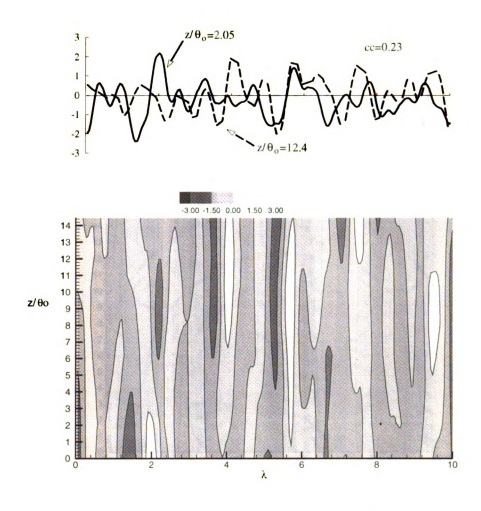


Figure 3.27 Velocity fluctuations at  $x/\theta_0$ =12.0,  $y/\theta_0$ =-5.37. See Figure 3.26 for description.

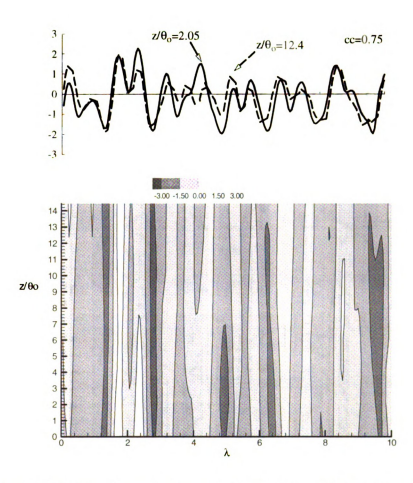


Figure 3.28 Velocity fluctuations at  $x/\theta_0$ =40.5,  $y/\theta_0$ =-10.9. See Figure 3.26 for description.

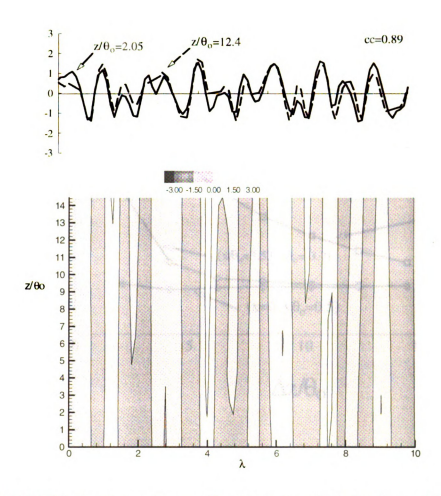


Figure 3.29 Velocity fluctuations at  $x/\theta_0$ =84.2,  $y/\theta_0$ =-19.6. See Figure 3.26 for description.

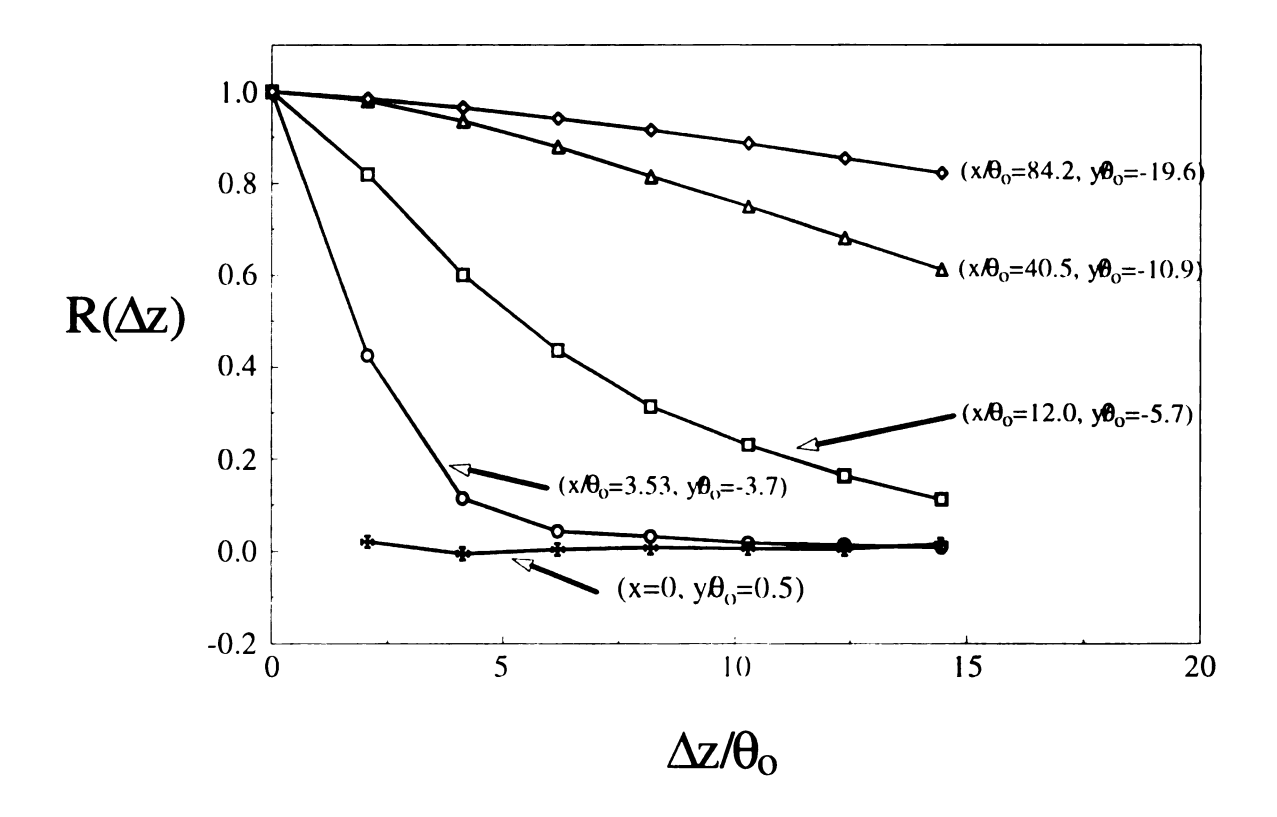
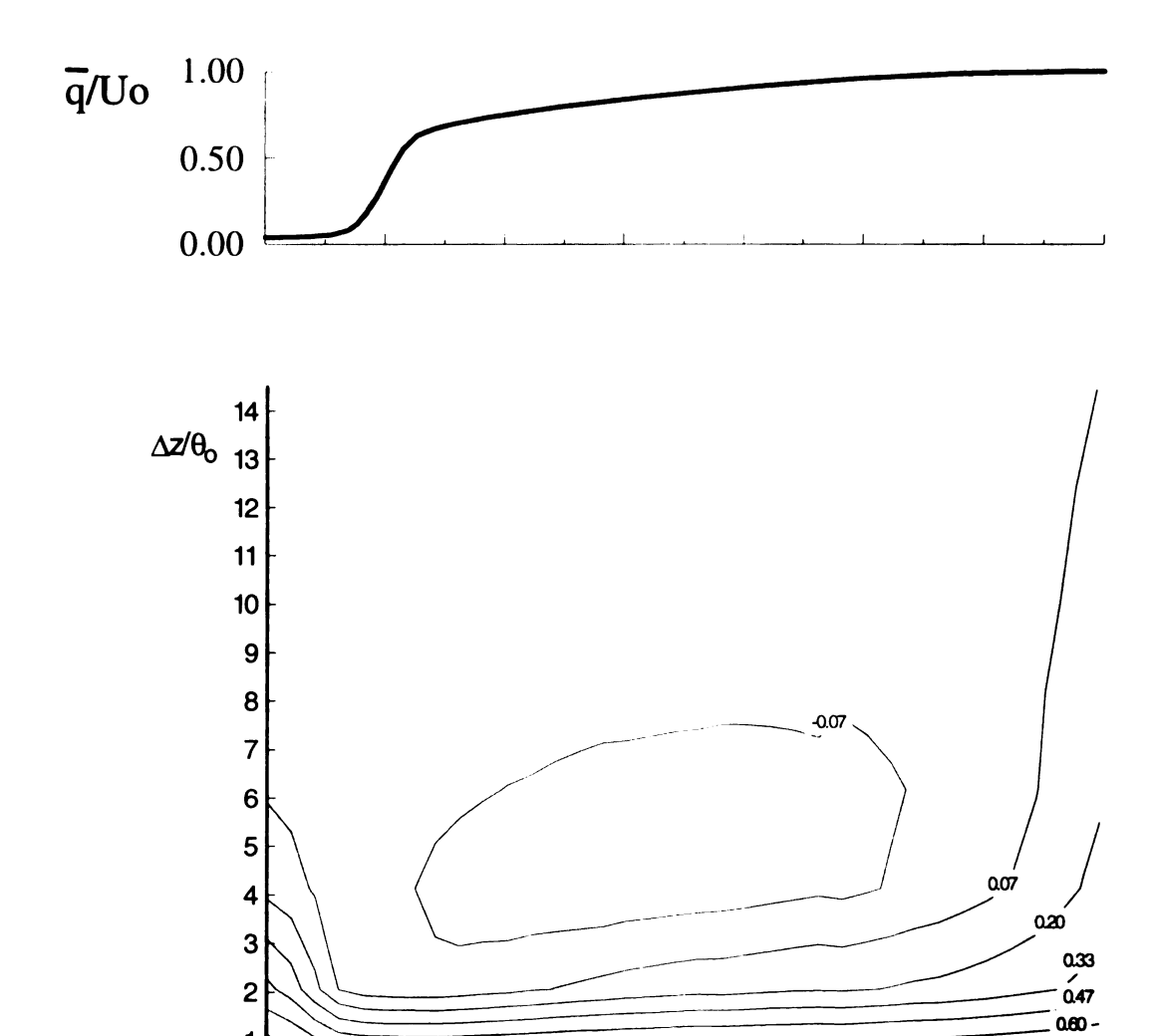


Figure 3.30 Spanwise correlation coefficient of the data shown in Figures 3.26 through 3.29.



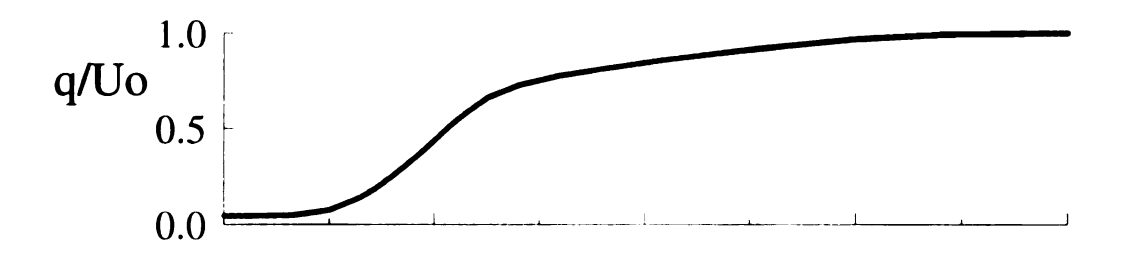
0.73

арт 10

Figure 3.31 Spanwise correlation field at  $x/\theta_0$ =3.53.

5

y/θ<sub>o</sub>



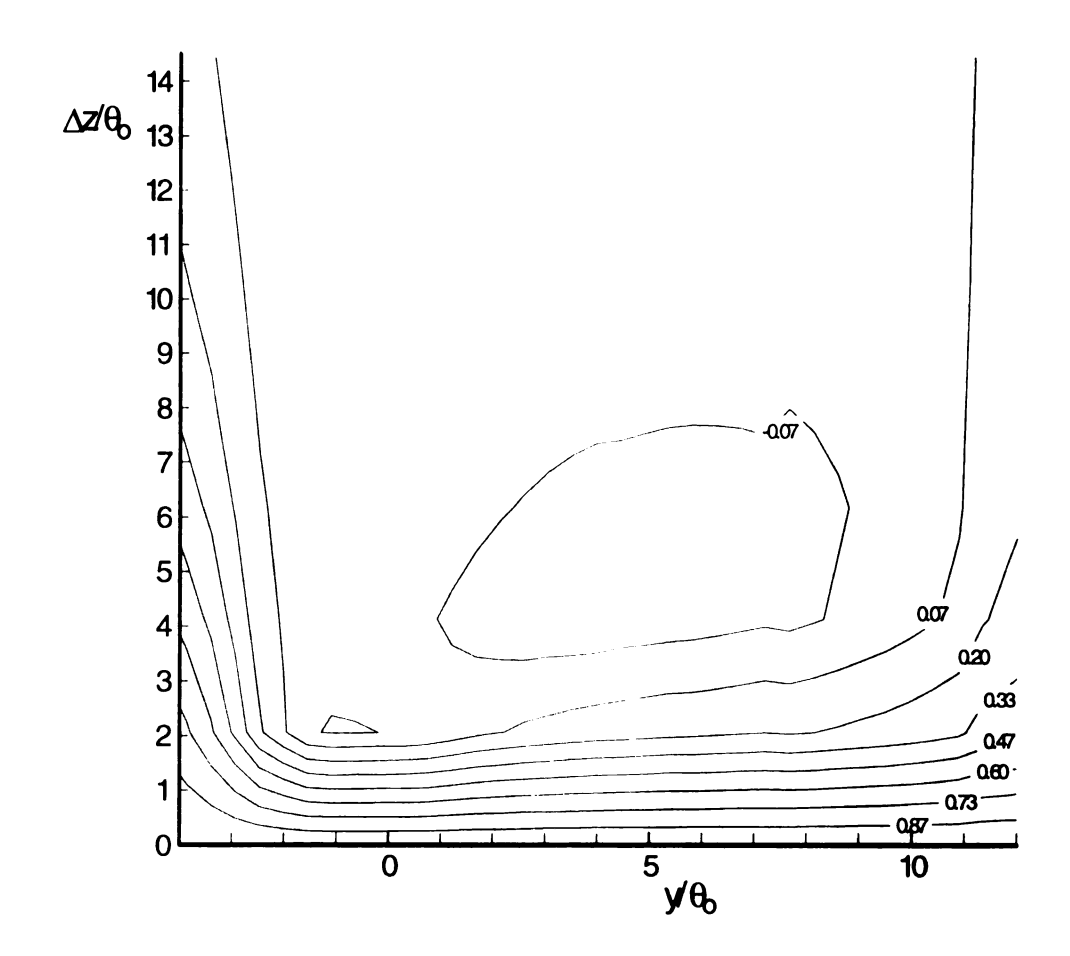
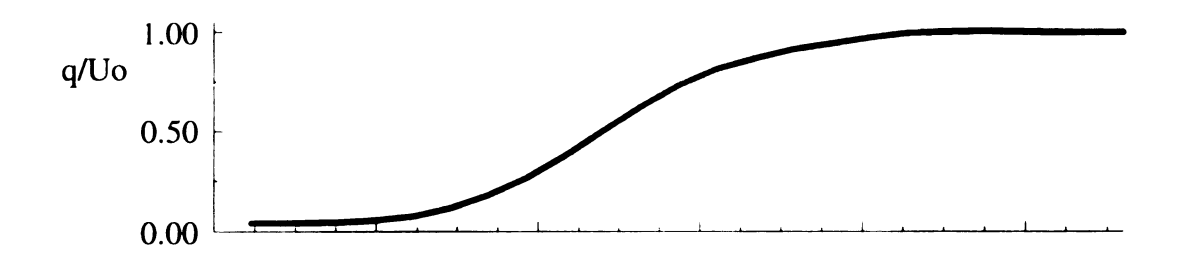


Figure 3.32 Spanwise correlation field at  $x/\theta_0$ =12.0



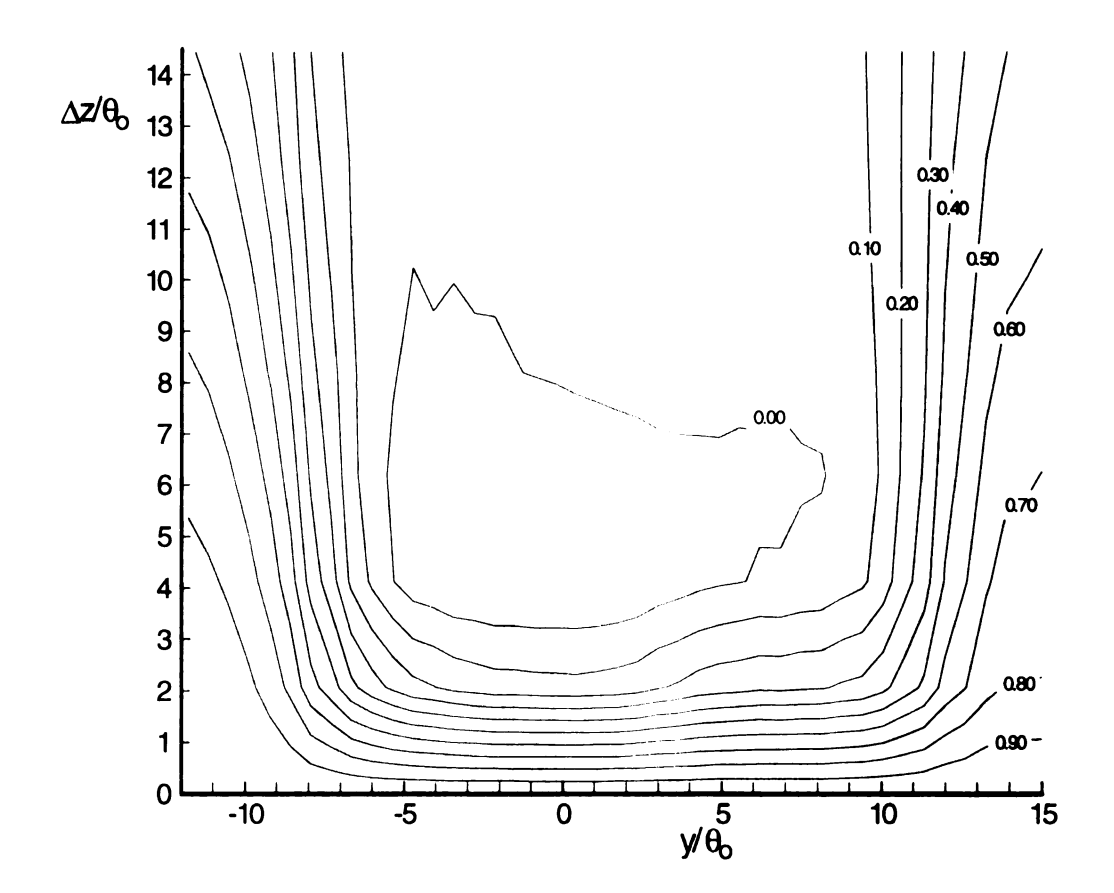
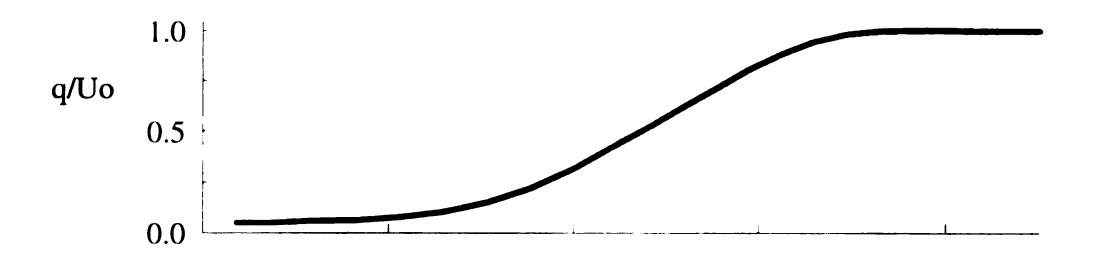


Figure 3.33 Spanwise correlation field at  $x/\theta_0$ =40.6



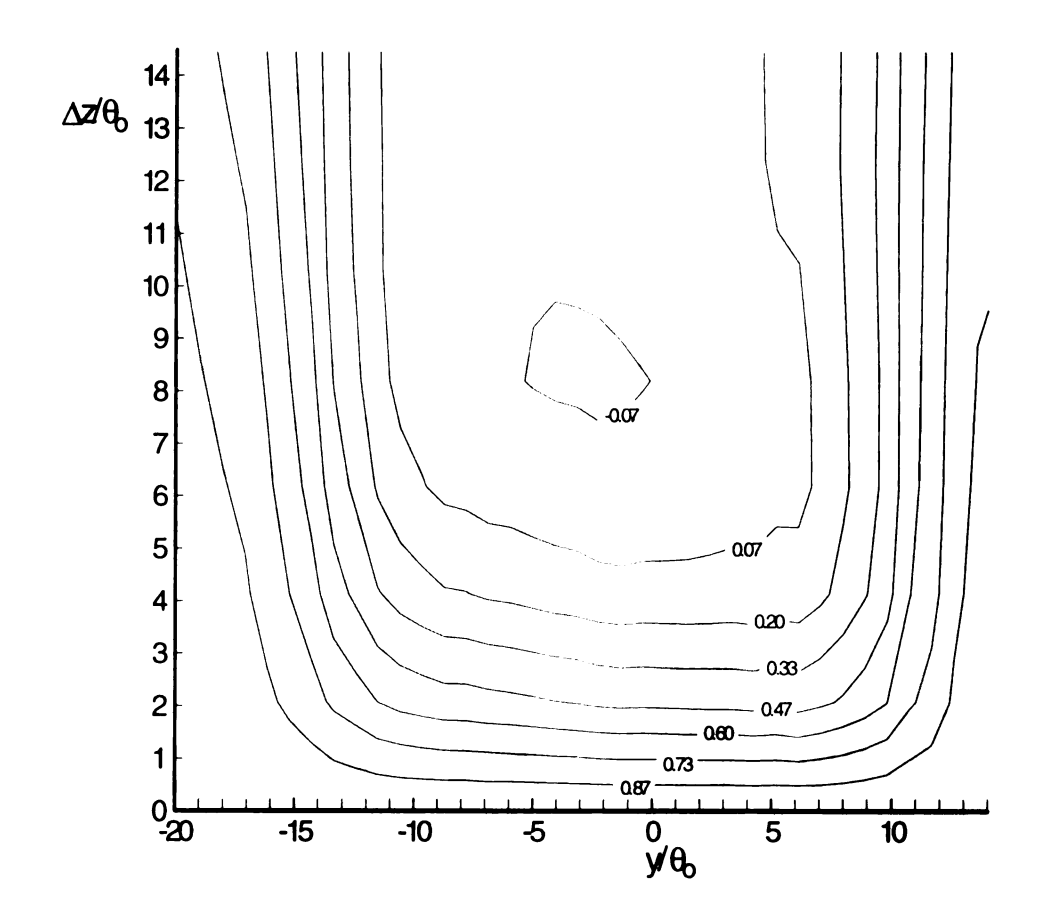


Figure 3.34 Spanwise correlation field at  $x/\theta_0$ =87.2

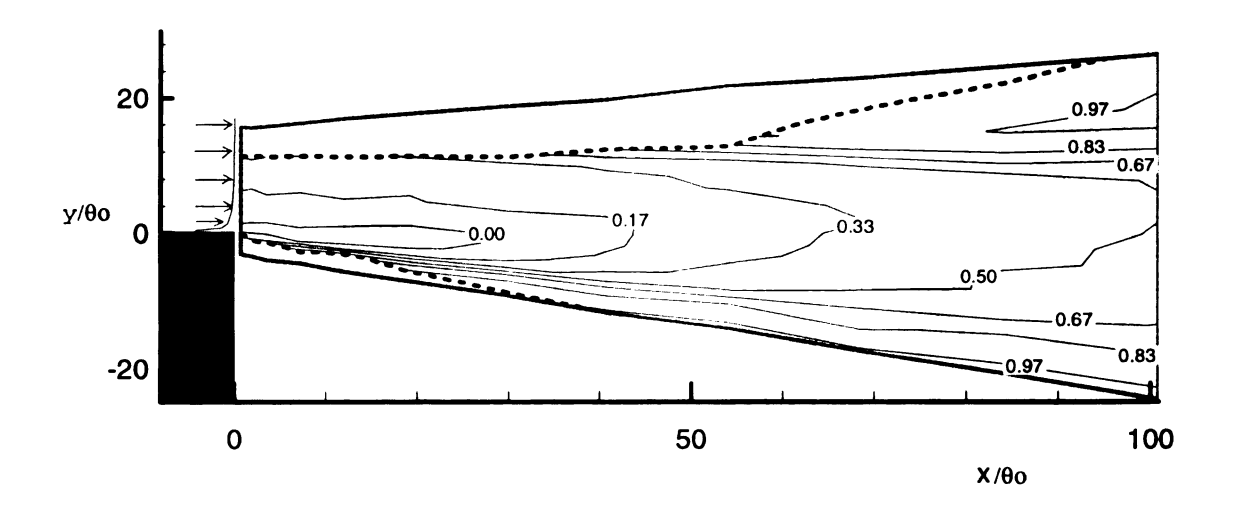


Figure 3.35 Correlation coefficient at  $\Delta z/\theta_o$ =2.08. Note that the solid boundary represents the spatial extent of the measurements (shown by the grid). The dashed boundary represents the region where  $u_{rms}/U_o>0.01$ . A schematic of the boundary layer mean profile near x=y=0 is shown for reference.

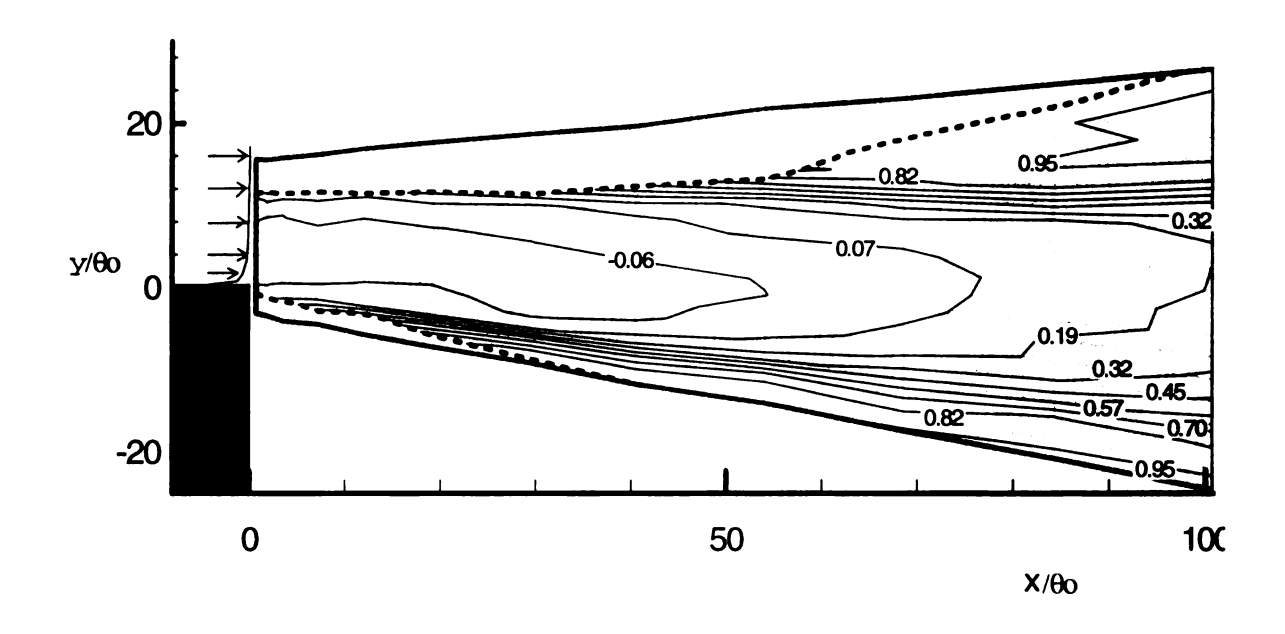


Figure 3.36 Correlation coefficient at  $\Delta z/\theta_0$ =4.16. See Figure 3.31 for description.

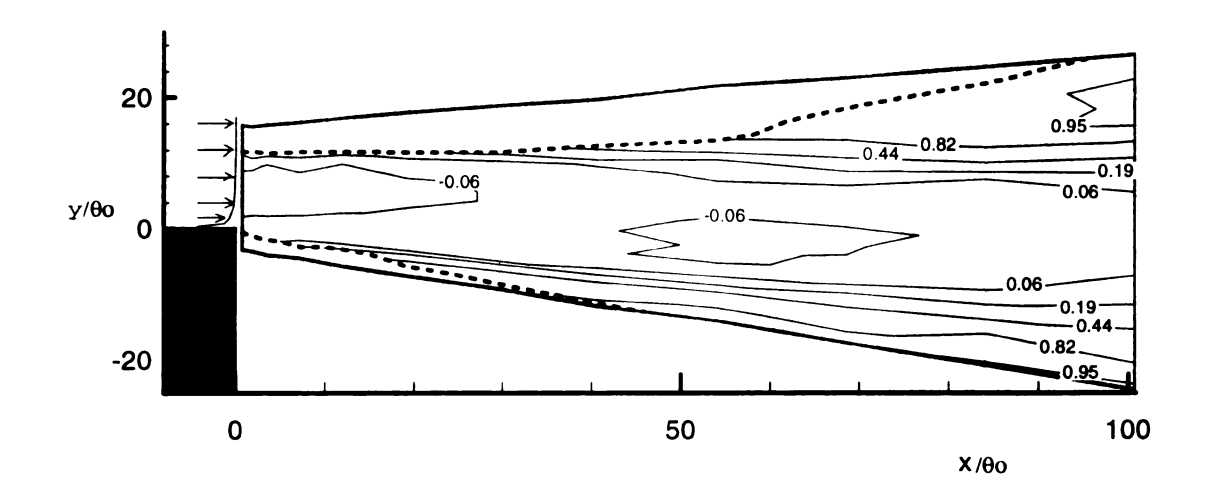


Figure 3.37 Correlation coefficient at  $\Delta z/\theta_0$ =6.24. See Figure 3.31 for description.

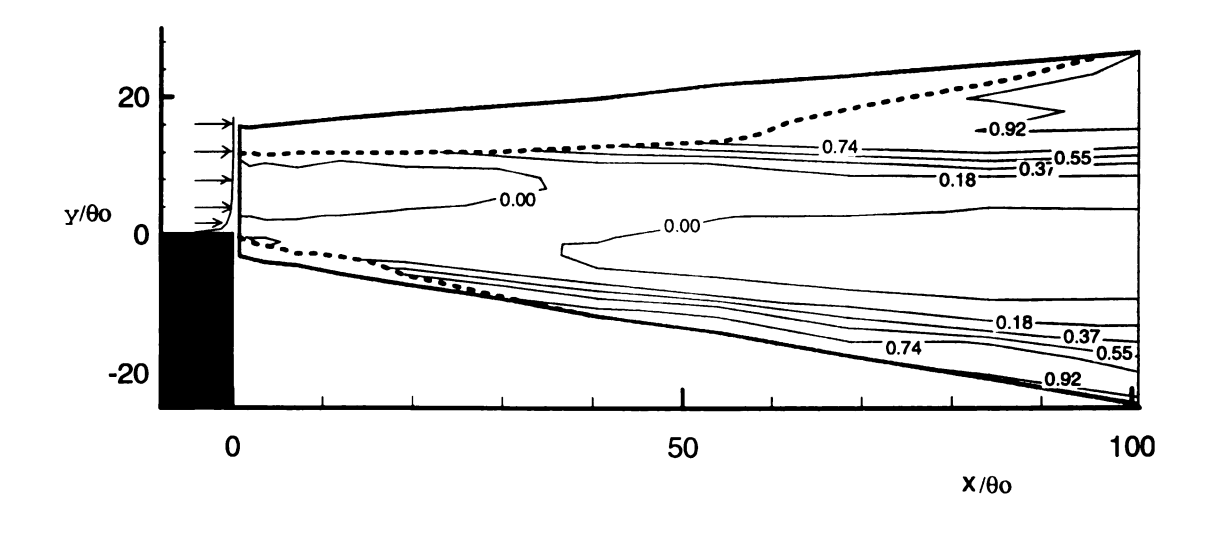


Figure 3.38 Correlation coefficient at  $\Delta z/\theta_o$ =8.32. See Figure 3.31 for description.

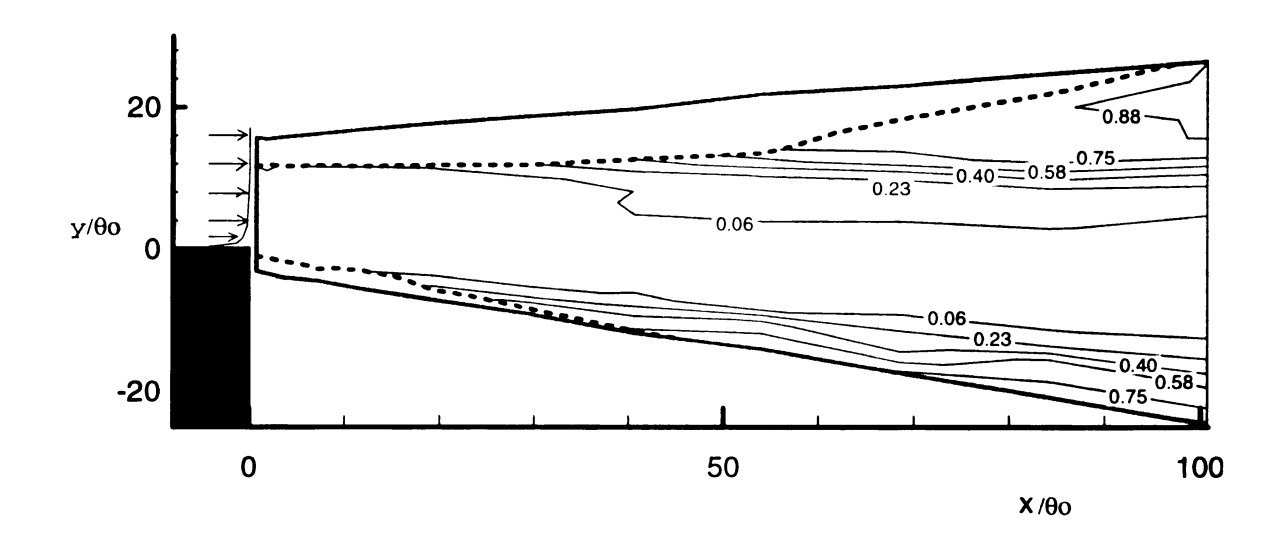


Figure 3.39 Correlation coefficient at  $\Delta z/\theta_o$ =14.5. See Figure 3.31 for description.

## 4.0 The Developed Single Stream Shear Layer

## 4.1 Introduction

This chapter presents the results from an investigation of the developed region of the shear layer. The word "developed" is used to indicate that the time averaged flow variables can be represented in a self-similar form. Specifically, any dimensionless stochastic quantity, say, a(x,y), can be written as a function of the dimensionless transverse coordinate:  $a((y-y_c)/l)$ , where  $y_c$  represents the "center" of the shear layer, and l(x) is a local integral length scale of the shear layer. In the present measurements, the momentum thickness:  $\theta(x)$  was used as the length scale of choice. In shear layers, this length scale grows linearly. That is,  $\theta \sim x$ . This was shown to be valid in the measurements presented in Chapter 3 for  $x/\theta_0 > 60$ . These data also indicated that the profile of the fluctuation intensity (see Figure 3.15) is approximately self-similar at streamwise locations  $x/\theta_0 > 300$ . This is consistent with the results of Hussain and Zedan (1978) and Bruns et al. (1991). The data presented in this chapter were acquired at downstream locations  $384 < x/\theta_0 < 707^{1}$ .

The following two sub-sections (4.1.1, 4.1.2) are organized as follows. The open research questions that have been considered in the present work are reviewed in Section 4.1.1. This will include a review of the relevant literature that will serve to outline where this research fits with respect to the current knowledge base. The second sub-section of this introduction will describe the experimental program. Because several different types of information can be drawn from a single data set, the details of the experiments will be

<sup>1.</sup> One exception is the PIV measurements used for the calculation of the circulation density. These data were acquired at  $x/\theta_0=170$ ; see Section 4.7.

described completely in section 4.1.2; the data presentation in sections 4.2 through 4.8 will then refer to these experiments.

## 4.1.1 Motivation and literature survey

The beginning point for most shear layer studies is the development of the mean velocity profile. Information about the self-similar nature of the mean flow variables is often described in turbulence text books. See, for example, Pope (2000), Tennekes and Lumley (1972), Holmes et al. (1992), and Townsend (1975). However, the discussions typically imply a two stream shear layer geometry. In the present work, the analysis for the mean flow variables will be given specifically for the single stream boundary conditions with the entrainment flow perpendicular to the free stream velocity vector. This has led to several new simplifications, and the identification of errors in the literature; see Section 4.2. Research papers which describe single stream shear layers include Leipmann and Laufer (1947), Wygnanski and Feidler (1970), Champagne et al. (1976), hereafter referred to as LL, WF and CPW, respectively. These papers support the self-similarity of the measured moments of the velocity values. For example, CPW compares the profiles of  $\bar{u}$ ,  $\bar{v}$ , and  $\overline{u'v'}$  for several downstream locations in their facility. In addition, they cite measurements from LL and WF and others. Although some differences between the LL data and those of WF and CPW are noted, these data support the assertion that the velocity field in the self similar region of the single stream can be considered universal. That is, the results are in agreement without significant dependence on the particular upstream and entrainment flow boundary conditions created by the different facilities.

There are a number of turbulent characteristics that can be inferred from the single and multi-point measurements of velocity time series. For example, velocity gradient statistics, which are described in Section 4.2, are used to compare the predictions of isotropic and axisymmetric turbulence. Also, WF used their velocity measurements to construct an estimate of the balance of the turbulent kinetic energy (TKE) equation. This balance was calculated for the present measurements as well; see Section 4.5. The value added from the present observations comes from the higher Reynolds number and improved spatial resolution of the present facility. This has allowed an improved ability to estimate terms such as dissipation, which are quite difficult to accurately obtain. Also, the present measurements were acquired at two streamwise locations which documents the scaling of the TKE equation.

The statistical characterization of the scales of fluid motion were also of interest, in addition to the point measurements described above. Multi-point measurements of the velocity field were acquired in the shear layer in order to document the spatial and temporal characteristics of the velocity field; see Section 4.6. The relatively large size of the present facility provides an opportunity to study fluid motion which range in length scale from approximately 1.2m for the largest motions, to 0.2mm for the smallest (Kolmogorov) length scales at the farthest downstream location of the tunnel. This has permitted sufficient spatial resolution to measure many of the features of the small scale turbulence at relatively high turbulence Reynolds number  $Re_{\lambda}\approx 10^3$ . This range of scales and the turbulence Reynolds number are at the upper end of what is usually achievable in laboratory flows.

Single and multi-point statistics of the vorticity field were also acquired in addition to the velocity measurements. The description of free shear flows is often considered based on the vorticity, rather than the velocity field. For example, vorticity measurements in turbulent boundary layers have received considerable attention; see, for example, Klewicki and Falco (1996), Ong and Wallace (1998), or Andreopoulos and Honkan (2001). Similarly, Antonia and coworkers have studied the statistical properties of turbulent wake flows, as well as grid turbulence; see Antonia et al. (1987, 1996, 1998), and Brown et al. (1987). Although the statistics of the velocity field in the single stream shear layer are well documented as described in the previous section, the vorticity field has received less attention; see, for example, Foss (1994), Bruns et al. (1991). In these references, time series of the spanwise vorticity are acquired and discussed. The moments of the population of measured values are described, as well as autocorrelation results. Many of the conclusions drawn from these references will be described throughout the discussion of the present vorticity measurements; See Section 4.3.

Vorticity in two stream shear layers has been studied by Balint and Wallace (1989), and Lang (1985) and Kim (1989). These references also describe many of the important features of the vorticity histogram and temporal characteristics. However, there are still a number of open questions about the vorticity field which remain unanswered by these research efforts that will be addressed in the present measurements. For example, the scaling of the vorticity field with both integral time scales and dissipation time scales will be compared. The vorticity fluctuations will also be compared to predictions based on isotropic and axisymmetric turbulence.

## 4.1.2 Measurement program

The measurement program is summarized as follows. Two spanwise vorticity probes (see Section 2.2.3.1) were traversed through the shear layer at the streamwise locations  $x/\theta_0$ = 384, and 675. These probes recorded time series of  $\omega_z$ .  $\omega_y$ , u, v, and w. Two data files were recorded at each spatial location. The first data set was acquired at a rate of 40kHz, for a duration of 30 seconds. The second was acquired at a rate of 1kHz, for a duration of 150 seconds at the location  $x/\theta_0$ =384, and 300 seconds at  $x/\theta_0$ =675. The purpose of the separate data files was to acquire sufficient statistical information about both the large and small scales of motion without excessive usage of computer disk space. The 40kHz data were used to obtain vorticity time series, and spectral information at high wave numbers. The 1kHz data were used to obtain moments of the pdf of the velocity time series and for spectral information at low wave numbers.

In a second and third experiment, the streamwise vorticity probe (section 2.2.3.2) and the multiple X-wire probe (section 2.2.3.3) were traversed through the same locations as the spanwise vorticity probe as described above. This provided time series of  $\omega_x$  and  $\partial \nu \partial z$ . The data were acquired in two sets as were the spanwise and lateral vorticity measurements.

Although the above measurements were sufficient to obtain statistical convergence for the computed moments of the pdf of velocity and vorticity, two separate experiments were executed in order to fully characterize the vorticity pdf at four different turbulent Reynolds numbers. Th first experiment used a single vorticity probe to measure  $\omega_z$  at the center of the shear layer, at the streamwise locations  $x/\theta_0=384$  and 707 with the shear layer facility

in its standard configuration. These data were acquired at a rate of 40kHz for 60seconds per file. A total of 30 files were then obtained for a total of 30 minutes of data acquisition for the two locations. This experiment was then repeated using the same physical probe locations, but with the free stream velocity set to 3.5m/s. This was accomplished simply by opening an access panel to the tunnel upstream of the first set of turning vanes. This allowed a significant fraction of the air supplied by the axial fan shown in Figure 2.1 to escape to the laboratory. Although this could potentially create both asymmetry and unsteadiness in the tunnel, measurements indicated that the dimensionless velocity profile at x=0 was unaffected by the change, except for a notably thicker boundary layer. The specific conditions of the shear layer at this new condition were not evaluated from surveys in the tunnel. However, the goal of the experiment was only to create similar conditions with a different turbulence Reynolds number (Re $_{\lambda}$ ). The comparison of the  $\omega_{z}$  histograms at these conditions is given in Section 4.3.

## 4.2 The Velocity Field

## 4.2.1 Integral constraints on the mean flow

The simple boundary conditions of the single stream shear layer allow several analytical results to be obtained for the mean velocity field. These relationships will be instructive when considering the self-similar growth of the shear layer. Because the flow is statistically invariant in the z direction, the following equations will be assumed to be "per unit width" of the flow. Figure 4.1 shows the control volume and coordinate system that will be used. It is assumed that the control volume has been drawn such that the line B-D is a streamline in the high speed side, and that the entrainment flow is perpendicular to the line A-C. The conservation of mass for this volume can be written as

$$\int_C^D \frac{u}{U_o} dy - \int_A^B \frac{u}{U_o} dy = \frac{v_e}{U_o} L.$$
**4.1**

The x component of the momentum equation can be written as

$$\int_{A}^{B} \frac{u^{2}}{U_{o}} dy - \int_{C}^{D} \frac{u^{2}}{U_{o}} dy = 0$$
**4.2**

since the mean pressure gradient is zero. Equations 4.1 and 4.2 can be added to obtain:

$$\int_{C}^{D} \left( \frac{u^{2}}{U_{o}^{2}} - \frac{u}{U_{o}} \right) dy - \int_{A}^{B} \left( \frac{u^{2}}{U_{o}^{2}} - \frac{u}{U_{o}} \right) dy = -\frac{v_{e}}{U_{o}} L$$
**4.3**

Noting the definition of the momentum thickness ( $\theta$ ) and taking the limit as  $L \to 0$ :

$$\frac{d\theta}{dx} = \frac{v_e}{U_o}.$$

This derivation has been taken directly from Bruns (1990), and has also been derived in other references. For example Holmes et al. (1996) integrate the x component of the Rey-

nolds averaged Navier-Stokes equation to arrive at the same result. Equation 4.4 indicates that the zero pressure gradient shear layer "growth-rate" is identically equal to the ratio of entrainment velocity to free stream velocity.

A similar result can be obtained for the displacement thickness of the shear layer. The displacement thickness is defined as:

$$\delta^* \equiv \int_A^B \left(1 - \frac{u}{U_o}\right) dy = \frac{1}{U_o} \int_A^B y \frac{\partial u}{\partial y} dy \approx \frac{1}{U_o} \int_A^B y \omega_z dy$$
 4.5

The equality above can be shown by integrating by parts, only if the origin of the coordinate system is located at point 'A', which ensures that  $\delta^*$  is positive definite. Equation 4.5 indicates that the displacement thickness also represents the position of the centroid of the spanwise vorticity. Although the definition of  $\delta^*$  is identical to that used in standard boundary layer analysis, the physical interpretation is different. Specifically,  $\delta^*$  is not actually a 'thickness', but rather a distance from the arbitrary origin at point 'A' to the location of the centroid of vorticity. As with boundary layer analysis, the displacement thickness also represents the location where a solid boundary could be located with a fictitious uniform inviscid flow which has the same mass flow rate as the actual viscous (non-uniform) mean velocity profile. This is illustrated in Figure 4.2. Note that the magnitude of  $\delta^*$  depends on the specific choice for point 'A'. However, in the following analysis only the derivative  $d\delta^*/dx$  will be considered, which does not have this dependence.

In wall bounded flows, the shear stress leads to an increased value of  $\delta^*$  in the streamwise direction. In the shear layer the addition of fluid from the entrainment side causes the displacement thickness to move in the negative y direction. This can be quantified leading to a result analogous to equation 4.4. This is obtained by taking the trivial integral:

$$\int_{A}^{B} 1 \ dy - \int_{C}^{D} 1 \ dy = 0$$
**4.6**

and adding to equation 4.1. This results in:

$$\int_{C}^{D} \left(1 - \frac{u}{U_o}\right) dy - \int_{A}^{B} \left(1 - \frac{u}{U_o}\right) dy = -\frac{v_e}{U_o} L.$$

Noting the definition of the displacement thickness ( $\delta^*$ ) and, again, taking the limit  $L \to 0$ :

$$\frac{d\delta^*}{dx} = -\frac{v_e}{U_o}$$
 4.8

Thus, the locus of points which represents the centroid of vorticity forms a line whose slope is equal to the negative of the ratio of entrainment to freestream velocities. The negative sign in equation 4.8 indicates the preferential "movement" of the vorticity towards the low-speed side.

From the relations given in equations 4.4 and 4.7, the "spreading parameter" can be defined as

$$\sigma \equiv \frac{v_e}{U_o} = \frac{d\theta}{dx} = -\frac{d\delta^*}{dx} \approx 0.035.$$

That is, the growth of the shear layer, the slope of the shear layer centroid with respect to the high speed streamline, and the entrainment of ambient fluid into the shear layer are necessarily equal. The value  $\sigma \approx 0.035$  was determined experimentally in the present facility; see Figure 3.13. Other researchers have found similar values for the growth rate of the shear layer. For example, Champagne et al. (1970) measured  $d\delta */dx = 0.035$ . Ali et al. (1985) directly measured  $v_e/U_o = 0.035$ , and  $d\theta/dx = 0.0352$ . Hussain and Zaman (1985) obtained a similar value of  $d\theta/dx = 0.032$ .

## 4.2.2 Velocity in Self-Similar Coordinates

The idea of self similarity in free shear flows is well documented in most standard text books on turbulent flow; see, for example, Pope (2000), Tennekes and Lumley (1972), or Townsend (1975). The analyses developed in these references are given for general shear layers (i.e, both single and two stream). The present analysis will be given specifically for the single stream shear layer. The self-similarity hypothesis is satisfied if the moments of the probability distribution function (pdf) for all field variables can be written as a function of a single dimensionless similarity parameter. This parameter represents the lateral position in the shear layer divided by a local length scale. In the present analysis, this will be defined as:

$$\eta \equiv \frac{y - y_c}{\theta}.$$

Note that the use of  $\theta$  for the transverse length scale of the flow is arbitrary. A general length  $l \sim x$  is often used to emphasize this point. It will be shown that the relationships to be derived will take a simpler form with the present definition.

The quantity  $y_c$  represents the "center" of the shear layer. The only requirement for the choice of  $y_c$  is that the locus of points representing  $y=y_c$  is an isotach (i.e., constant mean velocity). The locus of points which represent an isotach of mean velocity can be identified as any line with a fixed slope with respect to the high speed streamlines. This slope can be characterized by the definition of the parameter:

$$\alpha = \frac{dy_c}{dx}$$
. 4.11

For example, if the centroid of vorticity is chosen to define  $\eta=0$  ( $y_c=\delta^*$ ), then  $\alpha=-\sigma$ . Note that most authors choose  $y_c=y_{0.5}=y(u/Uo=0.5)$ . That is, the point where the mean velocity

equals half of the free stream velocity is defined as  $y_c$ . In the present study the centroid of vorticity was found to be at the location  $y(\bar{u}/U_o = 0.48)$ .

The analysis thus far has utilized the standard coordinates in which the x direction is aligned parallel to the boundary layer plate. This will be represented by the standard or "untilted" coordinates (x, y). It will be useful in the following sections to allow the coordinate system to rotate such that the streamwise (x) direction coincides with the isotach used in the definition of  $y_c$ . This is termed the "tilted" coordinates  $(\hat{x}, \hat{y})$ ; see Figure 4.3. In the  $(\hat{x}, \hat{y})$  system,  $\alpha=0$  by definition, and the boundary conditions will depend on the choice of  $y_c$ . This is contrast to the standard coordinates in which the value of  $\alpha$  depends on the choice of  $y_c$ , and the boundary conditions are fixed.

## 4.2.2.1 Mean Velocity Components

The streamwise component of velocity can be written in terms of the similarity variable as:

$$\bar{u}(x,y) = U_o \cdot f(\eta).$$

The boundary conditions for the (x, y) coordinate system are

$$f(\eta = -\infty) = 0, f(\eta = \infty) = 1.$$
 4.13

In the  $(\hat{x}, \hat{y})$  coordinates using  $\alpha = -\sigma$ , the boundary conditions are:

 $f(\hat{\eta} = -\infty) = \sin(\operatorname{atan}(\alpha)) = -0.0340 f(\hat{\eta} = \infty) = \cos(\operatorname{atan}(\alpha)) = 0.9994$ .4.14 Because the magnitude of  $\alpha$  is small, these boundary conditions are nearly identical to those of equation 4.13. Hence, the difference between the tilted and untilted coordinates does not represent a significant effect in the consideration of  $f(\eta)$ .

The streamwise velocity component was measured at the streamwise locations  $x/\theta_0=384$ , and 675 using an X-wire probe. The mean velocity calculated from these time series is shown in Figure 4.4. The curve fit shown was taken from Bruns (1990) using a different experimental facility. The "collapse" of the data onto a single curve indicates that the streamwise component of velocity does have a universal form for the single stream shear layer.

The time average lateral component of velocity can be written as:

$$\bar{\mathbf{v}}(x,y) = \sigma U_o \cdot g(\eta)$$
 4.15

where the factor of  $\sigma$  is used so that  $g(\eta)\sim O(1)$ . The relationship between the two similarity functions f and g can be determined from the two-dimensional continuity equation:

$$\frac{\partial u}{\partial x} + \frac{\partial v}{\partial y} = 0.$$

The spatial derivatives of  $\eta$  are given by:

$$\frac{\partial \eta}{\partial y} = \frac{1}{\theta}, \frac{\partial \eta}{\partial x} = -\frac{\sigma}{\theta} \left( \eta + \frac{\alpha}{\sigma} \right).$$

Equation 4.16 can be expressed in self-similar form by combining equations 4.12, 4.15, and 4.17:

$$g' = f'\left(\eta + \frac{\alpha}{\sigma}\right)$$
 4.18

This can be integrated to give:

$$g(\eta) = g(-\infty) + \frac{\alpha}{\sigma} f(\eta) + \int_{-\infty}^{\eta} \xi f'(\xi) d\xi.$$
 4.19

The last term can be integrated by parts to give an equivalent expression:

$$g(\eta) = g(-\infty) + \left(\frac{\alpha}{\sigma} + \eta\right) f(\eta) - \int_{-\infty}^{\eta} f(\xi) d\xi$$
**4.20**

The boundary conditions for  $g(\eta)$  are determined as follows. For the untilted coordinates, again,  $y_c = \delta^*$ , and  $\alpha = -\sigma$  are used. The integral on the right hand side of equation 4.19 is zero because the origin is defined as the centroid of f'. The boundary conditions for  $g(\eta)$  become:

$$g(\eta = -\infty) = 1, g(\eta = \infty) = 0$$
 4.21

which is consistent with equation 4.15. In the tilted coordinates however,  $\alpha$ =0, and the value of the integral on the right hand side of equation 4.19 will depend on the choice of  $y_c$ . For  $y_c$ = $\delta^*$ , the integral is again zero, and the boundary conditions become:

$$g(\hat{\eta} = -\infty) = g(\hat{\eta} = \infty) = 1.$$

The value of  $g(\hat{\eta} = \infty)$  is also apparent from the vector decomposition of the freestream velocity shown in Figure 4.3. The functions  $g(\eta)$  and  $g(\hat{\eta})$  were evaluated from equation 4.19, and are shown in Figure 4.5. Note that only the boundary conditions at  $\eta = -\infty$  were enforced. The fact that the correct values of  $\eta(+\infty)$  were obtained is an indication that  $f(\eta)$  was measured accurately, and that the analysis above is consistent.

Close examination of the functions  $g(\eta)$  and  $g(\hat{\eta})$  provide information about the shear layer which is not observed in the streamwise velocity profile. In the untilted coordinates,  $\bar{v}$  decreases on the low speed side of the shear layer which represents the mean streamwise acceleration  $(\partial u/\partial x > 0)$  of the entrainment fluid. Also,  $g(\eta) < 0$  is observed for

 $\eta > -0.38$ . This indicates a net flow of fluid, which originated on the high speed side, towards the center of the shear layer.

A consistent but different view of the flow field can be understood from the tilted coordinates. An interesting feature of the  $g(\hat{\eta})$  profile is the positive lateral mean velocity component observed for all  $\hat{\eta}$ . Thus, to an observer aligned with the centroid of vorticity, fluid is observed to move from the low speed side to the high speed side of the shear layer. In this view, the shear layer entrains and "extrains" fluid at the same rate, as already observed from the boundary conditions (equation 4.22).

Although the 'tilting' of shear layers with respect to the free stream flow has been recognized throughout the literature, the failure to recognize the non-zero value of  $\alpha$  in the formulation of the self-similar equations has resulted in incorrect statements and conclusions in the literature. For example, Holmes et al. (1996) derive the self-similar equations for a single stream shear layer. Because the movement of the shear layer into the low speed side is not explicitly accounted for, the equations imply  $\alpha$ =0. That is, the equations are derived in a tilted coordinate system. A contradiction is then encountered (see page 54 of Berkooz et al.) in which the statement is made that  $g(\hat{\eta}=\infty)=0$ . The argument is made that "extrainment is never physically observed." The resulting analysis (e.g., equation 2.23 of Holmes et al., 1996) is therefore incorrect.

Note that geometrical reasoning (based on equation 4.9) argues that the isotach aligned with the streamwise direction occurs at  $\hat{\eta}=1$ . Note however, that this istotach is not a streamline. In the untilted coordinates, a small negative value of  $\bar{v}$  is observed at  $\eta=1$ , indicating the movement of fluid towards the low speed side. The direct experimental

measurements in room coordinates show that the mean velocities which are acquired at constant y=0 location result in  $\bar{u}/U_o=0.685$ , corresponding to  $\eta$ =0.90. This small difference between the predicted value of  $\eta$ =1 and the determined value of  $\eta$ =0.9 is likely a result of the growth of the displacement thickness in the boundary layer of the outer (y=1m) wind tunnel wall.

## 4.2.2.2 Profiles of the Fluctuating Velocity

The probability distribution function (pdf) of the unsteady fluctuations of the three components of velocity can be characterized by profiles of the moments of the pdf. In this section the root mean square (RMS) of the fluctuations are considered. Higher order moments of the velocity field in a single stream shear layer are examined in detail in several references. See, for example, Wygnanski and Fielder (1970) or Champagne et al. (1976). The spatio-temporal characteristics of the velocity field will be considered in Section 4.6.

The RMS of the streamwise velocity fluctuations ( $\tilde{u}$ ) was calculated from the time series data acquired at  $x/\theta_0$ =384 and 675. These data are shown in Figure 4.6. Similarly, the RMS of the lateral (v) and spanwise (w) fluctuating components of velocity are shown in Figures 4.7 and 4.8 respectively. These measurements agree well with the measurements published in the literature. For example, the maximum value of  $\tilde{u}/U_o$  was reported to be 0.168 and 0.176, and 0.165 by Champagne et al. (1976), Wygnanski and Fiedler (1970), and Bruns et al. (1991) respectively. The present data indicate a value of  $\tilde{u}/U_o$  was found to be 0.12 by Wygnanski and Fiedler (1970), and 0.135 by both Champagne et al. (1976) and Bruns et al. (1991). The present data indicate a value of 0.12 at  $x/\theta_o$ =384, and 0.13 at  $x/\theta_o$ =384.

 $\theta_0$ =675. The general agreement of these statistics supports the inference that the facility provides a canonical single stream shear layer as studied in these other references, and that a self-similar state of the flow field was achieved.

## 4.2.3 Profiles of the velocity gradient variance

The determination of the velocity gradient moments:  $(\partial u_i/\partial x_j)^2$  is of interest. For example, the description of the flow field in terms of the vorticity field (Section 4.2) or the dissipation of kinetic energy (Section 4.4) will make explicit use of the measured values and their relations. Secondly, the velocity gradients represent information about the smallest scales of motion. The relationships between the various derivative moments can be used to validate assumptions about the small scale motions.

A complete description of these moments requires the measurement of nine independent gradients, written in matrix form as:

$$\frac{\partial u_i}{\partial x_j} = \begin{bmatrix} \frac{\partial u}{\partial x} & \frac{\partial u}{\partial y} & \frac{\partial u}{\partial z} \\ \frac{\partial v}{\partial x} & \frac{\partial v}{\partial y} & \frac{\partial v}{\partial z} \\ \frac{\partial w}{\partial x} & \frac{\partial w}{\partial y} & \frac{\partial w}{\partial z} \end{bmatrix} .$$
4.23

In the present work, only six of these, highlighted in bold face in equation 4.23, were measured. This choice of measured quantities is partially due to experimental limitations, and partly as a result of interest in the theories of locally isotropic and locally axisymmetric turbulence. These hypotheses require specific relationships among these terms, which can be validated with these measurements.

The measurements were obtained as follows. The streamwise derivatives were calculated using the Taylor microscale formulation (see, e.g., Pope (2000)). For example:

$$\overline{\left(\frac{\partial u}{\partial x}\right)^2} = 2\frac{\tilde{u}^2}{\lambda_{uu}^2}.$$

where  $\lambda$  is the Taylor microscale calculated from the autocorrelation function. The streamwise derivatives of v and w were calculated similarly. These approximations do, of coarse make use of the Taylor's "frozen turbulence" assumption. In regions where the fluctuation levels are not small compared to the mean velocity, this assumption can lead to significant errors. Lumley (1965), and later Wyngaard and Clifford (1977) derived corrections for the longitudinal and transverse derivative variances:

$$\frac{\left[\left(\frac{\partial u'}{\partial x}\right)^{2}\right]^{measured}}{\left[\left(\frac{\partial u'}{\partial x}\right)^{2}\right]^{corrected}} = 1 + \frac{\left(\overline{u'}^{2} + 2\overline{v'}^{2} + 2\overline{w'}^{2}\right)}{\overline{u}^{2}} = C_{u}$$
4.25

and

$$\frac{\left[\left(\frac{\partial v'}{\partial x}\right)^{2}\right]^{measured}}{\left[\left(\frac{\partial v'}{\partial x}\right)^{2}\right]^{corrected}} = 1 + \frac{\left(\overline{u'}^{2} + \overline{v'}^{2}/2 + \overline{w'}^{2}\right)}{\overline{u}^{2}} = C_{v}$$
**4.26**

These correction factors are plotted across the shear layer at the two streamwise locations  $x/\theta_0$ =384 and 675 in Figure 4.9. Since the individual terms on the right hand side of equations 4.25 and 4.26 have been shown to follow self-similar scaling, it is expected that these dimensionless corrections must also. This is found to be approximately the case. However, the small differences in the measurements on the low speed side are squared and added, leading to more noticeable deviations between the two streamwise locations. It is of interest to note that the magnitude of the correction in the low speed side is considerable, given the high levels of turbulence intensity in that region.

It is expected that the velocity gradient moments, along with the statistics previously described, should follow self-similar scaling. However, because the velocity gradients are related to the small scale motions of the flow, care is needed in the way in which the velocity gradients are normalized. The dimensions of  $(\partial u_i/\partial x_j)^2$  are (1/time<sup>2</sup>). Thus, a time scale of the flow must be used to normalize these statistics. The integral time scale  $\tau_0 = \theta(x)/U_0$ , will not properly scale the gradient statistics because  $\tau_0$  represents the largest time scales of the flow. The proper scaling is obtained from the Kolmogorov time scale since the spatial gradient of velocity is related to the small scale motions:

$$\tau_{\eta} = \sqrt{\frac{v}{\varepsilon}} \sim \sqrt{\frac{v\theta}{U_o^3}} = \frac{\tau_o}{\sqrt{Re_{\theta}}}$$
4.27

where  $\varepsilon$  is the rate of dissipation of kinetic energy. The use of dissipation to scale the velocity gradient statistics becomes obvious given the definition of dissipation in a homogeneous flow:

$$\varepsilon = \nu \left( \frac{\partial u_i \partial u_i}{\partial x_i \partial x_i} \right).$$
 4.28

Equation 4.27 relates the dissipation to the mean flow variables from the relation  $\varepsilon \sim U_o^3/\theta$ . This scaling can be argued based on the dimensionless form of the turbulent kinetic energy budget; see Section 4.5. Note that the ratio of the integral to dissipation time scale is proportional to the square root of the local Reynolds number. The velocity gradient statistics will be normalized by multiplying the measured values by  $\tau_{\eta}^2$ ; this will be referred to as dissipation scaling.

The measured values of  $(\partial u'/\partial x)^2$  for at the locations  $x/\theta_0=384$  and 675 are shown in Figure 4.10 normalized by dissipation scaling. The corrected and uncorrected symbols

refer to the use of equation 4.25. Similarly, the terms  $(\partial v'/\partial x)^2$  and  $(\partial w'/\partial x)^2$  were calculated from their respective autocorrelation functions, and are shown in Figures 4.11 and 4.12 respectively. The data indicate that the profiles of the velocity gradients are similar in shape to the fluctuating velocity components, although the data for  $\eta$ <-1 do not exhibit a monotonic decrease towards the low speed side. It is assumed that these measurements could have significant error due to Taylor's hypothesis that are not easily corrected by equations 4.25 and 4.26. It is also clear that the use of dissipation scaling properly scales the data (see  $\eta$ >1) from the two streamwise locations into self-similar form.

The terms:  $(\partial u'/\partial y)^2$  and  $(\partial u'/\partial z)^2$  were obtained using the parallel sensors of the Mitchell probe with 1.4mm spacing; see Figures 4.13 and 4.14. Lastly, the term  $(\partial v'/\partial z)^2$  was obtained using the double X wire probe described in Section 2.2.3.3. These data are shown in Figure 4.15. Because these measurements do not require the use of Taylor's hypothesis, the measurements show a more symmetric shape to the profile. In addition to providing information about the vorticity and dissipation fields, as will be discussed in later sections, the variances of the velocity gradients can also be used to test the symmetry of the turbulence properties. For example, if local isotropy is assumed, then only the term  $(\partial u/\partial x)^2$  is independent and need be measured. This theory is reviewed in detail by, for example, Monin and Yaglom (1975). The other eight terms are related by:

$$\overline{\left(\frac{\partial u}{\partial x}\right)^2} = \overline{\left(\frac{\partial v}{\partial y}\right)^2} = \overline{\left(\frac{\partial w'}{\partial z}\right)^2},$$
**4.29**

$$2\overline{\left(\frac{\partial u'}{\partial x}\right)^2} = \overline{\left(\frac{\partial u'}{\partial y}\right)^2} = \overline{\left(\frac{\partial v'}{\partial x}\right)^2} = \overline{\left(\frac{\partial u'}{\partial z}\right)^2} = \overline{\left(\frac{\partial v'}{\partial z}\right)^2} = \overline{\left(\frac{\partial w'}{\partial x}\right)^2} = \overline{\left(\frac{\partial w'}{\partial y}\right)^2} = \overline{\left(\frac{\partial w'}{\partial y}\right)^2}$$
**4.30**

The assumption of axisymmetric turbulence is less restrictive than the isotropic assumption, as originally put forth by Batchelor (1946). The set of relations between the derivatives are given by:

$$\overline{\left(\frac{\partial u}{\partial y}\right)^2} = \overline{\left(\frac{\partial u}{\partial z}\right)^2},$$
4.31

$$\overline{\left(\frac{\partial v}{\partial x}\right)^2} = \overline{\left(\frac{\partial w}{\partial x}\right)^2},$$
4.32

$$\overline{\left(\frac{\partial v}{\partial y}\right)^2} = \overline{\left(\frac{\partial w}{\partial z}\right)^2},$$
4.33

$$\left(\frac{\partial w}{\partial v}\right)^2 = \left(\frac{\partial v}{\partial z}\right)^2$$
, and 4.34

$$\overline{\left(\frac{\partial v}{\partial v}\right)^2} = \frac{1}{3} \overline{\left(\frac{\partial u}{\partial x}\right)^2} + \frac{1}{3} \overline{\left(\frac{\partial v}{\partial z}\right)^2}.$$

These relationships were derived and discussed by George and Hussein (1991). In order to test the validity of these assumptions, Browne et al. (1987) used the ratios of the derivatives:

$$K_{1} = 2 \frac{\overline{\left(\frac{\partial u}{\partial x}\right)^{2}}}{\overline{\left(\frac{\partial v}{\partial x}\right)^{2}}}, K_{2} = 2 \frac{\overline{\left(\frac{\partial u'}{\partial x}\right)^{2}}}{\overline{\left(\frac{\partial w}{\partial x}\right)^{2}}}, K_{3} = \frac{\overline{\left(\frac{\partial u}{\partial x}\right)^{2}}}{\overline{\left(\frac{\partial u}{\partial y}\right)^{2}}}, K_{4} = \frac{\overline{\left(\frac{\partial u}{\partial x}\right)^{2}}}{\overline{\left(\frac{\partial u}{\partial z}\right)^{2}}}$$
**4.36**

If the flow field is truly isotropic, then these ratios should be equal to unity. The axisymmetric assumption is less restrictive in that no prescribed values are required for the constants. The axisymmetric turbulence condition requires  $K_1=K_2$ , and  $K_3=K_4$ . The ratios of equation 4.36 are plotted in shear layer coordinates for the two streamwise locations in Figures 4.16 and 4.17. Note that the values with the Taylor correction factors were used. These ratios do not clearly support either the isotropic or axisymmetric assumptions. However, it could be argued that the values of  $K_3$  and  $K_4$  are closer to being equal than

they are to being unity. The same is true for  $K_1$  and  $K_2$  over much of the shear layer. The consequence of these observations is that the additional information obtained by measuring as many terms as possible will lead to improved accuracy in the predictions of moments of the vorticity fluctuations and the measurement of the dissipation.

#### 4.3 Statistics of the Vorticity Field

#### 4.3.1 Examples of Vorticity Time Series

Prior to the presentation and discussion of the statistical properties of the vorticity field, it is instructive to first view segments of the time series data. This will allow several of the qualitative aspects of the vorticity field to be observed. A sample of the spanwise vorticity  $(\omega_{\nu}(t))$  time series is shown in Figure 4.18. These data were acquired in the center of the shear layer:  $\eta \approx 0$  at the streamwise location  $x/\theta_0 = 675$ . The mean vorticity at this location was found to be  $-\partial \bar{u}/\partial y = -9$  (1/sec). Several features can be observed from this time series segment. First, there exist motions which appear very small in scale (high frequency), with very large vorticity magnitude compared to the mean vorticity. The root mean square of vorticity from the full time record was  $\tilde{\omega}_z = 176(1/\text{sec})$ . Although the largest excursions in magnitude appear to be of relatively short time scale, there also appear to be large regions of fluid whose vorticity is highly correlated. An example of this can be observed near the one second mark in Figure 4.18. The time duration of this large motion is approximately 0.24 seconds. Using Taylor's hypothesis, this corresponds to a length scale of 0.78m, or 3.50. This is a remarkably large scale vortical motion, especially since the sign of the vorticity is positive. That is, opposite that of the mean vorticity. A further discussion of the length scales of the vorticity field will be given in Section 4.5. Another notable feature of the time series data shown in Figure 4.18 is the presence of regions of fluid with near zero vorticity. It is possible that this results from large scale motions which transport fluid from either the high speed or low speed streams across the shear layer. In Figure 4.19, a second example of the vorticity time series is shown from the

same data set. These data show an extended period of time in which the fluid is rotational  $(|\omega_z| > 200(1/\text{sec}))$ , although there is little or no high frequencies observed. This behavior was first described by Haw et al. (1989), and considered in detail by Foss et al. (1995) in terms of the difference between "intermittency" and "activity intermittency".

A third example of vorticity time series is shown in Figure 4.20. The location of this measurement was  $x/\theta_0$ =675,  $\eta$ =3.9. Here, on the high speed side of the shear layer the mean velocity is not measurably different from the free stream velocity. The vorticity is, however, still quite intermittent. One can observe from these data that small regions of highly turbulent fluid convect past the probe.

#### 4.3.2 Histograms of Vorticity

The population of vorticity values that occur at a given spatial location can be characterized by the probability density function (pdf). This provides information regarding the scaling properties of the vorticity fluctuations. Although the shape of the pdf can be completely described by the moments of the distribution, it is first instructive to observe the pdf at various conditions. The present experimental facility provides an opportunity to observe the vorticity histogram over a range of Reynolds numbers and intermittency conditions.

The true (continuous) pdf is approximated experimentally by the histogram of the time series measurements. In order to "fill out" the entire histogram to best approximate the pdf, very long time series are required to converge the statistics of the vortical motions which occur relatively infrequently. Therefore, four time series were acquired in addition to the traverses described above. These data were acquired in the center of the shear layer,

at two streamwise locations:  $x/\theta_0$ =384 and 675, and two free stream velocities:  $U_0$ =3.5 and 7.1 m/s. Time series of  $\omega_z$  were acquired at a rate of 4000Hz for a duration of 30minutes. A summary of the four conditions, including several of the characteristics of the time series data, are shown in Table 4.1.

The histogram of the vorticity acquired at these points is shown in Figure 4.21. These data

Table 4.1: Measurement conditions data shown in Figure 4.21

	x/θ <sub>o</sub>	Uo (m/s)	$\frac{\bar{u}}{U_o}$	$rac{ ilde{u}}{U_o}$	λ <sub>uu</sub> (mm)	$ ilde{\omega}_z$	Skew ness (ω <sub>z</sub> )	${ m Re}_{\lambda}$
A	384	7.1	0.47	0.15	11.3	227	0.23	835
В	384	3.6	0.52	0.17	8.6	136	0.30	411
C	707	3.6	0.55	0.18	10.9	124	0.26	551
D	707	7.1	0.50	0.15	17.4	188	0.32	1210

are shown in semilog format, with each histogram shifted by an order of magnitude so that they can be distinguished. The first notable observation is that the shape of the histograms is similar in all four cases. This is quite remarkable given the range of Reynolds numbers between the measurements. The shape can be characterized by the exponential tails for large  $|\omega_z|$ , and a lack of symmetry in the population of measurements with small  $|\omega_z|$ . This characteristic shape is nearly identical to the histogram of vorticity measured by Antonia et al. (1988) in the wake of a cylinder. In that study, the measurements were taken in a turbulent region where the mean vorticity was non-zero, and with a turbulence Reynolds number of approximately  $Re_{\lambda} = \bar{u}\lambda_{u}/v = 60$ . The "cusp" near the  $\omega_z = 0$  location is

distinctive in both the shear layer and the cylinder wake, and clearly indicates the asymmetry of the population of measured  $\omega_z$  values.

The insensitivity of the exponential tails of the pdf to the Reynolds number is further supported by the direct numerical simulation (DNS) results of Cao et al. (1996). These computations were conducted using a cubic domain with periodic boundary conditions. Forcing at low wave numbers was used to balance the viscous dissipation of kinetic energy. The circulation of the flow field was calculated around small rectangular domains. In the limit of a very small circulation domain, this calculation closely resembles the micro-circulation algorithm used in the present experimental method (see Section 2.2.3.1). The population of circulation values was used to create a histogram of the realizations. It was found that large circulation areas led to histograms which appeared nearly Gaussian. However, as the circulation area decreased, thereby approximating a true vorticity measurement, the tails of the pdf became more exponential in character, with a distinct cusp at center of the histogram where  $\omega$ =0; see Figure 3 of Cao et al. (1988). Naturally, the cusp is symmetric in the computational work because of the symmetry of the boundary conditions.

Time series of spanwise vorticity in a high Reynolds number atmospheric boundary layer have also been acquired. The histogram of these data are provided here for comparison with the shear layer results; see Figure 4.23. The flow conditions are characterized as a flat wall boundary layer with  $Re_{\theta} \sim 10^6$ . The turbulence Reynolds number was determined to be  $Re_{\lambda} \approx 2500$  at the probe location  $y^+=3800$ . The ratio of the probe scale to the Kolmogorov length scale in this flow was 2.5. The features which are of interest in Figure 4.23

include the Gaussian-like region near the small values of  $|\omega_z|$  and the "tails" of the pdf which have an obvious positive curvature. Further discussion of these data is provided in the conclusions (Section 4.8).

The data and references described above vary in both geometry and Reynolds number, but do not account for varied intermittency levels. The histograms of  $\omega_z$  at the center of the shear layer ( $\eta$ =0) where the fluid is almost always rotational, and at the high speed edge ( $\eta$ =3.9) where the fluid is intermittently turbulent, are shown in Figure 4.22. It is observed that the  $\eta$ =3.9 histogram exhibits exponential tails similar to the  $\eta$ =0 data. Note also that the slope and magnitude of the exponential portion are not symmetric for positive and negative realizations. The central region ( $|\omega'|/\tilde{\omega}$ <1 of the histogram at  $\eta$ =3.9 is characterized by a Gaussian like histogram (note that a Gaussian distribution is represented by an inverted parabola in semilog coordinates).

## 4.3.3 Profiles of the Vorticity RMS

The unsteadiness of the fluctuating vorticity field can be partially characterized by the RMS level of each component of vorticity. These values were obtained directly using the time series from the vorticity probes, and indirectly using the velocity gradient information described in Section 4.1.3. If the assumption of homogeneous and isotropic turbulence is used, then the mean square of each component of vorticity is equal, and related to the streamwise velocity gradient by:

$$\overline{\omega_i^2} = 5 \overline{\left(\frac{\partial u}{\partial r}\right)^2}$$
 4.37

The assumption of axisymmetric turbulence can also be used to relate the vorticity to the velocity gradients. In this case, only the spanwise and lateral components are equal, and are given by George and Hussein (1991):

$$\overline{\omega_y^2} = \overline{\omega_z^2} = \left( \frac{\partial u}{\partial x} \right)^2 + \left( \frac{\partial v}{\partial x} \right)^2 + \left( \frac{\partial u}{\partial z} \right)^2$$
**4.38**

The estimates of the vorticity variances were calculated from the velocity gradient statistics presented in Section 4.2.3 based on equations 4.37 and 4.38. These data are shown along with the directly measured values of  $\tilde{\omega}_z$  and  $\tilde{\omega}_v$  in Figures 4.24 and 4.25. The data were scaled with both the integral time scales (  $\theta/U_o$  ) and dissipation time scales  $(\sqrt{v\theta/U_o^3})$ . The comparison of the two streamwise location indicate that the integral time scale leads to values of  $\tilde{\omega}_z\theta/U_o$  which increase substantially in the x direction. For example, the maximum value of  $\tilde{\omega}_z \theta / U_o$  increased from 4.8 at  $x/\theta_o = 384$  to a value of 7.25 at  $x/\theta_0$ =675. The dissipation time scale leads to values of  $\tilde{\omega}_z \sqrt{v\theta/U_o^3}$  which increased only slightly from 0.0182 to 0.0205 for the two streamwise locations. This relative agreement using the dissipation time scaling could be used to argue that the vorticity fluctuations scale self similarly. However, this increase is considerably greater than the estimated uncertainty of the measurement (roughly  $3x10^{-4}$  based on sample size and probe uncertainties, see Section 2.2.3.1.) This increase in vorticity fluctuation levels when using the dissipation scales will be discussed with the conclusions of this chapter (Section 4.8), since the explanation of this result will require the calculation of the one dimensional vorticity spectral density function, which is described in Section 4.6.

The agreement between all the directly measured values of  $\omega_y$  and  $\omega_z$  with the isotropic relation (4.37) is quite surprising, especially given the lack of isotropy shown in the various velocity gradient statistics in Figures 4.16 and 4.17. The agreement with the axisymmetric prediction (4.38) is also encouraging, although not surprising given the support for the axisymmetric assumptions shown previously, as well as the observation that  $\omega_y \approx \omega_z$  throughout most of the shear layer.

Measurements of the streamwise component of vorticity were also acquired. Because the measurement area of this probe is 5.6mm x 5.6 mm, it is explicit that the spatial smoothing of these measurements will severely under-predict the actual vorticity fluctuations. For comparison, the measured values were scaled by an arbitrary factor of 2.7, and plotted along with the axisymmetric calculation by Hussain and George (1991):

$$\overline{\omega_x^2} = -\frac{1}{3} \left( \frac{\partial u}{\partial x} \right) + \frac{8}{3} \left( \frac{\partial v}{\partial z} \right).$$
 4.39

These data are shown for both measurement locations in Figure 4.26. The arbitrary multiplier of 2.7 was only used to show that the shape of the directly measured and predicted profiles agree well. Assuming the values from the axisymmetric calculation (eqn. 4.39) are correct, the ratio  $\tilde{\omega}_x/\tilde{\omega}_z$  was found to be 1.28 at the shear layer center, compared to the value  $\tilde{\omega}_x/\tilde{\omega}_z \approx 1.35$  found by the direct measurements of Balint and Wallace (1989) in a two stream shear layer. Note that the nearly equal values of the spanwise and lateral components, and the larger values of the streamwise component of vorticity, supports the assumptions of the theory of axisymmetric turbulence over that of isotropic turbulence.

#### 4.4 Analysis of the Reynolds Stress

The Reynolds averaged Navier-Stokes equations can be written as:

$$\bar{u}_{j}\frac{\partial \bar{u}_{i}}{\partial x_{i}} = \frac{1}{\rho}\frac{\partial}{\partial x_{i}}(-\bar{P}\delta_{ij} + 2\mu\bar{S}_{ij} - \rho\bar{u}_{i}\bar{u}_{j})$$
**4.40**

where  $\bar{S}_{ij}$  represents the time averaged rate of strain tensor. The modeling of the Reynolds stress  $\bar{u}_i^{\dagger}\bar{u}_j^{\dagger}$  is the subject of considerable research; see, e.g., Pope (2000) for a review. The physical mechanisms which lead to the Reynolds stresses are still a topic of research, since no universal model has been found that relates these terms to the mean flow variables.

The single stream shear layer provides an interesting environment in which to study the Reynolds stresses. One reason for selecting this flow field for study is because the only off-diagonal component of the Reynolds stress tensor which is non-zero is  $\overline{u'v'}$ . Assuming that the mean viscous stress and pressure gradient are negligible, the momentum equation for the streamwise direction (i=1) becomes (see, e.g., Pope (2000) page 113):

$$\bar{u}\frac{\partial\bar{u}}{\partial x} + \bar{v}\frac{\partial\bar{u}}{\partial y} = -\frac{\partial\bar{u'v'}}{\partial y} - \frac{\partial(\bar{u''}^2 - \bar{v''}^2)}{\partial x}$$
**4.41**

The final term of equation 4.41 is usually neglected in thin shear flows, which results in what is usually termed the boundary layer form of the momentum equation:

$$\bar{u}\frac{\partial \bar{u}}{\partial x} + \bar{v}\frac{\partial \bar{u}}{\partial y} = -\frac{\partial \bar{u}'\bar{v}'}{\partial y}.$$

Given that the left hand side of this equation is composed of variables which have been found to be self similar, the Reynolds stress is assumed to be of the form:

$$h(\eta) = \frac{\overline{u'v'}}{\sigma U_o^2}.$$

The use of  $\sigma$  in the denominator of equation 4.43 is to make  $h(\eta)=O(1)$ . By combining equations 4.12, 4.19, 4.42, and 4.43, the dimensionless stress gradient can be written as:

$$h'(\eta) = f' \left\{ -1 + \int_{-\infty}^{\eta} f(\xi) d\xi \right\}.$$
 4.44

This equation was integrated, and plotted with the experimentally measured values in Figure 4.27. The agreement is satisfactory, and the values are similar to those measured by Bruns et al. (1991) and Champagne et al. (1976). Because the gradient of the stress appears in the mean momentum equation (4.42), it is instructive to look at the stress derivative as well. The profile of  $h'(\eta)$  was determined by fitting the data shown in Figure 4.27 with a polynomial, and differentiating; see Figure 4.28.

One feature of the Reynolds stress derivative is the zero crossing at  $\eta \approx 0.6$ . Consider the terms of equation 4.42 in the untilted (x,y) coordinate system at this location. In Section 4.2.2.1 it was observed that for  $\eta < 1$ ,  $\partial \bar{v}/\partial y$  is negative, and so  $\partial \bar{u}/\partial x$  must be positive. Since the right and left hand sides of equation 4.42 are zero at  $\eta \approx 0.6$ , then  $\bar{v}$  must be negative as is observed in Figure 4.5. Note that this is in conflict with the comments made by Townsend (1975). In the discussion following equation 6.10.3 of Townsend, it is stated that the Reynolds stress gradient is zero at the location where  $\bar{v} = 0$ . However, Townsend does not correctly account for the non-zero value of  $\alpha$  in his calculation of  $g(\eta)$ , which led to this incorrect conclusion.

The gradient of the Reynolds stress can be further studied using the tensor identity:

$$\frac{\partial}{\partial x_i} \overline{u'_i u'_j} = -\varepsilon_{ijk} \overline{u_j \omega_k} + \frac{1}{2} \frac{\partial}{\partial x_i} \overline{u'_j u'_j}.$$

Using i=1 as before, and ignoring the streamwise gradients, this reduces to

$$-\frac{\partial \overline{u'v'}}{\partial v} \approx \overline{v\omega_z} - \overline{w\omega_y}.$$

The velocity-vorticity correlation coefficients can be defined as:

$$C_{\mathbf{v}\omega_{z}} = \frac{\overline{\mathbf{v}'\omega_{z}'}}{\nabla \tilde{\omega}_{z}}, C_{w\omega_{y}} = \frac{\overline{w'\omega_{y}'}}{\overline{w}\tilde{\omega}_{y}}$$
 4.47

By combining equations 4.47, 4.43, and using the scaling relationship 4.27, equation 4.46 becomes:

$$-\sigma h'(\eta) = \left[ C_{v\omega_z} \sqrt{Re_{\theta}} \right] \left( \frac{\tilde{\mathbf{v}}}{U_o} \right) \left( \frac{\tilde{\mathbf{\omega}}_z}{\sqrt{U_o^3/v\theta}} \right) - \left[ C_{w\omega_y} \sqrt{Re_{\theta}} \right] \left( \frac{\tilde{\mathbf{w}}}{U_o} \right) \left( \frac{\tilde{\mathbf{\omega}}_y}{\sqrt{U_o^3/v\theta}} \right)$$
 **4.48**

It is useful to make the approximations  $\nabla \approx \tilde{w}$ , and  $\tilde{\omega}_z \approx \tilde{\omega}_y$  for a further understanding of equation 4.48,. These appear to be reasonable approximations, especially for  $\eta>0$ . The difference between the velocity-vorticity correlations can then be written as:

$$C_{w\omega_{y}} - C_{v\omega_{z}} = \left[\frac{U_{o}}{\tilde{v}}\right] \left[\frac{U_{o}^{3/2}}{\tilde{\omega}_{z}\sqrt{v\theta}}\right] \left[\frac{\sigma h'(\eta)}{\sqrt{Re_{\theta}}}\right]$$
**4.49**

It is now instructive to evaluate the right hand side of this expression for a given point in the shear layer, say,  $\eta=0$ . The first two bracketed terms are found to be 8.7 and 50.0 respectively. The values of  $h'(\eta)=-0.06$  and  $\sigma=0.035$  allow this expression to be written as

$$C_{w\omega_y} - C_{v\omega_z} = -0.91(Re_{\theta})^{-1/2}$$
 4.50

For example, at the streamwise location  $x/\theta_0=675$ ,  $Re_\theta=121,000$ , the left hand side of eqn. (4.50)  $C_{w\omega_y}-C_{v\omega_z}=-0.0026$ . The difference between these correlation coefficients is therefore very small, which helps to clarify the "balance" of the terms in equation 4.46. Specifically, the vortical motions which lead to the existence of the Reynolds stress gradient is not necessarily due to the lateral fluctuations of spanwise vorticity alone. Rather, it

is a very close balance between very large fluctuations of spanwise (z) vorticity component moving in the lateral (y) direction, and similar spanwise movement (z) of the lateral component of vorticity (y).

The values of  $C_{w\omega_y}$  and  $C_{v\omega_z}$  can be determined experimentally since the time series data used to calculate vorticity includes a measurement of the cross stream velocity component. These data are shown in Figure 4.29. The measured values, for the left hand side of 4.50, show a difference between the correlation coefficient that is of order 400 times larger than the right hand side of equation 4.50. It is apparent that the measured correlations cannot be measured with the required accuracy to observe the balance of equation 4.46.

### 4.5 Turbulent Kinetic Energy

The turbulent kinetic energy (TKE) equation is examined in detail in this section. This is of interest both for theoretical and modeling considerations. It is noted that Wygnanski and Fiedler (1970) previously constructed a budget for the TKE for the single stream shear layer at a single streamwise location. The purpose of the present repetition of this work is based on the higher Reynolds number, increased spatial resolution, and improved experimental capabilities of the present experiment. This has permitted the measurement of nearly all the terms in the TKE actuation, with particular emphasis on the measurement of the kinetic energy dissipation. This work was similar in scope to that of Liu (2000) who measured nearly all of the terms in the TKE budget for a wake flow with various pressure gradients.

The time averaged turbulent kinetic energy is defined as:

$$k = \frac{1}{2} \overline{u'_i u'_i}$$
 4.51

The time averaged transport of k can be stated as:

$$\frac{Dk}{Dt} = -\frac{\partial}{\partial x_i} \left[ u'_i \left( \frac{p'}{\rho} + k \right) + v u_j \left( \frac{\partial u'_i}{\partial x_j} + \frac{\partial u'_j}{\partial x_i} \right) \right] - \overline{u'_i u'_j} \frac{\partial n_j}{\partial x_i} - v \left( \frac{\partial u'_i}{\partial x_j} + \frac{\partial u'_j}{\partial x_i} \right) \frac{\partial u'_j}{\partial x_i} \quad \textbf{4.52}$$
(I) (II) (IV) (V) (VI)

The derivation of this equation is given in, for example, Hinze (1975). Each of the terms of the equation can be identified as follows. The left side of the equation (I) represents the time averaged material derivative of turbulent energy, usually termed the "convection" of energy given that  $\partial k/\partial t = 0$ . Terms (II) and (IV) represent the net work rate resulting from pressure fluctuations and viscous diffusion, respectively. Term (III) is the convective transport of k by turbulent motion., Terms II, III and IV are collectively referred to as the

the "diffusion" of turbulent energy. The next term (V) is the production of turbulent energy since the same term with opposite sign exists in the energy balance equation for the time averaged variables. Lastly, term (VI) represents the viscous dissipation of TKE. The measurement of the convection, diffusion, and production terms are relatively straight forward, and will be discussed in Section 4.5.2. The estimate of the dissipation term, however, presents a considerable challenge. It is therefore described independently in the following section.

# 4.5.1 Dissipation Measurements.

The dissipation is treated separately due to the difficulty of the measurement and its importance in both the energy balance of equation (4.52) and the scaling of turbulence quantities treated in following sections.

As shown in Pope (2000), the dissipation can be expanded as:

$$\varepsilon = 2\nu \overline{s_{ij}s_{ij}} = \nu \left( \frac{\partial u_i \partial u_i}{\partial x_j \partial x_j} + \frac{\partial u_i \partial u_j}{\partial x_j \partial x_i} \right) = \varepsilon + \nu \frac{\partial^2 \overline{u_i u_j}}{\partial x_i \partial x_j}$$
**4.53**

where  $\varepsilon$  is the "pseudo-dissipation". The last term of equation 4.53 is proportional to the spatial curvature of the Reynolds stresses, and is usually considered to be negligible in free shear flows. Therefore, as with most literature, the distinction between  $\varepsilon$  and  $\varepsilon$  is not made, and the approximation  $\varepsilon = v \left( \frac{\partial u_i \partial u_i}{\partial x_i \partial x_i} \right)$  is assumed to be valid.

In Cartesian coordinates the dissipation can be expanded as nine derivatives of the fluctuating velocity components as:

$$\frac{\varepsilon}{v} = \left(\frac{\partial u}{\partial x}\right)^2 + \left(\frac{\partial u}{\partial y}\right)^2 + \left(\frac{\partial u}{\partial z}\right)^2 + \left(\frac{\partial u}{\partial z}\right)^2 + \left(\frac{\partial v}{\partial x}\right)^2 + \left(\frac{\partial v}{\partial z}\right)^2 + \left(\frac{\partial w}{\partial z}\right$$

The direct measurement of all nine terms with adequate spatial resolution is difficult, and rarely attempted. Dissipation is typically estimated by using a set of assumptions about the relations between the different derivatives. Alternatively, dissipation can be estimated by assuming a specific form of the one dimensional spectral density of the velocity fluctuations.

The measurements of the velocity gradient statistics described in Section 4.2 as well as the one dimensional velocity spectra were used to estimate the dissipation using a variety of assumptions. The methods and assumptions for these calculations are given in the following paragraphs. Note that each type of estimate is given a capital letter that will be used as a subscript for  $\varepsilon$  in order to clarify which estimate is being discussed. The various estimates were calculated for the spatial location:  $x/\theta_0$ =675,  $\eta$ =0 for comparison; these results are summarized in Table 4.2.

The most common method used to obtain  $\varepsilon$  is to assume that the velocity fluctuations and their derivatives are isotropic. With this assumption, the relationships among the terms in equation 4.54 leads to the approximation:

$$\varepsilon = 15\nu \left(\frac{\partial u'}{\partial x}\right)^2$$
 4.55

The streamwise derivative variance can be calculated from the Taylor microscale using equation 4.24, as discussed in Section 4.2.3. The lateral component of velocity  $\mathbf{v}'(t)$  can be used to define the transverse Taylor microscale  $\lambda_g$ . In isotropic turbulence this is related to the streamwise microscale by:

$$\lambda_{v} = \lambda_{u} / \sqrt{2}$$

Two independent estimates of the dissipation can be calculated based on equation 4.55:

$$\varepsilon_A = 30v \frac{\overline{u'^2}}{\lambda_u^2}, \qquad \qquad 4.57$$

and

$$\varepsilon_B = 15 v \frac{\overline{u'^2}}{\lambda_v^2}.$$
 4.58

The use of Taylor's hypothesis is explicit in the calculation of  $\lambda_u$  and  $\lambda_v$  in these expressions, and can be corrected according to equations 4.25 and 4.26. These are shown in Table 4.2 as  $\epsilon_A^{\ TC}$  and  $\epsilon_B^{\ TC}$  where the superscript TC indicates Taylor Correction.

In homogeneous, isotropic turbulence, the dissipation can be directly related to the spanwise vorticity by

$$\varepsilon_C = 3v\tilde{\omega}_z^2$$
.

This was calculated using the variance of the spanwise vorticity as described in Section 4.3.

The next group of estimates attempt to measure several of the terms of equation 4.54 with assumptions that are less stringent than perfect isotropy. These are referred to as the "semi-isotropic" relationships. The first assumption is that of "axisymmetric turbulence" as discussed in Section 4.1.3. There are a number of equivalent expressions that can be written for the dissipation based on these assumptions. One possible expression that is easily estimated experimentally was derived in George and Hussein (1991):

$$\varepsilon_D = \mathbf{v} \left[ \frac{5}{3} \left( \frac{\partial u'}{\partial x} \right)^2 + 2 \left( \frac{\partial u'}{\partial z} \right)^2 + 2 \left( \frac{\partial v'}{\partial x} \right)^2 + \frac{8}{3} \left( \frac{\partial v'}{\partial z} \right)^2 \right].$$
 **4.60**

The techniques to measure all of the terms in this expression were described in Section 4.1.3.

A "semi-isotropic" approximation of  $\varepsilon$ , as given by equation (14) of Browne et al. (1987), is given by:

$$\varepsilon_E = 3v \left[ \left( \frac{\partial u'}{\partial x} \right)^2 + 2 \left( \frac{\partial u'}{\partial y} \right)^2 + \left( \frac{\partial u'}{\partial z} \right)^2 \right]$$
 4.61

A different semi-isotropic formulation was given by Wygnanski and Fiedler (1969):

$$\varepsilon_F = 3v \left[ \overline{\left( \frac{\partial u'}{\partial x} \right)^2} \left( 1 + 4K_1 \right) + 2 \overline{\left( \frac{\partial u'}{\partial y} \right)^2} \left( 2 + \frac{1}{2K_1} \right) \right]$$
 4.62

where  $K_1$  is given by equation 4.36.

Wygnanski and Fiedler (1970) used a semi-isotropic calculation that imposed the condition:

$$\overline{\left(\frac{\partial v}{\partial v}\right)^2} = \overline{\left(\frac{\partial v}{\partial z}\right)^2} = \overline{\left(\frac{\partial w}{\partial v}\right)^2} = \overline{\left(\frac{\partial w}{\partial z}\right)^2} = \overline{\left(\frac{\partial w}{\partial z}\right)^2}$$
**4.63**

where only the last of these terms is measured. The estimate then takes the form:

$$\varepsilon_G = \nu \left[ \frac{\partial u^2}{\partial x} + \frac{\partial u^2}{\partial y} + \frac{\partial u^2}{\partial z} + \frac{\partial u^2}{\partial z} + \frac{\partial u^2}{\partial x} + 5 \frac{\partial u^2}{\partial x} \right].$$
 4.64

The next two approximations to the dissipation are indirect methods. These assume that the spectral content of the velocity signal is assumed to have a universal form, from which the dissipation can be estimated. The first of these methods, assumes that the one dimensional spectrum of the velocity fluctuations satisfies the relationship:

$$E_{11}(k_1) = C\varepsilon^{2/3}k_1^{-5/3} . 4.65$$

over a certain range of  $k_1$ . In order for this relation to be a useful method of estimating the dissipation, the "universal constant", C must indeed be universal. Sreenivasan (1995) addressed this issue using data from a wide variety of flow geometries and Reynolds numbers. For each data set, the dissipation was established using equation 4.57. The conclu-

sion from this reference is that no perceivable dependence of C on Reynolds number or flow geometry can be observed. The mean value was found to be 0.53, with a standard deviation of 0.055. In the discussion of these results, Sreenivasan also noted that equation 4.57 always under predicts the true dissipation, indicating that the true value of C is likely closer to 0.50. Although this topic is still under consideration, the available evidence supports the idea that C truly is a constant at high enough Reynolds numbers, and that the scatter in the observed values of C are likely a result of errors in the estimate of  $\varepsilon$ , and errors in the measurement of  $E_{11}$  due to Taylor's hypothesis.

Based on equation 4.65, the dissipation can be written in terms of the compensated spectra:

$$\varepsilon_H = (2 \cdot k_1^{5/3} E_{11}(k_1))^{3/2}$$
.

This assumes C=0.5, and is only valid in the inertial range of the spectra. The conpensated spectra is plotted versus the normalized wave number  $k_1\eta_K$ ; see Figure 4.30 for the spatial location ( $x/\theta_0$ =675,  $\eta$ =0). The data indicated roughly 2 decades where the compensated spectra is relatively close to a constant value. The mean value taken from the range  $6 \times 10^{-4} < k_1\eta_K < 6 \times 10^{-2}$  was found to be 1.9 (m<sup>2</sup>/s<sup>3</sup>).

The assumption of isotropy also leads to a unique relation for the third order longintudinal structure function (see, e.g., Landau and Lifshitz, 1987):

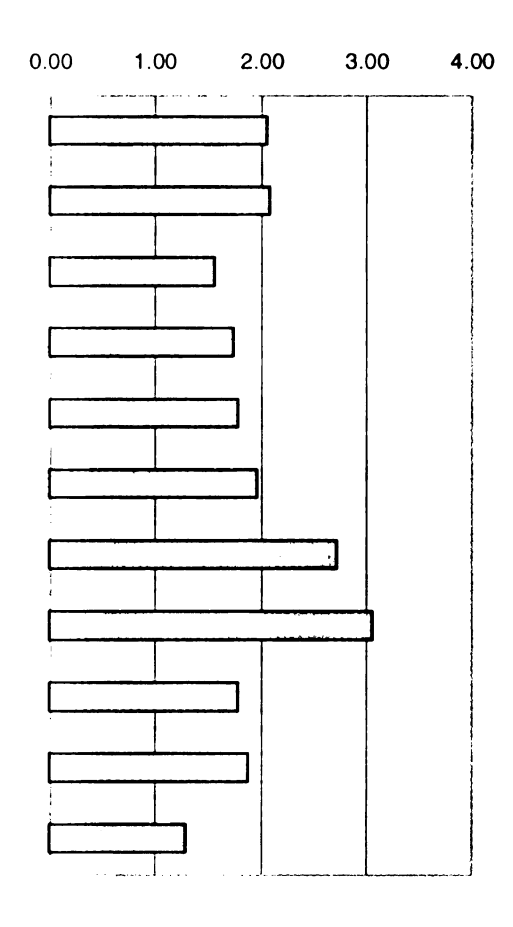
$$D_{111}(r_1) = \overline{\left[u'(x+r_1) - u'(x)\right]^3} = -\frac{4}{5}\varepsilon_1 r_1$$
 4.67

The interesting feature of this equation is that there is no arbitrary constant. The measurement of dissipation is then only a matter of achieving a high enough Reynolds number such that the compensated structure function  $D_{111}$  is constant over a wide enough range of

r/ $\eta$ . The compensated structure function for the present velocity field shown in Figure 4.31. This exhibits a relatively constant value near  $\epsilon_1$ =1.30 over the range 10<r/r/ $\eta_K$ <200.

**Table 4.2: Dissipation estimates** 

	equation #	value(m <sup>2</sup> /s <sup>3</sup> )
$\epsilon_{A}$	4.57	2.06
$\epsilon_{\mathrm{B}}$	4.58	2.09
$\epsilon_A^{TC}$	4.57, 4.24	1.57
$\varepsilon_B^{TC}$	4.58, 4.25	1.76
$\epsilon_{\mathrm{C}}$	4.59	1.79
$\epsilon_{\mathrm{D}}$	4.60	1.98
$\epsilon_{ m E}$	4.61	2.73
$\epsilon_{ extsf{F}}$	4.62	3.06
$\epsilon_{ m G}$	4.64	1.79
$\epsilon_{H}$	4.66	1.8
$\epsilon_{ m I}$	4.67	1.3



It is observed from the results summarized in Table 4.2 that the different methods of calculation lead to results which can differ quite widely. The mean value of these measurements is 1.99, with a standard deviation of 0.503. The estimate  $\varepsilon_F$  was nearly two standard deviations above the mean of the population, indicating that this is likely a poor method of estimating  $\varepsilon$ . Similarly, the estimate  $\varepsilon_I$  was far below the mean. Saddoughi and Veeravalli (1994) also found that using the third order structure function led to an underestimate of the dissipation. If the minimum ( $\varepsilon_I$ ) and maximum ( $\varepsilon_F$ ) are excluded, then the mean value is 1.95, with a standard deviation of 0.33. Although this does not provide a definitive cal-

culation of the true dissipation, it does provide insight into the variability introduced by the various approximations that are often used in the calculation of  $\varepsilon$ .

The profile  $\varepsilon(\eta)$  was calculated for four of the estimates described above ( $\varepsilon_B^{TC}$ ,  $\varepsilon_D$ ,  $\varepsilon_E$ , and  $\varepsilon_G$ ) at the location  $x/\theta_o$ =675; see Figure 4.32. This example shows that the relative magnitudes of the estimates is consistent across the shear layer. For example, the ratio of  $\varepsilon_E$  to  $\varepsilon_B$  was found to be in the range 1.6< $\varepsilon_E/\varepsilon_B$ <2.06.

# 4.5.2 Measurement of Kinetic Energy Budget

The terms of the kinetic energy budget of equation 4.52 will be described in this section. It is assumed that the flow is stationary  $(\partial(\cdot)/\partial t = 0)$ , and homogeneous in the spanwise direction (w = 0),  $(\partial(\cdot)/\partial z = 0)$ . Also, the viscous diffusion of energy is typically very small compared to the other terms, and will be ignored. Equation 4.52 can be re-written as:

$$0 = \left[ u \frac{\partial k}{\partial x} + v \frac{\partial k}{\partial y} \right] - \left[ \frac{\partial}{\partial x} \left( u' \frac{p'}{\rho} \right) + \frac{\partial}{\partial y} \left( v' \frac{p'}{\rho} \right) \right]$$

$$+ \left[ \frac{\partial}{\partial x^2} \left( u'^3 + u' v'^2 + u' w'^2 \right) + \frac{\partial}{\partial y^2} \left( u'^2 v' + v'^3 + v' w'^2 \right) \right]$$

$$- \left[ \left( u'^2 - \overline{v'}^2 \right) \frac{\partial \overline{u}}{\partial x} + \overline{u' v'} \left( \frac{\partial \overline{u}}{\partial y} + \frac{\partial \overline{v}}{\partial x} \right) \right] - \varepsilon$$

$$4.68$$

The four terms in square brackets represent the convection, pressure transport, diffusion, and production of turbulent kinetic energy, respectively. These terms have been computed, and are shown in Figure 4.33 for the streamwise locations  $x/\theta_0=384$  and 675. The mean velocity components were taken from Figures 4.4 and 4.5. The velocity-velocity correlations were calculated directly from the time series velocity data described in Section 4.1.

Lateral (y) derivatives were evaluated by fitting a smooth curve through the data. Streamwise derivatives were evaluated using:

$$\frac{\partial(\ )}{\partial x} = \frac{\partial(\ )}{\partial \eta} \frac{\partial \eta}{\partial x}$$
**4.69**

assuming self similar flow development and equation 4.17 for  $\partial \eta / \partial x$ . The dissipation was calculated using the axisymmetric relationship, equation 4.60.

The pressure transport term was calculated from equation 4.68. The term therefore also contains any residual errors from the measured terms. It is observed that the profiles of the pressure transport term exhibit quite small magnitudes, and an irregular shape which does not have a consistent pattern from the two streamwise locations. It is reasonable to assume that the pressure transport is quite small, and the magnitude of the observed values are mostly a result of the residual measurement errors. The small magnitude of the values also gives confidence to the accuracy of the directly measured terms.

The data shown in Figure 4.33 have been normalized by  $\theta/U_o^3$ . The agreement between the two downstream locations is satisfactory for all the measured terms. The data also compare quite well with the results of Wygnanski and Fiedler (1970), referred to as WF. Note that this reference uses a coordinate system in which positive  $\eta$  values are on the low speed side of the shear layer. The profiles of the measured values are very similar in shape between the present measurements and WF  $Re \approx 21000$ . As an example of the comparison between WF and the present data, the ratio of the peak value of the production to the peak value of dissipation was found to be 1.82 in the present data compared to 1.88 in WF. However, both the diffusion and convection terms were somewhat smaller in the present measurements, although the general shape of the curves was the same as WF.

### 4.6 The Scales of Turbulent Motion

The length and time scales of the fluid motions within the shear layer are discussed in this section. This view of the experimental data will be instructive with regards to the dynamics of the flow field. That is, the previous sections reported on the stochastic properties of the velocity and vorticity fields related to the pdf of the measurements without regards to the temporal and spatial scales which led to the observations. A more complete understanding of the fluid motions can be obtained through the study of the length and time scales of the flow. To this end, various data sets have been acquired that will be presented in the following sub-sections. First, Section 4.6.1 describes the correlation field of the shear layer. This will include both single point autocorrelations as well as multi-point cross-correlations of the velocity and vorticity fields. Section 4.6.2 will discuss the Fourier transform of the correlation functions, i.e., the spectra. Although the information contained in the correlations and the spectra are equivalent, different insights can be inferred from these two representations of the data. Specifically, the correlation measurements lend themselves towards the understanding of the large scale motions of the flow. For example, the zero crossing points and integral of the correlations are readily obtained from the correlations. The spectral representation of the velocity and vorticity show the contributions of the various wave numbers (i.e., length scales). In addition, hypotheses about the universal scaling of the small scale motions of the flow can most easily be observed and tested using the spectral representation.

### 4.6.1 Correlation measurements of velocity and vorticity

The correlation coefficient is defined as:

$$R_{ab}(\Delta \dot{\bar{x}}) = \frac{\overline{a(\dot{\bar{x}})b(\dot{\bar{x}} + \Delta \dot{\bar{x}})}}{a\bar{b}},$$
**4.70**

where a and b represent any two signals of interest. The spatial separation vector between the points of interest  $\Delta \hat{x}$  can be created using multiple sensors, or approximated using a single sensor with a time delay and suitable convection velocity.

The discussion of the correlation field will begin with single point measurements of the streamwise component of velocity. The separation variable used in this correlation was created using a time delay, which can be considered to be either a dimensionless time variable  $(t^*)$  or a dimensionless spatial coordinate  $(\Delta x/\theta)$ :

The use of the convection velocity  $U_c=U_0/2$  in the definition (4.71) (rather than the local

$$t^* = \Delta t \left(\frac{U_o}{2\theta}\right) = \frac{\Delta t \cdot U_c}{\theta} = \frac{\Delta x}{\theta}$$

mean velocity, for example) is used to represent the convection speed of the large scale motions of the shear layer. As discussed in Chapter 3, the convection velocity of the large scale motions was found to be  $U_0/2$  throughout the self-similar region of the shear layer. The autocorrelation  $R_{uu}(t^*)$  is shown in Figure 4.34 for three positions representing the high speed, center, and low speed regions of the shear layer. Data from both streamwise locations ( $x/\theta_0=384$  and 675) are shown for comparison. These data indicate that the correlation function also exhibits self-similarity. Figure 4.35 presents the same data on semi-log coordinates to show the detailed behavior at small  $t^*$ . Note that all curves approach zero correlation values at a value of  $t^*\approx20$ . This indicates that the large scale motion that are responsible for the relatively long correlation times of the velocity scale with the local momentum thickness. This result is consistent with previous research in

both single and two stream shear layers. For example, Browand and Trout (1985) calculated the autocorrelation of the velocity in the high speed side of a moderate Reynolds number two stream shear layer. Their results are nearly identical to the  $\eta$ =3.1 data shown in Figure 4.34. Specifically, the "undershoot" in their measurements was found to be roughly -0.5, after which the correlation approached zero. Koochesfahani et al. (1979) presents similar results, with an undershoot of -0.58 occurring at t\*≈8. The present data indicate a minimum correlation of -0.43 at t\*≈6.

Similar autocorrelation results were reported by Dimotakis and Brown (1976) for a two stream shear layer at a similar Reynolds number ( $\Delta U \theta / \nu \approx 10^5$ ) to the present measurements. In this reference, considerable attention is paid to the interpretation of the relatively long correlation times observed in the high speed stream. In particular, they defined the time delay to the first peak in the autocorrelation to be  $\tau_0$  and then define a length scale  $\lambda_{\nu}$  as:

$$\lambda_{v} = \tau_{o} U_{c}$$
 4.72

where  $U_c=U_o/2$  represents the convection velocity of the large scale motions of the flow. This is interpreted to be the average spacing between the large scale motions of the flow. This length scale can be made dimensionless using the local value of the vorticity thickness  $(\delta_\omega)$  which was defined as:

$$\frac{1}{\delta_{\omega}} = \left(\frac{1}{U_o} \cdot \frac{\partial u}{\partial y}\right)_{max}.$$

Dimotakis and Brown (1976) found the normalized  $\tau_0$  values to be in the range 3.1< $\lambda_v$ / $\delta_{\omega}$ <5.0, with a mean value of roughly 3.8. In the present measurements, the values were found to be in the range 3.2< $\lambda_v$ / $\delta_{\omega}$ <4.5. Koochesfahani et al. (1979), obtained a mean

value of 3.9 for  $\lambda_v/\delta_\omega$ . Note that the numerical calculations of Moore and Saffman (1975) predict a value of 3.5 based on the idea that a vortex can be "torn apart" by the strain field of nearby vortices.

The autocorrelations of the three components of velocity at the center of the shear layer are shown in Figure 4.36. From these data it is observed that the v and w components exhibit smaller correlations at smaller separations. This is made quantitative by comparing the Taylor microscale for each of the components. The values of  $\lambda_{uu}/\lambda_{vv}=1.43$ , and  $\lambda_{uu}/\lambda_{ww}$ = 1.49 were recovered from the data presented in Figure 4.36. These values compare quite well with the value of  $\sqrt{2} \approx 1.41$  that would be obtained in isotropic turbulence. The spatial correlation of velocity across the shear layer was also of interest. For this purpose, two single hot-wire probes were positioned locations  $y_a$  and  $y_b$ , with spacing  $(y_a-y_b)/$  $\theta$ =3.27. The velocity measured by the probe closest to the high speed side of the shear layer is denoted u<sub>a</sub>, and the velocity from the probe closer to the low speed side is u<sub>b</sub>. The time series data were acquired at a rate of 3,000Hz for 300 seconds, at the streamwise location  $x/\theta_0$ =529. The probes were then traversed across the shear layer with the fixed separation in the y direction. The time delayed cross correlation results are shown for five of these positions in Figures 4.37 through 4.41.

These data clearly reveal characteristics of the large scale motions. The long correlation times are evident as with the autocorrelation. The peak magnitude of the correlations in all of these figures was found to be of order 0.1 or higher. This magnitude is significant given the large separation between the probes. The asymmetric shape of the correlation function is quite evident. This has been considered previously in the experiments of Pui and Gart-

shore (1979), where time delayed cross correlation data in a moderate Reynolds number two stream shear layer were obtained. The results shown in Figure 9 of that reference are similar to those shown in Figures 4.37 and 4.38. It was argued that the positive values obtained at negative time delay, followed by the negative correlation at positive time delay were caused by large scale motions which are "tilted" at an angle with respect to the streamwise direction. If the coherent motions were perfectly round, the resulting cross correlation would be symmetric with a negative minimum occurring at zero time delay. The feature of the correlation function was observed in the time series data of a very low Reynolds number two stream shear layer; see Koochesfahani et al. (1979). If the large scale motions were tilted towards the high speed side, then the correlation measurements would shift towards positive time delay, as is indicated in the data. It is of interest to note that the correlations in Figures 4.37 and 4.38 are shifted such that the zero time delay results show a nearly zero correlation value. In terms of trigonometric functions, this would represent a "quarter-wave" shift between the two signals. The signals appear to be shifted by a "half-wave" in Figures 4.39 through 4.41. Further evidence that the tilted orientation of the large scale motions is a universal feature of shear layers was also given by the conditionally averaged measurements of Browand and Weidman (1976) in a two stream shear layer, and Hussain and Zaman (1985) in a single stream shear layer.

The proceeding results have commented on the temporal or quasi-streamwise correlations, and then on the lateral correlations of the velocity field. The next set of measurements will focus on the spanwise correlation field. Surprisingly, very few attempts have been made to document the spanwise organization of shear layers given that many references discuss the two-dimensionality of the large scale motions as a ubiquitous feature of the these flows

without making any out of plane measurements. A notable exception is that of Brownand and Trout (1980, 1985). As discussed already in Chapter 3, these two papers present the results of a 12 wire rake of sensors in the irrotational flow adjacent to a low Reynolds number two stream shear layer. They found that the spanwise correlation, measured in this way, led to spanwise length scales of order 20 times the local shear layer thickness. The inference from these measurements, was that the large scale motions approximate two dimensional disturbances. They do not, however, report on the spanwise correlation of the velocity in the active portion of the shear layer.

The streamwise development of the spanwise correlation field near the separation point was discussed in Chapter 3; see Figures 3.30 through 3.39. These results will be extended to the fully developed region in this section. The experiments were conducted using a rake of 8 straight wire sensors spaced in the spanwise direction. The rake was traversed across the shear layer at  $x/\theta_0=101$  with a maximum spanwise separation of 3.30, and at  $x/\theta_0=675$  with a maximum separation of 40. The downstream measurements were only executed for  $\eta>-1.8$  due to limitations with the traversing mechanism. These data were acquired for 300 seconds at a rate of 3000Hz.

The spanwise correlation of velocity is shown in Figures 4.42 and 4.43. The dimensionless data show excellent agreement between the two streamwise locations indicating that this statistic scales in self-similar coordinates. Several observations can be made from these figures. First, the two dimensionality of the flow in both the high and low speed regions is evident from the high correlation values, in agreement with the Browand and Trout (1980, 1985) results. For example, for  $\eta>3.5$  the correlation is 0.9 or larger for  $0<\Delta z/\theta<4$ . In contrast, in the central region of the shear layer the correlation falls quickly to zero at a span-

wise displacement of roughly 1.50. Note that the contours of constant correlation value are nearly horizontal in these figures in the range -1.5< $\eta$ <1.5. In other words, the scales of motion shown in this way are homogeneous in the y-direction in the central region of the shear layer. Given the long time scales provided by the autocorrelations of velocity at  $\eta$ =0, the magnitude of the lateral velocity correlations, and the two dimensional nature exhibited near the edges of the shear layer, one might expect that the spanwise correlation would indicate a high level of coherence over large spanwise lengths. Figures 4.42 and 4.43 are very instructive in this regard, in showing the very limited (~1.50) length of the spanwise correlation in the central region of the shear layer.

The focus of the discussion and data presentation thus far has been on the velocity field. The remainder of this section will discuss correlations of the vorticity field. Section 4.2 already described many aspects of the vorticity measurements, including examples of time series and profiles of the root-mean-square of the fluctuations. The following will explore the temporal and spatial aspects of vorticity. This is particularly important given the common interpretation of the large scale motions as "vortical structures" (see, for example, Thomas (1991), Dimotakis and Brown (1976), or Browand and Trout (1985)). These interpretations are typically made without regards to any measurements of the vorticity itself. Note that Hussain and Zaman (1985) and Browand and Weidman (1976) use the curl of a conditionally averaged velocity field to represent the "coherent vorticity". This is, in principal, quite different from the direct measurement of vorticity.

The autocorrelation of the vorticity components  $\omega_y$  and  $\omega_z$  are shown in Figure 4.44 at the location  $\eta$ =0, for both streamwise locations,  $x/\theta_o$ =384 and 675. The same data are also shown in Figure 4.45 in semilog format to show the detail of the correlation at small  $t^*$ 

values. In both of these figures the velocity autocorrelation from  $x/\theta_0$ =675 has been included for reference. The data show agreement for the two streamwise locations with both components of vorticity approaching zero correlation at  $t^*\approx 2.5$ . Note that the vorticity autocorrelation falls much faster than the velocity correlation, indicating the importance of the small scales of the vorticity.

A closer view of the zero crossing region is shown in Figure 4.46. Note that there is a small (0.04), but significant, region of negative correlation values. This "undershoot" then returns to a zero value at  $t^*\approx 10$ . When interpreted as a spatial distance ( $\Delta x/\theta$ ),  $t^*\approx 10$  corresponds to a vorticity correlation of nearly twice the shear layer thickness. Although the correlation is extremely small ( $|R_{\omega\omega}(t^*)| < 0.05$ ) in the range 2.5<t\*<10, this still represents a significant result in that the vorticity field is represented by motions of a wide range of scales. This is clearly important in the consideration of the large scale "structures" of the flow, which are considered to be related to the "phase correlated vorticity", see Hussain (1983). Further discussion will be considered in Section 4.8.

In addition to the autocorrelation of the vorticity, the spanwise correlation of  $\omega_z$  was also measured using two vorticity probes separated in the spanwise direction at  $\eta$ =0. These data are shown in Figure 4.47 along with the autocorrelation results for comparison. It is interesting that the spanwise correlation of vorticity is nearly identical in magnitude to the autocorrelation. This is in contrast to the velocity measurements where the spanwise correlation at  $\eta$ =0 approached zero at a much smaller length scale (~1.50) than did the autocorrelation (~60).

A final measurement related to the correlation field of the shear layer was created using a single hot-wire sensor in the high speed region of the flow ( $\eta$ =3.5), and a vorticity sensor in the center of the shear layer ( $\eta$ =0). The purpose of this measurement was to observe the correlation between the large amplitude irrotational fluctuations which occur in the high speed region, and the time series of spanwise vorticity. This correlation is shown in Figure 4.48. These data confirm that there is a measurable correlation between the irrotational fluctuations observed outside of the shear layer and the highly unsteady vorticity field. The asymmetric correlation data are also consistent with the concept of large scale motions which are "tilted" towards the high speed side. Further conclusions that can be drawn from these data are discussed in Section 4.8.

# 4.6.2 Spectral representation of velocity and vorticity

The spectral representation of the fluid motions are discussed in this section. The scaling of the small scales of motion are most easily examined from this viewpoint. The most important and complete theoretical understanding of the small scales of motion are given by Kolmogorov (1941), and subsequent refinements. The K41 theory, as it is often called, assumes that there exists a range of turbulent length scales that are not effected by the large scale motions of the flow, and therefore can be considered locally (in wave number space) isotropic. When the assumptions of homogeneous and isotropic turbulence is made, many predictions can be made about the behavior and scaling of the small scale motions; see, for example, Batchelor (1965) and Pope (2000).

There is a large number of research papers in the literature that are devoted to the experimental determination of the accuracy of the predictions that follow from the K41 theory.

Although a review of this literature is not the intent of this work, it suffices to note that the present experimental conditions provide a unique opportunity to compare the shear layer to several previously published results. For example, most of the flow fields which have been used for testing the K41 theory are decaying grid turbulence, the outer regions of a boundary layer, or a wake flow; see Sreenivasan and Antonia (1997) for a review. The shear layer is distinguished from these flows, and in some sense provides a closer approximation to the flows in many engineering applications given the well organized large scale motions which were discussed in the previous section.

The present discussion will begin with the formulation of a model spectrum. The model proposed by Pope (2000) will be used and compared with the various measured spectra in this section. The model is defined to be:

$$E(\kappa) = \left[C\varepsilon^{2/3}\kappa^{-5/3}\right] f_L(\kappa L) f_n(\kappa \eta_{\kappa})$$
 4.74

where  $\kappa$  is the wave number in three dimensional wave number space. The "universal equilibrium" is represented by the function in square brackets, where C=1.5 represents the universal constant. The value of  $\eta_K = \varepsilon^{1/4} v^{3/4} = 0.20 mm$  was found using the dissipation value ( $\varepsilon_B$ ) obtained from equation 4.58 at the location  $\eta$ =0,  $x/\theta_0$ =675. The functions  $f_L$  and  $f_\eta$  are given by:

$$f_L(\kappa L) = \left(\frac{\kappa L}{\sqrt{\kappa L^2 + c_L}}\right)^{\frac{11}{3}}$$
4.75

and

$$f_{\eta}(\kappa\eta_{K}) = \exp\left\{\beta c_{\eta} - \beta \left[\left(\kappa\eta_{K}\right)^{4} + c_{\eta}^{4}\right]^{1/4}\right\}.$$
 4.76

These are effectively curve fits to the large and smallest scale motions respectively. The value of  $c_L$ =6.78 was used as suggested by Pope. The value of L represents the integral, or largest scale of motion, and it is specified in terms of the ratio to the Kolmogorov length scale:  $L/\eta_k$ . This ratio was selected to provide the best agreement between equation 4.75 and the large scale portion of the spectra, using the measured  $E_{11}$  spectra as described below. The resulting L value of  $L = 6000 \cdot \eta_k$  is roughly equal to the shear layer width of 1.2m at  $x/\theta_0$ =675.

The values  $\beta$ =5.2,  $c_{\eta}$ =0 were suggested by Saddoughi and Veeravalli (1994) in their measurements of the spectra in a high Reynolds number boundary layer. Pope (2000) suggested  $\beta$ =2.1,  $c_{\eta}$ =0.4. The high wave number end of the present spectrum was fitted using values of  $\beta$ =5.2,  $c_{\eta}$ =0.33.

The modeled one dimensional energy spectra can be calculated from  $E(\kappa)$  from the isotropic relation:

$$E_{uu}(\kappa_1) = \int_{\kappa_1}^{\infty} \frac{E(\kappa)}{\kappa} \left[ 1 - \left(\frac{\kappa_1}{\kappa}\right)^2 \right] d\kappa$$
 4.77

The experimentally obtained spectrum  $E_{uu}(\kappa_1)$  was obtained by taking the twice the Fourier transform of the auto-correlation  $R_{uu}$  (see, for example, Bendat and Piersol (1986)). The wave number magnitude was calculated from the temporal frequency from  $\kappa_1 = 2\pi f/\bar{u}$ . These data are shown for the location  $\eta$ =0,  $\chi/\theta_0$ =675 along with the model spectra on Figure 4.49. The agreement is quite good for a large range of  $(\kappa_1\eta_K)$ . Given that Pope (2000) used this model spectrum to represent data from a wide range of Reynolds number and flow conditions, it is assumed that the one dimensional streamwise

velocity spectra does indeed have a universal form. Note that the differences observed at very high wave number are assumed to be caused by anemometer noise.

The one dimensional model spectrum of the v and w velocity components were also calculated. This is given in terms  $E(\kappa)$  by the isotropic relation:

$$E_{vv}(\kappa_1) = E_{ww}(\kappa_1) = \frac{1}{2} \int_{\kappa}^{\infty} \frac{E(\kappa)}{\kappa} \left[ 1 + \left( \frac{\kappa_1}{\kappa} \right)^2 \right] d\kappa$$
 4.78

The measured and model spectra for  $E_{vv}$  and  $E_{ww}$  are shown in Figures 4.50 and 4.51 respectively. The agreement is quite good for a wide range of wave numbers. This implies that the assumptions which led to equation 4.78, namely, homogeneous and isotropic turbulence, are reasonable in the description of the velocity spectra. Note that, as with all experimental verification of isotropic turbulence, equations 4.77 and 4.78 are necessary, but not sufficient to show that the flow actually exhibits local isotropy.

In addition to the auto-spectral density, the cross spectral density (CSD) is also of interest.

The normalized (CSD) is defined as the coherence function:

$$H_{uv}(\kappa_1 \eta_K) = \frac{\left| P_{uv} \right|^2}{E_{uu} \cdot E_{vv}}$$
 4.79

where  $P_{uv}$  is the twice the (complex) Fourier transform of the cross correlation  $R_{uv}$ . In truly isotropic flow, the coherence function  $H_{uv}(\kappa_1\eta_K)=0$  for all wave numbers. Since  $\overline{u'v'}\neq 0$  in the shear layer,  $H_{uv}$  must also be nonzero at some wave numbers. Figure 4.52 shows the coherence function at  $\eta=0$ ,  $x/\theta_0=675$ . These data indicate that nonzero coherence is present for  $\kappa_1\eta_K<0.01$ , and nearly zero values were obtained for  $\kappa_1\eta_K>0.01$ . This result is reasonable, and suggests that correlations between u and v are significant only at low wave number, and that local isotropy is supported for higher wave number.

Note that the coherence is more sensitive to anisotropy than is the auto-spectral density, since the auto-spectra  $E_{vv}$  and  $E_{ww}$  are both reasonably well approximated by the isotropic relation 4.78 over the entire range of the spectrum.

In addition to the auto and cross spectrum of velocity components, the vorticity spectra can also be computed from the experimental measurements. Antonia et al. (1987) derived the isotropic relationship between the one dimensional vorticity spectra and the energy spectra:

$$\phi_{\omega_{\varepsilon}}(\kappa_{1}) = \frac{\kappa_{1}}{2} \int_{\kappa_{1}}^{\infty} \frac{E(\kappa)}{\kappa} d\kappa + \frac{1}{4} \int_{\kappa_{1}}^{\infty} \frac{E(\kappa)}{\kappa} [\kappa^{2} + \kappa_{1}^{2}] d\kappa.$$
 4.80

The model spectrum (equation 4.74) was used to calculate what the vorticity spectra would be in an isotropic flow. This, along with the experimentally determined spectra of  $\omega_z$  are shown in Figure 4.53. These data are remarkable in that they are not similar to the isotropic prediction in any way. There is considerably less energy in the high wave number range, and considerably more energy at low wave numbers than that predicted by equation 4.80. This result is especially interesting given the excellent agreement between the measured and isotropic vorticity spectra shown in the boundary layer of the present facility shown in Chapter 3. Antonia et al. (1998) also found very good agreement between equation 4.80 and the directly measured vorticity spectra for grid turbulence, and Antonia et al. (1987 and 1996) found the similar results in wake flow. Ong and Wallace (1995) found the same in their boundary layer measurements.

A notable difference between the boundary layer and wake flow studies and the present measurements in the free shear layer which created the spectra shown in Figure 4.53 is the existence of the organized large scale motions of the flow. The relative contribution of the

different scales of motion to the vorticity variance can be observed by plotting the compensated spectra:  $k_1 \varphi_\omega$  in semilog format:

$$\overline{(\omega_z')^2} = \int_0^\infty \phi_{\omega_z}(\kappa_1) \ d\kappa_1 = \int_0^\infty \kappa_1 \cdot \phi_{\omega_z}(\kappa_1) \ d(\ln(\kappa_1))$$
 4.81

The integrand of the second right hand side  $(\kappa_1, \phi_{\omega}, \kappa_1)$  is plotted in Figure 4.54. It can be observed from this figure that a large portion of the integral contribution is from the low wave number range of the spectra.

# **4.7 Circulation Density**

A distinctive feature of the shear layer flow field is the existence of the large scale motions. Many previous research efforts have attempted to determine the nature of these motions, with the hope that an improved understanding of orderly structure may lead to improved turbulence modeling and control. The previous sections have described the results of single and multi-point measurements in the shear layer, which support the existence of these large scale motions. In particular, the scales of the velocity correlations (Figure 4.34), the temporal and spanwise coherence of the vorticity (Figure 4.47), and the velocity-vorticity correlation shown in Figure 4.48 all indicate that motions of relatively large length scales are an important part of the shear layer dynamics.

The large scale motions of a shear layer are often referred to as vortical or vortex motions, or coherent structures in the literature; see, for example, the review article by Thomas (1991). However, information about these motions is generally limited to information derived from two sources: flow visualization, and measurements in the irrotational fluid near the active shear layer. For example, the studies by Dimotakis and Brown (1976), Winant and Browand (1974), and Hileman and Samimy (2001) use results of flow visualization images to obtain information about the structure of the shear layer. The measured irrotational velocity fluctuations were used by Browand and Trout (1980, 1985). Both of these techniques were also used in the present observations which described the large scale motions of the near separation region in Chapter 3. However, these measurements do not easily quantify the importance of the large scale motions, and, could lead to significant misinterpretations about the flow field. As an example of the possible misinterpretations, Hama (1962) has shown that even an infinitesimal disturbance to an otherwise uniform

thin sheet of vorticity will produce streaklines that "roll-up" into what appear to be large scale vortices. Hama concludes with a comment about flow visualization data in which images of streakline patterns are recorded. He states that "practically no truth can be obtained as to the nature of time-dependent phenomena and that images, which one might receive from such observations, can be entirely misleading".

A technique for extracting information about the coherent motions of the shear layer not mentioned above is conditional averaging; see, e.g., Browand and Weidman (1976), and Hussain and Zaman (1985). Its application by these authors has made use of a trigger signal from the irrotational flow outside the active shear layer along with measurements of u and v in the shear layer. The velocity field is then averaged using points which satisfy a certain condition for the trigger signal. This technique is instructive, and supports the existence of large scale motions. Since only a fraction of the total time series of velocity (which corresponds to a specific event in the trigger signal) is used in the averaging process, conditional averages do not provide a complete description of the flow field at all times.

This preamble is to establish the author's motivation to obtain a measure of the "coherent structures" of the shear layer which is both quantitative, useful, and representative of the characteristics of the flow. Specifically, it is recognized that they to not simply seek to characterize a "conditional event." The *circulation density* ( $\gamma$ ) of the shear layer is proposed as an alternative response to this motivation. The circulation density is defined as the integral of the spanwise vorticity along a line perpendicular to the streamwise direction made dimensionless with  $U_0$ :

$$\gamma = \frac{1}{U_o} \int_{-\infty}^{\infty} \omega_z \, dy = -1 + \int_{-\infty}^{\infty} \frac{\partial (v/U_o)}{\partial x} dy$$
 4.82

That is,  $\gamma$  represents the "circulation per unit length." In general,  $\gamma$  can be a function of x, z, and t, since only the y dependence of vorticity has been integrated. However, note that a constant free stream velocity requires that the time average value of the integral on the right side of equation 4.82 at a given (x,z) location must be essentially zero, given that  $\partial(\bar{v}/U_o)/\partial x \ll 1$ . That is,  $\bar{\gamma} = -1$ .

In order to gain a better physical interpretation of the circulation density, schematic examples of  $\gamma$  in several stages of a temporal (y-t) shear layer are shown in Figure 4.55. In the first example, a uniform sheet of vorticity is shown in gray, with a corresponding constant value of  $\gamma$ =-1. The pdf of an experimentally determined population of  $\gamma$  values might look like a very narrow Gaussian distribution, with a variance corresponding to the uncertainty of the measurement.

The second example shows the case of a laminar shear layer undergoing a two-dimensional linear instability. The vorticity field during the linear and nonlinear stages of growth have been studied in detail both numerically (see, e.g., Pozrikidis and Higdon (1985)) and analytically (see, e.g., Michalke (1965)). During the linear stages of growth,  $\gamma$  has a sinusoidal shape with increasing amplitude. A measured pdf of  $\gamma$  for this case would be "double humped."

The third example represents the condition in which the coherent motions roll up into discrete vortex motions with a Gaussian core of vorticity. In this case, regions of nearly irro-

tational motion will exist between these motions as shown. A measured pdf of  $\gamma$  would have a local maximum near  $\gamma$ =0, and a second peak located at  $\gamma$ <-1.

These idealized examples illustrate that information about the circulation density in the turbulent shear layer will be instructive with regards to the large scale dynamics. Ideally, time series of  $\gamma$  at multiple (x,z) locations would permit a full characterization of the circulation field. However, experimental limitations do not permit such difficult measurements. In the present experiments, the pdf of  $\gamma$  at a single (x,z) location was acquired. Although far from complete, this does provide a significant amount of previously unavailable information. For example, if the large scale motions of the flow are comprised of regions of rotating fluid which exist between regions of relatively small circulation, then the pdf of  $\gamma$ would look something like that which is shown in Figure 4.55c. Note that this result assumes that each coherent motion contains the same net circulation. If coherent motions were to exist with a wide range of circulation values, then the histogram would be considerably wider, which could lead to a histogram of  $\gamma$  values that is no longer double peaked. As a final example, if no large scale motions exist and the turbulent fluctuations distribute the vorticity more evenly, then the pdf would show few realizations far from the mean value of -1.

The only reference to the circulation density of a turbulent shear layer in the literature is found in the direct numerical simulation (DNS) of a (y-t) shear layer by Rogers and Moser (1994). A similar definition as equation 4.82 is given, although they ignore the mean value, such that only the fluctuations:  $\gamma$  are considered. However, no information about  $\gamma$  is provided except to say "variations [in  $\gamma$ ] are still dominated by small scales." They then apply an arbitrary two dimensional spatial filter in the streamwise and spanwise directions

"to extra

that larg

Howev

examp!

4.7.1 E

The cir

nents o

4.56. T

size as:

The ve

(PIV)

EA1.(

of the

strear

The:

was '

tion

ure 4

Henc

been

"to extract the large-scale behavior." This "roller parameter" ( $\Re$ ) is successful in the sense that large scale quasi-two dimensional regions with  $\Re$ <0 are visible in the computed data. However, significant spatial smoothing is required in order to observe this structure. For example, it would be difficult, and of limited use, to derive a transport equation for ( $\Re$ ).

## 4.7.1 Experimental Configuration

The circulation density was experimentally determined by acquiring the u and v components of velocity along a narrow rectangular region. This is shown schematically in Figure 4.56. The integration defined in equation 4.82 is modified to account for the finite domain size as:

$$\gamma = \frac{\Gamma}{U_o \Delta x} = \frac{1}{U_o \Delta x} \oint (\vec{V} \cdot d\vec{s})$$
**4.83**

The velocity field was measured using a two camera digital particle image velocemetry (PIV) system. The equipment was a Dantec 2000 processor, with 1k x 1k Kodak Megaplus EA1.0 cameras, and a New Wave Research Minilase 3, ND: Yag laser. The configuration of the equipment is shown schematically in Figure 4.57. The primary and entrainment streams were both seeded using two Roskco 1600 smoke generators.

The streamwise location of the measurement was  $x/\theta_o=170$ . The momentum thickness was 71mm at this location. The 313mm extent of the integration area in the lateral direction was centered such that the range -2.21< $\eta$ <2.21 was measured. As observed from Figure 4.4, this corresponds to a range of mean velocity values equal to  $0.11 < \bar{u}/U_o < 0.94$ . Hence, 83% of the mean vorticity is captured in the field of view. Although it would have been preferable to capture a larger percentage of the total shear layer for the calculation,

order for farther promiss

The date mately which consider for farther promise the farther promise the farther promise the farther promise the farther for farther promise the farther prom

expec ity pr

data s

by th

The

of th

mea

usec

abilj

Sure

The

shov

this would have required moving the apparatus closer to the separation point. However, in order for the present results to be representative of a fully developed shear layer, locations farther downstream are preferred. The location  $x/\theta_0=170$  was chosen as a reasonable compromise between these two constraints.

The data were acquired in six groups of measurements. Each group contained approximately 100 data sets. The total number of PIV vector maps acquired was 615. The rate at which the images were acquired was 0.5Hz. At this data rate, each evaluation of  $\gamma$  can be considered to be statistically independent.

## 4.7.2 Circulation Density Results

The magnitude of the circulation density was calculated from each of the acquired 615 data sets. The mean value was found to be  $\bar{\gamma}=-0.84$ . This corresponds well to the expected value of -0.83 based on the extent of the interrogation area and the mean velocity profile. Since the true mean value of  $\gamma$  should be -1, the measured values were scaled by the factor 1.19. The histogram of the scaled measured values is shown in Figure 4.58. The RMS of the distribution was computed to be  $\tilde{\gamma}=0.57$ . The third and fourth moments of the distribution, were 0.19 and 3.55 respectively. A Gaussian distribution with the same mean and RMS is also shown in the figure. Note that because the scaling factor (1.19) was used, this only represents an approximation to the true  $\gamma$  distribution. Specifically, the variability of the net circulation which occurred at the edges of the shear layer was not measured.

The observed histogram of  $\gamma$  is instructive when compared to the model shear layers shown in Figure 4.55. That is, the nearly Gaussian probability distribution indicates that

the large scale motions do not fully collect the vorticity into large scale motions as in the low Reynolds number shear layer as studied by (Koochesfahani et al., 2000). This conclusion is drawn from the relatively rare occurrence of  $\gamma$  values near zero. However, the large standard deviation of the histogram suggests that the vorticity is very nonuniformly distributed in space. If these large excursions in  $\gamma$  were spatially correlated, this could lead to the observed streakline patterns in flow visualization studies. Further comment will be added in the conclusions section.

#### 4.8 Conclusions

This section presents conclusions that are based on the data and analysis that were presented in the previous sections of this chapter. These conclusions are presented in a numbered format, followed by a discussion of relevant data and examples which support each conclusion. These have not been listed in a particular order, although the discussion will reference previously given arguments when possible.

1. Rotating the coordinate system such that the x axis is aligned with the centroid of vorticity provides an alternative formulation of the mean flow variables. In these coordinates, a net mass flux of fluid across the surface which represents the centroid of vorticity can be observed.

The derivation of the equations in both tilted and untilted coordinates has been given in Section 4.2. It is noted that any coordinate system can be formally correct. However, if the standard "untilted" coordinates are to be used, the movement of the shear layer centroid away from the x axis must be explicitly accounted for in the formulation of the self-similar equations. The coordinate rotation provides a different viewpoint of the velocity field. This has only a negligible effect on the mean streamwise component of velocity, or the moments of the fluctuating velocity vector. However, this rotation has a significant effect on the boundary conditions and the shape of the mean lateral component of velocity:  $(\bar{\mathbf{v}})$ . It was observed in Figure 4.5 that  $\bar{\mathbf{v}} > 0$  for all  $\eta$  in the rotated coordinates as introduced in Section 4.2. That is, a positive mass flux exists across any surface parallel to the  $\hat{x}$  axis, which supports the second statement of the conclusion given above. Note that the surface representing the centroid of vorticity is given by  $\hat{\eta} = 0$ , where  $g(\hat{\eta}) = 0.375$ . It is inter-

esting to contrast this result with the observation that mass cannot cross a time steady sheet of vorticity. That is, the unsteady character of the vorticity field must be taken into account in order to explain this conclusion about the mean flow variables.

It would also be of interest to extend this result to two stream shear layers. For example, the flow visualization results of Brown and Roshko (1974) clearly indicate the movement of the shear layer towards the low speed side. This movement, as well as the angle of the bounding wall, which defines the low speed entrainment rate in a two stream shear layer, could then be correlated to the shear layer growth rate.

2. The flow field is three dimensional in nature, as illustrated by the spatio/temporal velocity and vorticity correlation fields. However, a volume integral of the vorticity can be written which is two dimensional.

The length scales of the shear layer can be divided into three general categories for the purpose of the following discussion. In the turbulence literature these are usually termed the energy containing, inertial, and dissipation length scales. Conclusions regarding the nature of the inertial and the dissipative scales will be given later in this section. The large scales of motion are of primary interest because they contain a large fraction of the turbulent kinetic energy. They are responsible for the majority of the material and momentum transport. In contrast to the small scales, it is considerably more difficult to develop strong conclusions about the nature of the large scale of the fluid motions.

The present conclusion and discussion examines the large scale motions through the spatial correlation of velocity and vorticity. An interesting summary of these correlations is obtained by observing the spatial separation required for the first zero crossing of the cor-

relations acquired at  $\eta$ =0. These results are tabulated in Table 4.3. These data show some relative agreement that indicates that the large scale motions are correlated over a length scale of order 2.50 both in the streamwise and spanwise directions.

The exception to this result is the autocorrelation of the streamwise velocity ( $R_{uu}(t^*)$ ) which exhibits longer correlation times. It is thought that this is due to the use of the time delay variable rather than a true spatial correlation. That is, the large scale motions have a temporal correlation which is quite long (sometimes referred to as "quasi-periodic") which leads to the long correlation time of the streamwise component of velocity. Further support for this observation can be drawn from the comparison of ( $R_{uu}(t^*)$ ) at the locations  $\eta=0$  with those acquired in the high and low speed irrotational flow; see Figure 4.34. Specifically, the correlations decrease towards zeto approximately the same rate (e.g.,  $|R_{uu}(t^*)| < 0.05$  for  $t^*>22$ ).

A distinct point of contrast can be made when these results are compared to the spanwise correlation of velocity obtained in the irrotational flow in both the high and low speed sides of the shear layer; see Figures 4.42 and 4.43. These data indicate high (>0.9) correlation values over length scales of order of the shear layer thickness. This is in close agreement with the results of Browand and Trout (1980, 1985) in which correlation lengths of order 200 were observed in a lower Reynolds number two stream shear layer. The interpretation of the large scale motions as "two-dimensional" structures can be explored from these results. The term two-dimensional implies  $\partial(\cdot)/\partial z = 0$  as a necessary condition. However, the measurements of velocity gradients shown in Section 4.2 as well as the vor-

ticity measurements in Section 4.3 have shown that the smallest scales of motion exhibit many of the properties of homogeneous and isotropic turbulence.

It is therefore instructive to examine what is two-dimensional in the shear layer. The approximation  $\partial u(t)_{(|\eta| > 3.2)}/\partial z \approx 0$  has been shown from the correlation measurements shown in Figures 4.42 and 4.43. This velocity can be written in terms of the vorticity in the shear layer as:

$$\vec{u}(\eta > 3.2) = \frac{1}{4\pi} \iiint \left(\frac{\vec{\omega} \times \vec{r}}{r^3}\right) (dx)(dy)(dz)$$
**4.84**

where the limits of integration are given by the bounding walls of the facility. The derivative of this expression can be take with respect to the z direction to give:

$$\frac{\partial u}{\partial z} = \frac{\partial}{\partial z} \frac{1}{4\pi} \iiint \left( \frac{\vec{\omega} \times \vec{r}}{r^3} \right) (dx)(dy)(dz) = 0.$$
 4.85

That is, the volume integral of the vorticity field expressed in equation 4.84 is two dimensional, even though the vorticity itself is highly three dimensional. That is, it is the integral properties of the vorticity field which lead to the observations of two dimensional motions.

Table 4.3: Summary of zero crossing points of correlation functions acquired at  $\eta$ =0.

Correlation	Location of first R=0 condition
$R_{uu}(t^*)$	4.89
$R_{vv}(t^*)$	2.97
$R_{ww}(t^*)$	2.84
$R_{\omega,\omega_{\cdot}}(t^*)$	2.35
$R_{\omega,\omega_{\bullet}}(t^*)$	2.40
$R_{\omega,\omega}(\Delta z/\theta)$	2.0
$R_{uu}(\Delta z/\theta)$	1.56

3. The histogram of circulation density values indicates that the description of the large scale motions of the flow may be more accurately stated as fluctuations in the circulation density, rather than "structures" or "vortices".

Considerable research has been devoted to the characterization and understanding of the large scale motions of shear layers. Observations from both flow visualization and velocity measurements in the irrotational flow adjacent to the shear layer have been used to infer the properties of the large scale motions. For example Brown and Roshko (1971) used a shadowgraph technique to investigate the large scale structure of a two stream shear layer. Since then, significant research efforts have focused on the characterization, prediction, and control of these motions (see Thomas (1991) for a review). These results often lead to an idealized conceptual picture of the velocity/vorticity fields which exist in high Reynolds number shear layers.

The circulation density measurements provide informatino about how the vorticity is distributed within large scale motions of the flow. For example, the pdf of  $\gamma$  is nearly Gaussian, and not double peaked. The relatively large standard deviation of  $\gamma$  values measured indicates that considerable variability exists in the motions which convect past a given streamwise location. Also, the occurrence of  $\gamma$ =0 is observed to be a fairly rare occurrence. These results are not inconsistent with the observations of the large correlation lengths observed in the velocity and vorticity data. These latter observations suggest that the fluctuations in the circulation density also have a significant correlation in both space and time. The suggested spatial correlation of the circulation density is consistent with the flow visualization results of Brown and Roshko (1971), and Dimatokis and Brown (1976).

That is, spatially correlated fluctuations in  $\gamma$  could lead to the observed "roll-up". Future research would be needed to confirm this statement. Conclusion 3 above states that this perspective of the large scale motions may be more useful than the generalization of the flow field as containing coherent structures or vortices.

4. The energy spectra have been found to be well represented by a model spectrum, and the assumptions of local isotropy. In contrast, the vorticity spectra do not appear to be even qualitatively similar to the predicted spectra using the same assumptions.

The conclusion regarding the velocity spectra is apparent from Figures 4.49 through 4.52. The model spectrum provides a close representation of the  $E_{11}(k_1)$  data. Assuming both homogeneous and isotropic turbulence, the model spectrum also represents both  $E_{22}$  and E<sub>33</sub> quite well. This is especially notable at the lowest wave numbers where the fluid motions are clearly non-isotropic. The H<sub>12</sub> data (see Figure 4.52) however, are more discriminating in that  $k_1\eta > .01$  is required for local isotropy to be approximately valid. Given these results, it is quite striking that the vorticity spectra cannot be predicted by local isotropy predictions as shown in Figure 4.53. Note that the one dimensional spectrum of vorticity in an isotropic flow does not have a log-linear region as does the energy spectrum. Rather, the one dimensional spectra "flattens out" as shown, leading to decreased contribution from the small wave numbers. In isotropic turbulence the enstrophy spectra also represents the dissipation spectra. It is consistent with K41 theory that small wave numbers would have minimal contribution to the enstrophy. However, the anisotropy of the large scale motions of the flow have led to vorticity correlations which

are non-zero over a large spatial extent indicating that the vorticity spectra contains significant contributions from the low wave number range.

The fact that the vorticity spectra does have a log-linear region with slope of  $k^{-1}$  is also of interest. This is because the compensated spectra  $(k_1 \varphi_\omega)$  shown in Figure 4.54 is relatively constant over a wide rage of wave numbers. This implies that the relatively large scales also cause a significant contribution to the vorticity fluctuations. This is in contrast to the homogeneous-isotropic result where the vorticity and dissipation spectra are related only by viscosity, and the dissipation spectra obtains the majority of the contributions from the high wave number range.

5. The stochastic values of the velocity, velocity fluctuations, and velocity gradient fluctuations scale in a self similar manner, whereas the vorticity fluctuations increase with increasing Reynolds number.

It is recognized that exact self-similarity cannot be achieved in a shear layer. This is because the ratio of the smallest length scales to the largest length scales is a function of Reynolds number. By scaling the dissipation with  $U_o^3/\theta$ , the ratio of the integral to Kolmogorov scales is found to be  $\theta/\eta_K \sim Re^{3/4}$ . Stochastic quantities which scale only with the integral scales of motion (that is, have no dependence on  $\eta_K$ ) will exhibit self-similar scaling. Similarly, variables which depend only on the Kolmogorov length scales, with no explicit dependence on the integral scales of motions will also scale in a self-similar way. It will be shown in the following discussion that the vorticity fluctuations depend both on  $\theta$  and on  $\eta_K$ , and that this leads to a direct dependence on the Reynolds number.

The spectral representation of the vorticity field exhibits a log-linear region with a slope  $\phi_{\omega_z} \sim k^{-1}$ . This can be observed by the roughly constant value observed in the compensated spectra shown in Figure 4.54. The dimensionless variance of the vorticity fluctuations can be expressed as the integral of the spectral density:

$$\overline{(\omega_z')^2} = \int_0^\infty (\phi_\omega) \ d(k_1 \eta_K) = \int_{k_1 \eta_K = \eta_K \neq 0}^{k_1 \eta_K = 1} (k_1 \phi_\omega) \ d[\log(k_1 \eta_K)]$$
 **4.86**

In the right hand expression, the limits of integration are modified to account for the observation that there is little or no contribution to the integral at scales larger than the integral scales of the flow, nor is there a substantial contribution from scales smaller than the Kolmogorov length scale. The Reynolds number dependence of the vorticity variance can now be concluded from the observation that the ratio of largest to smallest length scales varies as  $\mathrm{Re}^{3/4}$ ; see, for example, Pope (2000). Therefore the integrand  $(k_1 \phi_{\omega})$  is roughly constant, and the lower limit of integration decreases with increasing Reynolds number as observed in Figure 4.54. Therefore, the value of the integral increases with increasing Reynolds number.

The maximum values of the vorticity RMS measured at  $\eta$ =0,  $x/\theta_0$ =384 and 675 support this conclusion; see Figures 4.24 and 4.25. Additional support has been found by compiling the vorticity measurements of several authors in other shear layer facilities. These include Bruns (1990), Lang (1985), Loucks (1998), and Balint and Wallace (1988). These data are summarized in Figure 4.59. Each of the data sets reported (where more than one streamwise location was measured) indicates an increase in the dimensionless vorticity RMS with increasing Reynolds number. The compilation of all these data also support the

conclusion. The scatter observed between the different data sets is larger than that which would be expected from the uncertainty calculations of the individual measurements. This most likely represents the effects of the different boundary conditions of these studies, such as velocity ratio and the state of the boundary layer at separation.

 The pdf of vorticity is highly insensitive to Reynolds number, but quite sensitive to the level of intermittency.

This conclusion was drawn from the comparison of the histogram of observed vorticity values obtained for the following flow conditions: a cylinder wake at  $Re_{\lambda}$ =60 (Antonia et al. (1988)), DNS calculations of isotropic turbulence at  $Re_{\lambda}$ =216 (Cao et al. (1996)), shear layer measurements in the range 411< $Re_{\lambda u}$ <1210 (Figure 4.21), and near wall boundary layer measurements at  $Re_{\lambda u}$ =2500 (Figure 4.23). In all these measurements, the intermittency was above 95%. That is, turbulent fluid occupied the measurement volume more than 95% of the time.

The similarities between these histograms is striking given the 40:1 range in Reynolds number and differences in the boundary conditions. The specific features include an asymmetric "hump" in the range of small vorticity fluctuations, and long "tails" which extend several standard deviations in both directions. These tails can be characterized by the distribution:

$$P(\omega') \sim \exp\left(-\beta \left(\frac{|\omega'|}{\tilde{\omega}}\right)^n\right)$$
 4.87

where the exponent n characterizes the curvature of the distribution when shown in semilog coordinates, and  $\beta$  is a fitted constant. For example, n=2 for a Gaussian distribution, and n=1 for an exponential distribution. A least squares curve fit of equation 4.87 to the shear layer measurements gives  $n=0.95\pm0.04$ . Antonia et al. (1988) do not report a value for n, although visual observations of their data indicate  $n\approx1$ .

A distinctive feature that is observed in the data shown in Figure 4.23 is the concave-up nature of the tail region of the histogram. The fit of equation 4.87 to these measurements gives n=0.95±0.04. Three possible reasons are suggested to account for this observation: Reynolds number effects, near wall effect, or probe resolution. The latter reflects the condition that the ratio of the probe dimensions to the Kolmogorov length scale of the flow was 2:1 in the boundary layer measurements, compared to 6:1 in the shear layer data. The relatively large size of the probe in the shear layer measurements will lead to spatial averaging that could cause the exponent to be underestimated. This explanation is further supported by the calculations of Cao et al. (1996). Specifically, they plot the exponent (n) as a function of the length scale of the domain over which the circulation is calculated. The results indicate n=0.7 for very small (highly resolved) circulation domains, and a monotonic increase to n=2 for domains of the order of the inertial scales of turbulent motion.

7. The relative magnitudes observed between the velocity gradient variances, the vorticity, and the dissipation indicate that the assumptions of axisymmetric turbulence may provide a more accurate description of the flow than does isotropic turbulence.

This conclusion supports the findings of Hussein and George (1991). Specifically, Figures 4.16 and 4.17 indicate that the  $K_1 \approx K_2$ , and  $K_3 \approx K_4$ .

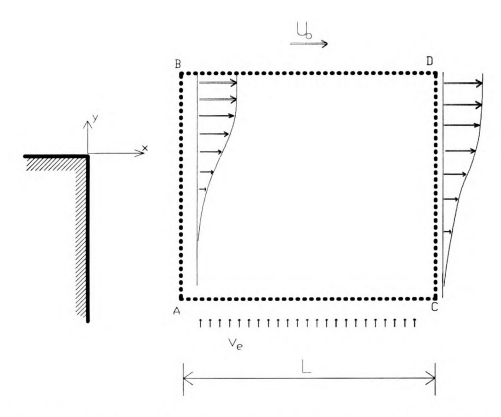


Figure 4.1 Schematic of control volume and coordinate system used in Section 4.1. Note that the growth rate is not shown to scale.

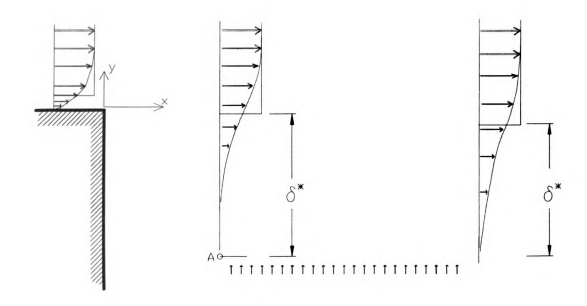


Figure 4.2 Illustration of the physical interpretation of  $\delta^*$  in the boundary and shear layer

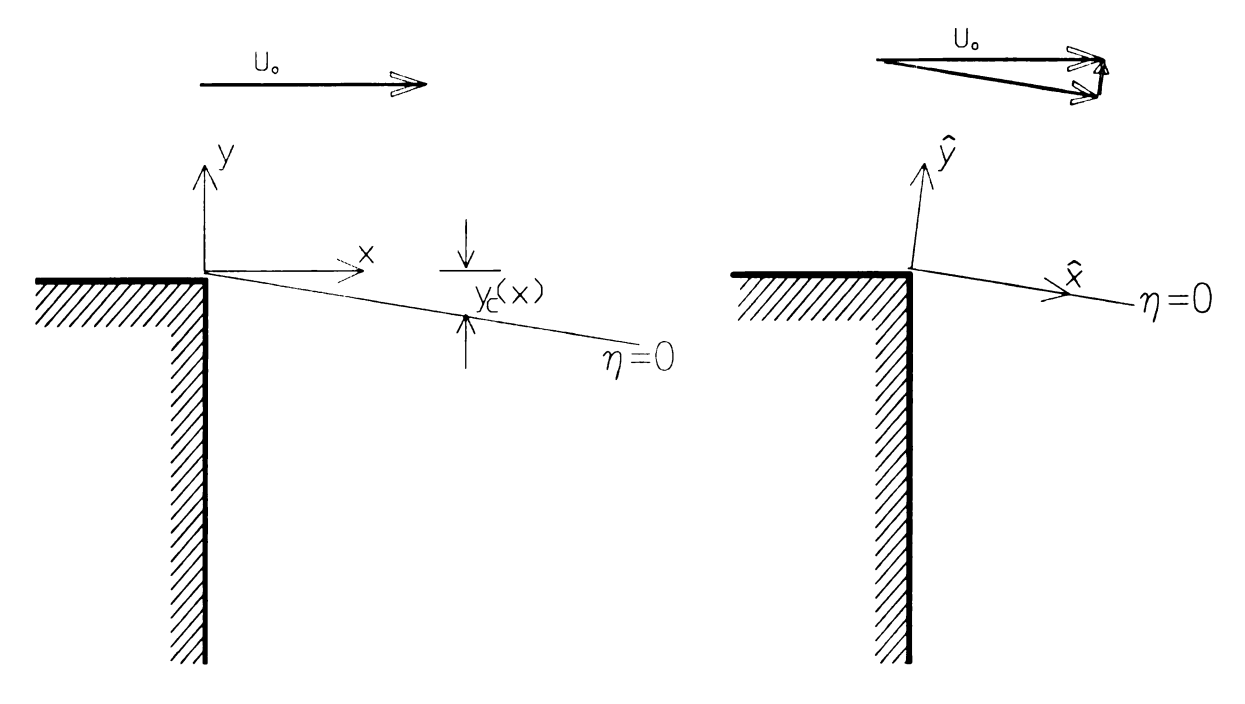


Figure 4.3 Schematic of the un-tilted coordinates (left and the tilted coordinates (right) for use in similarity analysis

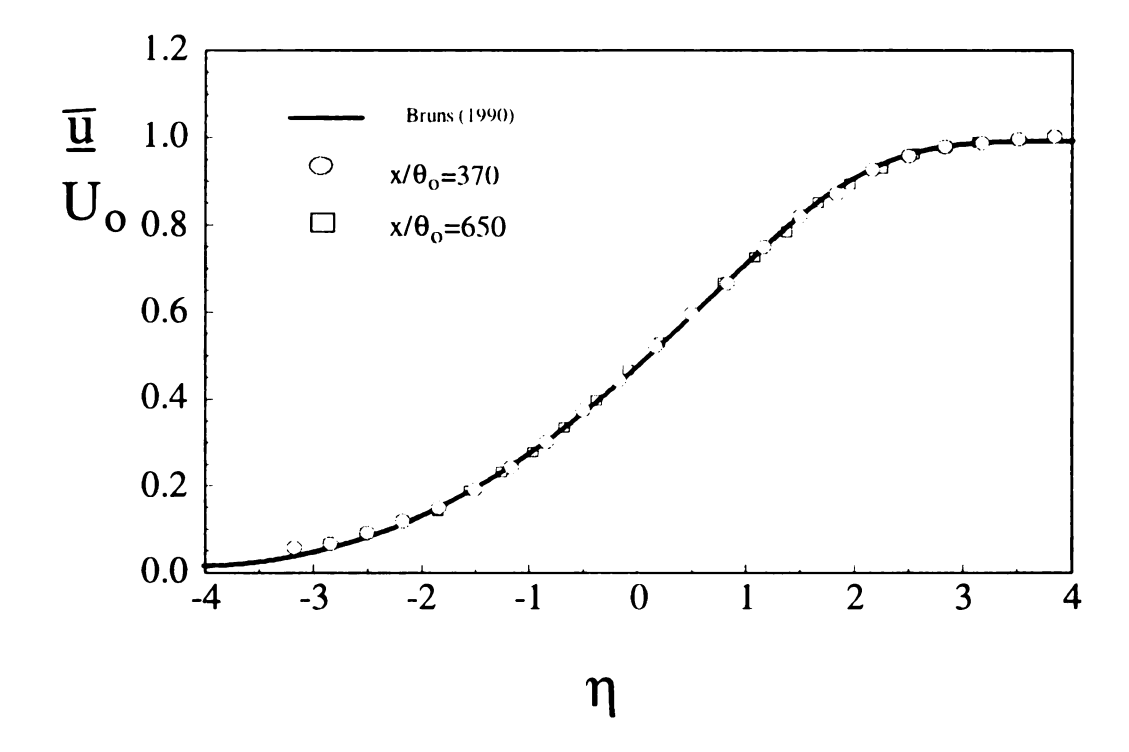


Figure 4.4 Streamwise mean velocity  $f(\eta)$ 

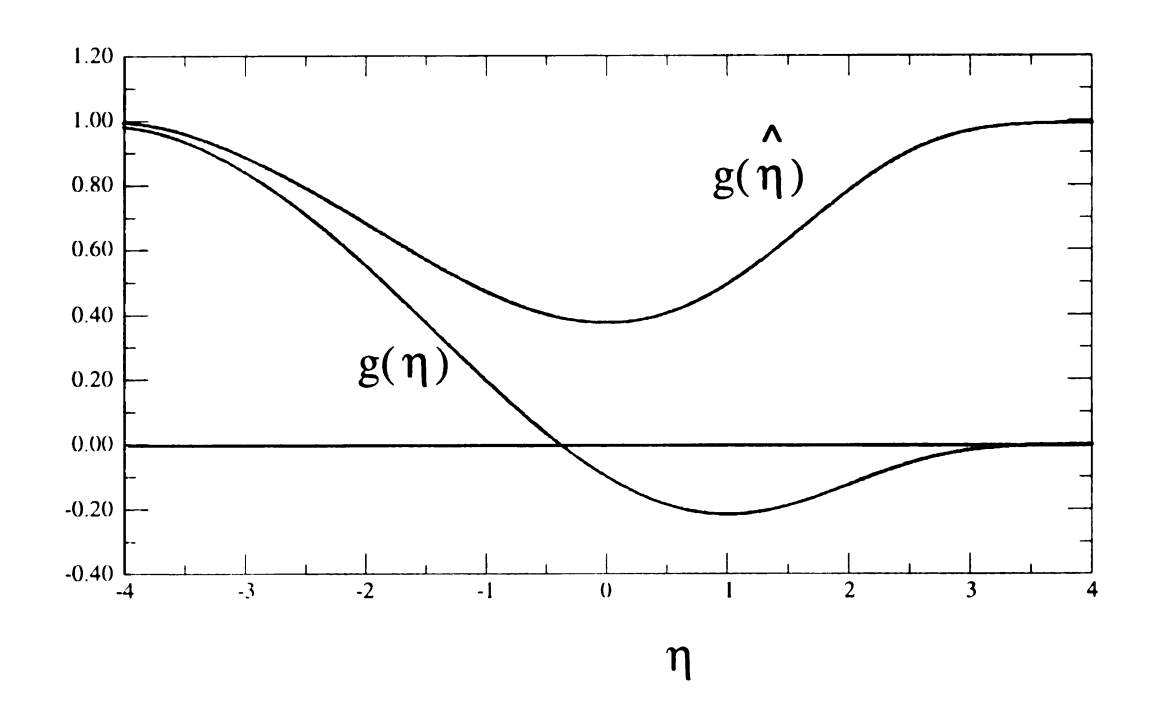


Figure 4.5 Lateral mean velocity:  $g(\eta)$  in tilted and untilted coordinates.

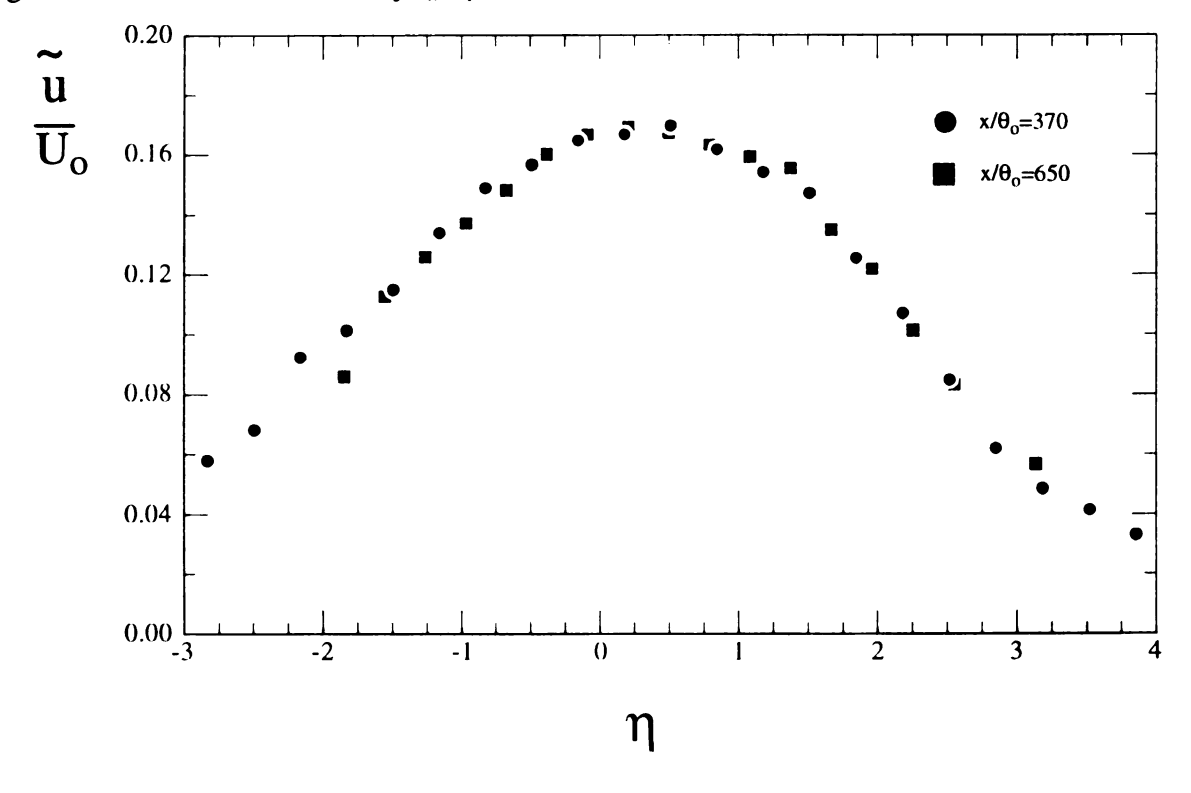


Figure 4.6 Root mean square of the streamwise velocity fluctuations

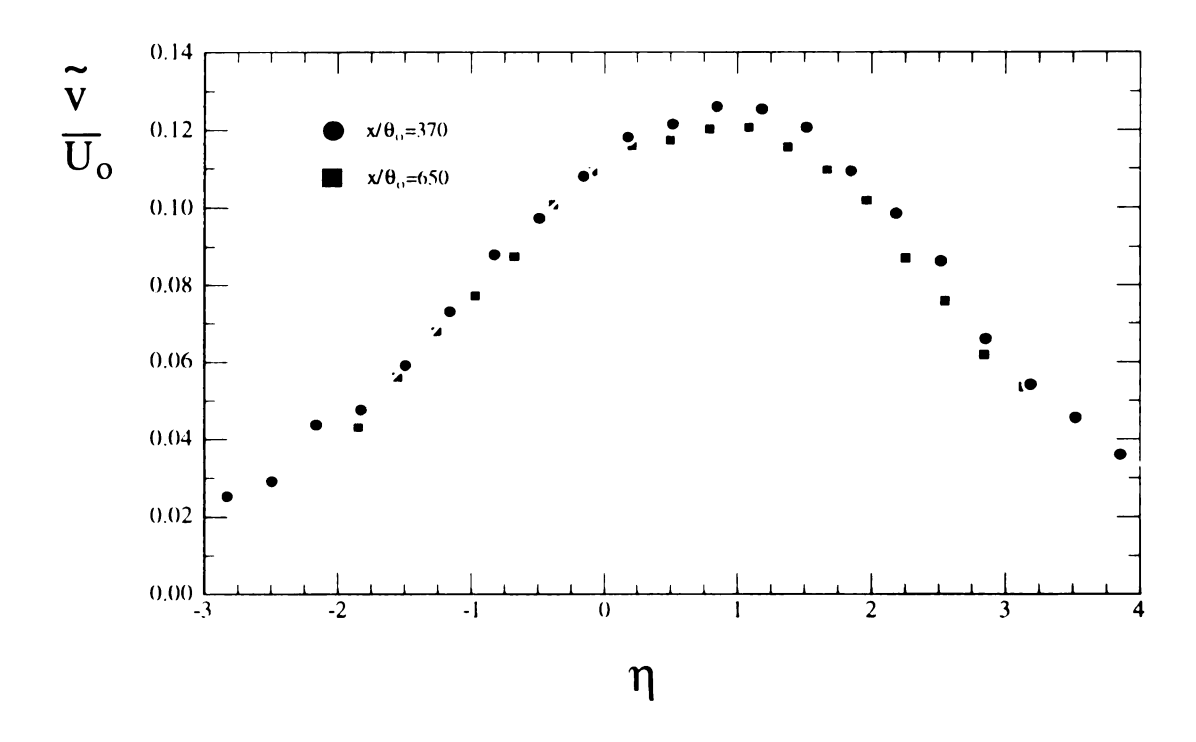


Figure 4.7 Root mean square of the lateral velocity fluctuations

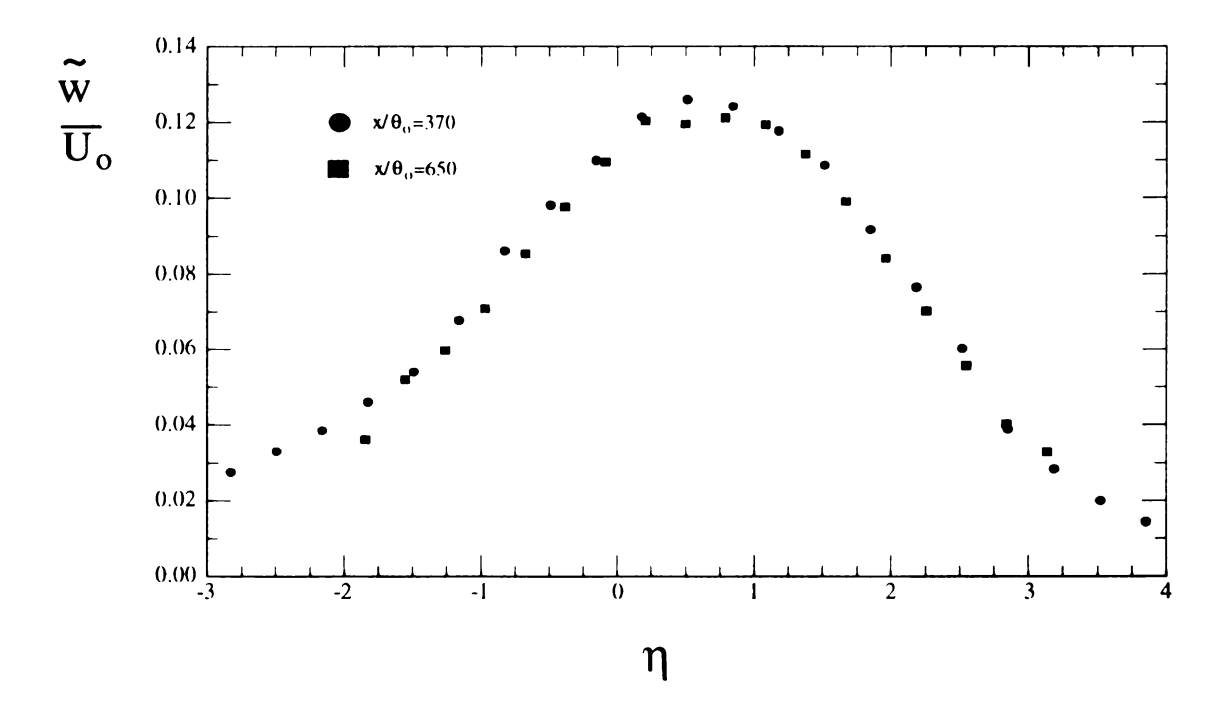


Figure 4.8 Root mean square of the spanwise velocity fluctuations

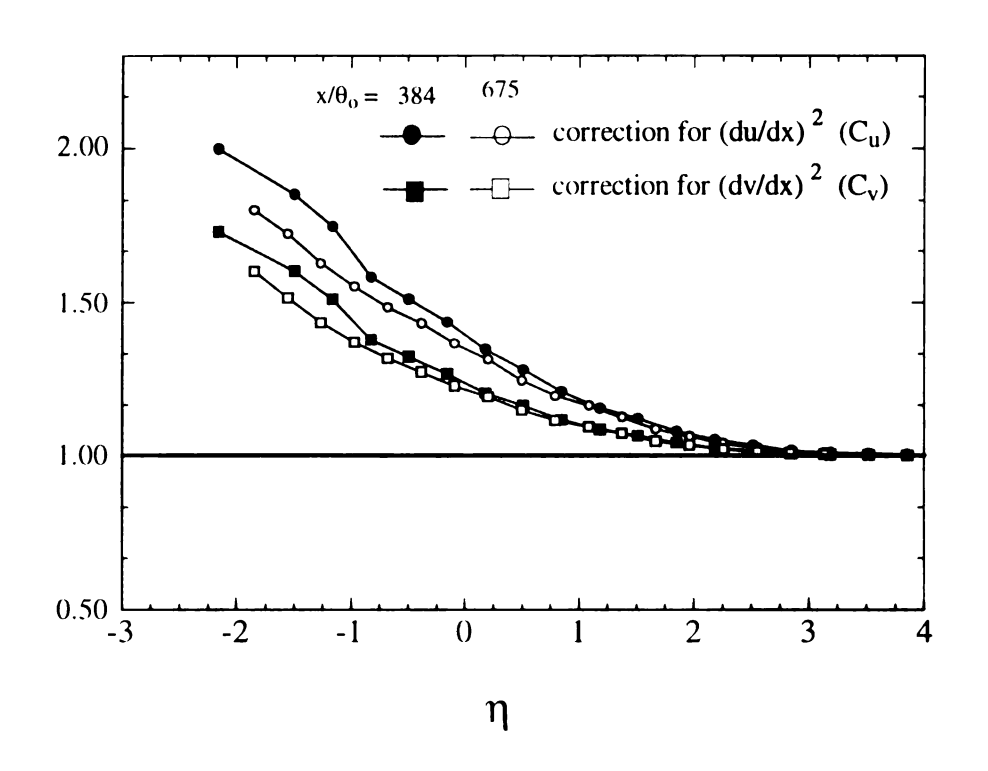


Figure 4.9 Profile of correction factor for streamwise and transverse velocity gradients (see equations 4.25 and 4.26)

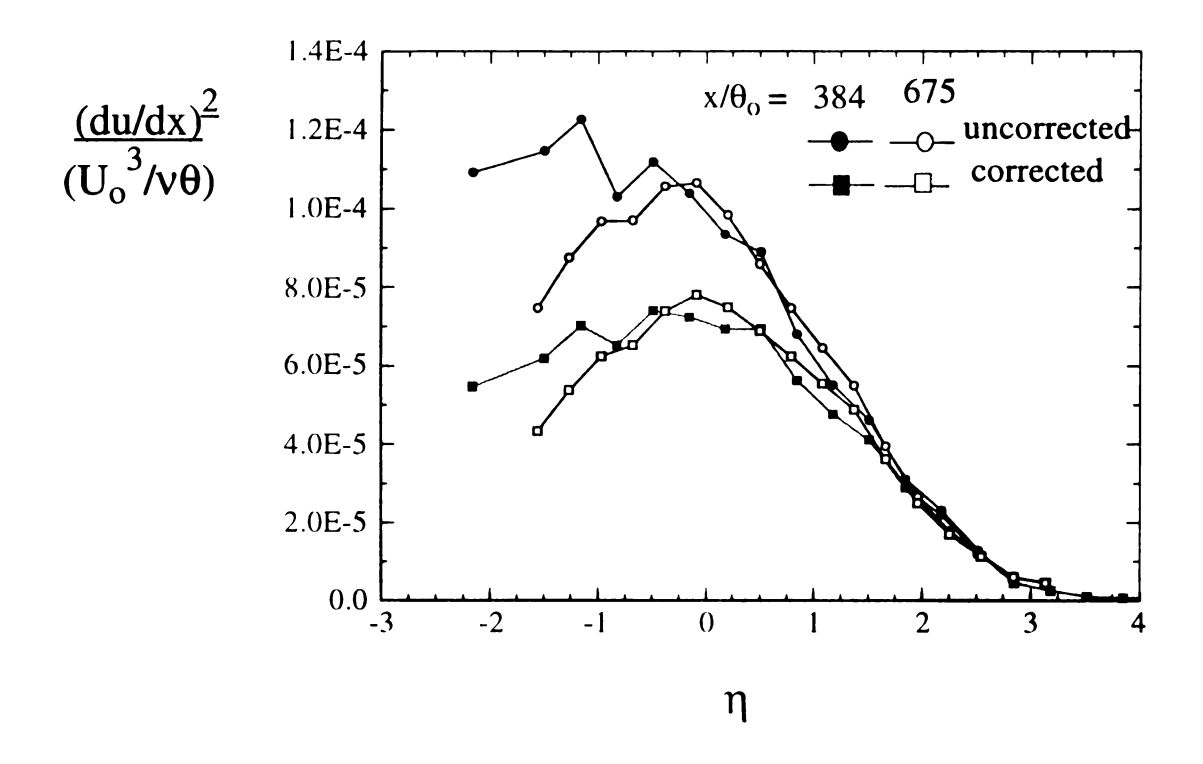


Figure 4.10 Profile of velocity gradient fluctuations: du/dx

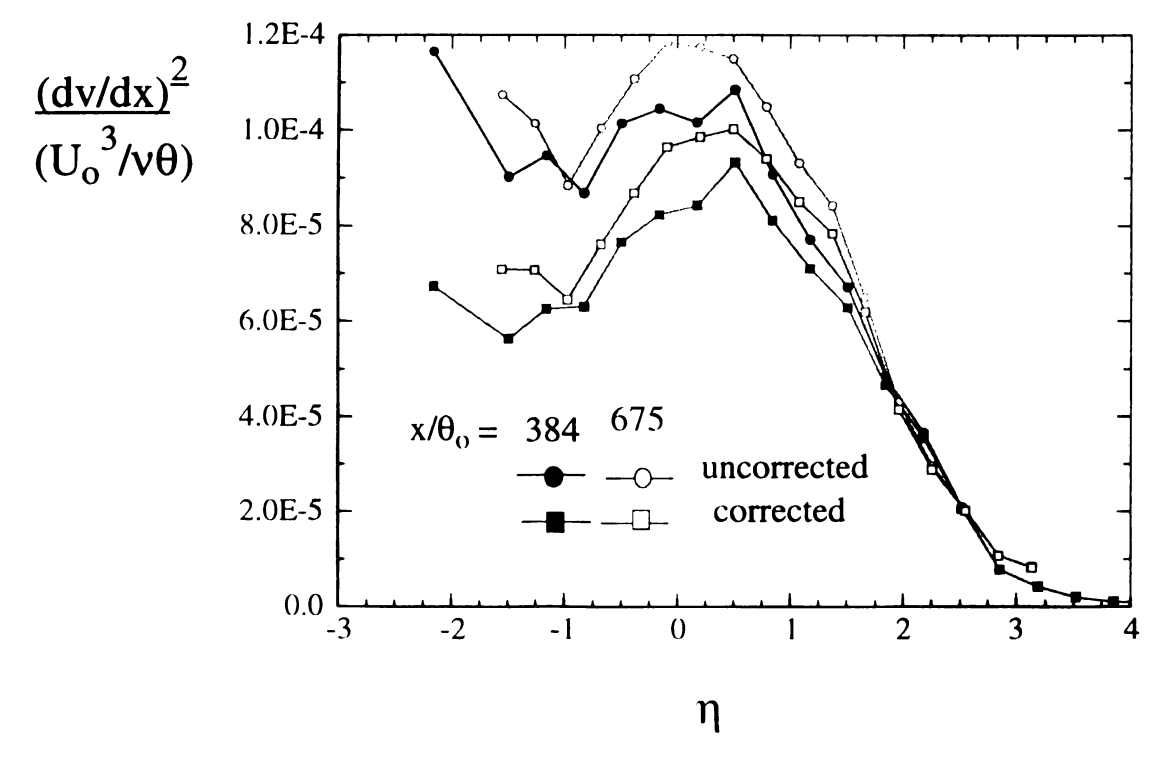


Figure 4.11 Profile of velocity gradient fluctuations: dv/dx

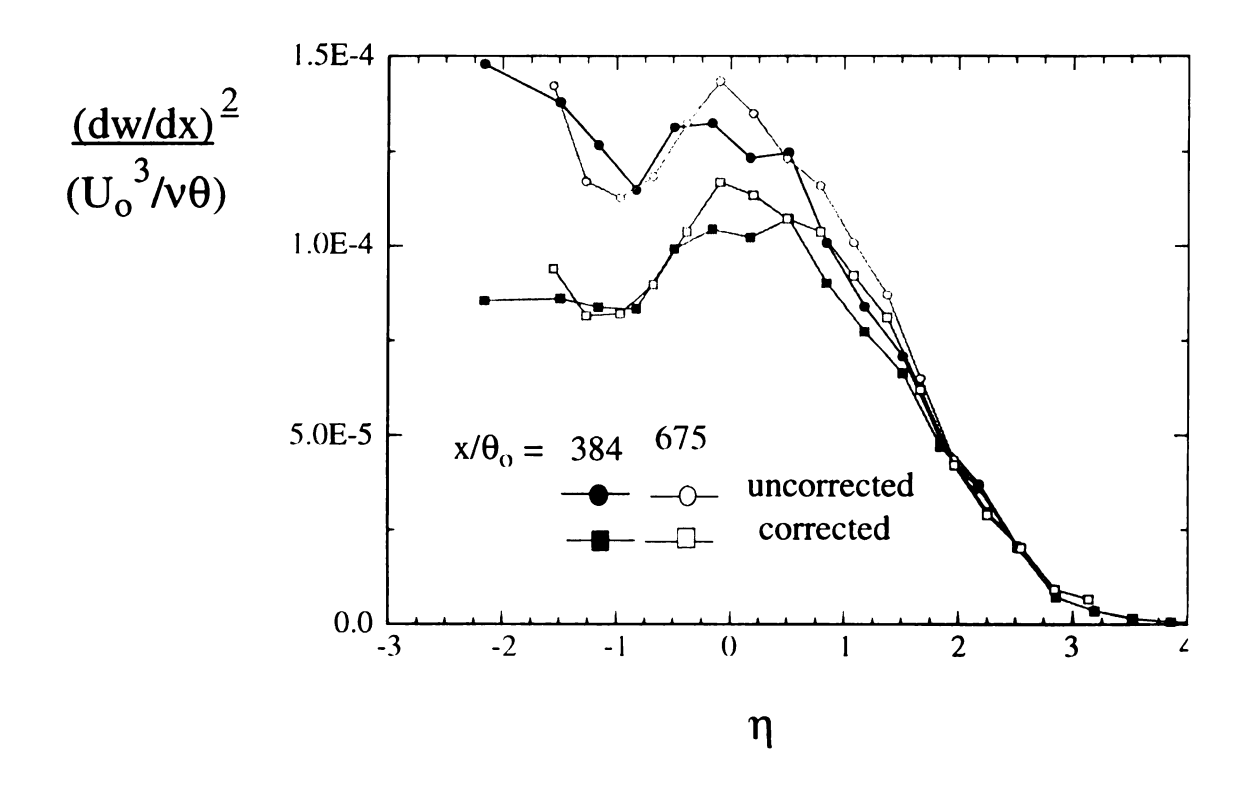


Figure 4.12 Profile of velocity gradient fluctuations: dw/dx

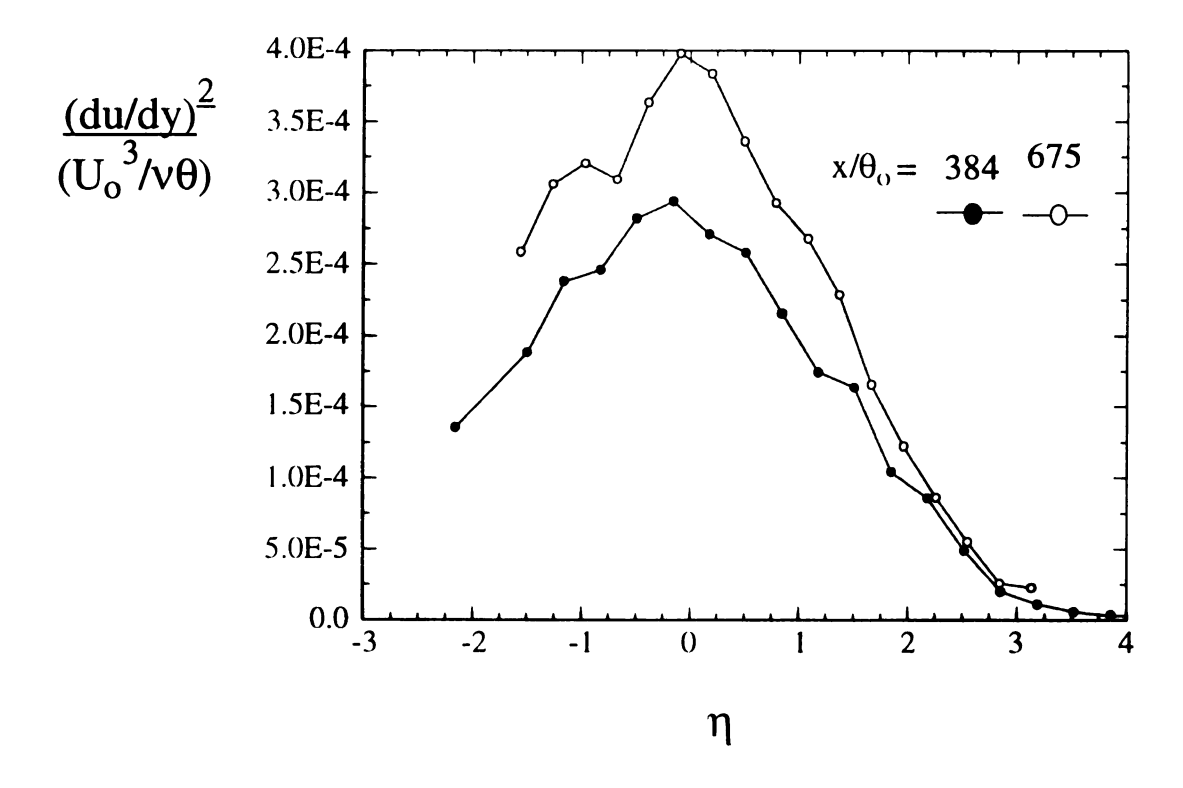


Figure 4.13 Profile of velocity gradient fluctuations: du/dy

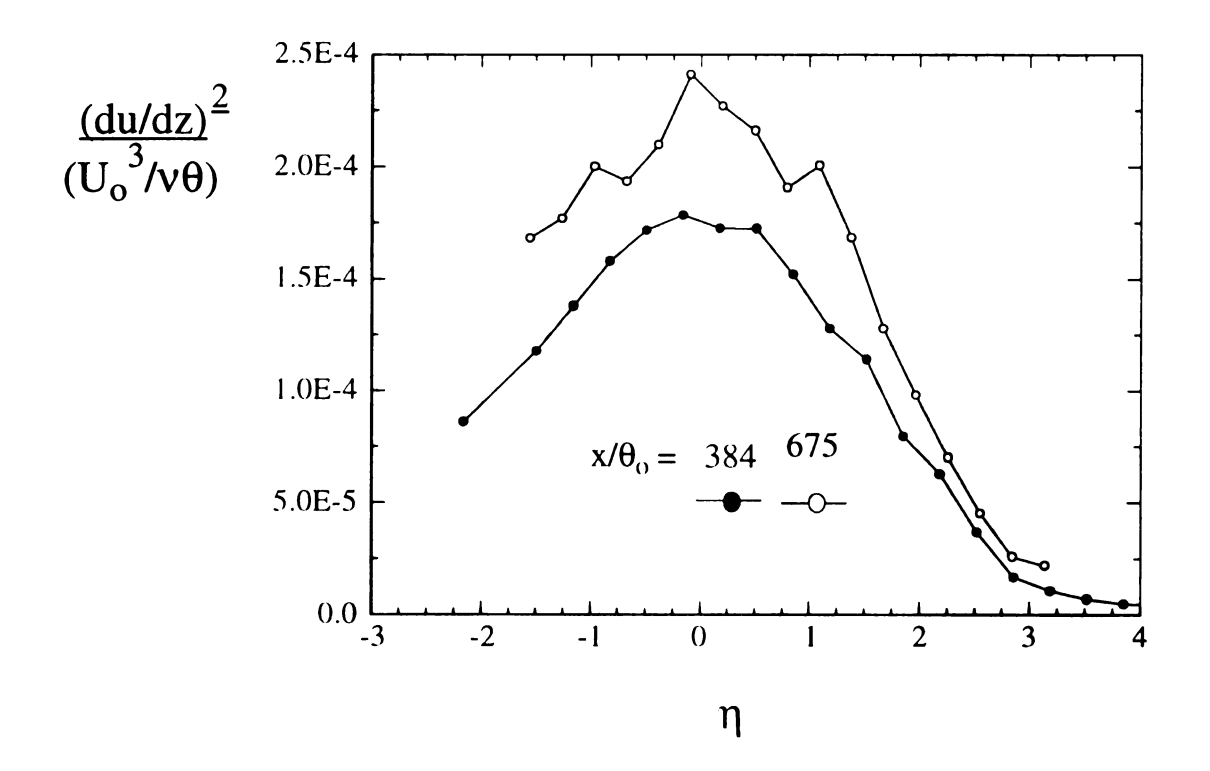


Figure 4.14 Profile of velocity gradient fluctuations: du/dz

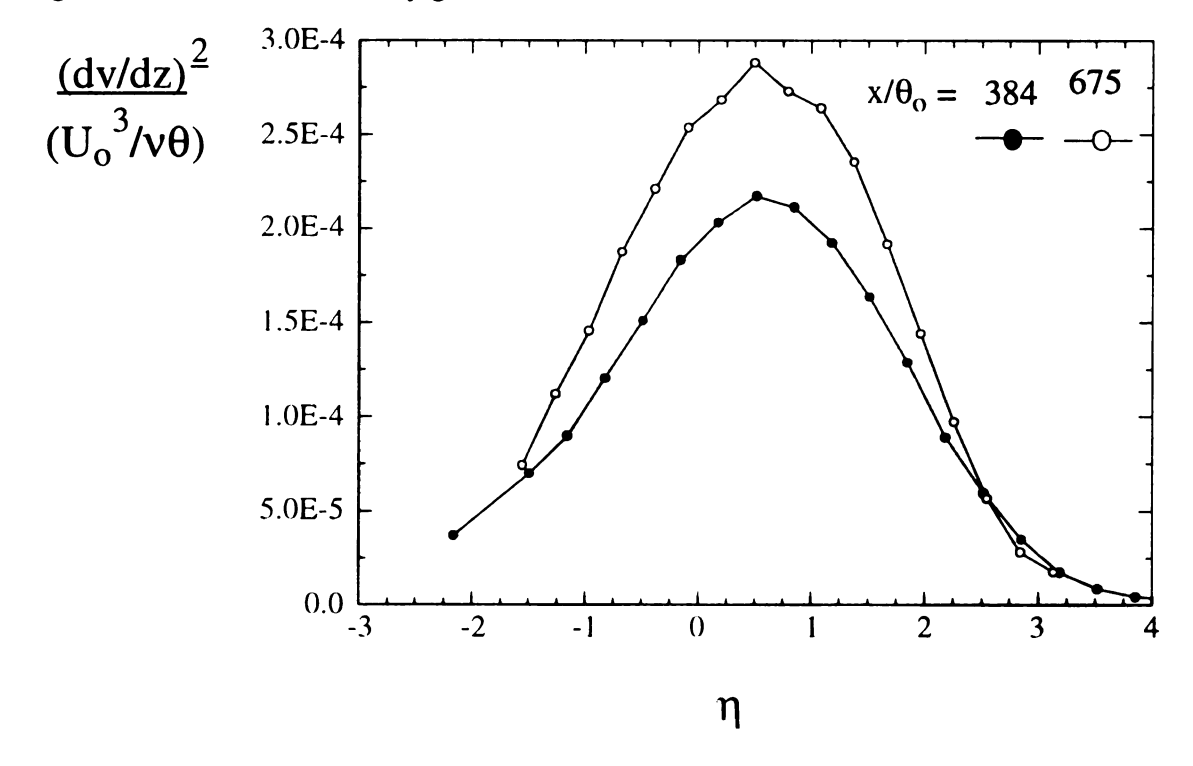


Figure 4.15 Profile of velocity gradient fluctuations: dv/dz

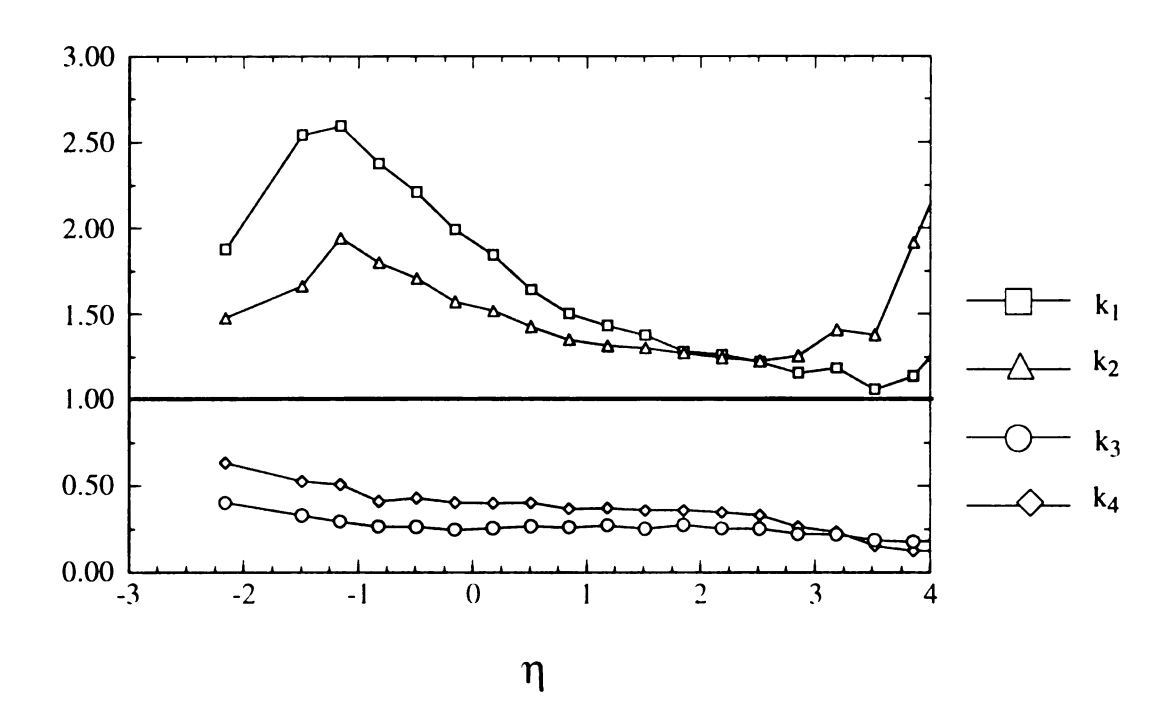


Figure 4.16 Ratio of velocity gradient variances for  $x/\theta_0$ =384.

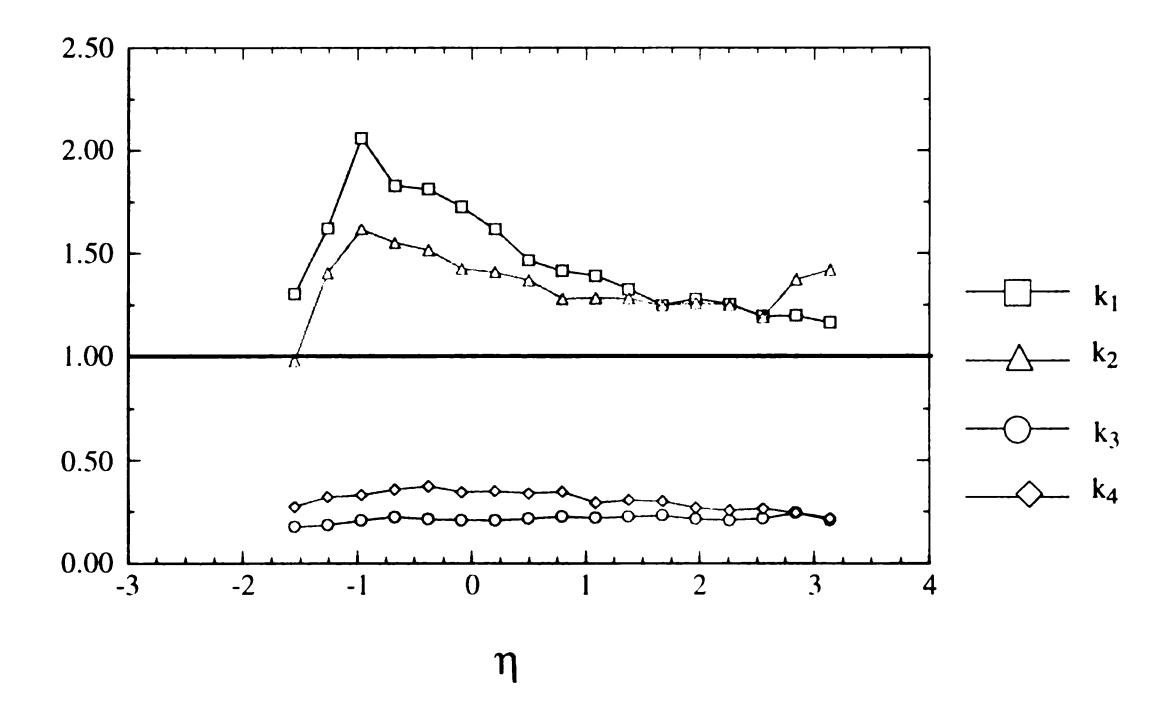


Figure 4.17 Ratio of velocity gradient variances for  $x/\theta_0$ =675.

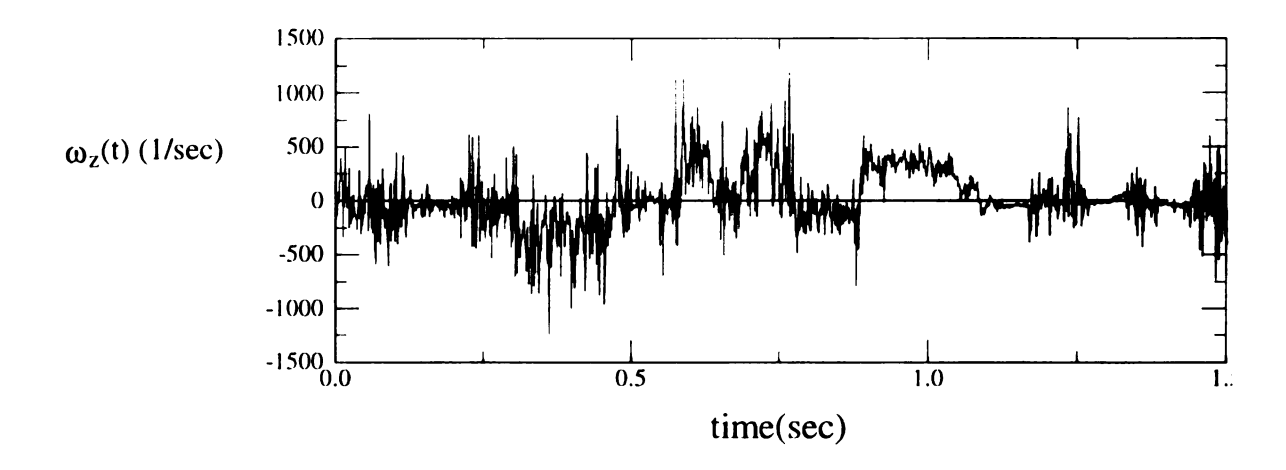


Figure 4.18 Example of vorticity time series at  $x/\theta_0 = 707$ ,  $\eta \approx 0$ . Periods of irrotational fluid are observed.

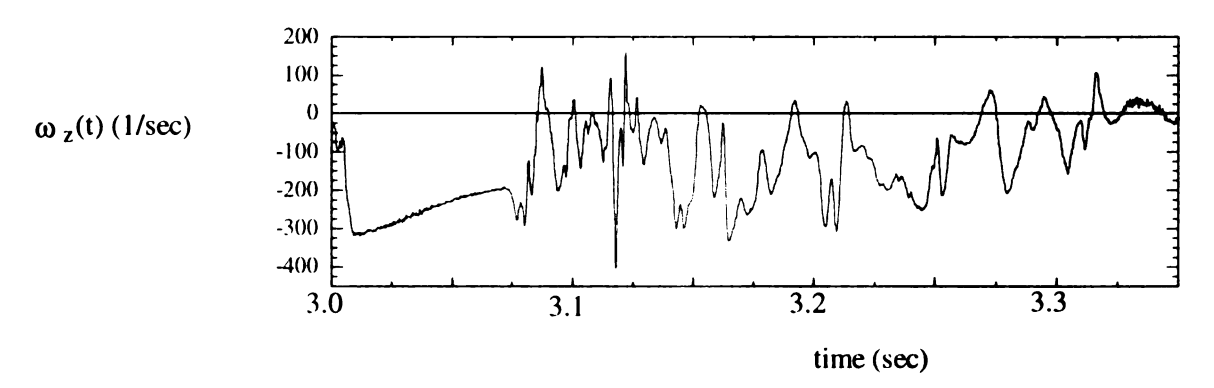


Figure 4.19 Example of vorticity time series at  $x/\theta_0=707$ ,  $\eta\approx0$ . Note the extended period of rotational fluid with little high frequency content near the beginning of the time record

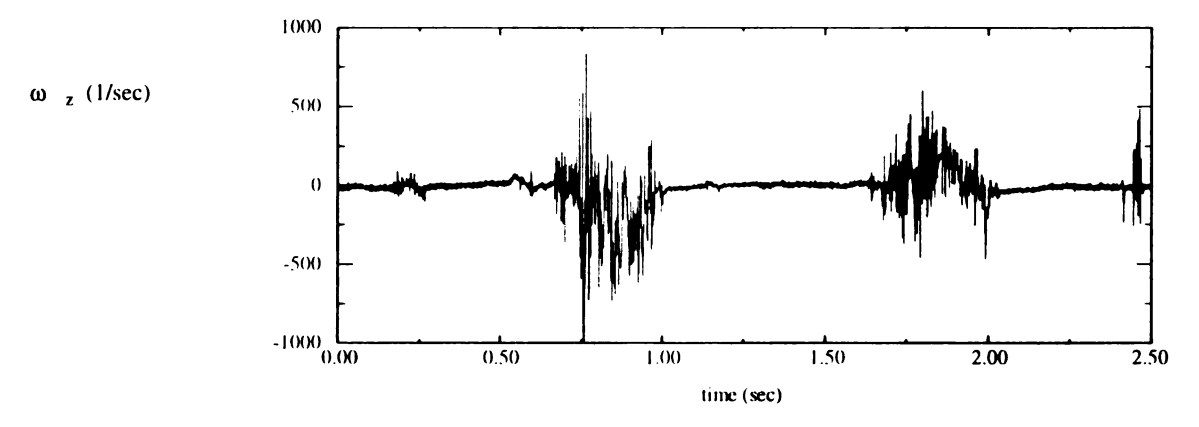


Figure 4.20 Example of vorticity time series at  $x/\theta_0=707$ ,  $\eta=3.9$ . The fluid is mostly irrotatoinal with intermittent bursts of highly fluctuating vorticity.

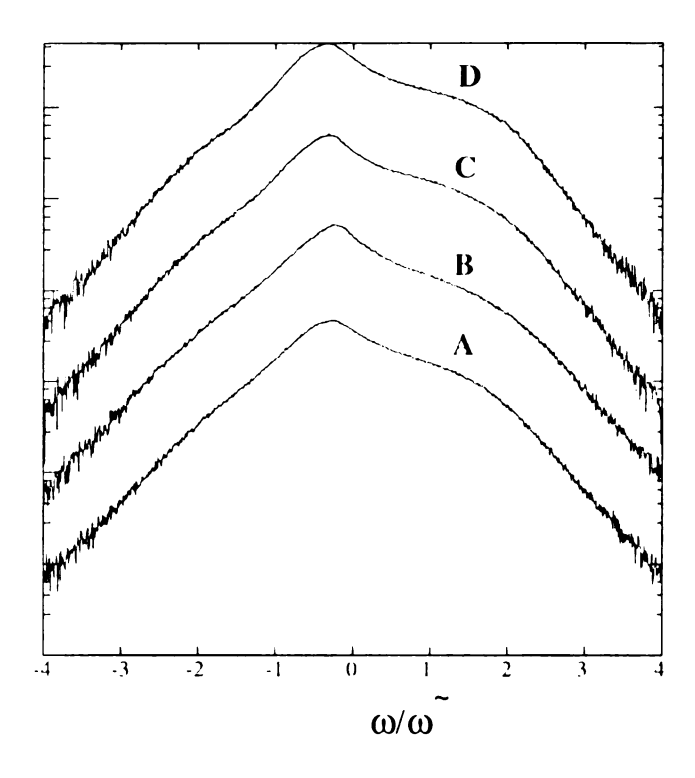


Figure 4.21 Histogram of vorticity from conditions A,B,C, and D; see Table 4.1.

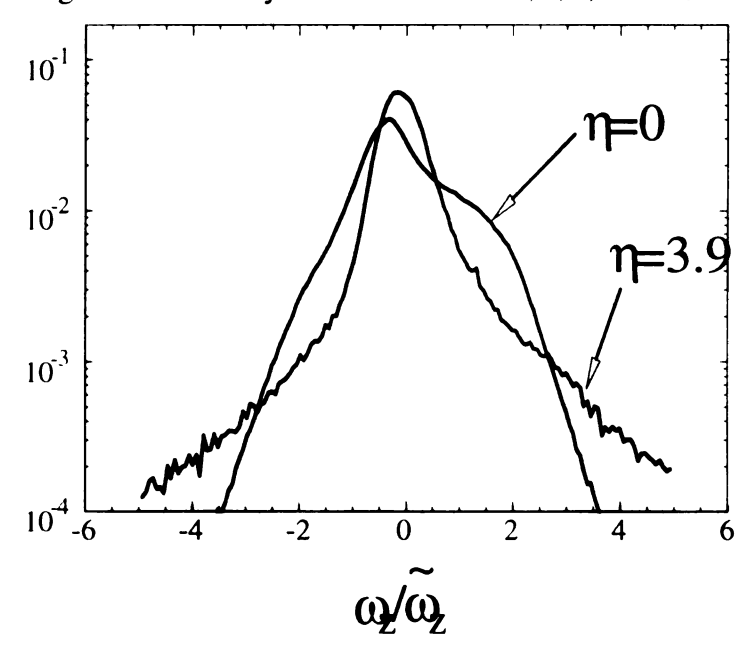


Figure 4.22 Comparison of vorticity histogram between points of high and low intermittency.

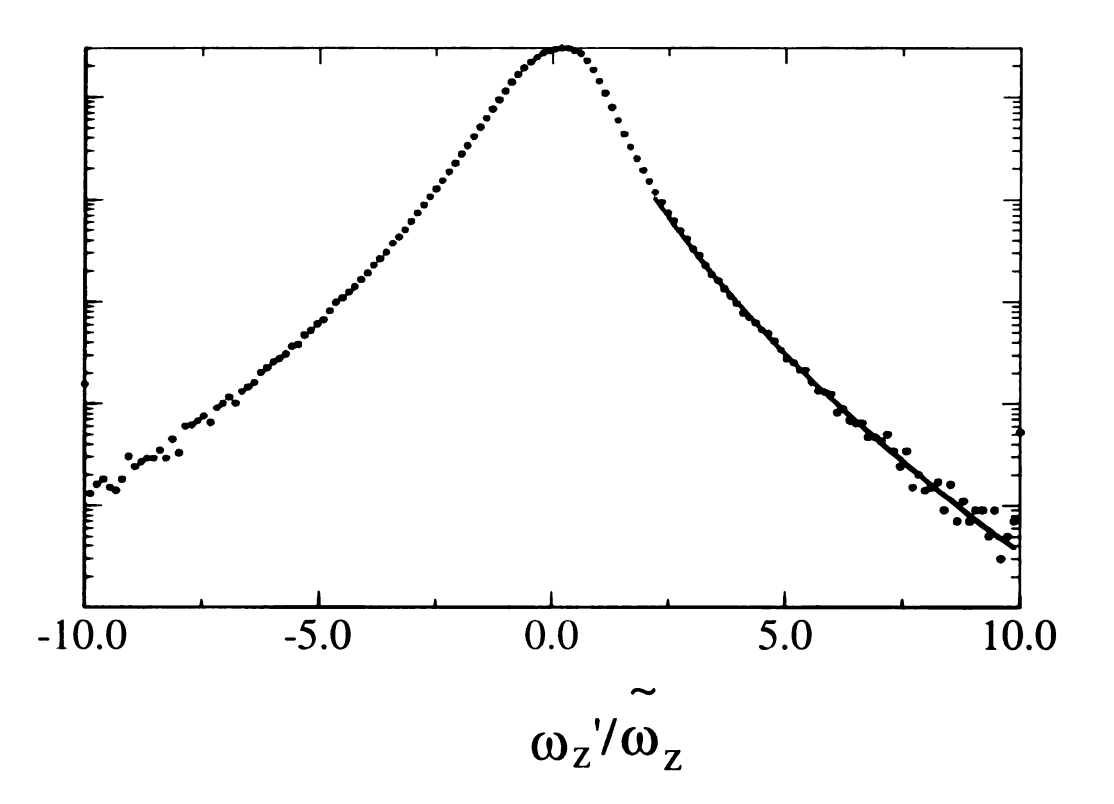


Figure 4.23 Histogram or spanwise vorticity in the atmospheric boundary layer at  $Re_{\lambda}=2500$ . Solid line represents the curve fit given by equation 4.87.

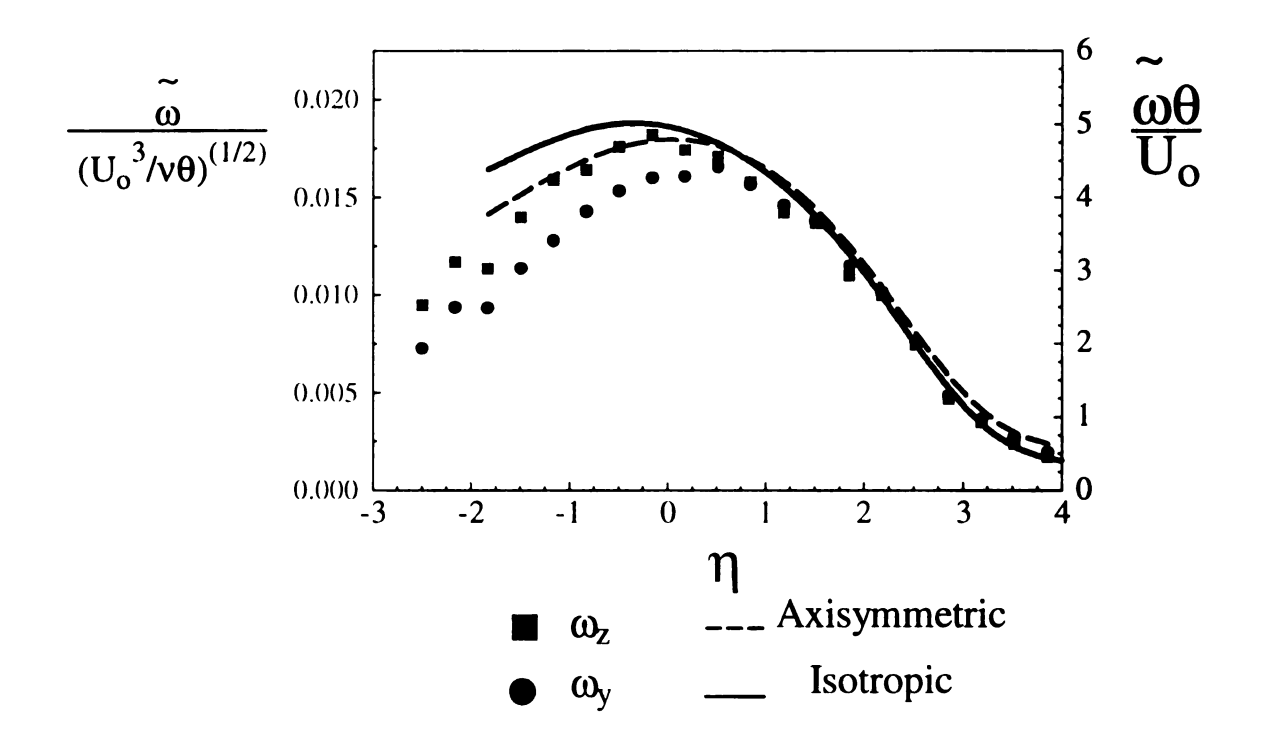


Figure 4.24 The RMS of the spanwise and lateral vorticity fluctuations at  $x/\theta_0$ =384 (Re<sub>0</sub>=7.1x10<sup>4</sup>). The isotropic and axisymmetric results were calculated from the measurements of the velocity gradient variances.

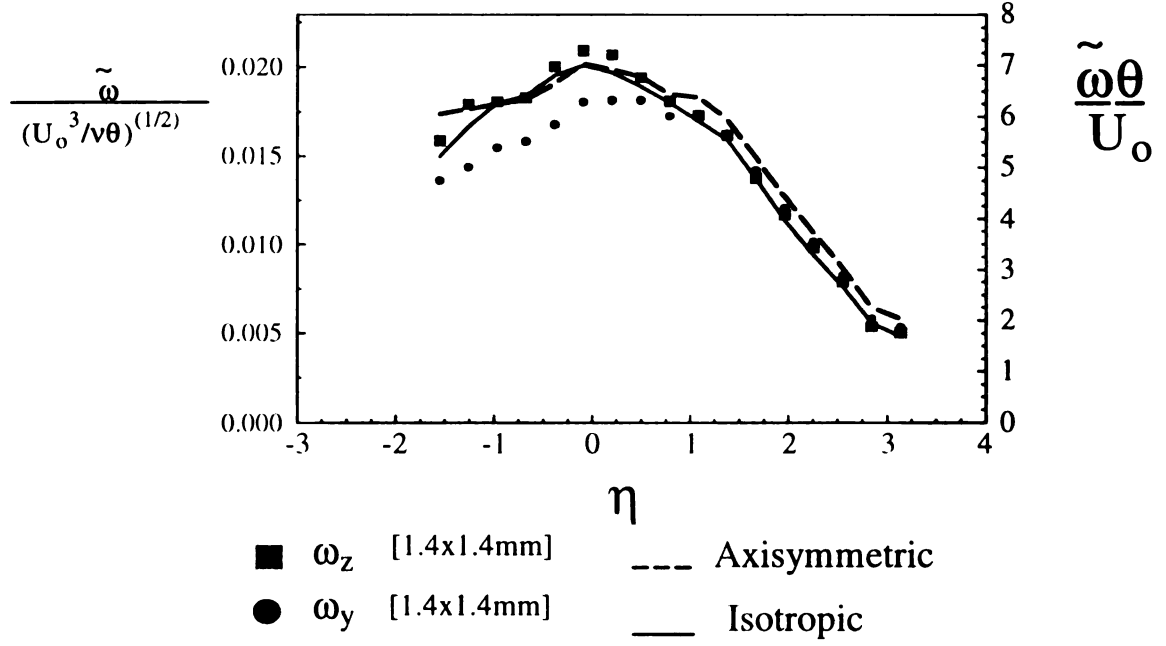


Figure 4.25 The RMS of the spanwise and lateral vorticity fluctuations at  $x/\theta_0$ =675 (Re<sub>0</sub>=1.2x10<sup>5</sup>). The isotropic and axisymmetric results were calculated from measurements of the velocity gradient variances.

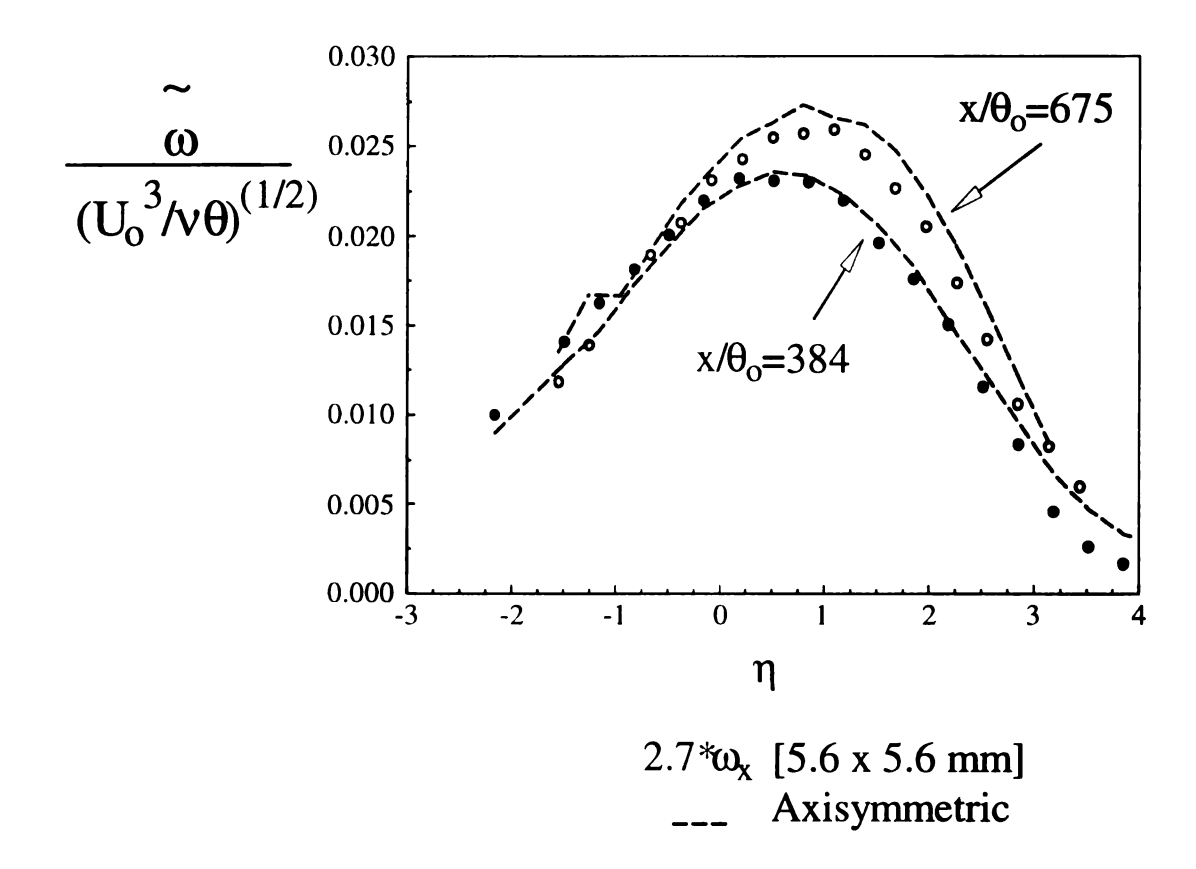


Figure 4.26 RMS of streamwise vorticity. Broken lines represent the predicted values from the measured velocity gradient terms assuming axysymmetric turbulence. The symbols are directly measured values from the 8-wire probe, that have been multiplied by the arbitrary factor of 2.7.

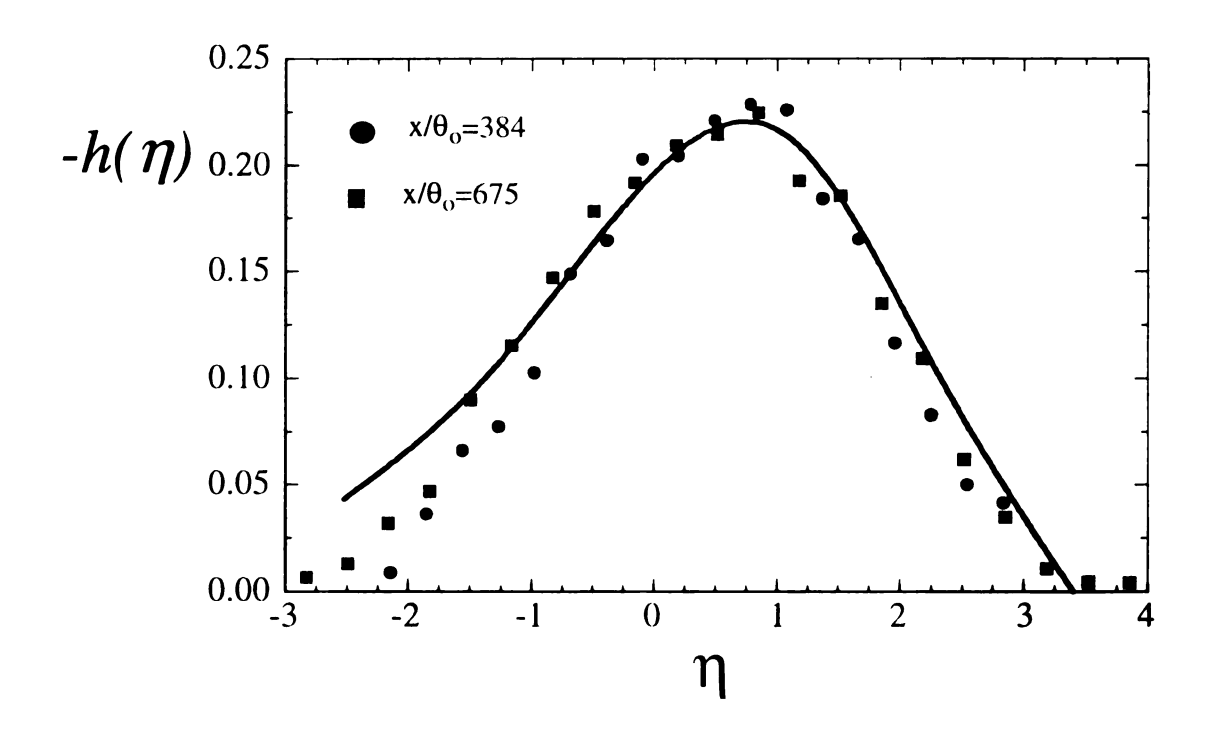


Figure 4.27 Measured and calculated Reynolds stress.

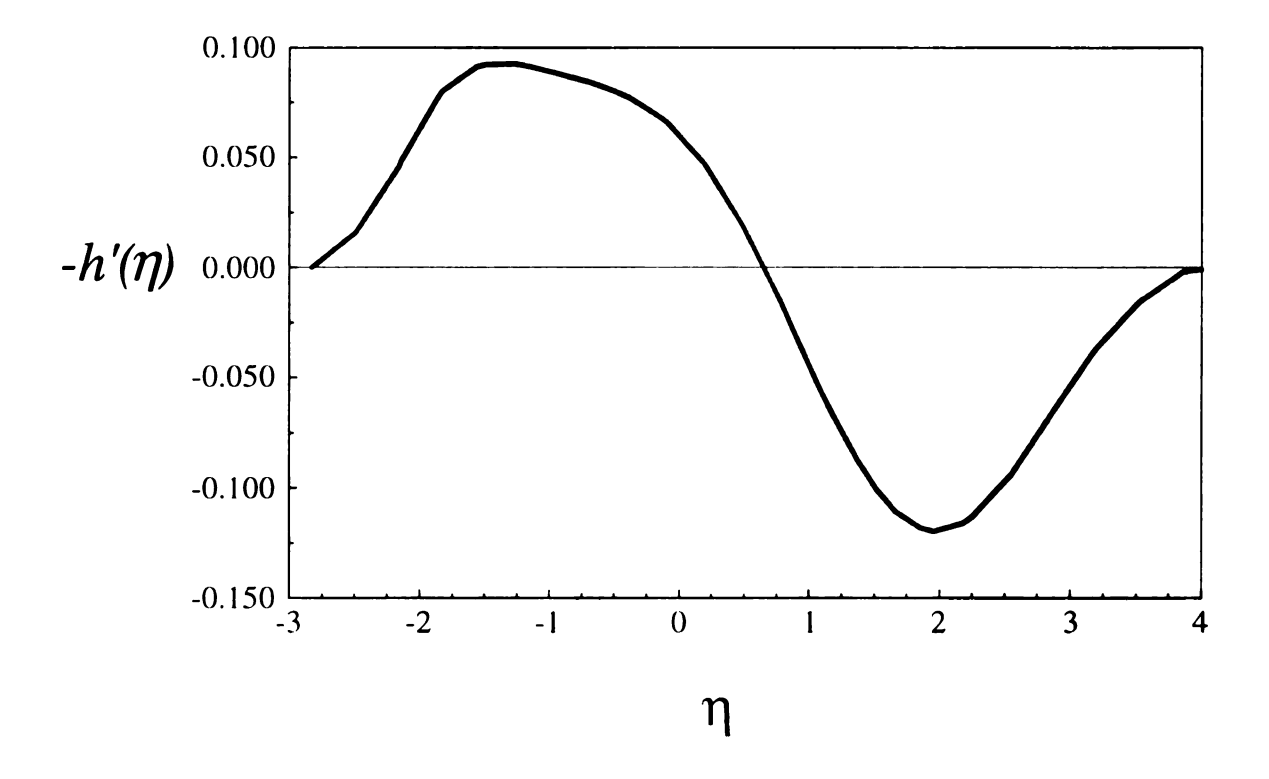


Figure 4.28 Gradient of the Reynolds stress.

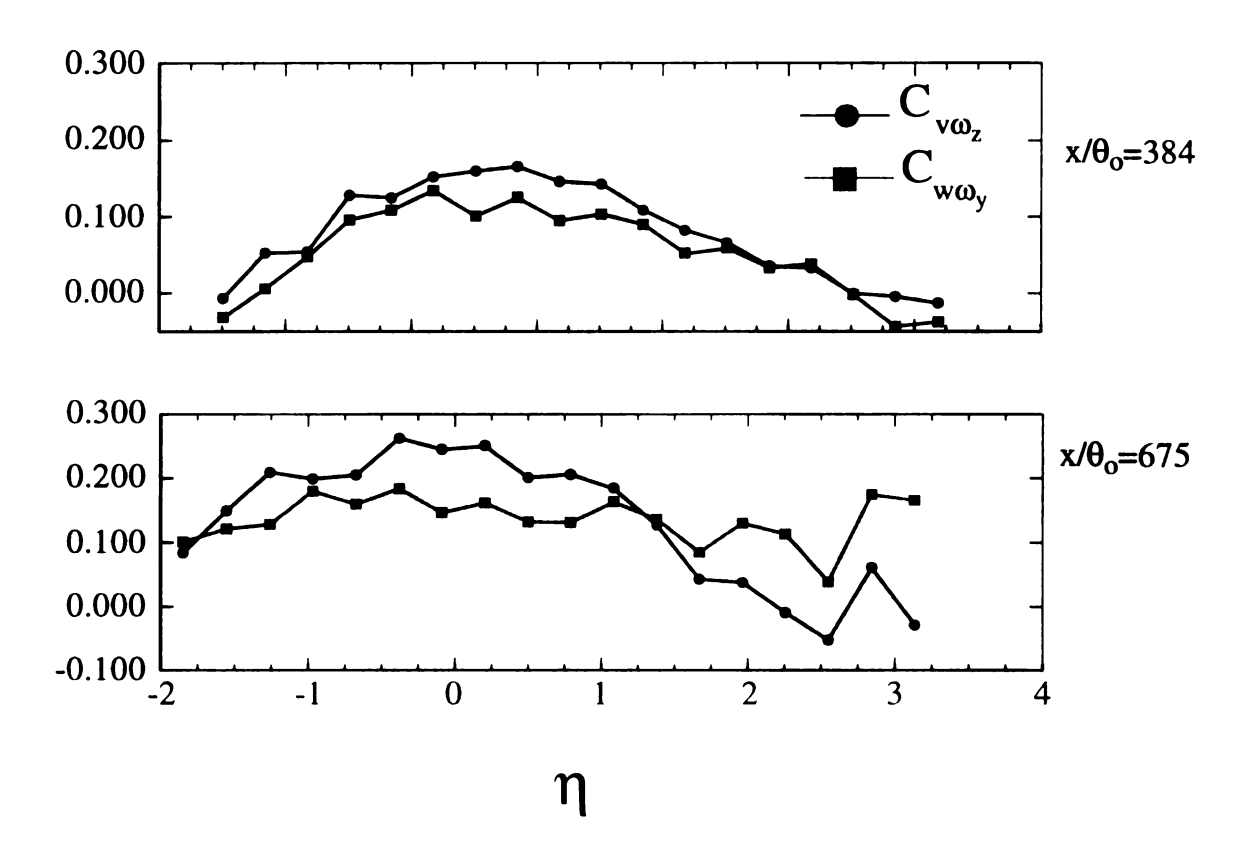


Figure 4.29 Measured velocity-vorticity correlations.

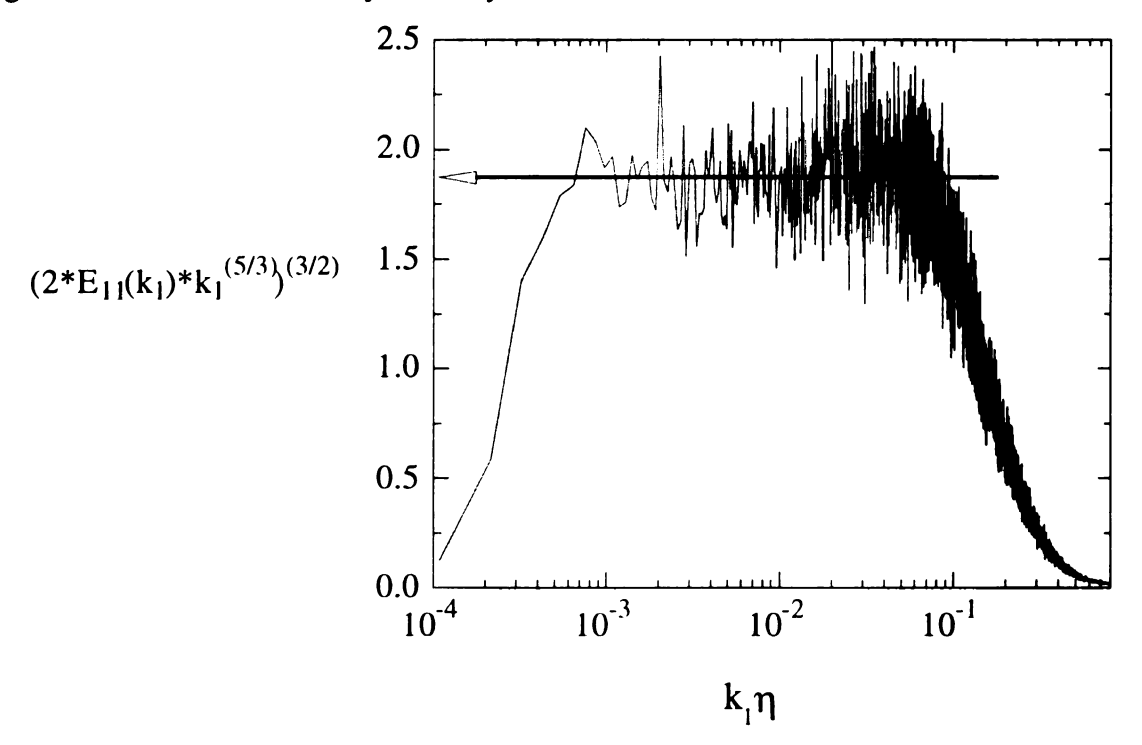


Figure 4.30 Measured dissipation from compensated energy spectra:  $E_{11}(k_1)$ 

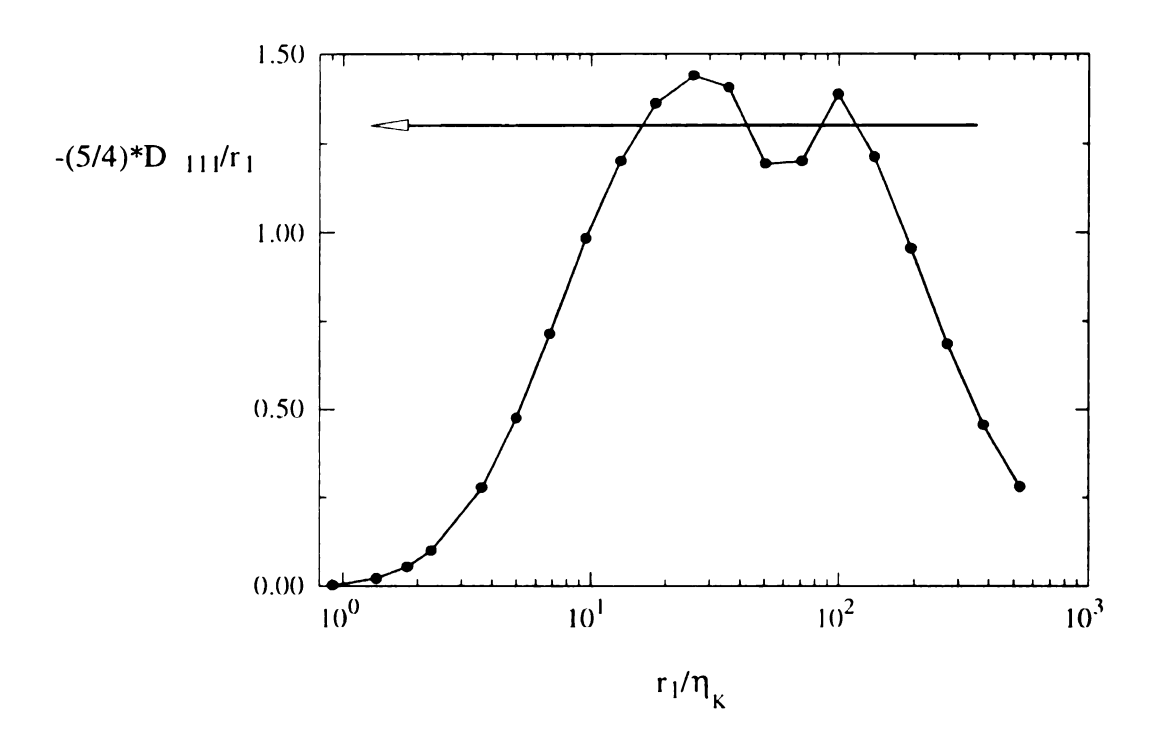


Figure 4.31 Measured dissipation from compensated third order structure function:  $D_{111}$ 

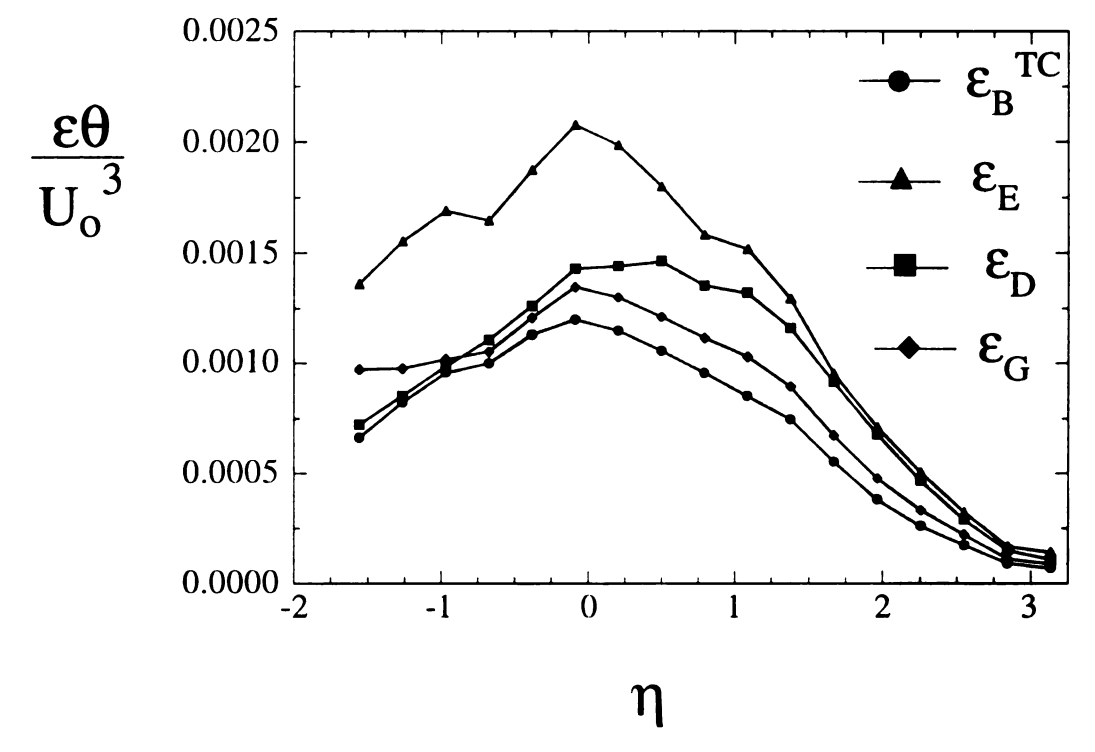
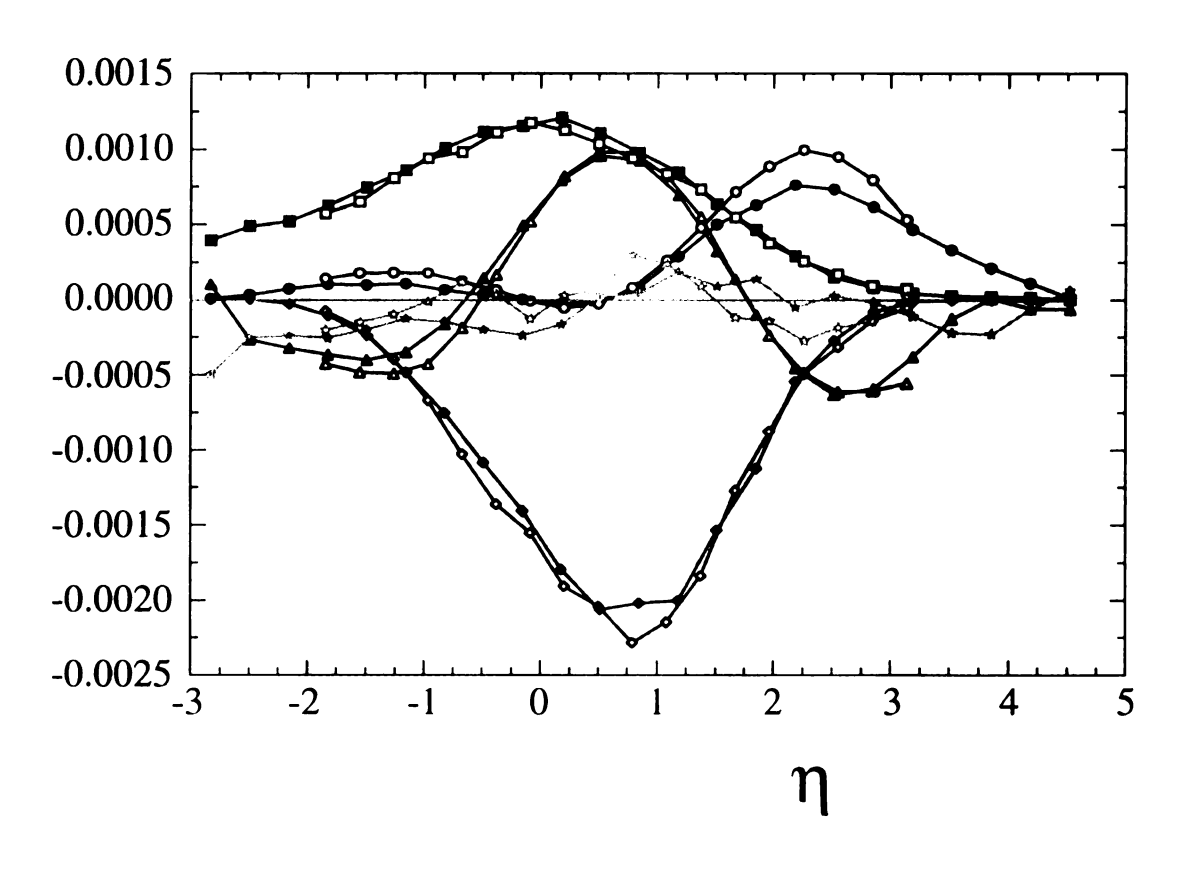


Figure 4.32 Comparison of the profiles of several dissipation estimates at  $x/\theta_0$ =675. The estimate  $\varepsilon_B^{TC}$  assumes isotropic turbulence, whereas the others assume various semi-isotropic properties.



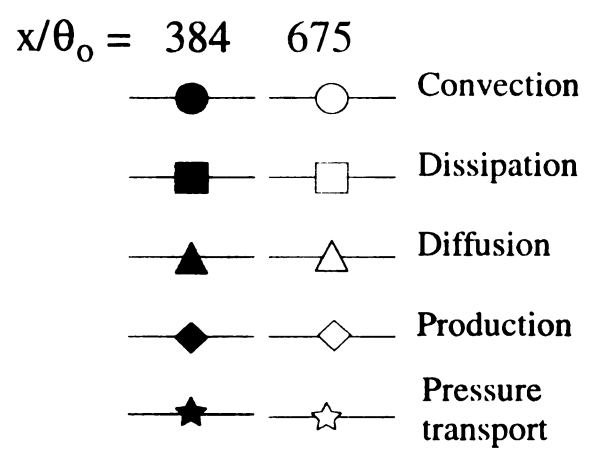


Figure 4.33 The measured budget of turbulent kinetic energy. The ordinate represents the magnitude of the bracketed terms in equation 4.68 scaled by  $\theta/U_o^3$ .

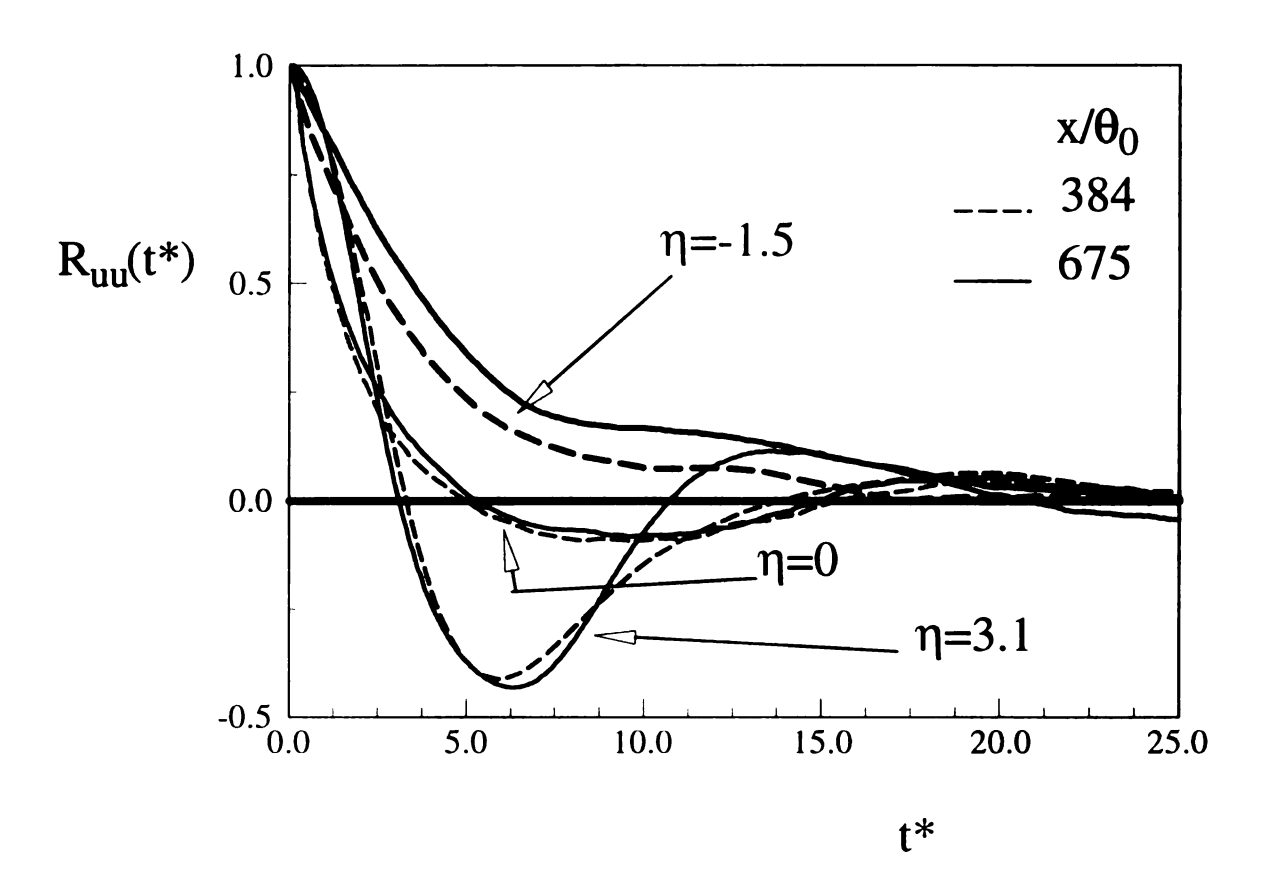


Figure 4.34 Velocity autocorrelations from three  $\eta$  locations

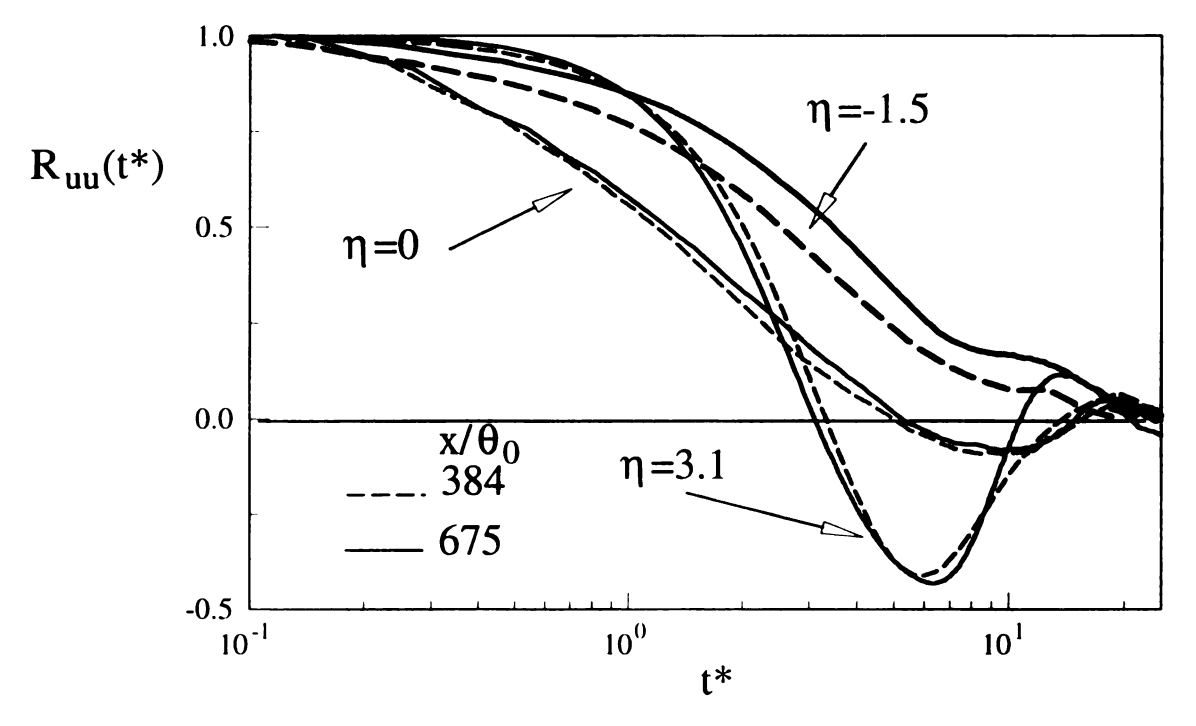


Figure 4.35 The autocorrelations of Figure 4.34show in semilog format

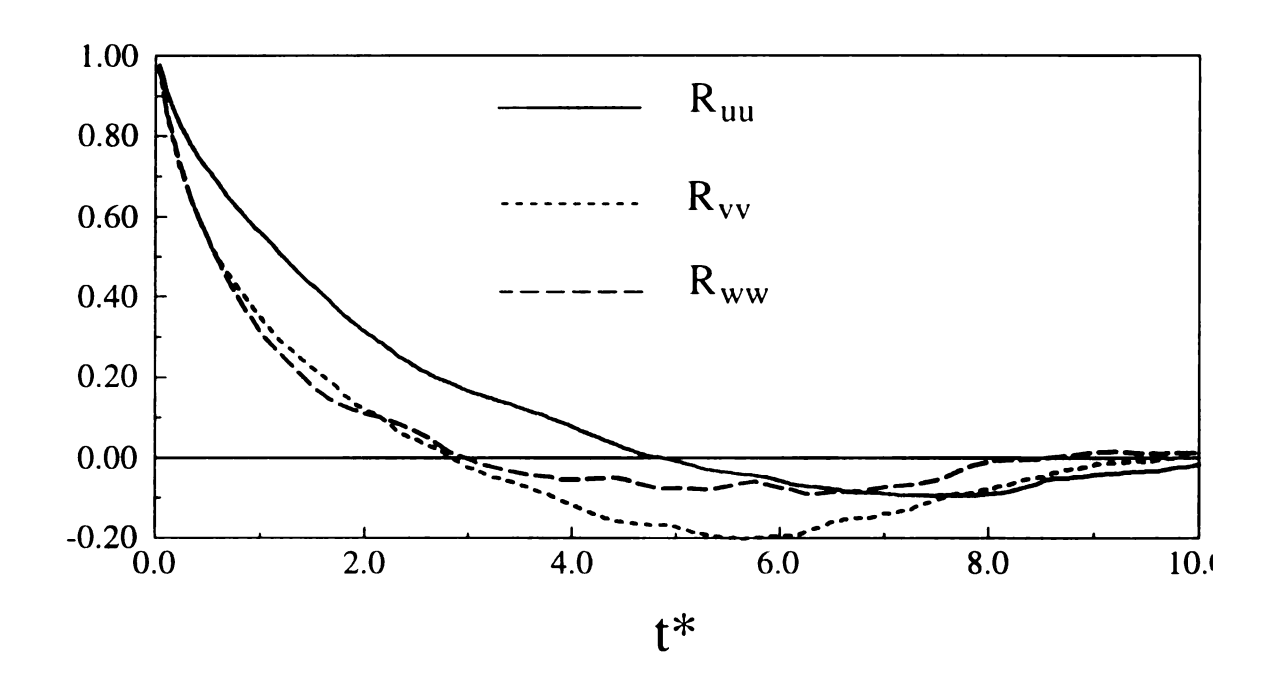


Figure 4.36 Autocorrelations of u,v, and w at  $x/\theta_0$ =675,  $\eta$ =0.

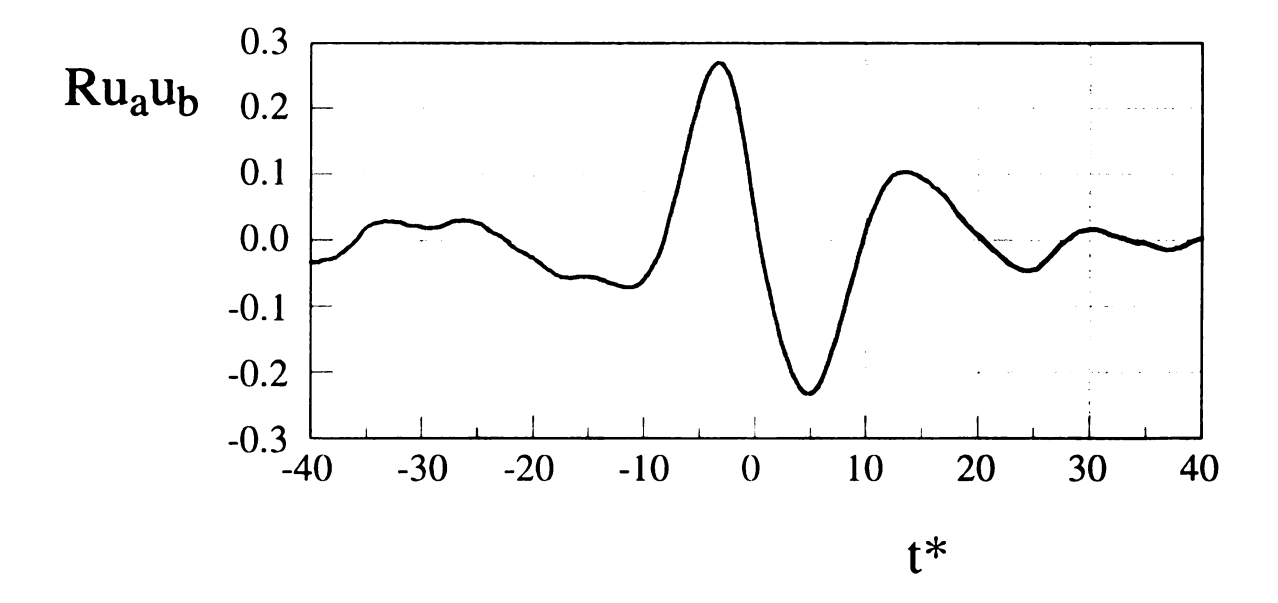


Figure 4.37 Cross Correlation between probe (a) located at  $\eta$ =4.53, and probe (b) located at  $\eta$ =1.26.

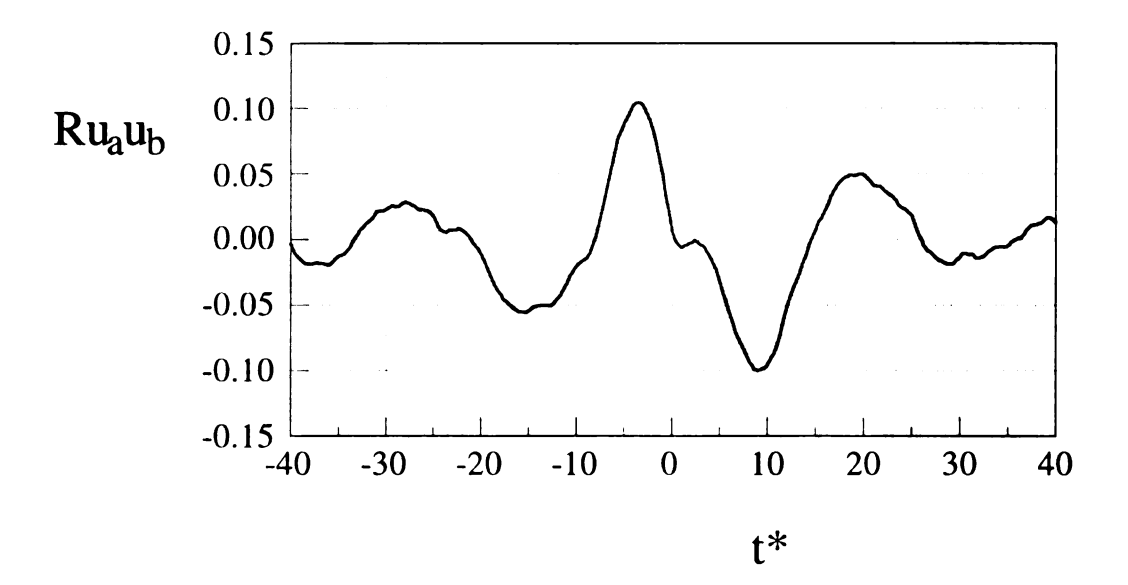


Figure 4.38 Cross Correlation between probe (a) located at  $\eta$ =3.08, and probe (b) located at  $\eta$ =-0.194.

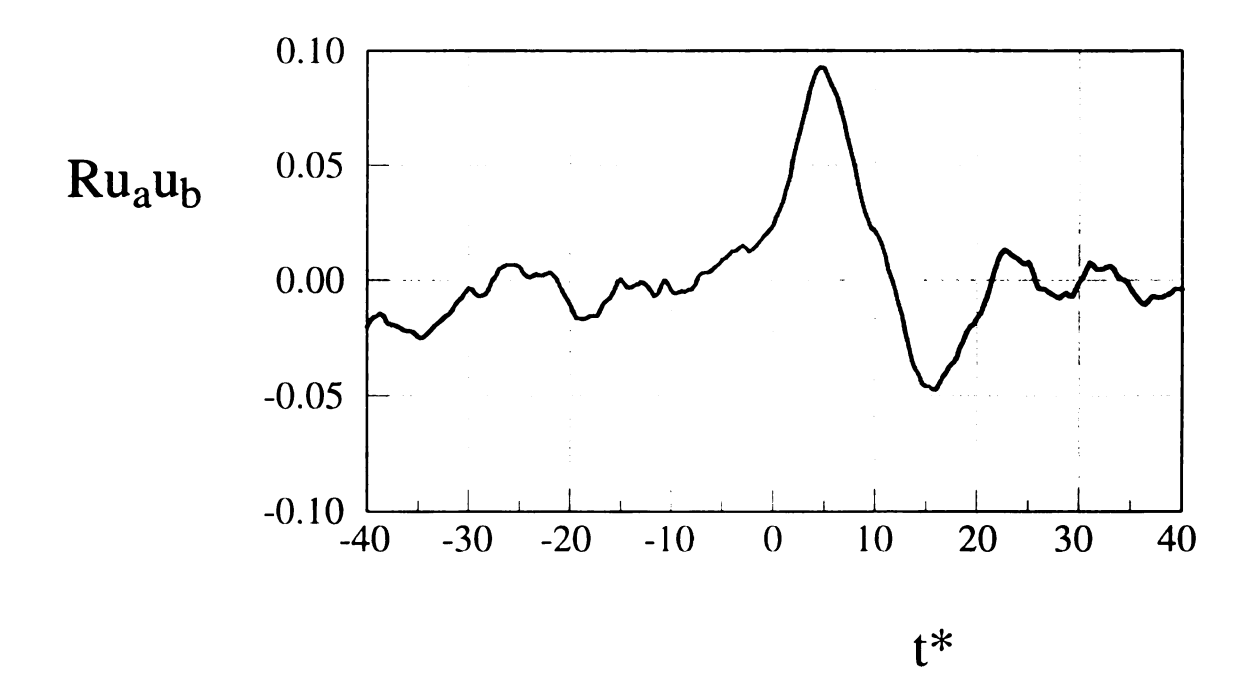


Figure 4.39 Cross Correlation between probe (a) located at  $\eta$ =1.76, and probe (b) located at  $\eta$ =-1.52.

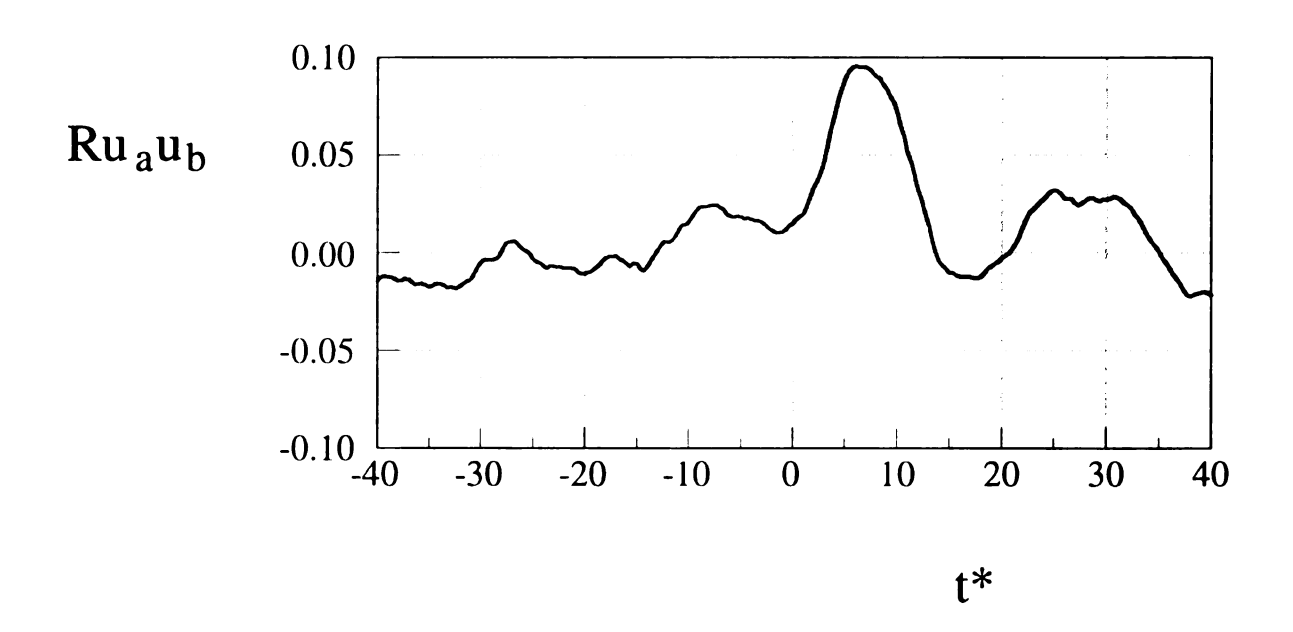


Figure 4.40 Cross Correlation between probe (a) located at  $\eta$ =.434, and probe (b) located at  $\eta$ =-2.84.

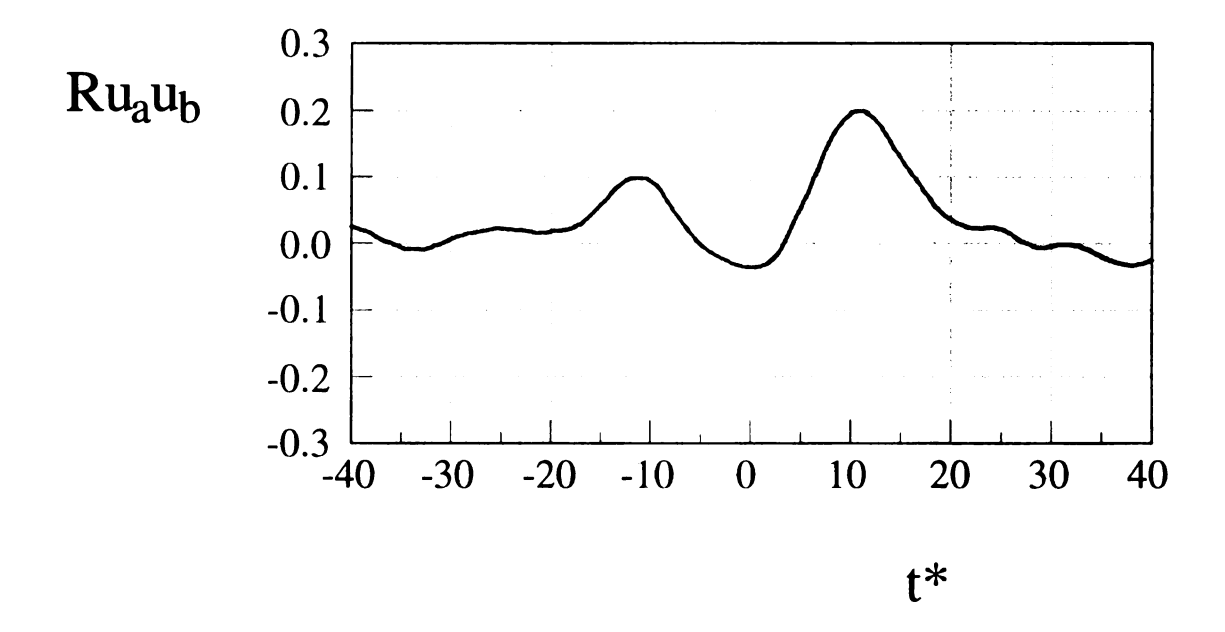


Figure 4.41 Cross Correlation between probe (a) located at  $\eta$ =-0.888, and probe (b) located at  $\eta$ =-4.16.

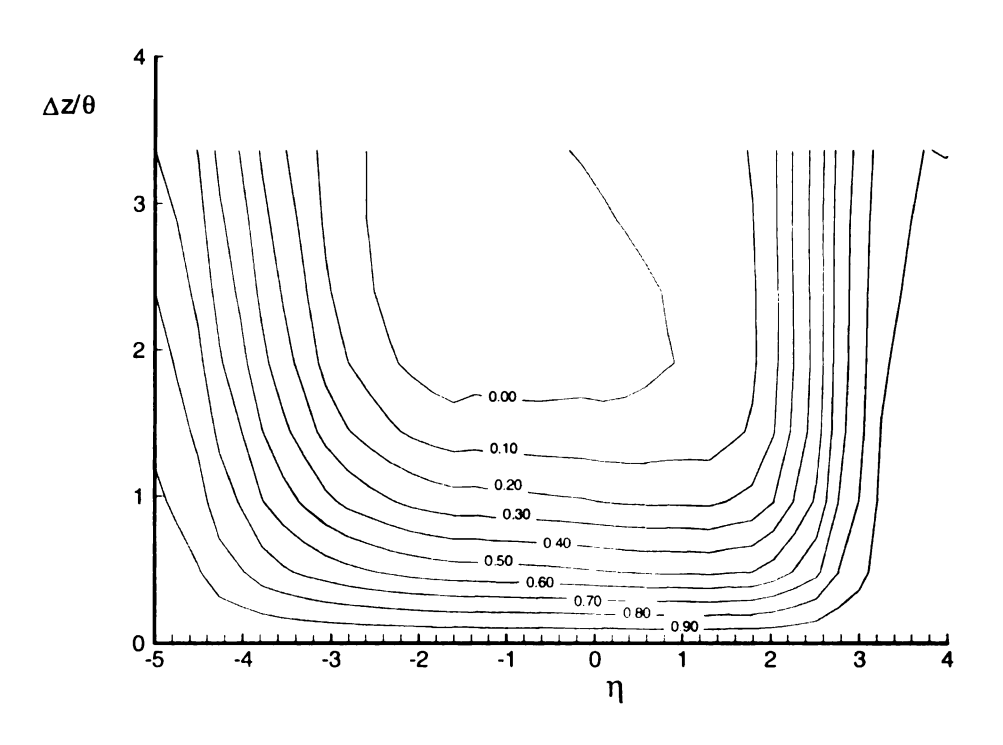


Figure 4.42 Spanwise correlation of velocity at  $x/\theta_0=101$ .

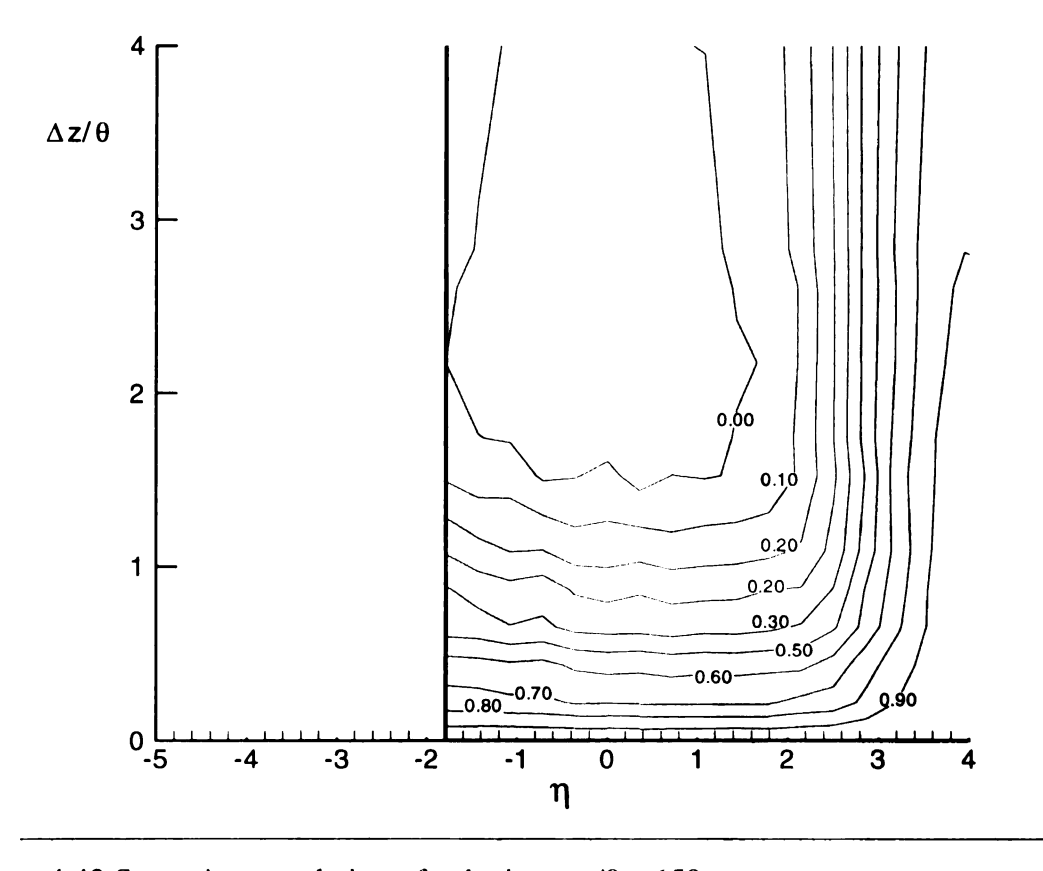


Figure 4.43 Spanwise correlation of velocity at  $x/\theta_0$ =650.

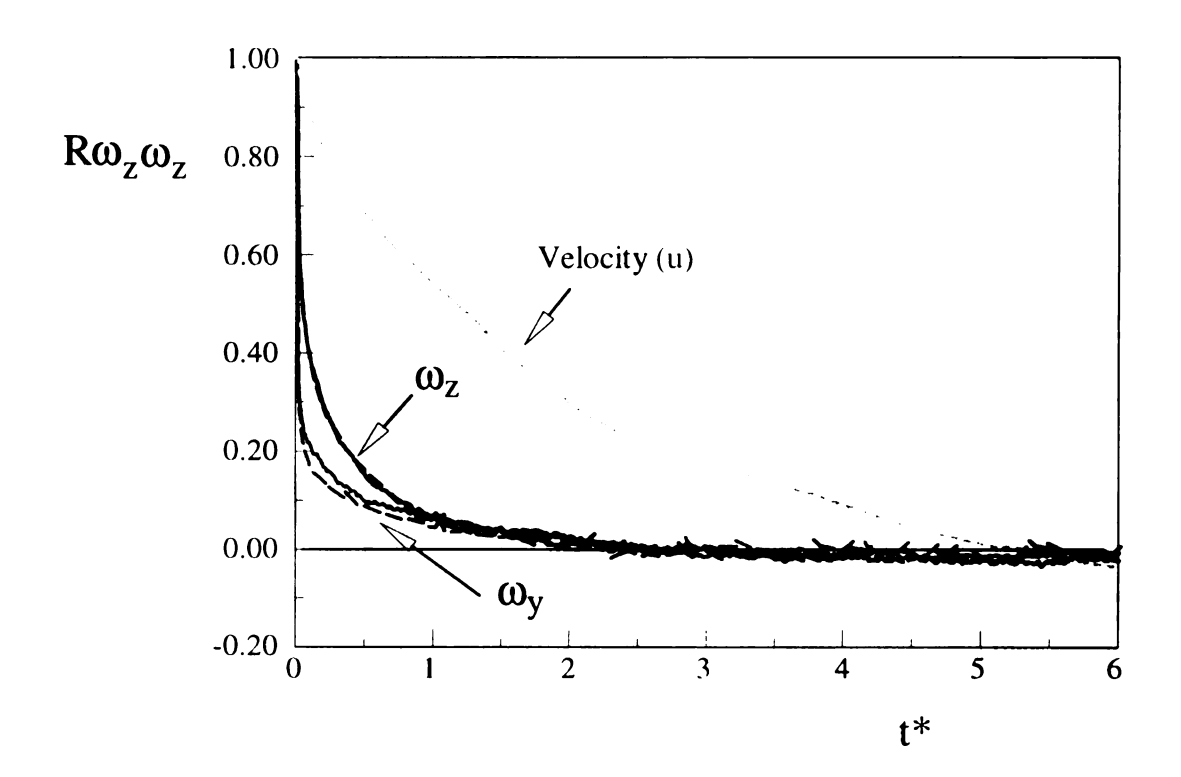


Figure 4.44 Autocorrelation of spanwise and lateral components of vorticity

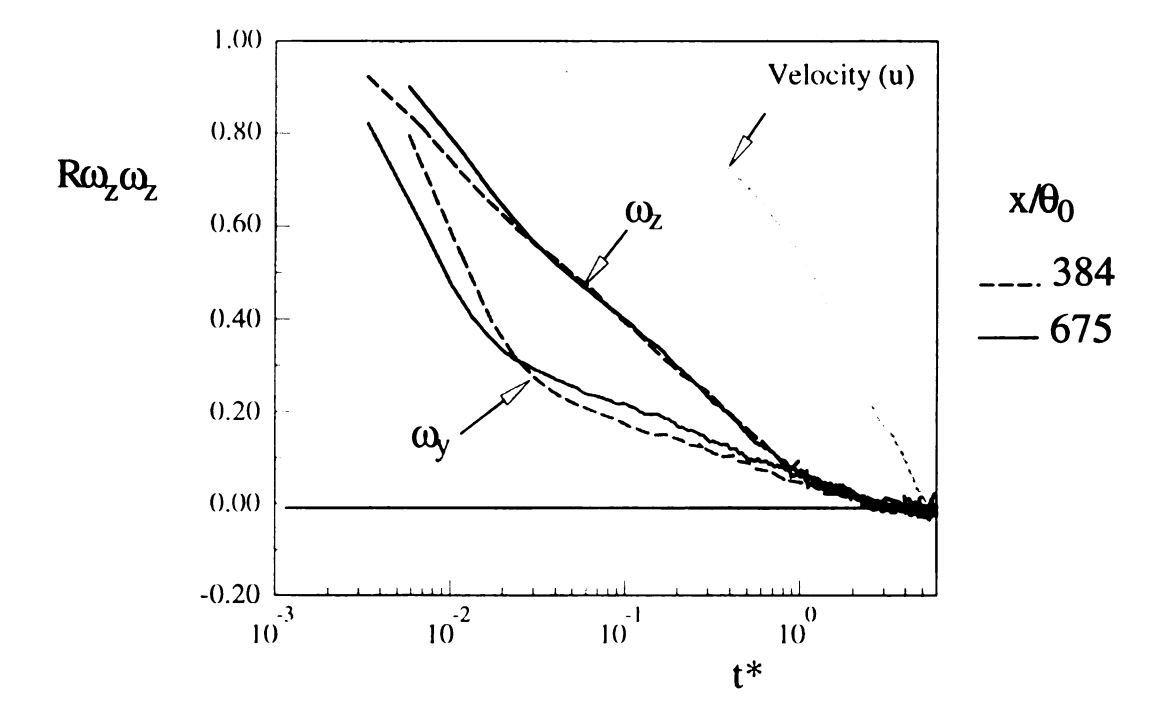


Figure 4.45 Autocorreltion of spanwise vorticity in semilog format

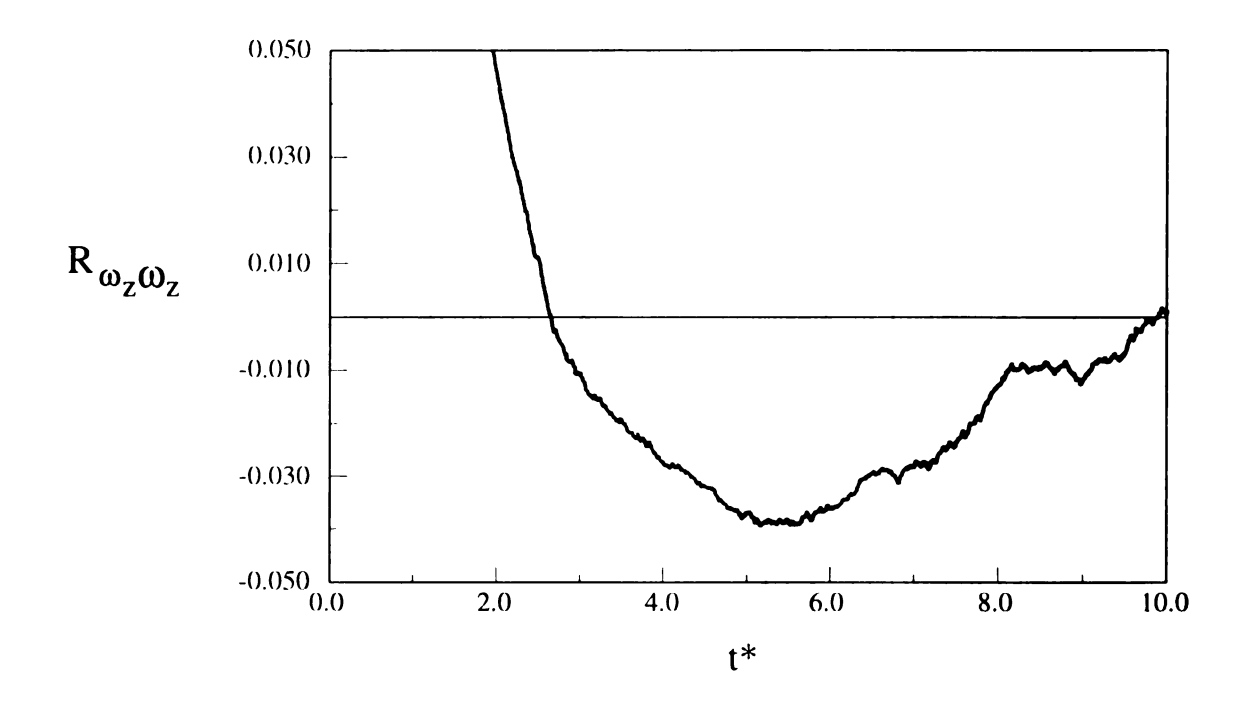


Figure 4.46 Close view of the zero crossing region of the  $\omega_z$  autocorrelation.

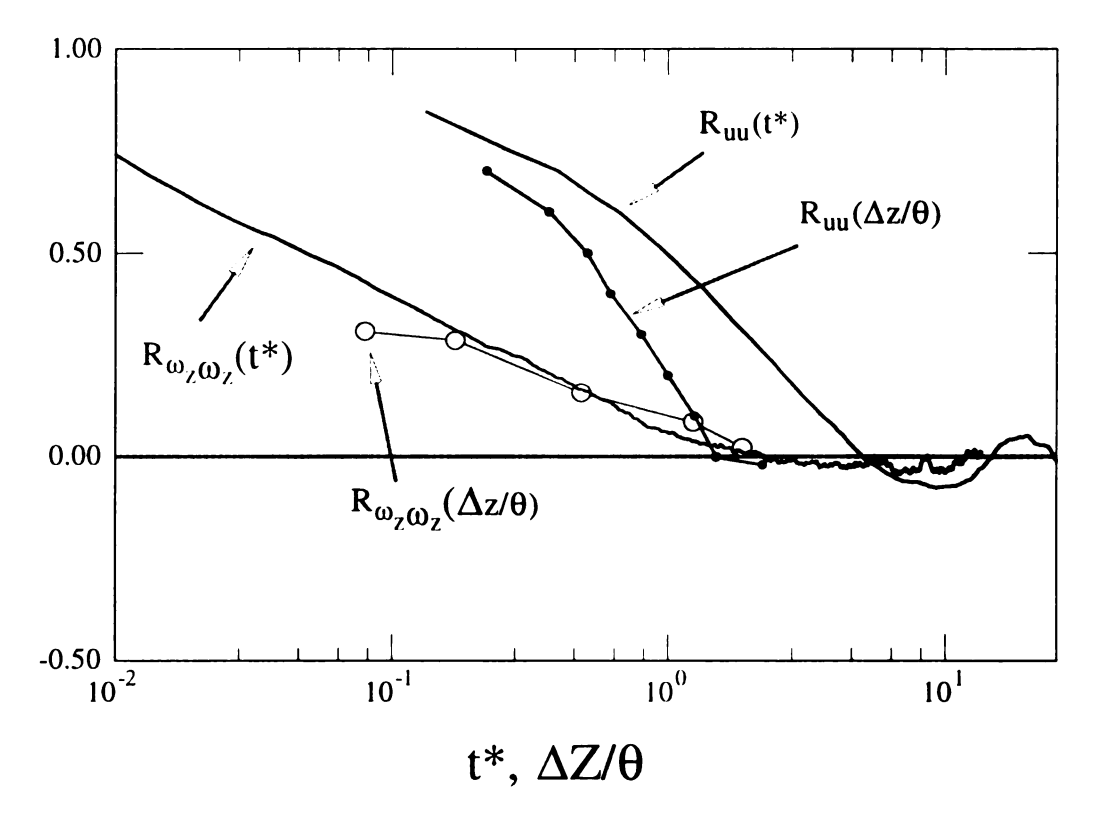


Figure 4.47 Spanwise correlation of u and  $\omega_z$  at  $\bar{u}/U_o = 0.5$  Autocorrelations of  $\omega_z$  and u are included for comparison.

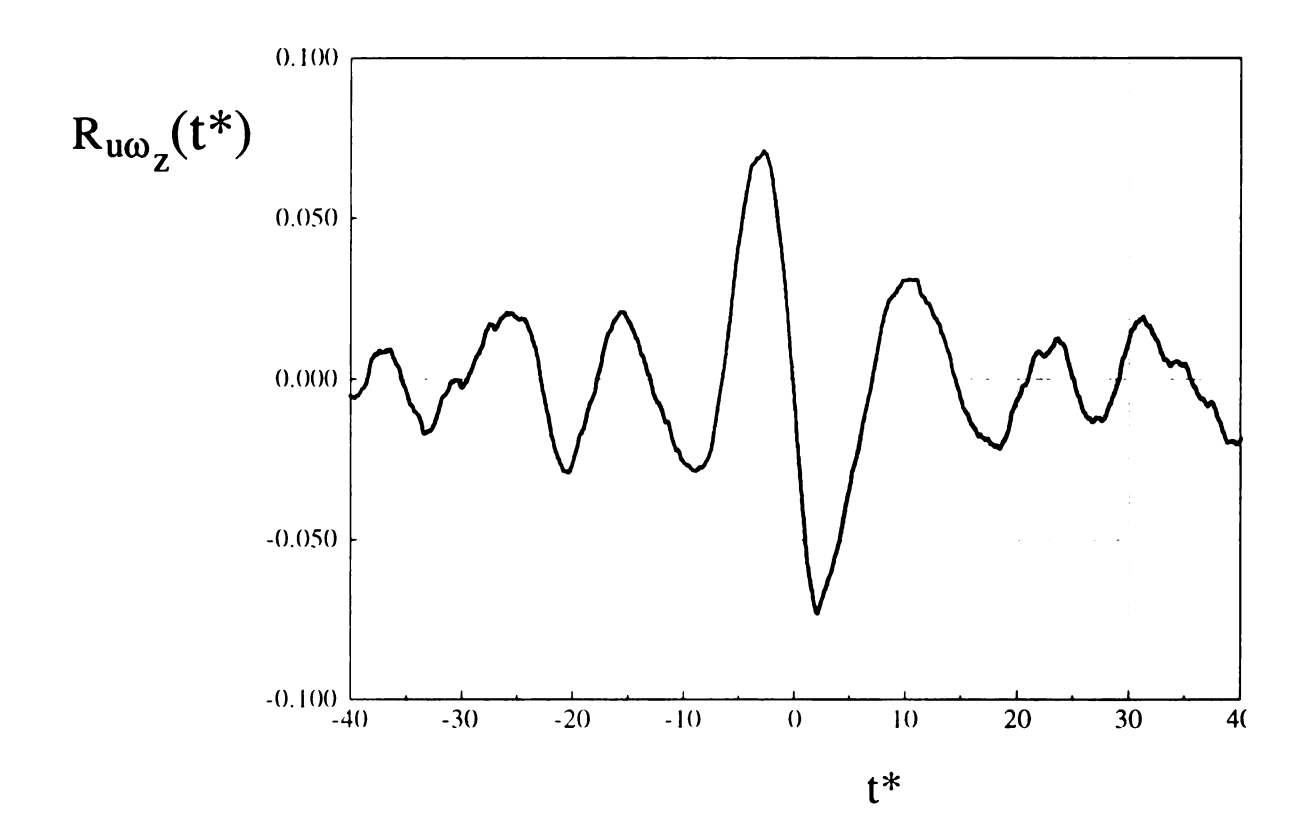


Figure 4.48 Correlation between high speed irrotational velocity fluctuations and  $\omega_z$  at  $\eta$ =0.

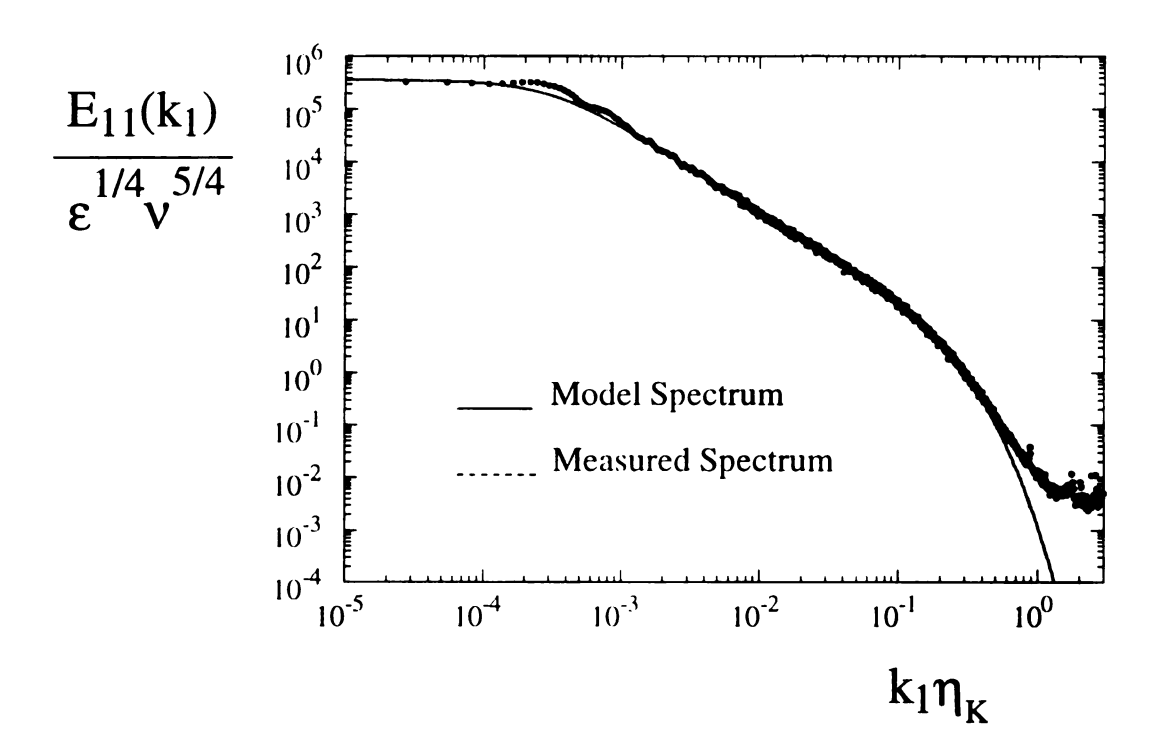


Figure 4.49 Measured and modeled one dimensional energy spectra:  $E_{11}(k_1)$ 

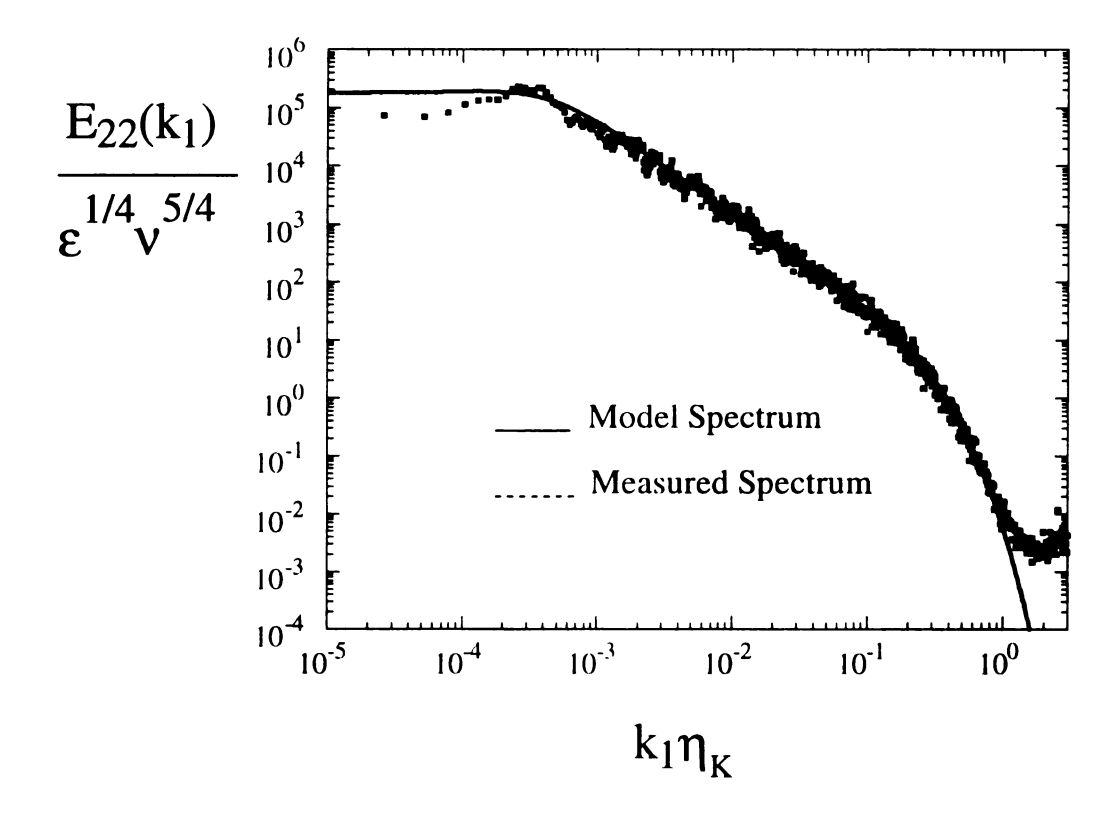


Figure 4.50 Measured and modeled one dimensional energy spectra:  $E_{22}(\kappa_1)$ 

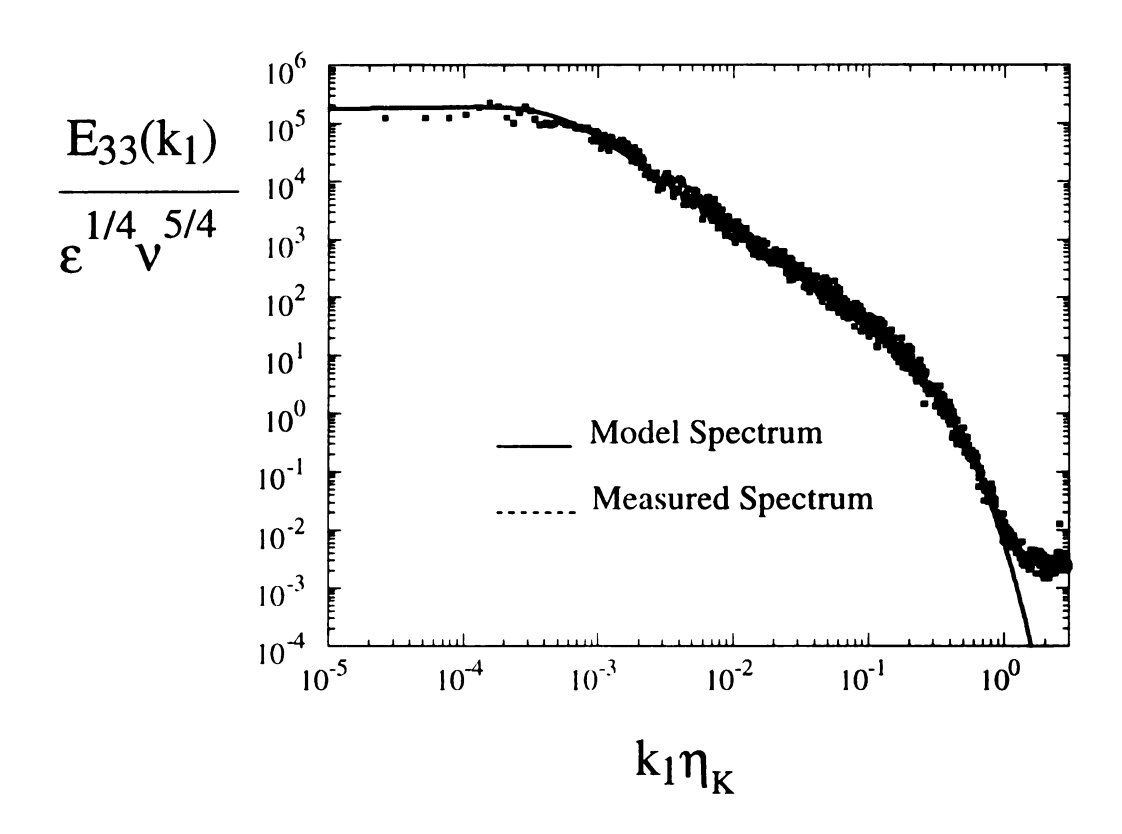


Figure 4.51 Measured and modeled one dimensional energy spectra:  $E_{33}(\kappa_1)$ 

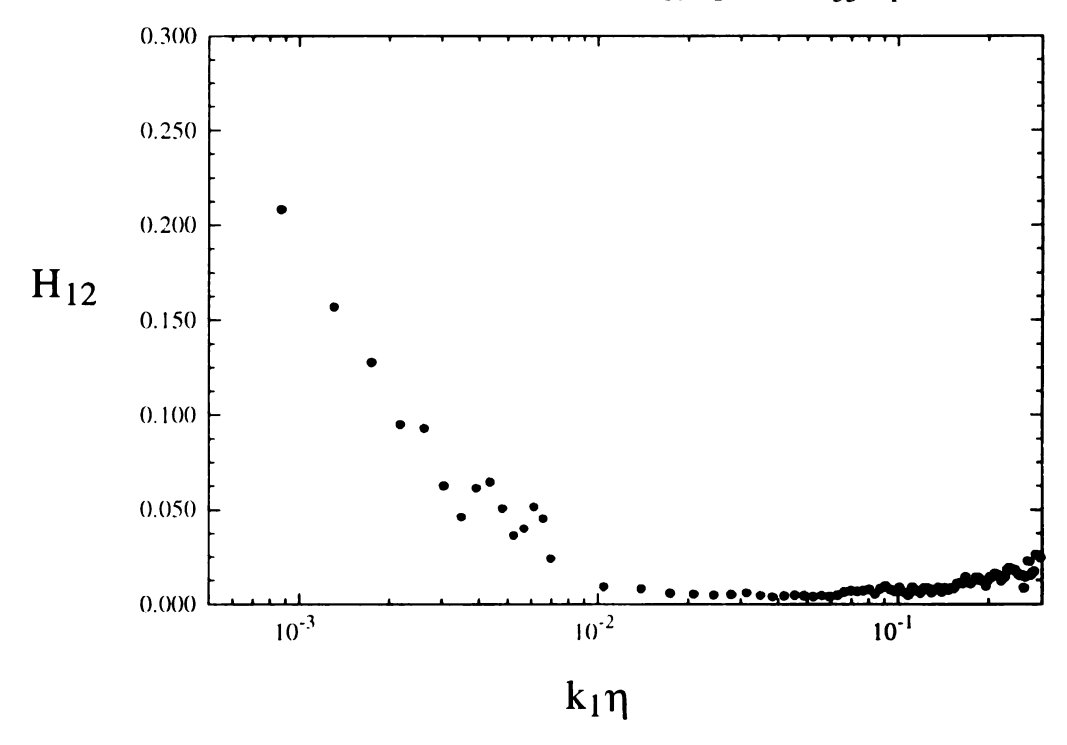


Figure 4.52 Spectral coherence function  $H_{12}$ . Note the  $k_1\eta$  rage is changed from previous figures.

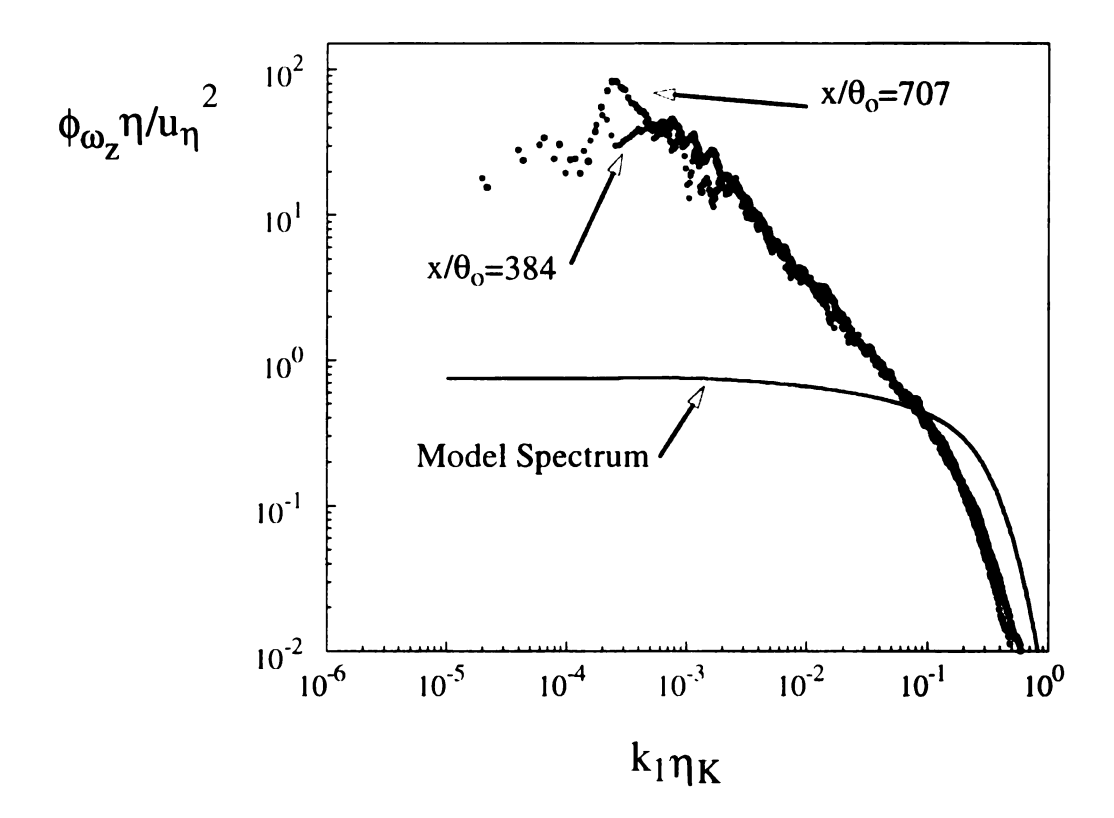


Figure 4.53 Autospectral function of vorticity. Model spectrum is from isotropic relation to  $\rm E_{11}$ .

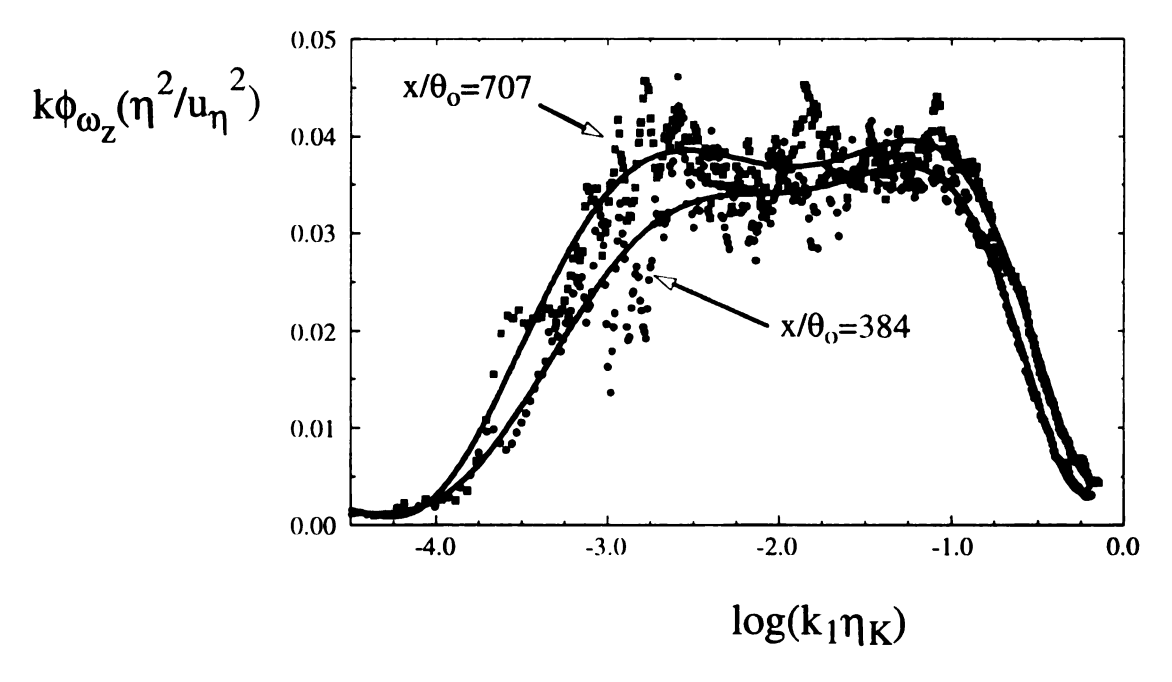


Figure 4.54 Compensated vorticity spectra to show energy contribution to enstrophy integral.

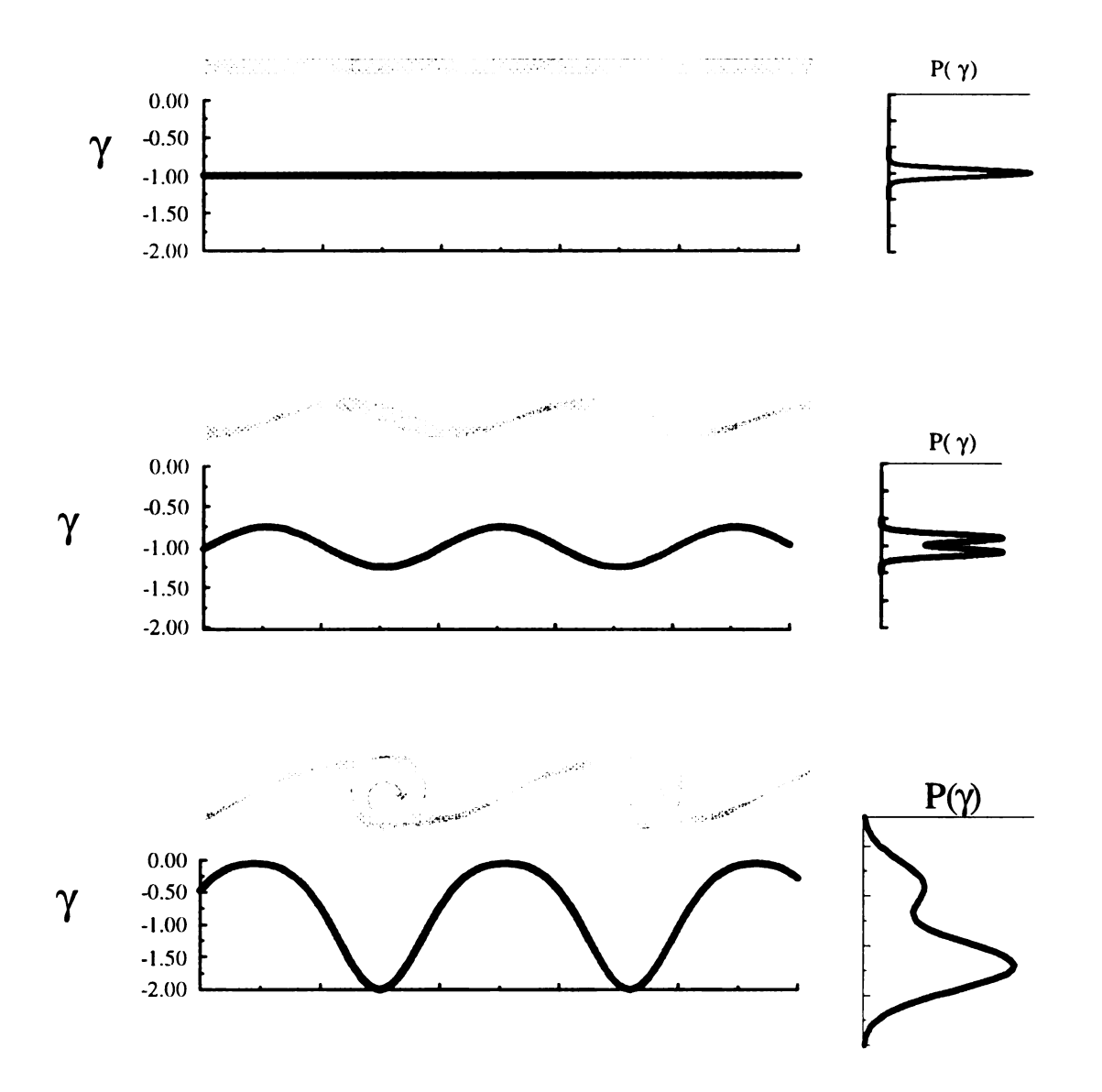


Figure 4.55 Schematic examples of  $\gamma$  for: (a) a thin uniform sheet of vorticity, (b) a sinusoidally perturbed shear layer, (c) a rolled up shear layer into Gaussian vortices. The P( $\gamma$ ) curves on the right show a likely pdf that would be experimentally recovered for each condition with Gaussian noise.

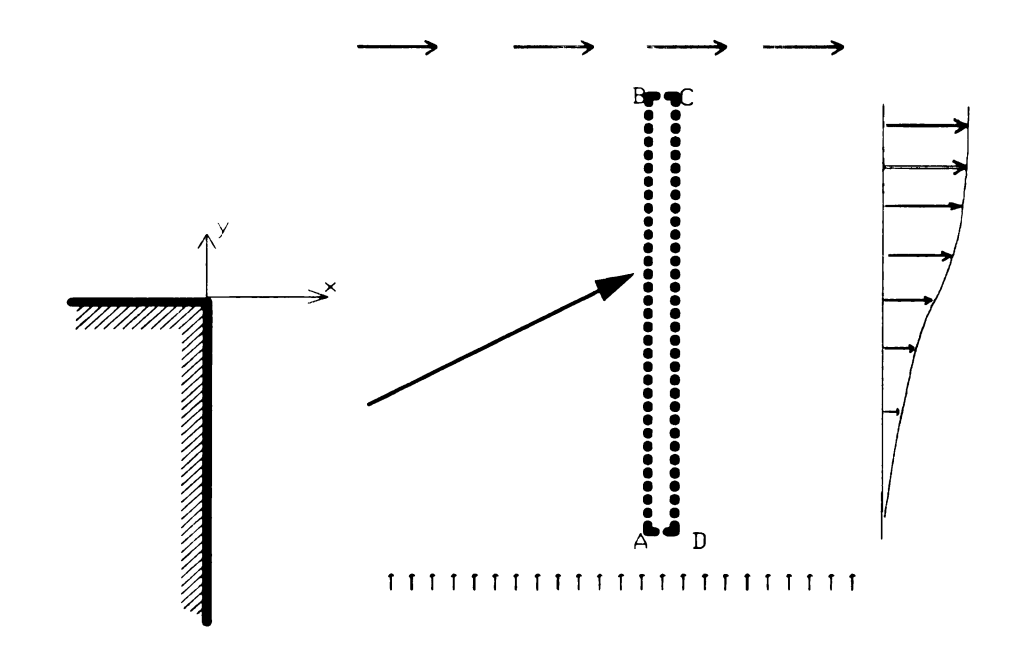


Figure 4.56 Schematic of showing the finite area of integration for the calculation of  $\gamma$ 

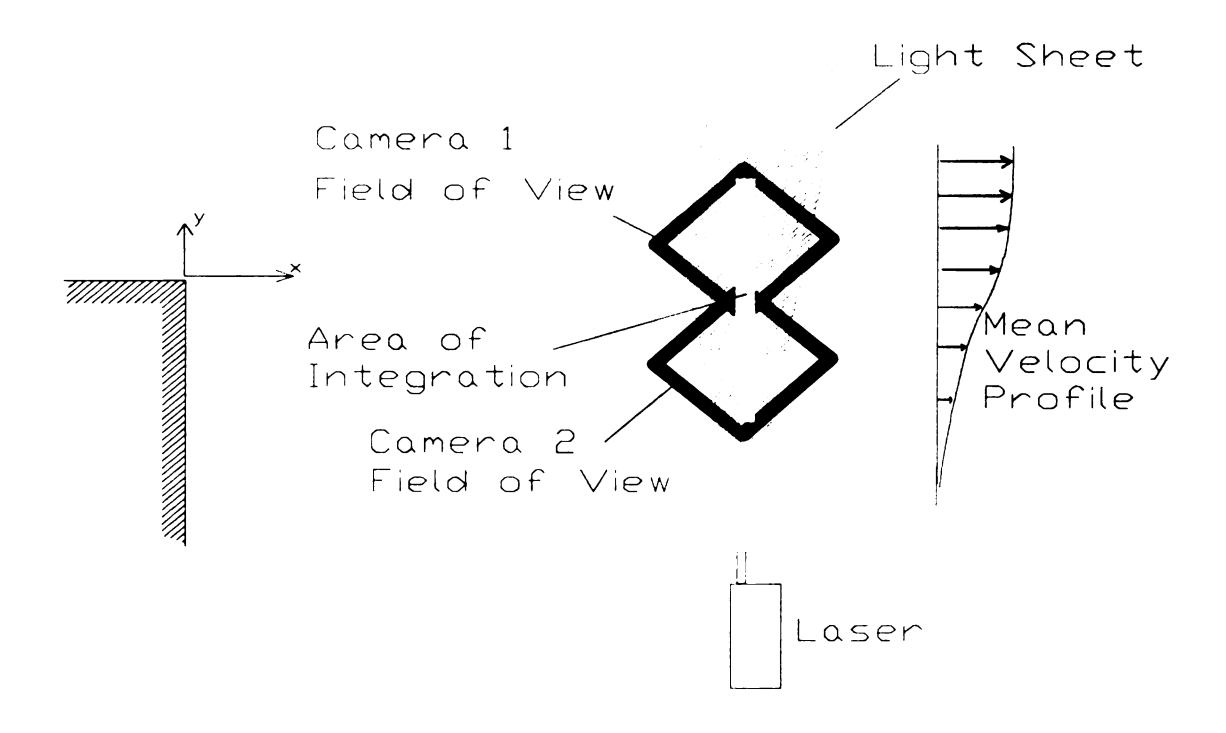


Figure 4.57 Experimental configuration for γ measurement

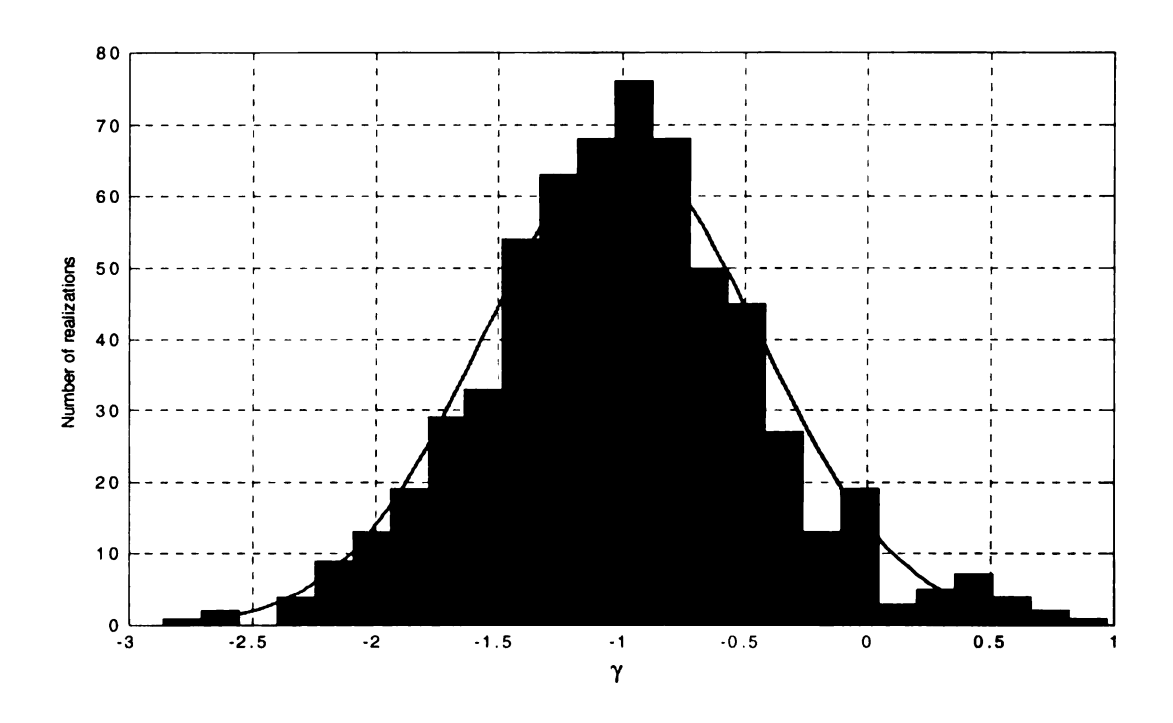


Figure 4.58 Histogram of measured  $\gamma$  values. Note that the measured vales have been corrected by a factor of 1.19 to account for the limited field of view; see Section 4.7.2.

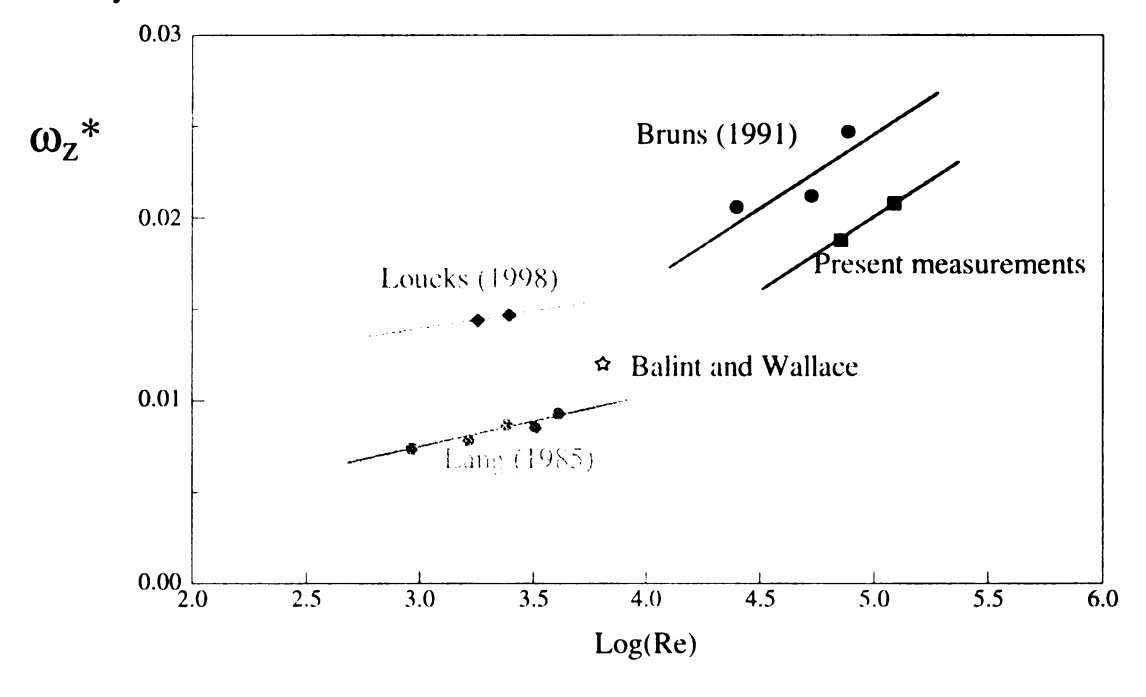


Figure 4.59 Peak vorticity measured by various researchers.

This ap This re

sented

is give

The r

entra

the s

fere cid

mo

clu

giv this

It is

me

mo

•

## Appendix A

This appendix introduces a final conclusion which is not given in the body of this thesis.

This result is related to the mechanism of entrainment, and is not central to the results presented in section 4.8. It is therefore given here as a final point of interest. The conclusion is given as the following.

The phenomenon of entrainment, defined as the movement of fluid towards the shear layer from the low speed side, would exist even if the fluid viscosity were zero. It is supposed that the observed magnitude of the entrainment would not change if the fluid viscosity were zero.

The motivation for arriving at this conclusion originated from the lack of understanding of how fluid is entrained into the shear layer. One concept is verbalized by the term "viscous entrainment." This implies the high speed fluid acts to "drag along" the fluid adjacent to the shear layer through the viscous diffusion of momentum. A second, and distinctly different concept of entrainment is termed "engulfment" by Roshko (1979). This is an inviscid entrainment mechanism in which the unsteady pressure field created by the large scale motions act to move the entrained fluid into the shear layer. As stated in the previous conclusion, fluid is also extrained from the shear layer to the high speed side. The analysis given in the following paragraphs will seek to clarify physical mechanisms that lead to this asymmetrical movement of fluid.

It is noted that Dimotakis (1986) utilized a model of point vortices to explain an inviscid mechanism of entrainment. Although the predictions of the entrainment rate given by this model are in agreement with many experimental results, the argument is heuristic in

nature, and is too simple to describe many other features of high Reynolds number shear layers. The present conclusion and the following discussion are not given to support any particular model, but simply to provide a solid argument that the mechanism which causes entrainment is an inviscid one.

The proof of the conclusion stated above begins with the results of stability theory. Specifically, it has been shown by several authors (see, for example Michalke (1965)), that the inviscid, linear stability theory implies that the shear layer is inherently unstable and that this instability will lead to disturbances which grow spatially. Huerre and Monkewitz (1985) have provided a general result for shear layer instability based on the velocity ratio  $\Delta U/2\bar{U}$  where  $\Delta U$  is the velocity difference between the two streams and  $\bar{U}$  is their average velocity. The results of Huerre and Monkewitz (1985) have shown that for values of  $\Delta U/2\bar{U} > 1.315$ , the linear instability mechanism will lead to a temporally growing shear layer; values of  $\Delta U/2\bar{U} < 1.315$  will lead to a spatially growing shear layer. For the present case ( $\Delta U/2\bar{U} = 1$ ), this result implies that disturbances will undergo spatial growth. The nonlinear growth that results from this will lead to a nonzero value of  $d\Theta/dx$ . Equation 4.4 therefore requires that the entrainment is nonzero, just as equation 4.8 requires that the shear layer is tilted at a non-zero angle with respect to the constant velocity free stream.

It is concluded from these statements that if a shear layer could exist with a fluid which has zero viscosity, the shear layer would be convectivly unstable. The resulting spatial growth would lead to entrainment. However, this does not imply that the observed rate of entrainment ( $\sigma \approx 0.035$ ) would be unchanged by the hypothetical case of zero viscosity, as

indicated by the supposition above. The following arguments will support the notion that entrainment is an *entirely* inviscid phenomenon.

The first argument is given by the observation that the growth rate is linear. That is,  $d\Theta / dx$  is not a function of the Reynolds number, and therefore neither is the entrainment velocity. It is not correct to literally take this limit to Re= $\infty$ , because the Navier-Stokes equations become singular. However, the physical implications of the singular nature of the momentum equation are usually only important near solid walls where the boundary conditions must be applied. In summary, since the value of the Reynolds number does not effect the velocity of entrainment, it can be inferred that the phenomenon responsible for entrainment is not effected by the viscosity of the fluid.

In addition to supporting the inferences above, additional insight can be obtained by observing the mechanism of viscous entrainment in two model flow fields. First, the idea of viscous entrainment can be studied from the "scraping plate" problem. This is described as steady flow of a viscous fluid in the upper half plane (y>0), with the boundary conditions (u,v)=(U<sub>0</sub>,0) at y=0,  $x \in (-\infty,\infty)$ . The entrainment rate is found to be  $v_e = v(x,\infty) \sim \sqrt{x}$ . This solution shows that a viscous boundary conditions with constant velocity leads to an entrainment field which is dependent on the streamwise coordinate. The second idealized flow considered is the "stretching plate" problem. The boundary conditions are similar to the scraping plate problem, except the wall boundary condition is accelerating spatially at a rate a. That is, u(x,0)=ax, v(x,0)=0. The solution of this problem for large distances from the wall yields the entrainment rate:  $v_e = v(x,\infty) = \sqrt{av}$ , where v is the kinematic viscosity of the fluid. In this solution, the entrainment velocity is a con-

stant, as it
the work?
observed
That is, t
In summ
through
movem
ena, w
scale r

of the

stant, as in the actual shear layer. It is then instructive to note that if air were to be used as the working fluid, the acceleration parameter that would be required to generate the value observed in the present physical shear layer:  $v_c = 0.035U_o = 0.25 \text{m/s}$ , is a=4160m/s/m. That is, the wall velocity would be: u(x=1,0)=4160m/s, u(x=2,0)=8320m/s, etc.

In summary, these model flows indicate that the induction of fluid towards the shear layer through the viscous diffusion of momentum is not likely to be significant. Rather, the movement of fluid towards the shear layer from the low speed side is an inviscid phenomena, which is believed to be related to the unsteady pressure field associated with the large scale motions of the flow. In this way, the present conclusion serves to motivate several of the results that were described in the bode of this thesis regarding the large scale motions of the flow.

## **REFERENCES**

Adrian, R. J., C. D. Meinhart, and C. Tomkins. 2000. Vortex organization in the outer region of the turbulent boundary layer. *Journal of Fluid Mechanics* **422**, 1–53.

Ali, S.K., Klewicki, C.L., Disimile, P.J., Lawson, I., Foss, J.F., 1985, "Entrainment region phenomena for a large plane shear layer," proceedings, Fifth symposium on Turbulent Shear Flows.

Andreopoulos, Y., Honkan, A., 2001, "An experimental study of the dissipative and vortical motion in tubulent boundary layers," vol. 439, pp. 131-163.

Antonia, R.A., Browne, L.W., Shah, D.A., (1987) "Characteristics of vorticity fluctuations in a turbulent wake," *J. Fluid Mech*, vol. 189, pp349-365.

Antonia, R.A., Shafi, H.S., Zhu, Y., (1996) "A note on the vorticity spectrum," Phys. Fluids 8 (8), p2196.

Antonia, R.A., Zhou, T., Zhu, Y., (1998) "Three-component vorticity measurements in a turbulent grid flow," J. Fluid Mech, vol. 374, pp29-57.

Balint, J.L., Wallace, J.M., 1988 "Statistical properties of the vorticity field of a two-stream turbulent mixing layer," Advances in Turbulence 2, Springer-Verlag, NY.

Batchelor, G. K., (1946) "The theory of axisymmetric turbulence," *Proc. R. Soc. Lond. A* **186**, 480-502.

Bejan, A., 1995, Convective Heat Transfer, John Wiley and Sons, New York.

Bradshaw, P., 1966, "The effect of initial conditions on the dvelopment of a free shear layer," *J. Fluid Mech.*, vol. 26, pp25-236.

Browand, F.K., Latigo, B.O., 1979, "Growth of hte two-dimensional mixing layer from a turbulent and nonturbulent boundary layer," *Phys. Fluids*, vol. 22, No. 6, pp 1101-1019.

Browand, F.K., Trout T.R., 1980, "A note on spanwise structure in the two-dimensional mixing layer," *J. Fluid Mech.*, vol 117, pp771-781.

Browand, F.K., Trout T.R., 1985, "The turbulent mixing layer: geometry of large vortices," *J. Fluid Mech.*, vol 158, pp489-509.

Browand, F.K., Weidman, P.D., 1976, "Largest scales in the developing mixing layer," *J. Fluids Mech.* Vol 76, pp127-144.

Browne, L.W.B., Antonia, R.A., and Shah, D.A., (1987) "Turbulent energy dissipation in a wake," *J. Fluid Mech.*, vol. 179, pp307-326.

Brown, G.L., Roshko, A., "On density effects and large structure in turbulent mixing layers," *J. Fluid Mech.*, vol 64, pp775-816.

Bruns, J., 1990, "Evaluation of hot-wire velocity and transverse vorticity measurements in a single stream shear layer and its parent boundary layer," Diplomarbeit, Technische Hochshule Aachen.

Bruns, J.M., Haw, R.C., Foss, J.F., 1991, "The velocity and transverse vorticity field in a single stream shear layer," in the <u>Eighth Symposium on Turbulent Shear Flows</u>, Technical University of Munich, September 9-11.

Bruun, H.H., 1995, *Hot-wire Anemometry*, Oxford University Press.

Cao, N., Chen, S., Sreenivasan, K.R., 1996, "Properties of velocity circulation in three-dimensional turbulence," *Phys. Rev. Let.* Vol. 76, No. 4, pp 616-619.

Champagne, F.H., Pao, Y.H., Wygnanski, I.J., 1976, "On the two-dimensional mixing region," *J. Fluid Mech.* Vol. 74, pp.209-250.

Dimotakis, P.E., 1986, "Two-dimensional shear-layer entrainment," AIAA Journal, Vol. 24, No. 11, pp1791-1796.

Dimotakis, P., Brown, G., 1976, "The mixing layer at high Reynolds number: large-structure dynamics and entrainment," *J. Fluid Mech.*, vol 78, pp535-560.

Foss, J.F., 1981, "Advanced techniques for transverse vorticity measurements," Proceedings, 7th Biennial Symposium on Turbulence, Univ. of Missouri-Rolla.

Foss, J.F., 1994, "Vorticity considerations and planar shear layers," *Experimental Thermal and Fluid Sciences*, Vol. 8, pp. 260-270.

Foss, J.F., 1998, Private communication.

Foss, J.F., Haw, R.C., 1990, "Transverse vorticity measurements using a companct array of four sensors," In The Heuristics of Thermal Anemometry, ed. DE STock, SA Sherif, AJ Smits, ASME-FED 97: 71-76, pp98.

Foss, J.F., Bohl, D.G., Kleis, S.J., 1995, "Activity Intermittency in a two-stream shear layer," Proceedings of the Tenth Symposium on Turbulent Shear Flows, The Pennsylvania State University, University Park, PA.

Freymuth, P., 1966, "On transition in a separated laminar bloundary layer," *J. Fluid Mech.* Vol. 25, pp.683-704.

Hama, F.R., 1962, "Streaklines in a perturbed shear flow," Phy. of Fluids, Vol. 5, No. 6, pp 644-650.

Haw, R.C., Foss, J.K., Foss., J.F., 1989, "Vorticity based intermittency measurements in a single stream shear layer," in <u>Advances in Turbulence 2</u>, eds. Fernholz, H., and Fiedler, H., Springer-Verlag, Berlin.

Ho, C., Huerre, P., 1984, "Perturbed free shear layers," Ann. Rev. Fluid Mech., vel 16, pp365-424.

Holmes, Lumley, Berkooz, 1992, <u>Coherent Structures</u>, <u>Symmetry</u>, <u>Dynamical Systems and Turbulence</u>, Cambridge University Press.

George, W.K., Hussein, H.J., (1991) "Locally axisymmetric turbulence," *J. Fluid Mech.* Vol. 233, pp.1-23.

Hamelin, J. Alving, A.E., 1996, "A low-shear turbulent boundary layer," *Phys. Fluids*, vol. 8, No. 3 pp 789-804.

Hileman, J., Samimy, M., 2001, "Turbulence Structures and the Acoustic Far-Field of a Mach 1.3 Jet," AIAA Journal, Vel. 39, No. 9, pp1716-1727.

Huerre, P., Monkewitz, P.A., 1985, "Absolute and convective instabilities in free shear layers," *J. Fluid Mech.*, Vol. 159, pp. 151-168.

Hussain, A.K.M.F., Zedan, M.F., 1978, "Effects of the initial condition on the axisymmetric free shear layer: effects of the initial momentum thickness," *Phys. Fluids*, Vol. 21, No. 7.

Hussain, A.K.M.F., Zaman, K.B.M.Q., 1985, "An experimental study of organized motions in the turbulent plane mixing layer," *J. Fluid Mech.* Vol. 159, pp.85-104.

Kim, J.H., 1989, PhD thesis, University of Berlin.

Klewicki 1989, PhD thesis, Michigan State University.

Klewicki, J.C., Falco, R.E., Foss, J.F., 1992, "Some characteristics of hte vortical motions in the outer region fo turbulent boundary layers," *J. of Fluids Engineering*, Vol. 114, pp. 530-536.

Kock am Brink, B., Foss, J.F., 1993, "Enhanced Mixing via Geometric Manipulation of a Splitter Plate," AIAA paper no. 93-3244, AIAA Shear Flow Conference, July 6-9, Orlando, FL.

Kolmogorov, A.N., 1941, "The local structure of turbulence in incompressible viscous fluid for very large Reynolds number," translated in <u>Turbulence and Stochasite Processes:</u> <u>Kolmogorov's ideas 50 years on</u>, ed. Hunt, J.C.R., Phillops, O.M., and Williams, D., The Royal Society, London, 1991.

Koochesfahani, M.M., Catherasoo, C.J., Dimotakis, P.E., Gharib, M, and Lang, D.B., (1979) "Two-point LDC measurements in a plane mixing layer," *AIAA J.*, Vol. 17, No. 12, pp1347-1351.

Koochesfahani, M.M., Cohn, R., MacKinnon, C., 2000, "Simultaneous whole-field measurements of velocity and concentration fields using a combination of MTV and LIF," *Meas. Sci. Technol.* Vol. 11, pp 1289-1300.

Lang, D.B., 1985, PhD Dissertation, Cal. Inst. of Tech.

Liepmann, H.W., Laufer J., 1947, "Investigations of free turbulent mixing," NACA Report No. 1257.

Loucks, R.B., 1998, "An Experimental Examination of the Velocity and Vorticity Fields in a Plane Mixing Layer," Ph.D Thesis, University of Maryland.

Lui, X., 2000, Ph.D. Thesis, Department of Aerospace and Mechanical Engineering, University of Notre Dame.

Lumley, J.L., (1965) "Interpretation of time spectra measured in high-intensity shear flows," Phys. Fluids. 8, 1056-1062.

Mehta, R.D., Westphal, R.V., 1986, "Near-field turbulence properties of single and two-stream plane mixing layers," *Experiments in Fluids*, 4, pp. 257-266.

Michalke, A., 1965, "On spatially growing disturbances in an inviscid shear layer," *J. Fluid Mech*, vol. 23, pp521-544.

Monin, A.S., Yaglom, A.M., 1975, <u>Statistical Fluids Mechanics: Mechanics of Turbulence, Vol 2</u>, The MIT Press, Cambridge.

Naguib, A., 1992, PhD thesis, Illinois Institute of Technology, Chicago, IL.

Narayanan, S., Hussain, F., 1996, "Measurements of spatiotemporal dynamics in a forced plane mixing layer," *J. Fluid Mech.*, vol 320, pp71-115.

Ong, L., Wallace, J.M., 1998, "Joint probability density analysis of the structure and dynamics of the vorticity field of a turbulent boundary layer," vol 367, pp. 291-328.

Ong, L., Wallace, J.M., 1995, "Local isotropy of hte vorticity field in a boundary layer at high Reynolds number," in Advances in Turbulence V, edited by R. Benzi (Kluwer, Dordrecht), p. 392.

Panton, R.L., 2001, "Overview of the self-sustaining mechanicsm of wall turbulence," *Progress in Aerospace Sciences*, Vel. 37, pp. 341-383.

Pope, S., 2000, Turbulent Flows, Cambridge University Pres.

Pozrikidis, C., Higdon, J.J.L., 1985, "Nonlinear Kelvin-Helmholtz instability of a finite vortex layer," J. Fluid Mech., Vol. 157, pp. 225-263.

Pui, N.K., Gartshore, I.S., (1979) "Measurements of the growth rate and sturcture in plane turbulent mixing layers," *J. Fluid Mech.*, vol. 91, pp111-130.

Rogers, M.M., Moser, R.D., 1994, "Direct simulation of a self-similar turbulent mixing layer," *Phys. Fluids*, Vol. 6, No. 2.

Roshko, A., 1979, "Structure of turbulent shear flows: a new look," AIAA Journal, Vol. 14, No. 10, pp1349-1357.

Saddoughi, S.G., Veeravalli, S.V., 1994, "Local isotropy in turbulent boundary layers at high Reynolds number," *J. Fluid Mech*, vol. 189, pp333-372.

Schmidt, T.P., Ali, S.K., and Foss, J.F., 1986, "Relative efficiencies for parallel and perpendicular entrainment flow paths," *AIAA Journal*, Vol. 24, No. 9.

Slessor, M.D., Bond, C.L., Dimotakis, P.E., 1998, "Turbulent shear-layer mixing at high Reynolds numbers: effects of inflow conditions," *J. Fluid Mech*, vol. 376, pp115-138.

Sreenivasan, K.R., Antonia, R.A., 1997, "The phenomenology of small-scale turbulence," *Ann. Rev. Fluid Mech.*, Vol 29, pp. 435-472.

Tennekis and Lumley, 1972, A First Course in Turbulence, MIT Press.

Thomas, F.O., 1991, "Structure of mixing layers and jets," *Appl. Mech. Rev.*, vol 44, No 3.. pp119-153.

Townsend, 1975, The Structure of Turbulent Shear Flow, Cambridge University Press.

Wallace, J.M., Foss, J.F., 1995, "The Measurement of Vorticity in Turbulent Flows," Annu. Rev. Fluid Mech. 27, pp469-514.

Winant, C.C., Browand, F.K., 1974, "Vortex pairing: the mechanism of turbulent mixing layer growth at moderate Reynolds number," *J. Fluid Mech.*, Vol. 63, pp. 237-255.

Wygnanski, I., Fiedler, H.E., 1970, "The two-dimensional mixing region," *J. Fluid Mech.* Vol. 41, pp.327-361.

Wyngaard, J. C., and Clifford S.F., (1977) "Taylor's hypothesis nad high-frequency turbulence spectra," *J. Atmos. Sci.* 34, 922-929.

